UNIVERSITÀ DELLA CALABRIA

Dipartimento di Fisica

Dottorato di Ricerca in

SCIENZE E TECNOLOGIE FISICHE, CHIMICHE E DEI MATERIALI
IN CONVENZIONE
CON IL CONSIGLIO NAZIONALE DELLE RICERCHE

CICLO

XXIX

Smart composite nanomaterials for atmospheric pollution detection

Settore Scientifico Disciplinare CHIM/05

Coordinatori
Supervisori/Tutor: Ch.mo Prof. Nicola Pirrone

                  Dott.ssa Antonella Macagnano

                  Dott.ssa Barbara Richichi

Coordinatore
di dipartimento: Prof. Vincenzo Carbone

Dottoranda: Dott.ssa Viviana Perri

To myself, to my determination

and to those who have always believed in me

Index

Acknowledgements

At the of this long and wonderful experience, I feel obliged to express my gratitude to the people who have supported me in every way during the months of laboratory work and for the preparation of this thesis work, especially in the hardest and most delicate moments; it is on these occasions that a word of comfort can be useful to regain strength and move on.

A special thanks to Professor Nicola Pirrone for giving me the opportunity to attend an important and authoritative scientific reality as the Institute of Atmospheric Pollution of National Council of Research and for not having never miss his support whenever I needed.

A big hug filled with gratitude to Dr. Antonella Macagnano and to all scholars and technicians of the structure for welcoming me in the group with loyalty, professionalism and sympathy and for the invaluable advice for my final work.

The same dose of affection comes to Dr. Barbara Richichi and the wonderful group of researchers, now become very dear friends, of the Scientific Centre of the University of Florence in Sesto Fiorentino.

I will never forget the long study days spent together and the moments of leisure who saw me grow up, meet new people, visit wonderful places and broaden my knowledge in a field of science almost unknown.

Thank you, finally, to my wonderful family for financial, moral and psychological support and for believing and supported all my choices of life, work and study. The same family that already on the occasion of my graduation had answered quietly and proudly to who, some years before, had not confided in me to achieve important and prestigious objectives. Mom and dad taught me that work and the sacrifices always pay and also this time they have "seen along."

Viviana

Preface

The content of this Ph.D thesis has been organized as follows: after a brief introduction on nanotechnologies and their main applications, the electrospinning technology will be described as a successful strategy to create smart and ultrasensitive nanosensors. The main characteristics of gas sensors will be listed in Chapter 3 focusing on sensitive nanocomposite materials designed for chemical sensors, more specifically suitable polymers as polyaniline and poly-3-hydroxybutirrate (PANi and PHB), semiconductor metal oxides (QDs, TiO_2) and gold nanoparticles (AuNPs). In subsequent chapters it will be described in detail the manufacture, the characteristics, the detection mechanism and numerous advantages of nanosensors obtained using materials just mentioned. As will be described in Chapter 5, the combination of suitably functionalized nanofibers of titania with core/shell QDs nanoparticles has allowed to obtain a chemical sensor, in the solid state, capable to detect nitrogen compounds into the atmosphere. The resulting fibers were studied as potential optical sensors due to the quenching of the fluorescence after interaction with the gas (NH_3). Ammonia, furthermore, with other pollutants such as VOCs (triethylamine and acetic acid), have been detected using a biodegradable chemical sensor, described in Chapter 6, obtained by electrospinning technology depositing a polymer blend containing polyaniline and poly-3-hydroxybutirrate (PANi/PHB) on chemoresistors (IDEs). Chapters, 7 and 8 respectively, will focus on two new detection systems, an active sensor (IDEs) and a passive sampler for the monitoring of elemental mercury ($Hg°$), another abundant pollutant in the atmosphere. For the manufacture of both systems, the photocatalytic properties of titania have been exploited providing a selective growth irradiation of gold nanoparticles, using a precursor of the gold nanoparticles (AuNPs) and a suitable organic capping reagent under UV-light

exposure. Finally, in summary and conclusions, all the research activity will be resumed enhancing the novelty, the potentials and the future perspectives.

Introduction

The exhaust from automobiles, emissions from manufacturing industries and factories, suspended particles and gases are among the unwanted substances that are deteriorating the quality of air around us and represent one of the major causes of air pollution. These harmful substances (solid particles, liquid droplets, or gases) can have adverse effects on humans and the ecosystem and are introduced in the air from various sources that can be of natural origin or man-made. Most of the pollution of the air is caused because of the ignorance and negligence of humans but it is also true that some time the air can be polluted by natural causes. Forest fires produce giant masses of smoke which tend to drift over nearby villages and cities. Occasional eruptions of volcanoes can eject huge amount of volcanic ash and lava onto the earth surface which introduces dust and smoke into the atmosphere thereby polluting the air. Natural air pollution can also be caused from the decay of rocks over time and the release of gases such as radon which has adverse effects on our health. Air pollutants can be distinguished into two types: primary and secondary pollutants. Primary pollutants are usually produced from a process, such as ash from a volcanic eruption. Other examples include carbon monoxide gas from motor vehicle exhaust, or the sulfur dioxide released from factories. Secondary pollutants are not emitted directly. Rather, they are formed in the air when primary pollutants react or interact. Ground level ozone is a prominent example of a secondary pollutant. Some pollutants may be both primary and secondary, they are both emitted directly or formed from other primary pollutants. Major primary pollutants produced by human activity include: carbon dioxide (CO_2); sulfur oxides (SO_x), particularly sulfur dioxide; nitrogen oxides (NO_x) , particularly nitrogen dioxide; carbon monoxide (CO); volatile organic compounds (VOC), VOCs are a well-known outdoor air pollutant. They are categorized as either methane (CH_4) or non-methane

(NMVOCs); particulates, alternatively referred to as particulate matter (PM), atmospheric particulate matter, or fine particles, are tiny particles of solid or liquid suspended in a gas; persistent free radicals; toxic metals, such as lead and mercury, especially their compounds; chlorofluorocarbons (CFCs); ammonia (NH_3), emitted from agricultural processes; odors, such as from garbage, sewage, and industrial processes; radioactive pollutants, produced by nuclear explosions. Secondary pollutants include: particulates created from gaseous primary pollutants and compounds in photochemical smog; ground level ozone (O_3) formed from NO_x and VOCs. Many studies have confirmed that indoor air quality is highly affected by outdoor air quality. Therefore, to solve our pollution problems, both indoor and outdoor environment should be considered. A number of air pollutants have been recognized to exist indoors, including NO_x, SO_2, O_3, CO, volatile and semi-volatile organic compounds (VOCs), PM, radon, and microorganism. Some of these pollutants (e.g., NO_x, SO_2, O_3, PM) are common to both indoor and outdoor environments, and some of them may be originated from outdoors. These air pollutants can be inorganic, organic, biological or even radioactive. Their effect on humans depends on their toxicity, concentration and exposure time, and may vary from person to person. The most common effect is called sick building syndrome (SBS), in which people show effects such as irritation of nose, eyes and throat, skin ailments, allergies, and so on. The cause may not be identified, but the syndrome may disappear after that an affected person leaves the office or building. Indoor air quality can be improved and SBS can be reduced when the ventilation rate of the room is improved **(Wargocki, P. et al., 2000).** The indoor air quality also affects the performance of workers and office staff. Wyon (2004) found that the performance of real office work would be significantly and substantially affected by changes in indoor environmental quality and that the work performance could be significantly enhanced by removing common indoor sources of air pollution **(Wyon, D. P., 2004).** Air pollution besides to cause to serious health problems such as respiratory

4

diseases, cardiovascular and cancer, it is responsible of hundreds of thousands premature deaths in several countries in the world. WHO estimated in 2012 that air pollution claimed the lives of almost 3.7 million people around the world in just one year. This research project was carried out mainly at the Institute of Atmospheric Pollution Research of National Research Council (IIA-CNR) in Rome. Taking into account the need to support European directives, international treaties and programs of atmospheric and environmental pollution (i.e., UNECE-LRTAP, Minamata Convention, UNEP, GEOSS, Earth Cube) and the need to reduce investment costs and operating of observing sites in remote locations and difficult to access, the study has been focused on developing sensor devices low-powered and nanostructured composite materials for monitoring different pollutants and complex environments, specifically, nitrogen derived gaseous pollutants (NH_2, NO_2, NO_x) and elemental mercury (Hg°). The goal of the research project has been therefore to develop composite nanostructured materials for obtain "advanced" and "smart" sensors characterized by selectivity, sensitivity and small size, which do not require high investment and operating costs, which allow an environmental monitoring also in situ and that they are equipped by advanced interfaces for data transmission and their remote management.

Chapter 1

Nanotechnology: nanomaterials, nanocomposite, applications and potentiality.

1.1 Nanotechnology

The term "nanotechnology" is gaining more and more popularity. It is, in fact, used to describe a variety of fields of research and development, often interdisciplinary **(Laurecin, C. T. et al., 2009)** and shall be defined as the science, engineering, and technology conducted at the scale that range between 1 to 100 nanometers. The prefix "nano" is derived from the ancient Greek "nanos", meaning "dwarf". Today, "nano" is used as a prefix that means "billionth" or a factor of 10^{-9}. Coupling the word "nano" with the unit "meter" brings the term "nanometer", which indicates a unit of spatial measurement that is one billionth of a meter. By comparison, the diameter of an average human hair is approximately 100,000 nm and a red blood cell is about 7,000 nm in diameter **(Alberts, B. et al., 2004)** (**Figure1.1**).
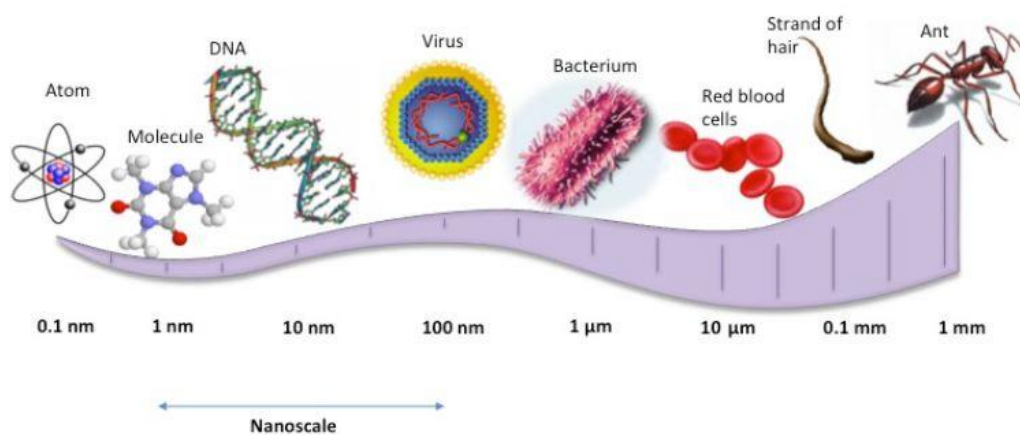
Figure 1.1: Examples of the size and the scale of nanotechnology

The "nanoworld" is thus populated by objects such as atoms, molecules, which can be properly assembled into "nanostructures". The nanotechnology objectives are precisely realize, study and take advantage of the nanostructures.

The concept of nanotechnology was introduced for the first time by the physicist Richard Feynman, at the American Physical Society meeting at the California Institute of Technology (CalTech) in 1959, with a talk entitled "There's Plenty of Room at the Bottom". In his talk, Feynman described a process in which scientists would be able to manipulate and control individual atoms and molecules **(Feynman, R., 1960).** However, the modern era of nanotechnology began only in 1981, when the scanning tunneling microscope that could "see" individual atoms was developed and used **(Binnig, G. et al., 1982)**. Already in 1974, it was, however, patented the first molecular electronic device by IBM **(Eigler, D. M. et al., 1990)**. In 1985 he came to the discovery of fullerene **(Thrall, J. H., 2004)** and subsequently to carbon nanotubes **(Ajayan, P. M. et al., 1999).** The fullerene, together with the graphite and the diamond, is the only stable molecule composed solely of carbon atoms. It is also referred to as C60 carbon, as constituted by sixty carbon atoms and has the shape of an icosahedron which has been truncated to 12 vertices. In 1991 Sumio Iijima, researcher of NEC Corporation, discovered that the carbon could be organized, as well as in spheres, even in pipes from a few nanometers variable diameter. These structures are called nanotubes and represent the absolute best known nanomaterials **(Ajayan, P. M. et al., 1999).** Subsequent developments have led to nurture interest in the single-electron devices **(Konstantin, K., 1999),** devices based on DNA **(Christof, M. et al., 2002),** molecular electronics and has led to study nanocrystals and quantum dots **(Rao, C. N. R. et al., 2004; Smith, M. et al., 2009).** However, nanotechnology anticipated applications range from optoelectronics **(Gisev, A. I. et al., 2006; Kamat, P. V. et al., 1997)**, single electron transistors and light emitters **(Klein, D. L. et al., 1997; Liu, C. H. et al., 2007)**, non-linear optical

devices (**Wang, Y., 1991; Gleiter, H., 2000**), catalysis (**Skorokhod, V. et al., 2001; Pokropivny, V. V. et al., 2007**), solar energy conversion (**Hagfeldth, A. et al., 2000; Bueno, J. T. et al., 2004**) photonic band gap materials (**Moran, C. E. et al., 2004**) and biomedical applications (**West, J. L. et al., 2000; Salata, O. V., 2004**). Innovation in knowledge and technology is the key element of the development and welfare of this new society; micro and nanotechnologies offer the ability to design and introduce innovation to the stairs, where the effects on the characteristics and performance of the products develop the maximum potential. One of the parameters that are strongly connected to miniaturization and nanotechnology is surface-to-volume ratio. This parameter is of fundamental importance in applications involving chemical catalysis and nucleation of physical processes. In general, surface area to volume ratio increases with a decrease in the characteristic dimensions of a material, and vice versa. A particle with a size of 30 nm has 5% of its atoms on its surface, whereas a particle of 3 nm has as much as 50% of its atoms on the surface (**The Royal Society, 2004**). Therefore, as the material size decreases, a greater portion of the atoms are found at the surface compared to those inside. It has also been found that some materials that are inert in their bulk form are reactive when produced in a nanoscale form. Therefore, nanomaterials have a much greater surface area per unit volume compared with larger particles. This leads to nanoparticles that are more chemically reactive, because molecules at the surface of a material do not have full allocation of covalent bonds and are in an energetically unstable state. Since many more molecules located at the surface are in energetically unstable states, nanomaterials are more reactive compared to the non-nanoscale material. With the high reactivity, almost all types of nanomaterials are capable of catalyzing reactions and free nanomaterials tend to agglomerate into bigger particles. Owing to the specific physiochemical properties of nanoparticles, they are expected to interact with substances such as proteins, lipids, carbohydrates, nucleic acids, ions, minerals and water present in food,

biological, or desalination processes. Other potential applications for this reactivity are drug delivery, clothing insulation, and more. Another factor that shapes the nanoscale behavior is the predominance of quantum effects that takes place as the electrons are confined by the dimensions of the nanostructure. As the size is reduced to a few tens of nanometers, the quantum effects starts to dominate the properties of matter, affecting the optical, electrical and magnetic behavior of materials **(Ostiguy, C. et al., 2006).** The development of knowledge and technology at the nanoscale is leading a revolution in the way we conceive, design and produce innovative products and systems. The materials sector is the one that more was influenced by the "nanotechnology revolution".

1.1.1 Application and potentiality

The concepts and fields of application of nanotechnology emerged in recent decades show a profound influence both on basic research both on industrial technologies, directing them towards largely unpredictable directions. The nanostructured products materials are polymeric materials, metallic materials, ceramic materials, semiconductors materials, magnetic materials and their benefits are particularly evident in the following areas (**Figure 1.2**):

- **Electronics**: nanotechnologies can have a big impact on the development, processing and application of electronic devices, such as nanodiodes, OLED, plasma displays, computer devices, chip design, nanotransistors, etc;

- **Energy saving**: in the renewable energy improves energy efficiency in production, and the absorption and storage of energy. Moreover, the miniaturization and the new materials increase the efficiency of the products. Nanotechnology applications can be found in the fields of photovoltaic solar cells, fuel cells, batteries, etc (**Tian, B. et al., 2007**);

- **Environment**: the nanotechnology contributes significantly to environmental sanitation and the solution of environmental problems. Recent results have shown great impact of nanomaterials used for environmental cleanup, such as the membranes for the purification and de-contamination of underground water (**Zhang, W. X., 2003; Long, T. C. et al., 2006**), the nanostructured traps for the removal of pollutants from industrial spills; the maintenance of industrial sustainability by significant reductions in material and energy used; reducing sources of pollution and increased recycling opportunities. In the security field they are important the detectors of chemical and biological agents;

- **Biotechnology:** development of innovative biosensors and systems for intelligent distribution of drugs. Develop biosensors means making molecular analysis; it is necessary to realize devices capable of interacting with complex organic molecules and give recognition signals, in real time related to the type of molecule and to its concentration. Technological perspectives and innovative potential applications for the analysis of DNA and RNA, proteins and other biological molecules or even cells;

- **Medicine**: Nanotechnology provides new options for drug delivery and drug therapies such as in cancer. Nanotechnology allows researchers to build nanosized devices that, when conjugated with antibodies, can

target tumor cells with high specificity and affinity. This enables drug delivery systems, in which small drug molecules can be encapsulated in micelles formed by nanomaterials that transport them to the desired location, thereby lowering the total drug consumption and side effects **(Jain, K. K., 2010).** Researchers have also developed an imaging technique to measure the amount of an antibody-nanoparticle complex that accumulates specifically in plaque, thereby serve as an early diagnosis of atherosclerosis **(Wickline, S. A. et al., 2006)**; Nano dentistry will assist in the maintenance of complete oral health by employing nanomaterials, biotechnology, including tissue engineering, and ultimately, dental nanorobotics. New probable treatment opportunities in dentistry may include, local anesthesia, dentition renaturalization, permanent hypersensitivity cure, complete orthodontic realignments during a single office visit, covalently bonded diamondised enamel, and continuous oral health maintenance using mechanical dentifrobots. In medical filed, scientists have developed a surgical nanorobot, programmed or guided by a human surgeon that can act as a semiautonomous on site surgeon inside the human body, when introduced into the body through vascular system or cavities. Such a device could perform numerous functions such as searching for pathology and then diagnosing and correcting lesions by nanomanipulation, coordinated by an on-board computer while maintaining contact with the supervising surgeon via coded ultrasound signals **(Robert, A. et al., 2005).**

- **Fabrics:** Nanotechnology is also applicable in clothing. The properties familiar materials are being changed by manufacturers who are adding nanosized components to conventional materials to increase performance.

11

- **Food and agriculture safety:** This technology is used to improve the quality of food. There are multiple applications of nanoparticles in food and agriculture safety.

- **Automotive and aeronautics industries**: tires reinforced with abrasion resistant nanoparticles and recyclable; paint dust; plastic non-flammable and low cost; electronic control; coatings and self-repairing materials;
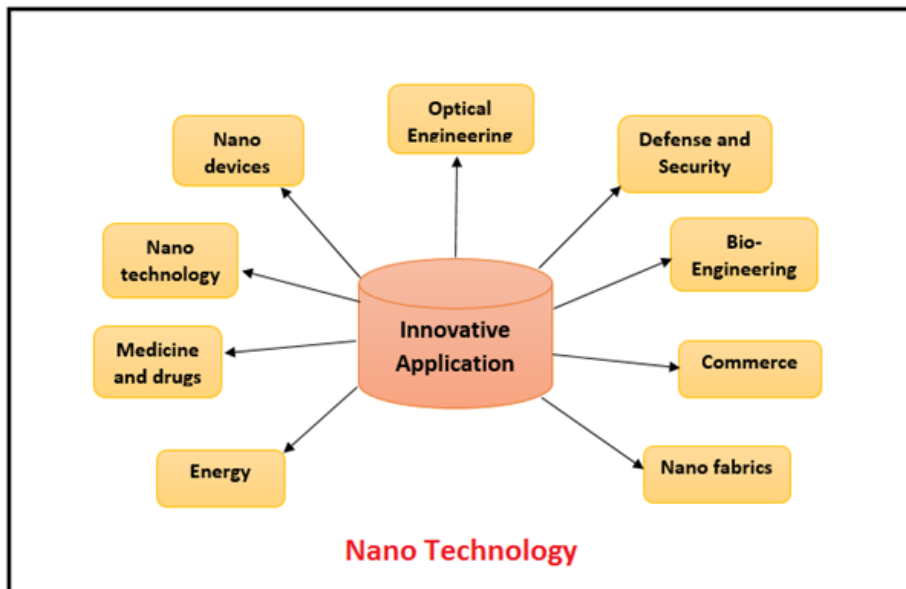
Figure 1.2: Example of some fields of nanotechnology applications

1.2 Nanostructured materials (NSMs)

One of the basic results of the materials science is the insight that most properties of solids depend on the microstructure. A reduction in the spatial dimension, or confinement of particles or quasi-particles in a particular crystallographic direction within a structure generally leads to changes in

physical properties of the system in that direction **(Pokropivny, V. et al., 2007).** An object that has at least one dimension in the range of 1-100 nm is defined a nanostructure. Nanostructured materials have been shown to exhibit high strength, increased diffusivity, reduced sintering temperatures, useful catalytic properties, and attractive physical properties. Due to their novel and improved properties and varied potential applications in different fields of technology, these materials are attracting increasing attention from researchers all over the world. Some excellent reviews are available in the literature detailing the synthesis, characterization, properties, and potential applications of nanostructured materials **(Suryanarayana, C., 1995; Suryanarayana, C., 2005).**

1.2.1 Classification of nanostructured materials (NSMs)

Nanoscale materials have always existed from both natural and anthropogenic sources **(Klaine, S. J. et al., 2008).** The fine fraction of desert sand, fumes originating from volcanic activity or from forest fires, and certain atmospheric dusts, all represent nanoparticles produced by nature **(Ostiguy, C. et al., 2006).** In addition, a majority of biological processes occur at the nanoscale range and can be considered as nature's own nanotechnology. For instance, the ribosome acts as a nanosized factory combining amino acids in a specific order to create proteins **(Ashby, M. F. et al., 2009)**, and hemoglobin, the oxygen-transporting protein found in red blood cells, is 5.5 nm in diameter. Other nanomaterials are unintentionally released into nature from anthropogenic sources, which is byproducts of human activity, such as car exhaust, industrial emissions and welding fumes **(Nowack, B. et al., 2007, Ostiguy, C. et al., 2006).** Nanomaterials can be classified in a number of ways, inasmuch, the research and the rapid development of nanotechnology

have resulted to the creation of different nanomaterials in terms of materials types, physical dimensions and structures. First classification of nanostructures materials (NSMs) was proposed by Gleiter in 1995 **(Yoffe, A. D., 1993)** and further was explained by Skorokhod in 2000 **(Reetz, M. T. et al., 1995).** Nanomaterials can be categorized primarily according to their chemical composition **(Handy, R. D. et al., 2008; Buzea, C. et al., 2007).** This classification separates nanomaterials into broad categories such as carbon-based structures including CNTs and fullerene C60; metal-containing nanoparticles including metal oxides, such as titanium dioxide (TiO_2); or semiconductor nanocrystals, also known as quantum dots (**Figure 1.3).**
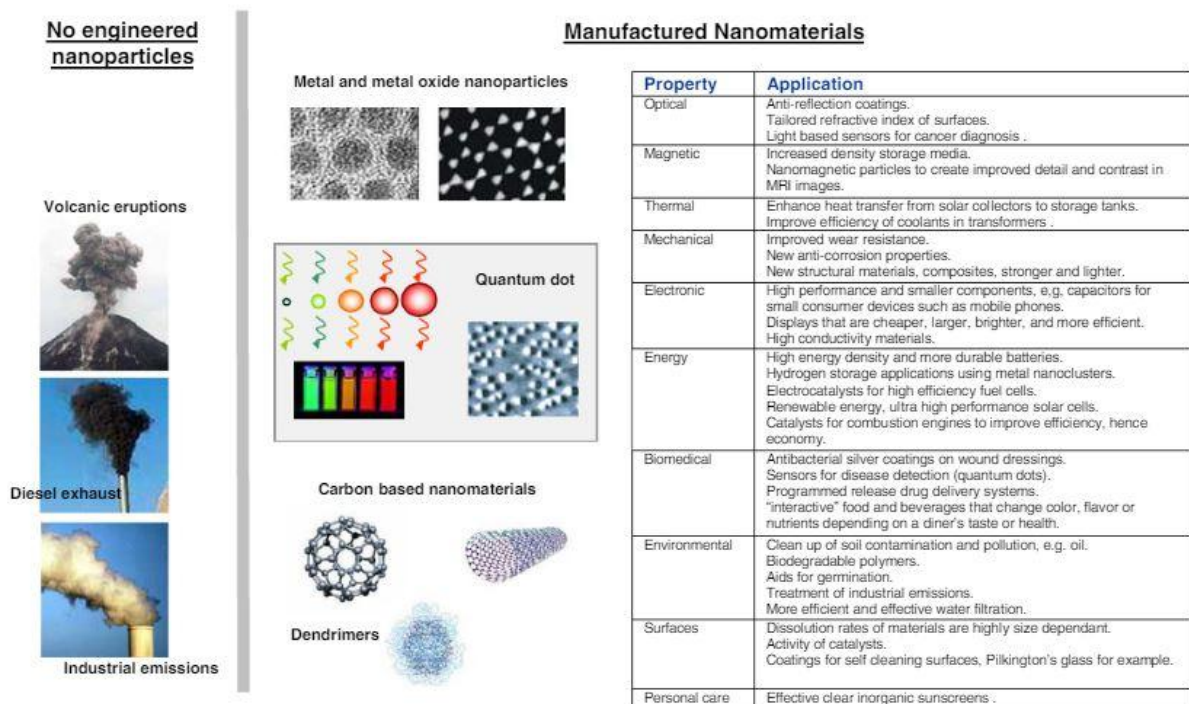
Figure 1.3: Natural and engineered nanoscale substances (Farré et al., 2009)

Another way of categorizing nanomaterials is based on their dimensionality **(Buzea, C. et al., 2007, Krug, H. F. et al., 2011).** There are two main types of nanomaterials, according to the International Organization for Standardization (ISO/2011), nanostructured materials and nanoobjects (**Figure1.4**).

14
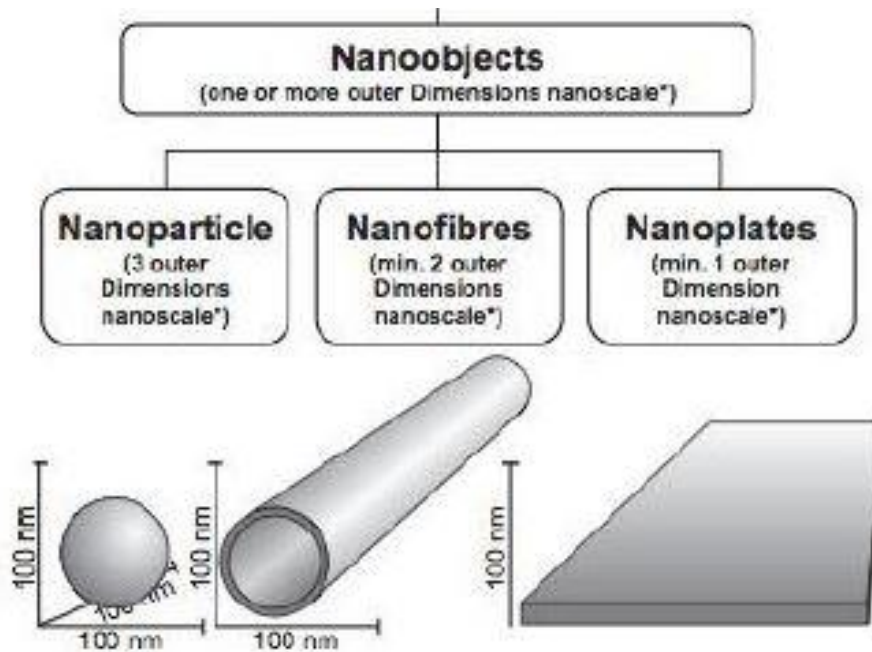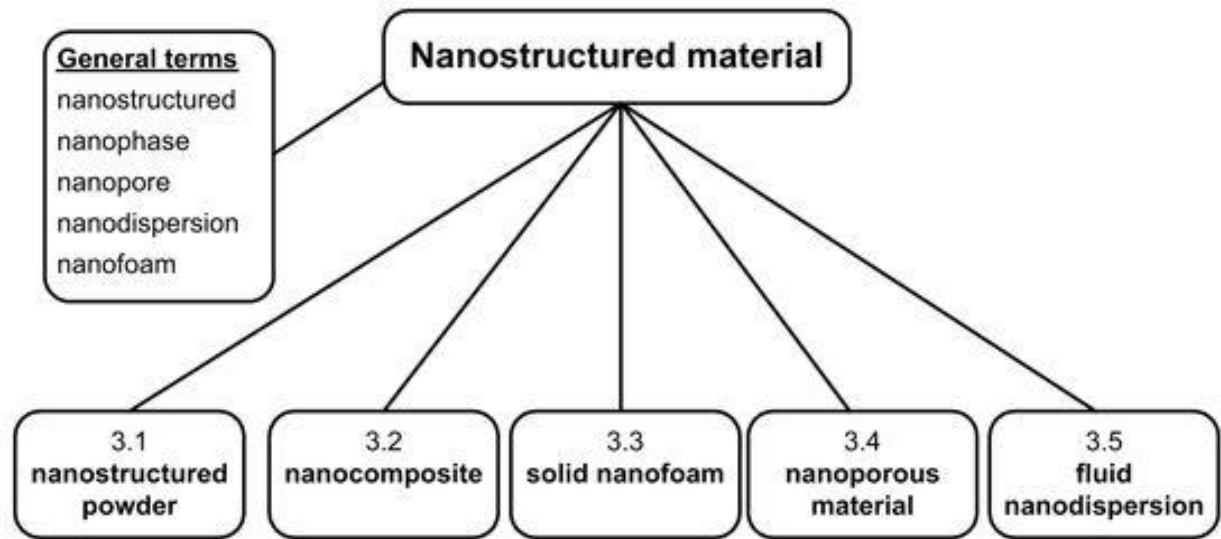
Figure 1.4: The ISO/2011 definition of nanostructures material and nanoobjects. The shape of nanoobjects reflects the number of dimensions confined to the nanoscale (Krug and Wick, 2011).

Nanostructured materials include nanoporous materials (which have nanosized pores within particles that may or may not be of nanoscale dimensions), nanocrystalline materials (which have nanosized crystalline grains within particles that may or may not be of nanoscale dimensions), and complex fluids

containing nanosized objects. Therefore they comprise a broad class of materials that contain nanosized structures, without necessarily having an overall nanoscaled size. The classification of nanoobjects essentially depends on the number of dimensions which lie within the nanometer range, separating them into nanoplates, nanofibers, and nanoparticles. Nanoplates, including nanofilms, nanolayers, and nanocoatings, are stretched out in two dimensions whereas one dimension is confined to the nanoscale. Nanofibers have three dimensions within the nanoscale, and include nanotubes, nanorods and nanowires. Carbon nanotubes (CNTs) have been given a lot of attention, and these nanofibers with hollow interior is widely explored for their use in medical applications **(Bianco, A. et al., 2003, Bianco, A. et al., 2005).** Nanoparticles have all their dimensions measured within the nanoscale, and are often synthesized to form spheres **(Ashby, F. M. et al., 2009; Krug, H. F. et al., 2011).**

1.2.2 Synthesis: Top-down and Bottom-up approach

Nanomaterials can be fabricated either by using physical methods or chemical (wet) methods. Both methods can follow both Top-down approach that Bottom-up approach (**Figure 1.5**):

- **Top down**: the method consists in reaching nanometric dimensions, starting from a larger material. The massive material, "bulk," is divided into smaller particles, using mechanical energy, chemical or in other forms.
- **Bottom up**: the nanomaterial is obtained from the individual atoms, suitably assembled, by means of chemical reactions, allowing the precursor to increase with the size and the desired characteristics.
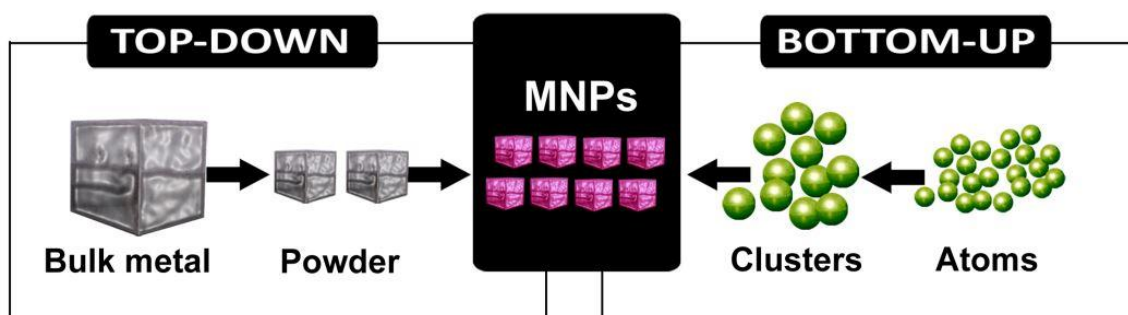
Figure 1.5: Top-down or Bottom-up approach

Both approaches can be conducted in a gas, in liquid, in fluids supercritical, solid or vacuum state. Most of the synthesis systems have as its central objective to control the size of the particles, their shape; the size distribution; the settlement; and the degree of agglomeration (in case colloidal systems). The control of these parameters is becoming increasingly necessary, in fact in the field of Nanotechnology the structure-property matching is enhanced, but is still unknown the potential of nanomaterials **(Viau, G. et al., 2001).**

1.3 New nanoheterogeneous systems: Nanocomposite

According to IUPAC definition, **nanocomposite** is "a composite in which at least one of the phases has at least one dimension of the order of nanometers" **(Aleman, J. et al., 2007).** In the broadest sense this definition comprises colloids, gels, porous media and copolymers, but usually it refers to the solid combination of a bulk matrix and a nanodimensional phase differing in structural and chemical properties. Natural structures are often comprised of and utilize nanocomposites, and scientific researchers commonly learn from the surrounding nature. In 1998, Oriakhi published a work entitled 'Nano sandwiches' **(Oriakhi, C. O., 1998)** stating "Nature is a master chemist with

incredible talent". As a matter of fact, a number of biological arrangements are organized involving nanocomposite structures, thanks to ability of nature to conjugate, at nanometric level, organic and inorganic compounds, allowing the fabrication of smart materials with specific properties (mechanical, thermal, physical, electrical and/or chemical) and biological functions (e.g. biomineralization in diatoms, crustacean, mollusk shells, teeth and bones; inorganic catalytic activity in amino acids condensation **(Mann, S., 1996)** The resulting properties exhibited by these tiny materials can be noticeably different and unique from those of the substances with the same composition but in a larger size. In the 50s, the interest towards organic-inorganic composites increased due to their industrial applications in manufacturing paints (inorganic nanopigments suspended in organic mixtures), papers (cellulosic polymers cross-linked by metal oxo-species), coupling agents for glass, ceramics and metals modification (silanes, silicones, metallo-organics etc.). By the 1970s polymer/clay composites became a popular matter of discussion in textbooks, although the word "nanocomposites" had not been adopted, yet. In the early 1990s, an investigation onto a Nylon-6 loaded with a very small percentage of nanofillers, carried out by Toyota Central Research Laboratories, reported an evident improvement of mechanical and thermal features of the basic polymer, and pointed out that the properties of nanocomposite materials depended not only on the properties of their individual parents (nanofiller and nylon, in this case) but also on their morphology and interfacial characteristics. More recently, due to nanotechnology advance, polymer matrix-based nanocomposites have become a noticeable area of the research and development **(Paul, D. R. et al., 2008; Sanchez, C. et al., 2005).** Such materials, ranging between organic and inorganic chemistry, sounded highly versatile, offering a widespread range of possibilities to create customized materials both in terms of processing procedures and chemical and physical parameters **(Sanchez, C. et al., 2004).** Additionally, the fabrication of organized hybrid materials both within

nanomicroscale and bulk materials plays a crucial role not only for academic research but overall for innovative industrial applications. Nowadays, new hybrid materials have been involved in a plethora of niche markets linked for instance to new generations of smart textiles, photovoltaic and fuel cells, antennas and satellite communications, optoelectronics, new catalysts and coatings, smart therapeutic vectors with controlled drug delivery properties, new ultra-sensitive sensors, cosmetics, smart papers, etc (**Figure 1.6**). The resulting nanoheterogeneous materials typically associate several aspects deriving not only from the mere sum of individual contributions but also related to the role of the inner interfaces, which could sometime be predominant. In the case of particles and fibres, the surface area per unit volume is inversely proportional to the material diameter; thus, the smaller the diameter, the greater the surface area per unit volume **(Luo, J. J. et al., 2003).** Common shapes of inorganic nanostructures when dispersed in a matrix (nanoparticles, nanotubes, nanofibres, fullerenes, and nanowires) and their respective surface area-to-volume ratios are reported in the **(Figure 1.7**).
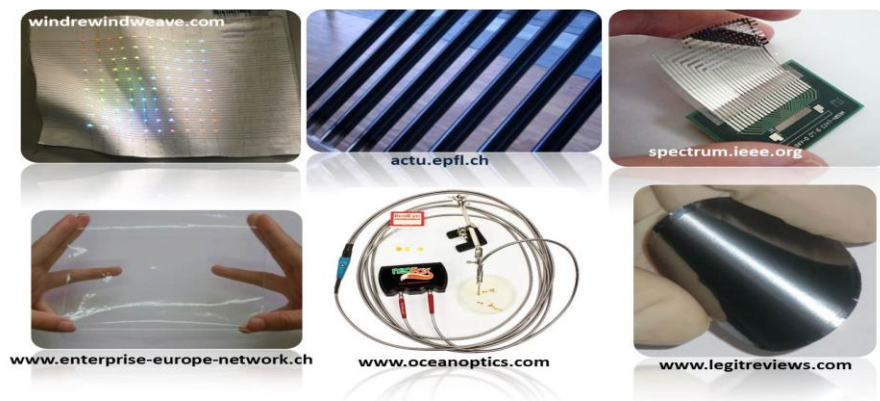
Figure 1.6: Examples of new generations of smart textiles
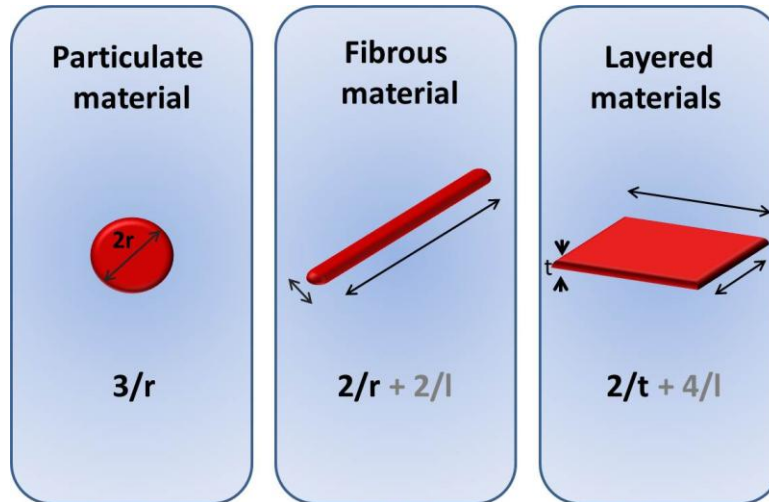
Figure 1.7: Common shapes of inorganic nanostructures dispersed in a matrix (nanoparticles, nanofibres, nanowires) and their respective surface area-to-volume ratios.

The properties of a nanocomposite are significantly influenced by the size scale of its component and phase, its ratio to the matrix phase and the degree of mixing between the two phases. Depending on the nature of components used and the method of preparation, significant differences in composite properties may be obtained. A typical example is reported in (**Figure 1.8**), where the classical diagram of the three types of arrangement of layered silicate materials within a polymer is depicted. When the polymer is unable to intercalate between the silicate sheets, a phase-separated composite is usually obtained, and the resulting properties are comparable to the traditional microcomposites **(Alexandre, M. et al., 2000).**
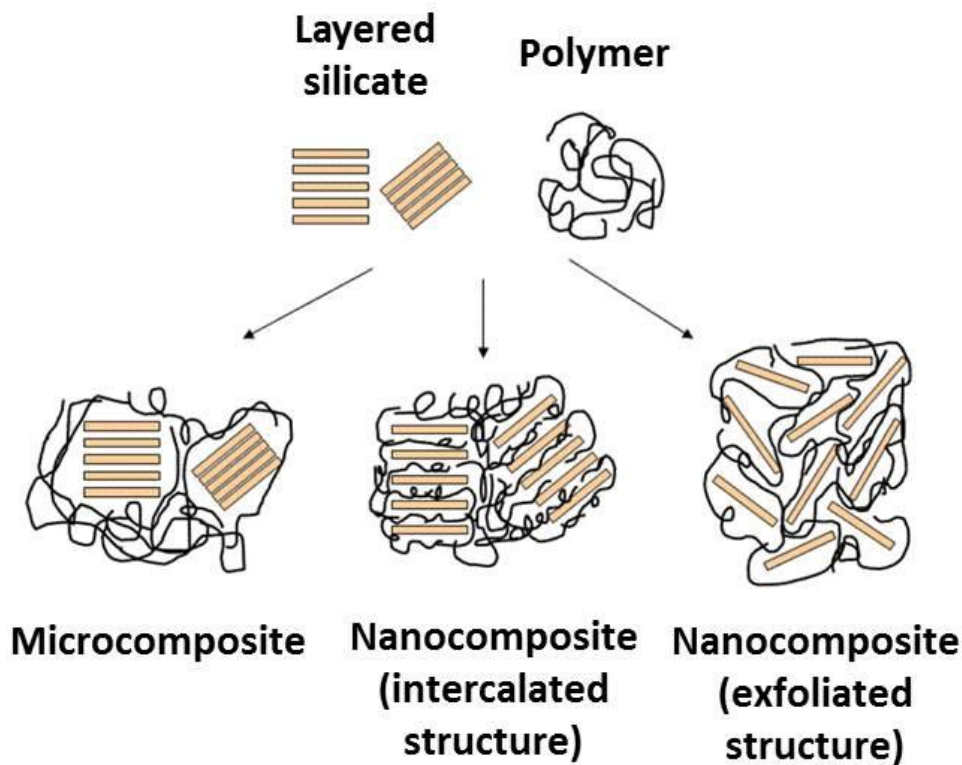
Figure 1.8: Classical diagram of the three types of arrangement of layered silicate materials within a polymer is depicted.

A better configuration is achieved when a single extended polymer chain can penetrate between the silicate layers (intercalated structure), forming a well-ordered multilayer morphology with alternating polymeric and inorganic layers. When the silicate layers are completely and uniformly dispersed in a continuous polymer matrix, an exfoliated or delaminated structure is achieved. In any case, the physical properties of the resultant composite are appreciably different. Likewise, in fibrous or particle-reinforced polymers, dispersion of the nanoparticle and their interaction with the matrix at the interface, play fundamental roles in determining the mechanical properties of the nanocomposite. Without proper dispersion, the nanomaterial will not provide any improvement in mechanical properties, when compared to conventional composites. In addition, the properties of the overall nanocomposite can be tailored by optimizing the interfacial bond between the particle and the matrix

21

(e.g. a good adhesion improves interlaminar shear strength, delamination resistance, fatigue and corrosion resistance). Therefore, physical parameters like mobility and conformation of polymer chain and crystallinity degree were demonstrated to depend on the interface with the reinforcement into the bulk of the matrix **(Ajayan, P. M. et al., 2003).** A list of common nanoparticles and fillers is reported in (**Figure 1.9**). The introduction of small amounts of nanoparticles in matrices is expected to induce dramatic changes also in thermal, physical, electrical and chemical properties of the matrices themselves, depending on density and size parameters. Thus, particles with one dimension ≤ 5 nm, for example, tune catalytic activity, with ≤ 50 nm act on refractive index. More recently, a plethora of nanocomposite films consisting of either metal-metal oxide, mixed metal oxides, polymers mixed with metals or metal oxides, and carbon nanotubes mixed with polymers, metals or metal oxides have been synthesized and investigated for their application as active materials for sensors **(Dongfang, Y., 2001).** Design of the nanocomposite films for gas sensor applications requires that many factors are taken into account, such as the surface area, interfacial characteristics, electrical conductivity, nanocrystallite size, surface and interfacial energy, stress and strain, etc., all of which depending significantly on the material selection, deposition process methods and parameters. Finally, in addition to nanocomposite thin layer fabrication, nanocomposite polymer fibres (nanoparticles dispersed within single nanofibres) have aroused great interest among academic disciplines and industrial sectors for their huge potentials and intriguing applications into smart textiles, cell scaffolding, drug delivery, filtering, sensing and biosensing.

Common Nanoparticles and Fillers

	Approximate Shape*	Smallest Dimension (nm)*	Aspect Ratio**	Elastic Modulus (GPa)	Electrical Conductivity (S/cm)	Thermal Conductivity (W / mK)	Commercial Uses
Traditional Fillers							
Carbon Black	Agglomerate of Spheres	10-100	1 - 5	na	10-100	0.1-0.4	tires, hoses, shoes, elastomers
Carbon Fiber	Rods	5,000-20,000	10-50	300-800	0.1-10	100-1000	aerospace, automotive, marine, sporting, medical
Carbon Graphite	Plate	250-500	15-50	500-600	1-10	100-500	gaskets, seals
E-Glass	Rod	10,000-20,000	20-30	75	na	na	marine, automotive, construction, filtration
Mineral: $CaCO_3$	Sphere Platelet	45-70 600-4,000	~1 1-30	35	na	3-5	paper, paint, rubber, plastics
Mineral: Silica	Agglomerate of Spheres	8,000-30,000	5-10	30-200	na	1-10	reinforced plastics, thermal insulator, paint, rubber reinforcing agent
Mineral: Talc, China Clay	Platelet	5,000-20,000	5-10	1-70	na	1-10	paper, consumer goods, construction
Nanoscale Fillers							
Carbon NanoFiber	Rod	50-100	50-200	500	700-1000	10-20	hoses, aerospace, ESD/EMI shielding, adhesives
Carbon MWNT	Rod	5-50	100-10000	1,000	500-10,000	100-1000	automotive, sporting, ESD/EMI shielding
Carbon SWNT	Rod	0.6 - 1.8	100 - 10,000	1,500	1000-10,000	1000	filters, ESD/EMI shielding
NanoGraphite / Graphene	Plate	0.4-10	100-1000	1,000	1000-10000	1000	ESD/EMI shielding
Aluminosilicate Nano-Clay	Plate	1-10	50-1000	200-250	na	1-10	automotive, packaging, sporting, tires, aerospace
Nano TiO_2	Sphere	10-40	~1	230,000	10^{-11}-10^{-12}	12	photocatalysis, gas sensors, paint
Nano Al_2O_3	Sphere	300	~1	50	10^{-14}	20-30	seal rings, furnace liner tube, gas laser tube, wear pads
Nano-Cellulose	Rod	10-100	~100	100-200	10^{-12}	1-10	construction, automotive, commercial

Winey & Vaia, MRS Bulletin, 2007

Figure 1.9: A list of common nanoparticles and fillers

1.3.1 Nanocomposite thin film fabrication methods

Traditional synthesis approaches for manufacturing nanophased composite materials at the solid state can be grouped into four strategies, such as melt intercalation (co-extrusion), functionalization of the NPs, in-situ polymerization and surfactant assisted dispersion, respectively. An accurate description of these approaches is reported in literature **(Mittal, V., 2012).** As far as sensor construction is concerned, a chemical layer should be placed on a suitable transducer or substrate. Several technologies allow nanocomposite thin film depositions (up to a few micrometers) on several substrates through a variety of methods such as physical vapor deposition (PVD), chemical vapor

deposition (CVD) and wet chemical processes (i.e. sol-gel and electrochemical deposition, thermolysis, flame spray pyrolysis, etc.). The kind of deposition technique used strongly affects the properties of the composite layer. To fabricate heterogeneous films consisting of materials with very different nature, e.g. a metal or a metal oxide with a polymer is obviously much more challenging than to deposit films comprised only of a single type of material. Such a deposition process should be able to vaporize or alloy materials of different nature onto the same substrate at the same time. Within this section the most common deposition methods used to fabricate nanocomposite films for gas sensing will be summarized.

1.3.1.1 Physical Vapor Deposition

PVD involves only physical processes, such as high temperature vacuum evaporation, using electron beam, plasma sputtering, resistance heating and pulsed laser deposition under vacuum. The deposition of a thin film commonly occurs by condensation of the vaporized form of materials onto various substrate surfaces. To obtain a nanocomposite film the energy sources have to be able to vaporize all the component materials under the same processing parameters (i.e. vacuum levels, temperature etc.) and simultaneously condense them onto the same substrate. Sputtering, which is one of the PVD processes, occurs whenever any particle strikes a surface with enough energy to dislodge an atom from the surface, with a yield resulting from the ratio of the number of emitted particles per incident particle:

$$Y = N_{emitted\ particles} / N_{incident\ particles}$$

Sputter deposition is achievable whatever the incident species, including atoms, ions, electrons, photons and neutrons as well as molecules and

molecular ions. The yield for bombardment of a surface with an ion or an atom of the same energy will be practically identical; physical sputtering relies on the transfer of physical momentum and kinetic energy from the incident particle to the surface atoms, and this is independent from the particle charge (**Figure 1.10**).
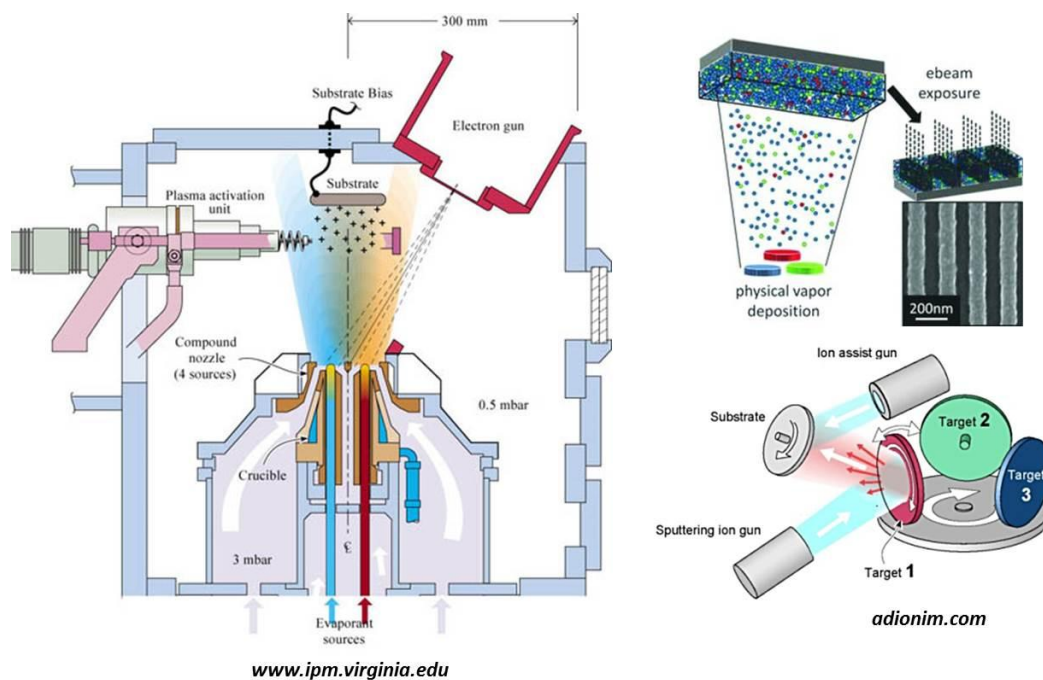
Figure 1.10: A typical PVD apparatus used to deposit nanocomposite films.

A gas sputtering, such as argon or nitrogen, impacting composite material sources (targets consisting of pre-mixed compounds or a few targets simultaneously sputtered by ions) is able to deposit a composite thin film (mixture of metal oxides, a metal together with a metal oxide, or a metal and a polymer). Another PVD process that usually used to deposit nanocomposite films is pulsed laser deposition (PLD) **(Douglas, B. et al., 1994)**,where a high power pulsed laser beam inside a vacuum chamber is focused to strike a target of the material that needs to be deposited. This material is vaporized from the target (in a plasma plume) and deposits as a thin film on a substrate facing the

target. This process can occur in ultra-high vacuum or in the presence of a background gas, such as oxygen that is commonly used for depositing oxides to fully oxygenate films. The process of PLD can generally be divided into four main steps:

1. laser ablation of the target material and creation of a plasma;
2. dynamic of the plasma;
3. deposition of the ablation material on the substrate;
4. nucleation and growth of the film on the substrate surface.

All steps are essential for the uniformity, crystallinity and stoichiometry of the resulting layer. The ablation of the target material upon laser irradiation and the creation of plasma are very complex processes. The removal of atoms from the bulk material is obtained by vaporization of the bulk at the surface region in a state of non-equilibrium. During this process the incident laser pulse penetrates into the surface of the material until a depth dependent on the laser wavelength and the index of refraction of the target material at the applied laser wavelength. Typical values of such a depth for most materials are in the region of 10 nm. The strong electrical field generated by the laser light is sufficiently strong to remove the electrons from the bulk material within the penetrated volume. The free electrons oscillate within the electromagnetic field of the laser light and can collide with the atoms of the bulk material, thus transferring part of their energy to the lattice of the target material within the surface region. The surface of the target is then heated up and the material goes finally into the vapor form. In the plasma dynamic step, the material expands in a plasma, parallel to the normal vector of the target surface and towards the substrate, due to Coulomb repulsion, and recoil from the target surface. The third step, i.e. deposition on the substrate, determines the quality of the deposited films by triggering nucleation and growth of films on the substrate surface. Finally, the nucleation depends on several growth

parameters, including laser energy, surface temperature and structure of the surface substrate, gas pressure. Since PLD source does not interact with the gas phase species and it is very easy to manipulate, the dynamic range of deposition pressures is the largest, when compared to other vacuum deposition processes. In addition, since typical laser wavelengths used in PLD process are less than 250 nm, any material can be virtually laser evaporated, within such a short wavelength, then allowing to deposit composite films consisting of a variety of materials. Therefore, nanocomposite thin film can be easily fabricated through PLD when a target consists of a powder of pre-mixed source materials or when multiple targets of different materials are ablated simultaneously. The ability of the technique to reproduce the target composition is a unique feature to control the composition of nanocomposite films. Another PVD process suitable to get nanocomposite layers is the high temperature vacuum evaporation: it works heating the material (by an electrically resistive heater or electron beam) until evaporation at low pressure (less than 10-5 torr) and condensing it onto a substrate by a flux of vapor. The material to vaporize is typically heated until its vapor pressure is high enough to produce a flux of several Ångströms per second. In order to deposit nanocomposite films, powders of two or more materials may be mixed and compressed into pellets usable for evaporation. It is also possible to evaporate different materials using multiple heating sources. In this case, each time of flight can be ruled separately by increasing or decreasing the power of the heating source. Vacuum evaporation is very useful to fabricate nanoheterogeneous thin films due to ease to obtain uniform mixing over a wide range of concentrations.

1.3.1.2 Chemical Vapor Deposition

Chemical vapor deposition (CVD) is a chemical process often used in the semiconductor industry to produce thin films. The substrate is exposed to more than one volatile precursor reacting and/or decomposing on the substrate surface to produce the desired composite films in various forms, including mono- and polycrystalline, amorphous and epitaxial. However, only recently CVD process has been used to produce nanocomposite films for gas sensor applications **(Russel, B. et al., 2011).** The methodologies are based on the incorporation of an aerosol into the process, essentially the use of a liquid-gas aerosol to transport precursors to a heated substrate. The use of an aerosol allows to carry preformed nanoparticles, these may be incorporated into a conventional CVD flow (hybrid CVD) or transported with another semiconductor precursor (aerosol assisted CVD or AACVD). The main benefit of this technique is its great flexibility since many preformed nanoparticle solutions can be used, and combined with any chemically compatible precursor, to fabricate a huge variety of nanoheterogeneous layers. In addition, it comprises a relatively simple one-step process without special handling steps. Flame spray pyrolysis **(Madler, L. et al., 2002)** is a one-step combustion process of solution precursors able to get nanocomposite materials of mixed oxides. The precursors can be directly solved in the solvent (e.g. ethanol, iso-octane or methanol), and then introduced into the hot reaction zone (e.g. a flame) **(Tani, T. et al., 2000)**, for a high-velocity spray jet for rapid quenching of aerosol formation. The particles sizes usually range 1-500 nm, depending on the process parameters, with production rates up to 250 g/h.

1.3.1.3 Wet-chemical deposition

The sol-gel process is a wet-chemical technique (chemical solution deposition) that is extensively used to fabricate nanocomposite layers, even on very large surface areas. Primarily, such methods are used for the deposition of materials (usually metal oxides) starting from a colloidal solution (sol) acting as the precursor for an integrated network (or gel) of either discrete particles or network polymers. Typical precursors are metal alkoxides and metal salts (such as chlorides, nitrates and acetates), which undergo hydrolysis and polycondensation reactions. During the process, a sol (or solution) containing sources for component materials (such as metal alkoxides and metal chlorides precursors for metal oxides, metallic nanoparticles for metals, tetraethoxysilane for silica matrix, catalyzers, stabilizers and other additives for porosity generation) is arranged first. The sol then undergoes hydrolysis and polycondensation reactions, gradually evolving towards the formation of a gel-like network containing both a liquid and a solid phase. The basic structure of the solid phase can range from discrete colloidal particles to continuous chain-like polymer networks. The main deposition techniques to create the precursor layer on a substrate are dip coating (**Brinker, C. J. et al., 1997**) spin coating (**Vorotilov, K. et al., 1995**) or casting. In the first deposition technique, the substrate is normally withdrawn vertically from a coating solution: the film results from a complex process involving gravitational draining with concurrent drying and continued condensation reactions. Therefore, a substrate is removed from the solution at a defined withdrawal speed under controlled environmental conditions (temperature, humidity and air flow). The formation of thin films occurs through solvents evaporation (mainly ethanol and water), which concentrates non-volatile species in the system, then leading to aggregation and gelation. The resulting layer depends on size and structure of precursors, relative rates of condensation and

evaporation, capillary pressure, substrate surface and withdrawal speed. Specifically, film thickness is mainly controlled by withdrawal speed, non-volatile species content and solution viscosity. It is the oldest and the most widely used deposition technique in industry probably due to its ease of use, its cost efficiency, high coating quality and its flexibility **(Aegerter, M. A. et al., 2004).** In spin coating, few drops of a desired liquid are put onto the substrate held in place using a rotatable fixture; then, spinning is accelerated until high angular velocities in order to spread out the fluid by centrifugal force leaving a thin uniform film. This technique involves the equilibrium between the centrifugal forces and the viscosity of the solution: thickness and homogeneity depend on the rotational speed, the content of non-volatile species in the sol and the volatility of the liquid. Such technique is not expensive and is reproducible, simple and able to coat different smooth and flat substrates. Further steps to fabricate nanocomposite films are comprised of decomposition and pyrolysis of organic compounds, water and residual organics elimination and crystallites nucleation and growth as a network. Specifically, the process uses inorganic or metal organic compounds as raw ingredients diluted in aqueous or organic solvents. Such substrates are hydrolyzed and condensed to form inorganic polymers characterized by M−O−M bonds. In the case of inorganic compounds, hydrolysis proceeds through a proton removal from an aquo ion $[MO_NH2_N]^{2+}$ to form a hydroxo (M−OH) or oxo (M=O) ligand. Then, condensation reactions involving the hydroxyl ligands create M−O−M bonds with water removal. The thermal decomposition behavior of the gel precursor plays an important role in crystallites size and in film porosity: it is often necessary to favor a further polycondensation and enhance mechanical properties and structural stability via final sintering, densification and grain growth. Therefore, sol-gel sounds like an excellent technique for preparing high purity multicomponent films. Even small quantities of dopants can be introduced in the sol and end up dispersing uniformly in the final product. Great scientific interest is focused on this

relatively simple and not expensive strategy to fabricate heterogeneous systems. For instance, Choi et al. **(Choi, Y. J. et al., 2011)** fabricated nanocomposite layers of polystyrene with a self-assembled layer of gold nanoparticles (d=18-22 nm), synthesized directly via aminosilane, with distance between nanoparticles controllable via a sol–gel reaction. Ponemareva et al. **(Ponemareva, A. A. et al., 2012)** prepared nanocomposite SiO_2-SnO_2 thin films on oxidized silicon substrates using the sol-gel technique mixing $SnCl_2 \cdot 2H_2O$. Finally, other wet coating techniques can be used to fabricate a thin film such as spray coating **(Langlet, M. et al., 1994)**, ink-jet printing **(Emine, T. et al., 2008)** doctor blading **(Pitchunami, R. et al., 1995)** and capillary or meniscus coating **(Belleville, P. F. et al., 1994)**, all of which depending on the area and the quality of the surface to be deposited. Spray technique is suitable for fast coating of irregular surfaces: very fine droplets are ejected from the solution using nebulizers or atomizers and are then driven by a gas carrier onto a substrate. Ink-jet deposition is commonly used for nanotechnologies, organic electronics and tissue engineering due to its ability to precisely deposit picoliter volumes of solutions or suspensions in well-defined patterns. Doctor blading, commonly used for coating large substrates, is able to produce thin films with a well-defined thickness by placing a linearly moving sharp blade at a fixed distance from the substrate surface to coat, then leaving a thin wet film. Capillary or meniscus technique is capable of coating flat substrates at room temperature with a very high uniformity of the thickness: the deposition comprises a substrate that is taken under vacuum onto a chuck, while a tubular dispense unit gradually is moved ensuring a continuous solution feed. No physical contact occurs during the deposition travel, but the narrow gap between substrate and applicator allows the formation of a spontaneous meniscus.

1.3.1.4 Electrospinning:one-dimensional composite nanomaterials creation

Among a series of advanced techniques developed to create 1D nanostructures with well-controlled morphology and chemical composition, **Electrospinning** sounds to be the most versatile technique capable of generating, even in a single step, composite nanostructures from a great assortment of polymers. Such a technique is a variation of the electrospray process where liquid drops are elongated with the increasing of the electric field, until generating micro-nanofibrous structures **(Joachim, H. et al., 2012).** This technique is discussed in detail in the following chapter.

1.4 Characterization techniques

Characterization tools are decisive to comprehend the physical and chemical basic properties of nanocomposites. Depending on the final application, it facilitates the study of emerging materials by providing information about some intrinsic properties. The nanocomposite materials can be analyzed and tested in relation to six main different aspects: mechanical, thermal, chemical, physical, morphological and electrical properties. Therefore in this paragraph are described various techniques of characterization performed on studied and designed nanocomposites which will be described in the following chapters.

1.4.1 Morphological characterization

Nanocomposites morphology deals with all the structure of systems, mostly in solid state. For instance, nanostructured materials morphology is studied because of the strong relationship occurring between morphology and properties. Indeed, morphological characterization can supply a lot of information, mostly about the structure of homopolymers, copolymers, polymer blends and the size, shape and dispersion of micro- and nanocompound within a matrix. For morphological characterization of our nanocomposites have been used some advanced microscopic techniques: Scanning Electron Microscopy **(SEM),** Transmission Electron Microscopy **(TEM),** high-resolution transmission electron microscopy **(HRTEM)** and Atomic Force Microscopy **(AFM).**

Scanning Electron Microscopy (SEM): in nanotechnology, Scanning Electron Microscopy is the most common technique to investigate the morphology of thin films or fibers (or other nanostructures) with and without nanofillers, since it is like a photograph of the sample at a very high magnification (up to 2000000X) and high resolution (up to 0.5 nm). Thus it depict a 3D-like structure of the surface, enhancing the roughness, fractures, clusters, composite dispersion and all the relevant information related to the topography of a nanocomposite (shape, size and positions of particles). The Scanning Electron Microscope (SEM) is a microscope that uses electrons instead of light to form an image. A beam of electrons is produced at the top of the microscope by an electron gun. The electron beam follows a vertical path through the microscope, which is held within a vacuum. The beam travels through electromagnetic fields and lenses, which focus the beam down toward the sample. Once the beam hits the sample, electrons and X-rays are ejected from the sample. Detectors collect these X-rays, backscattered electrons, and secondary electrons and convert them into a signal that is forwarded to and

displayed on a monitor (presently a computer monitor) as final image. All metals are conductive and require no preparation before being used. Generally, all non-metals matters need to be made conductive by covering the sample with a thin layer of conductive material (such as gold) by a "sputter coater." Non-conductive specimens, in fact, tend to charge when scanned by the electron beam, especially in the secondary electron imaging mode. This can cause scanning faults and other image artifacts. SEM provides then images concerning surface features associated with a sample. Therefore, SEM micrographs can reveal the surface morphological changes caused by the nanofillers within the thin matrix. However, there are two other well-known branches of microscopy, Scanning Probe Microscopy and Scanning Tunnelling Microscope, which are very useful in nanotube research. In Scanning Probe Microscopy, a physical probe inside a specific microscope (SPM), commonly a sharp tip, scans the sample surface in order to obtain an image from the interactions occurring between the tip and the specimen, as a function of position. In Scanning Tunnelling Microscopy, instead, a sharp conducting tip inside a specific microscope (STM) is held sufficiently close to a surface (typically about 0.5 nm), such that electrons can 'tunnel' across the gap. This method provides surface structural and electronic information at atomic level.

Transmission Electron Microscopy (TEM): Recently, several studies have been conducted to investigate the behavior of polymer-based nanocomposites. In contrast to SEM, which scans a surface to produce its image, in the specific microscope fabricated according to Transmission Electron Microscopy principles (TEM), the electron beam is transmitted through an ultra-thin sample to observe the density of its constituents and thus producing an image through density variations: electrons penetrate and cross to the opposite side of the sample producing a projected image on a phosphor or fluorescent screen, or more recently on a computer monitor after the sensor detection of a CCD camera. TEMs use electrons as "light source" and their much lower

wavelength make it possible to get a resolution a thousand times better than with a light microscope. Instead of glass lenses focusing the light in the light microscope the TEM uses electromagnetic lenses to focus the electrons into a very thin beam. The electron beam is accelerated under vacuum at 100-1000 kV and travels through the specimen to 0.6-0.9 *c* (approaching the speed of light). Depending on the density of the material present, some of the electrons are scattered and disappear from the beam. At the bottom of the microscope the unscattered electrons hit a fluorescent screen, which gives rise to a "shadow image" of the specimen with its different parts displayed in varied darkness according to their density. The image can be studied directly by the operator or photographed with a camera. Compared to SEM performances, TEM can achieve a magnification above 50 million times, with a resolution below 0.5 Ångströms, higher than SEM features. However, SEM images have a better depth of field compared to TEM produced images. Another point of difference is the sample thickness, "staining," and preparations (requires more time-consuming for TEM). The sample in TEM is cut thinner in contrast to a SEM sample and usually fixed onto a TEM grid. In addition, a TEM sample has to be "stained" by an element (such as uranyl acetate, tetroxide of osmium or ruthenium or lead) that captures the scattered electrons. However, up to now, such technique is surely the best strategy to visualize the dispersion and the orientation of the nanocompounds (such as nanotubes, nanorods and nanowires) within a matrix. Resolution of the TEM is limited primarily by spherical aberration, but a new generation of aberration correctors has been able to partially overcome spherical aberration to increase resolution. Hardware correction of spherical aberration for the **high-resolution transmission electron microscopy (HRTEM)** has allowed the production of images with resolution below 0.5 angstrom (50 pedometers) and magnifications above 50 million. The ability to determine the positions of atoms within materials has made the HRTEM an important tool for nanotechnology research and development.

Atomic Force Microscopy (AFM): The Atomic Force Microscopy is one of the foremost techniques used in imaging, measuring, and manipulating matter at nanoscale. The specific microscope fabricated according to Atomic Force Microscopy principles (AFM) is essentially a very high resolution kind of scanning probe microscope: the information is gathered by "feeling" the surface with a mechanical probe leaded by piezoelectric elements that facilitate tiny but accurate and precise movements on (electronic) command enable the very precise scanning. AFM consists of a cantilever with a sharp tip (the probe) at its end that is used to scan the sample surface. The cantilever has a tip radius of curvature on the order of nanometers. When the tip is brought into closeness of a sample surface, forces between the tip and the sample (such as Van Der Waals forces, capillary forces, chemical bonding, electrostatic forces, magnetic forces, solvation forces) deflect the cantilever (Hooke's law). Along with force, additional quantities may simultaneously be measured through the use of specialized types of probes (see scanning thermal microscopy, scanning joule expansion microscopy, photothermal microspectroscopy, etc.). Typically, the deflection is measured using a laser spot reflected from the top surface of the cantilever into an array of photodiodes. The resulting image is strictly related to the sample topography providing a three-dimensional surface profile. AFM works perfectly well in ambient air and can also be combined with a variety of optical microscopy techniques, further expanding its applicability. In contrast to the conventional electron microscopy, (AFM) represents an effective alternative method to study the dispersion of the nanocomposites without any limitations regarding the sample preparation, the contrast and the resolution. In addition, AFM can also measure fundamental properties of sample surfaces, e.g., local adhesive or elastic properties on nanoscale.

1.4.2 Chemical Analysis by Spectroscopic Techniques

Spectroscopy concerns the identification of elements and compounds and recognition of atomic and molecular structures by measuring the radiant energy absorbed, transmitted or emitted by a substance at specific wavelengths of the spectrum, because such emission or absorption behavior is a unique property useful to discover the presence of that element.

Ultraviolet-Visible Spectroscopy (UV-Vis): UV (approximately 200-400 nm) and/or visible light (400-800 nm) are used for irradiating the sample. Absorption of visible and ultraviolet (UV) radiation is associated with excitation of electrons, in both atoms and molecules, to higher energy states. All molecules undergo electronic excitation upon absorption of light. Unlike IR spectroscopy, UV-Vis spectroscopy addresses to electronic transitions. UV-VIS spectroscopy is useful to characterize the absorption, transmission, and reflectivity of a variety of technologically important materials, coatings, thin films and solutions. When white light passes through or is reflected by a colored substance, a characteristic portion of the mixed wavelengths is absorbed. The light remaining unabsorbed (transmitted) will then assume the complementary color to the wavelength(s) absorbed. Particularly intriguing is, for example, the intense scattering and absorption of light from noble metal nanoparticles, which confer beautiful colors in stained glass windows. These nanoparticles exhibit a strong UV-vis absorption band that is not present in the spectrum of the bulk metal, but depending on size, shape, and local dielectric environment. It is well known that metal nanoparticles display surface plasmon resonance bands in the UV–vis region due to the excitation of electrons.

X-ray fluorescence (XRF): XRF (X-ray fluorescence) is a non-destructive analytical technique used to determine the elemental composition of materials. XRF is widely used as a fast characterization tool in many analytical labs

across the world, for applications as diverse as metallurgy, forensics, polymers, electronics, archaeology, environmental analysis, geology and mining. X-Rays form part of the electromagnetic spectrum, and are characterized by energies lying between ultra-violet and gamma radiation. Wavelengths are typically in the range 0.01 to 10 nm, which is equivalent to energies of 125 keV to 0.125 keV.

On reaching a material, some of the x-rays will be absorbed, and some scattered if neither process occurs, the X-Rays will be transmitted through the material. When absorption occurs, the X-Rays interact with the material at the atomic level, and can cause subsequent fluorescence – it is this X-Ray Fluorescence which forms the basis of XRF spectroscopy. In addition to the absorption/fluorescence process, the X-Rays can also be scattered from the material. This scattering can occur both with and without loss of energy, called Compton and Rayleigh scattering respectively. The ratio of absorption/fluorescence, Compton and Rayleigh scatter and transmission depends on the sample thickness, density and composition, and the X-Ray energy. X-Ray Fluorescence (XRF) can be considered in a simple three step process occurring at the atomic level:

1.   An incoming X-Ray knocks out an electron from one of the orbitals surrounding the nucleus within an atom of the material;

 2.   A hole is produced in the orbital, resulting in a high energy, unstable configuration for the atom;

3.   To restore equilibrium, an electron from a higher energy, outer orbital falls into the hole. Since this is a lower energy position, the excess energy is emitted in the form of a fluorescent X-Ray.

The energy difference between the expelled and replacement electrons is characteristic of the element atom in which the fluorescence process is occurring thus, the energy of the emitted fluorescent X-Ray is directly linked to a specific element being analyzed. It is this key feature which makes XRF such a fast analytical tool for elemental composition. In general, the energy of

the emitted x-ray for a particular element is independent of the chemistry of the material. Since most atoms comprise a number of electron orbitals (eg, K shell, L shell, M shell) a number of possible fluorescent transitions are possible. Thus, for a single element, a number of XRF peaks are possible, and typically these will all be present in the spectrum, with varying intensities. They form a characteristic fingerprint for a specific element. The absorption of X-Rays by a particular material varies according to energy of the X-Rays. As a rule of thumb, low energy X-Rays are absorbed more than high energy photons. In order to expel an electron from one of the orbitals, the X-Ray energy must exceed the binding energy of that electron – however, if the X-Ray energy is too high, then the coupling between X-Ray and electron is inefficient, and only a few electrons will be knocked out. As the X-Ray energy reduces, and approaches the electron binding energy, so the yield of expelled electrons increases. Just below this binding energy, a drop in absorption is observed, since the energy is not sufficient to emit electrons from that shell, and is too high in energy to emit electrons from the lower energy shells. The instrument used to obtain information on the elemental composition of a particular material using XRF Spectroscopy is a XRF spectromer. The key components of a typical XRF spectrometer are: 1- Source of X-Rays used to irradiate the sample; 2- Sample; 3- Detection of the emitted fluorescent X-Rays. The resulting XRF spectrum shows intensity of X-Rays (usually in counts per second) as a function of energy (usually in eV). There are two main types of XRF spectroscopy. Energy Dispersive XRF (**EDXRF)** and Wavelength Dispersive XRF **(WDXRF)**, which differ primarily in the way the fluorescent X-Rays are detected and analyzed. An energy dispersive (EDXRF) detection system directly measures the different energies of the emitted X-Rays from the sample. By counting and plotting the relative numbers of X-Rays at each energy an XRF spectrum is generated. The principle of the energy dispersive (ED) detector (such as the HORIBA Xerophy™) is based on the generation of electron-hole pairs in a semiconductor material (often

silicon). An incident X-Ray, of energy EX, is absorbed by the detector material, and will cause one or more electron-hole pairs to form. The energy, E^{EHP}, to do this is fixed for that particular material. The X-Ray will form as many electron-hole pairs as its energy will allow: number of electron-hole pairs = E^X / E^{EHP}. Once this has occurred, the electrons are pulled off the detector, and the resulting current is proportional to the number of electron-hole pairs, which in itself is directly related to the X-Ray energy. This analysis process is repeated at a very high rate, and the results sorted into energy channels. A wavelength dispersive (WDXRF), detection system physically separates the X-Rays according to their wavelengths. The x-rays are directed to a crystal, which diffracts the X-Rays in different directions according to their wavelengths (energies).On a sequential system a detector is placed at a fixed position, and the crystal is rotated so that different wavelengths are picked up by the detector. The XRF spectrum is built up point by point. In a simultaneous system, a number of crystal/detector units are used, so that a range of elements can be detected simultaneously. The principal difference between ED and WDXRF techniques lies in the achievable energy (spectral) resolution. WDXRF systems can routinely provide working resolutions between 5 eV and 20 eV, depending on their set up, whereas EDXRF systems typically provide resolutions ranging from 150 eV to 300 eV or more, depending on the type of detector used.

References

Aegerter M. A., Menning M. Sol_Gel technologies for glass producers and users. Kluwer Academic Publishers, Boston/Dordrecht/New York/London (2004).

Ajayan P. M., Charlier J. C., Rinzler A. G. Carbon nanotubes: from macromolecules to nanotechnology. PNAS (1999), Vol. 96 (25)**,** pp. 14199-14200

Ajayan P. M., Schadler L. S., Braun P. V. Nanocomposite science and technology. Wiley. ISBN: 3-527-30359-6

Alberts B., Bray D., Hopkin K., Johnson J., Lewis J., Raff M., Roberts K., Walter P. Essential Cell Biology. Cent Eur J Publ Health (2004), Vol. 12 (2), pp. 175

Aleman J., Chadwick V., He J., Hess M., Horie K, Jones R. G., Kratochvil P., Meisel I., Mita I., Moad G., Penczek S., Stepto R. F. T. Definitions of terms relating the structure and processing of sols, gels, networks, and inorganic-organic hybrid materials (IUPAC Recommendations 2007). Pure Appl. Chem (2007), Vol. 79, pp. 1801-1829

Alexandre M., Dubois P. Polymer-layered Silicate Nanocomposites: Preparation, Properties and Uses of a New Class of Materials. Mater. Sci. Eng. Rep. (2000), Vol. 28, pp. 1-63 Applications. The Chemistry of Nanomaterials (2004), Vol.2, pp. 761

Ashby M. F,. Schodek D. L., Ferreira P. J. S. G. Nanomaterials, nanotechnologies and design: an introduction for Engineers and Architects. Butterworth-Heinemann (2009)

Belleville P. F., Floch H. G. J Sol-Gel Sci Technol (1994), Vol. 3, pp. 23-29

Bianco A., Kostarelos K., Prato M. Applications of carbon nanotubes in drug delivery. Current Opinion in Chemical Biology (2005), Vol. 9**,** pp**.** 674-679.

Bianco A., Prato M. Can Carbon Nanotubes be Considered Useful Tools for Biological Applications?. Advanced Materials (2003), Vol. 15**,** pp. 1765-1768

Binnig G., Rohrer Gerber Ch., Weibel E. Surface studies by scanning tunneling microscopy. Phys Rev Lett (1982), Vol. 49, 1982, pp. 57

Brinker C. J., Frye G. C., Hurd A. J., Ashley C. S. Fundamentals of sol-gel dip coating, Thin Solid Films (1997), Vol 201, pp. 97-108

Bueno J. T., Shchukina N., Ramos A. A. A substantial amount of hidden magnetic energy in the quiet Sun. Nature (2004), Vol. 430, pp. 326-329

Buzea C., Pacheco II., Robbie K. Nanomaterials and nanoparticles: sources and toxicity. Biointerphases (2007), Vol. 2**,** pp. 17-71

Choi Y. J., Chiu C. K., Luo T. J. Spontaneous deposition of gold nanoparticle nanocomposite on polymer surfaces through sol-gel chemistry. Nanotechnology (2011), Vol 22, pp. 045601-8

Christof M., Niemeyer Prof. Dr., Michael Adler Dr. Nanomechanical Devices Based on DNA. Angewandte Chemie International Edition (2002)**,** Vol. 41, pp. 3779-3783

Daniel I.M. Characterization and Modeling of Mechanical Behavior of Polymer/Clay Nanocomposites. Compos. Sci. Technol. (2003), Vol. 63(11), pp. 1607-1616

Dongfang Y. Nanocomposite Films for Gas Sensing. Advances in Nanocomposites - Synthesis, Characterization and Industrial Applications (2011), Dr. Boreddy Reddy (Ed.), ISBN: 978-953-307-165-7, InTech.

Douglas B., Chrisey and Graham K. Pulsed Laser Deposition of Thin Films. Hubler, John Wiley & Sons (1994), ISBN 0-471-59218-8

Eigler D. M., Schweizer E.K. Positioning single atoms with a scanning tunneling microscope. Nature (1990), Vol. 344, pp. 524

Emine T., Patrick J. S., Ulrich S. S. Inkjet printing as a deposition and patterning tool for polymers and inorganic particles. Soft Matter (2008), Vol. 4, pp. 703-713

Feynman R. There's plenty of room at the bottom. Engineering and Science (1960), Vol. 23, pp. 22-36

Gisev A.I., Moscow., Fizmatlit. Nanomaterials, Nanostructures, and Nanotechnologies. Inorganic Materials (2006), Vol. 42, pp. 696-697

Gleiter H. Acta Mater (2000), Vol. 48 (1), pp.1-384

Hagfeldt A., Gratzel M. Molecular photovoltaics. Acc. Chern. Res (2000), Vol. 33, pp. 269-277

Handy R. D., Owen R., Valsami-Jones E. The ecotoxicology of nanoparticles and nanomaterials: current status, knowledge gaps, challenges, an future needs. Ecotoxicology (2008), Vol. 17**,** pp 315-25

ISO/TS 80004-4:2011(en). Nanotechnologies -Vocabulary - Part 4: Nanostructured materials.

Jain K. K. Advances in the field of nanooncology. BMC medicine (2010), Vol. 8**, pp.** 83

Joachim H. W., Greiner A., Ramakrishna S., Seema Agarwal. Electrospinning: Materials, Processing and Applications. John Wiley & Sons (2012), ISBN: 978-3-527-32080-6

Kamat P.V., Meisel D. Studies in Surface Science and Catalysis Semiconductor and Nanoclusters-Physical, Chemical, and Catalytic Aspects. Elsevier (1997), Vol. 103

Klaine S.J., Alvarez P.J.J., Batley G.E., Fernandes T.F., Handy R.D., Lyon D.Y., Mahendra S., Mclaughlin M.J., Lead J.R. Nanomaterials in the environment: behavior, fate, biovailability, and effects. Environmental Toxicology and Chemistry (2008), Vol. 27(9)**,** pp. 1825-1851

Klein D. L., Roth R., Lim A. K. L., Alivisatos A. P., McEuen P. L. A. Single electron transistor made from a cadmium selenide nanocrystal. Nature (1997), Vol. 389, pp. 699-701

Konstantin K. Likharev. Single-Electron Devices and Their Applications. Published in Proc. IEEE (1999), Vol. 87, pp. 606-632

Krug H. F., Wick P. Nanotoxicology: An Interdisciplinary Challenge. Angew Chem Int Ed (20011), Vol. 50**,** pp. 1260-1278

Langlet M., Vautey C., Mazeas N. Thin Solid Films (1994), Vol. 299, pp. 25-32

Laurencin CT., Kumbar SG., Nukavarapu SP. Nanotechnology and orthopedics: a personal perspective. Wiley Interdiscip Rev Nanomed Nanobiotechnol (2009), Vol. 1(1), pp. 6-10

Liu C.H., Zapien J. A., Yao Y., Meng X. M., Lee C.S., Fan S.S., Lifshtz Y., Lee S.T. High-density, Ordered ultraviolet light-emitting ZnO nanowire arrays. Adv. Mater (2003), Vol. 15, pp. 838-841

Long T. C., Saleh N., Tilton R. D., Lowry G. V., Veronesi B. Titanium dioxide (P25) produces reactive oxygen species in immortalized brain microglia (BV2): implications for nanoparticle neurotoxicity. Environ Sci Technol (2006), Vol. 40, pp. 4346-52

Mädler L., Kammler H. K ., Mueller R., Pratsinis S. E. Controlled synthesis of nanostructured particles by flame spray pyrolysis. Journal of Aerosol Science (2002), Vol. 33, pp. 369-389

Mann S. Biomimetic Materials Chemistry. John Wiley & Sons, Inc. NY (1996), pp.1-383

Mittal V. In-situ synthesis of polymer nanocomposites. Wiley-VCH Verlag (2012), pp. 1-2088

Moran C. E., Steele L. M.; Halas N. L. Chemical and dielectric manipulation of the plasmonic band gap of metallodielectric arrays. Nano Lett (2004), Vol. 4, pp. 1497-1500

Nowack B., Bucheli T, D. Occurrence, behavior and effects of nanoparticles in the environment. Environmental Pollution (2007), Vol. 150**,** pp. 5-22

Oriakhi C. O. Nano Sandwiches. Chem. Br (1998), Vol. 34, pp. 59-62

Ostiguy C., Lapointe G., Menard L., Cloutier Y., Trottier M., Boutin M., Antoun M., Normand C. Nanoparticles: Actual Knowledge about Occupational Health and Safety Risks and Prevention Measures (2006)

Paul D.R., Robeson L.M. Polymer nanotechnology: nanocomposites. Polymer (2008), Vol 49, pp. 3187-3204

Pitchunami R., Karbhari V. M. J. Am Ceram Soc (1995), Vol. 78, pp. 2497-2503

Pokropivny V., Lohmus R., Hussainova I., Pokropivny A.,Vlassov S. Introduction in nanomaterials and nanotechnology. University of Tartu (2007), pp. 225

Pokropivny V.V., Skorokhod V.V. Mater Sci Eng C (2007), Vol. 27, pp. 990

Ponomareva A. A., Moshnikov V. A., Suchaneck G. Mesoporous sol-gel deposited SiO2-SnO2 nanocomposite thin films. Materials Science and Engineering (2012), Vol. 30, pp. 012003

Rao C.N.R., Muller., Achim., Cheetham., Anthony K. Synthesis, Properties and Applications (2004), Vol. 2, pp. 761

Reetz M. T., Quaiser S. A., Breinbauer R., Teshe B. A new strategy m heterogeneous catalysis: the design of cortex catalysts. Angew Chern Int Ed (1995), Vol. 34, pp. 2728-2730

Robert A., Freitas Jr. Nanotechnology, nanomedicine and nanosurgery. International journal of surgery (2005), Vol. 3 (4),243-246

Russell B., Ivan P. Parkin. Novel Chemical Vapour Deposition Routes to Nanocomposite Thin Films. Advances in Nanocomposites - Synthesis, Characterization and Industrial Applications (2011), Dr. Boreddy Reddy (Ed.), ISBN: 978-953-307-165-7

Salata O. V. Applications of nanoparticles m biology and medicine. J Nanobiotech. (2004), Vol. 2 (1), pp. 3

Sanchez C., Julian B., Belleville P., Popall M. Applications of hybrid organic-inorganic nanocomposites. J. Mater. Chem. (2005), Vol. 15, pp. 3559-3592

Sanchez, C., Gomez-Romero P. Functional Hybrid Materials. Wiley VCH, Weinheim (2004)

Skorokhod V., Ragulya A., Uvarova I. Physico-chemical kinetics in nanostructured systems. Academperiodica (2001), pp.180

Smith A. M., Nie, S. Next-generation quantum dots. Nature Biotechnology (2009), Vol. 27 (8), pp. 732-733.

Suryanarayana C. Nanocrystalline Materials. Internat Mater Rev (1995), Vol. 40, pp. 41

Suryanarayana C. Nanostructured Materials. Adv Eng Mater (2005), Vol. 7, pp. 983

Tani T, Mädler L, Pratsinis S. E. J. Nanopart. Res (2002), Vol. 4, pp. 337

The Royal Society. Nanoscience and nanotechnologies: opportunities and uncertainties. Report by the Royal Society and The Royal Academy of Engineering (2004)

Thrall J. H. Nanotechnology and Medicine. Radiology (2004), Vol. 230 (2), pp. 315-318

Tian B., Zheng X., Kempa T. J., Fang Y., Yu N., Yu, G., Huang J., Lieber C. M. Coaxial silicon nanowires as solar cells and nanoelectronic power sources. Nature (2007), Vol. 449, pp. 885-9

Viau G., Toneguzzo P., Perrard A., Acher O., Fièvet-Vincent F., Fievet F. Scripta Mat (2001), Vol 44, pp. 2263

Vorotilov K., Petrovsky V., Vasiljev V. Spin coating process of sol-gel silicate films deposition: Effect of spin speed and processing temperature. Journal of Sol-Gel Science and Technology (1995), Vol. 5, pp. 173-83

Wang Y. Nonlinear optical properties of nanometer-sized semiconductor clusters. Acc. Chern. Res (1991), Vol. 24, pp.133-13

Wargocki P., Wyton D. P., Sundell J., Clausen G., Fanger O. P. The Effects of Outdoor Air Supply Rate in an Office on Perceived Air Quality, Sick Building Syndrome (SBS) Symptoms and Productivity. Indoor Air (2000), Vol. 10, pp. 222-236

West J. L., Halas N. J. Applications of nanotechnology to biotechnology: commentary, Curr Opin Biotech (2000), Vol. 11, pp. 215-217

Wickline S. A., Neubauer A. M., Winter P., Carythers S., Lanza G. Applications of nanotechnology to atherosclerosis, thrombosis, and vascular biology. Arteriosclerosis, thrombosis, and vascular biology (2006), Vol. 26**,** pp**.** 435-41

Wyton D. P. The effects of indoor air quality on performance and productivity. Indoor Air (2004), Vol. 14, pp. 92-101

Yoffe A. D. Low dimensional systems-quantum-size effects and elctronic properties of semiconductor microcrystallites (zero-dimensional systems) and some quasi-2-dimensional systems. Adv Phys (1993), Vol. 42, pp. 173-266

Zhang, W. X. Nanoscale iron particles for environmental remediation. An overview Journal of Nanoparticle Research (2003)*,* Vol. 5**,** pp. 323-332

Introduction

A strategy to improve the sensing features of chemical sensors is to increase the specific surface of the interacting material: the higher the specific surface area of a sensing material the higher its sensor ability to interact, such as biological sensing structures do. Indeed, in nature, surfaces and receptors are in essence a macroscopical extension of the molecular structure of a material, where the properties of surfaces and receptors are directly related to their structure down to the molecular level. Similar structures can be reconstructed 'in vitro' for sensor and detecting systems of exceptional sensitivity and remarkable specificity. As a consequence, many techniques have been used to augment the surface of sensing layers with fine structures, especially to form controlled nanostructures, as it happens in natural systems, taking advantage of the large specific area of nanostructured materials. Accordingly nanostructured sensors, when compared to the conventional ones, showed desired properties like faster adsorption and minimized bulk effects (i.e. long diffusion–desorption time, analyte entrapment, etc.). From recent literature, electrospinning technology has been confirmed to be one of the best candidates among the various nanotechnologies for designing and developing smart and ultra-sensitive sensing systems, both for the uniqueness of the resulting nanostructures and for production rate and cost. Developments of electrospun nanomaterials have allowed chances to fabricate more efficient interfaces with electronic components also due to their compatibility with semiconductor processes. Since electro spinning is a technique capable of continuously creating polymeric fibers, i.e. with no interruption during the process, it sounds appropriate for the production of huge quantities of nanofibers (micron size yarns consisting of nanofibers can be produced at high rates, up to 70 m/min), then also potentially appealing to the sensor market. An in-depth review of research activities on the development of nanofibers, fundamental understanding of the electrospinning process, and properties of

nanostructured fibrous materials and their applications is provided in this chapter. A detailed account on the type of fibers that have been electrospun and their characteristics is also elaborated.

Chapter 2

Electrospinning and nanofibers

2.1 History of Electrospinning

The origin of electrospinning as a viable fiber spinning technique can be traced back to the early 1930s. In 1934, Formhals patented his first invention relating to the process and the apparatus for producing artificial filaments using electric charges **(Raja, T. et al., 2014).** Though the method of producing artificial threads using an electric field had been experimented with for a long time, it had not gained importance until Formhals' invention due to some technical difficulties in earlier spinning methods, such as fiber drying and collection. Formhals' spinning process consists of a movable thread collecting device to collect the threads in a stretched condition, like that of a spinning drum in the conventional spinning. Formhals' process was capable of producing threads aligned parallel on to the receiving device in such a way that it can be unwound continuously. In his first patent, Formhals reported the spinning of cellulose acetate fibers using acetone as the solvent **(Raja, T. et al., 2014).** The first spinning method adopted by Formhals had some technical disadvantages. It was difficult to completely dry the fibers after spinning due to the short distance between the spinning and collection zones, which resulted in a less aggregated web structure. In a subsequent patent, Formhals refined his earlier approach to overcome the aforementioned drawbacks **(Formhals, A., 1939).** In the refined process, the distance between the feeding nozzle and the fiber collecting device was altered to give more drying time for the electrospun fibers. Subsequently in 1940, Formhals patented another method for producing composite fiber webs from multiple polymer and fiber substrates by electrostatically spinning polymer fibers on a moving base

substrate (**Formhals, A., 1939**)**.** In the 1960s, fundamental studies on the jet forming process were initiated by Taylor. In 1969, Taylor studied the shape of the polymer droplet produced at the tip of the needle when an electric field is applied and showed that it is a cone and the jets are ejected from the vertices of the cone (**Taylor, G. I., 1969**)**.** This conical shape of the jet was later referred ~~to~~ by other researchers as the "Taylor Cone" in subsequent literature. By a detailed examination of different viscous fluids, Taylor determined that an angle of 49.3 degrees is required to balance the surface tension of the polymer with the electrostatic forces. The conical shape of the jet is important because it defines the onset of the extensional velocity gradients in the fiber forming process (**Buchko C. J. et al., 1999**). Following this, investigations of the process have been carried out by a number of researches (**Baugmarten, P. K., 1971; Reneker, D. H. et al., 2000; Lim, T. C. et al., 2004;Yang, F. et al., 2005**)**.** In subsequent years, focus shifted to studying the structural morphology of nanofibers. Researchers were occupied with the structural characterization of fibers and the understanding of the relationships between the structural features and process parameters. Wide-angle X-ray diffraction (WAXD), scanning electron microscopy (SEM), transmission electron microscopy (TEM), and differential scanning calorimetry (DSC) have been used by researchers to characterize electrospun nanofibers. After a hiatus of a decade or so, a major upsurge in research on electrospinning took place due to increased knowledge on the application potential of nanofibers in different areas, such as high efficiency filter media, protective clothing, catalyst substrates, cells scaffoldings and adsorbent materials.

2.2 Electrospinning Process

Typically, the process of electrospinning takes place between the so-called "spinning head" (nozzle or nozzle-less) with a capillary orifice, where a high voltage is applied (typically 10-30 kV) and a rotating drum or static plate acting as a grounded nanofiber collecting counter electrode. The spinning head is connected with a feeding reservoir of polymer solution. The high voltage difference between the spinning head and the ground results in a nano-to micron-sized fiber jet, which is drawn out of the Taylor cone formed at the opening of the spinning head. The polymer jet is formed when an applied electrostatic charge overcomes the surface tension of the solution (**Figure 2.1**).
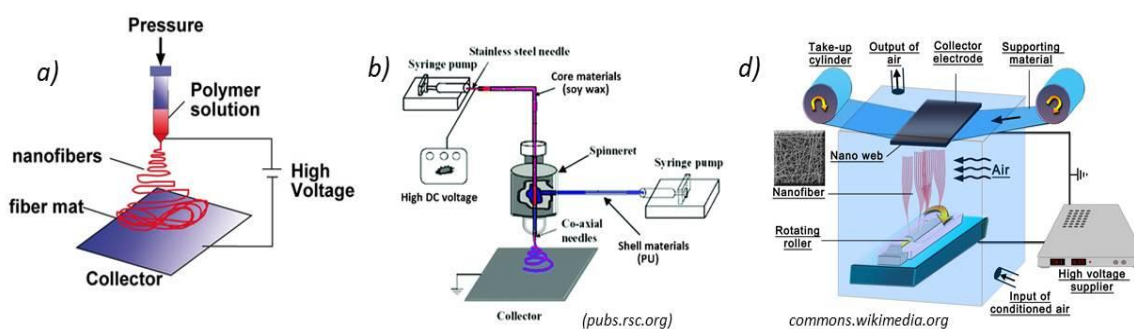
Figure 2.1: Electrospinning Setup

There is a minimum concentration for a given polymer, termed as critical entanglement concentration, below which a stable jet cannot be achieved and no nanofibers will form - although nanoparticles may be achieved (electrospray). The solvent rapidly evaporates during this process and a continuous thread of nanofibers is deposited at the ground electrode, under optimal condition. Depending upon the collector system, the electrospun nanofibers are deposited either in a random fashion in the form of a nonwoven web or as organized (e.g. parallelized) nanofiber patches. Generally, the electrospinning setup consists of a high-voltage power supply, a spinneret, and an electrically conductive collector, though all the three blocks can be

54

modified depending on the specific application. In a typical electrospinning experiment, the liquid (a polymer solution or melt) for electrospinning is pumped into a syringe with a thin nozzle with an inner diameter ranging between 100 μm and 1 mm. The nozzle works as an electrode, while the collector is connected with another electrode (grounded): between them a high electric field is applied ranging from 100 to 3000 kV m^{-1}. The distance between the nozzle and the collector is usually 5-25 cm in most laboratory systems, but it could change in industrial equipment. In many cases, a syringe pump is also needed to provide the solution through the spinneret at a constant and controllable rate. The applied voltage makes the pendent drop of the polymer solution highly electrified and the charges induced therein are evenly distributed over the surface. Once the strength of the electric field is high enough to allow the electrostatic forces to overcome the surface tension of the polymer solution, a liquid jet forms and moves to the counter electrode. During the flight of the liquid jet, the solvent evaporates (or the melt solidifies) and solid fibers with definite diameters are precipitated as a randomly oriented, non-woven mat on the counter electrode. In addition to the distance between the nozzle and the collector and the applied voltage, both the solution (or melt) features, such as viscosity, conductivity, solvent volatility, etc., and environmental conditions, such as humidity and temperature, also affect the formation and the resulting morphology and structure of the electrospun nanofibers. In order to obtain reproducible nanostructures, the above parameters must be carefully controlled. Several studies have demonstrated that aligned fibers could be deposited by using a collector rotating at a high speed **(Matthews, J. A. et al., 2002; Subramanian, D. et al., 2005).** The deposition of electrospun fibers can be obtained not only onto a solid collector but also on some common liquid **(Reneker, D. H. et al., 1996)** demonstrated that continuous uniaxial fibres bundle yarns, aligned along the longitudinal axis of the yarn, could be prepared by electrospinning onto a liquid reservoir collector **Smith, E. et al., 2005**; **Khil, M. S et al., 2005).**

Therefore by changing some parameters of the electrospinning setup, it is possible to control the assembling of the electrospun nanofibers.

2.3 Electrospinning: Parameters Process

Working parameters are very important to understand not only the nature of electrospinning but also the conversion of polymer solutions into nanofibers through electrospinning. Those parameters can be broadly divided into three parts such as polymer solution parameters, process parameters, and ambient parameters. Each of those parameters can affect the fibers morphologies and by proper control of those parameters we can fabricate electrospun fibers with desired morphologies and diameters **(Figure 2.2).**
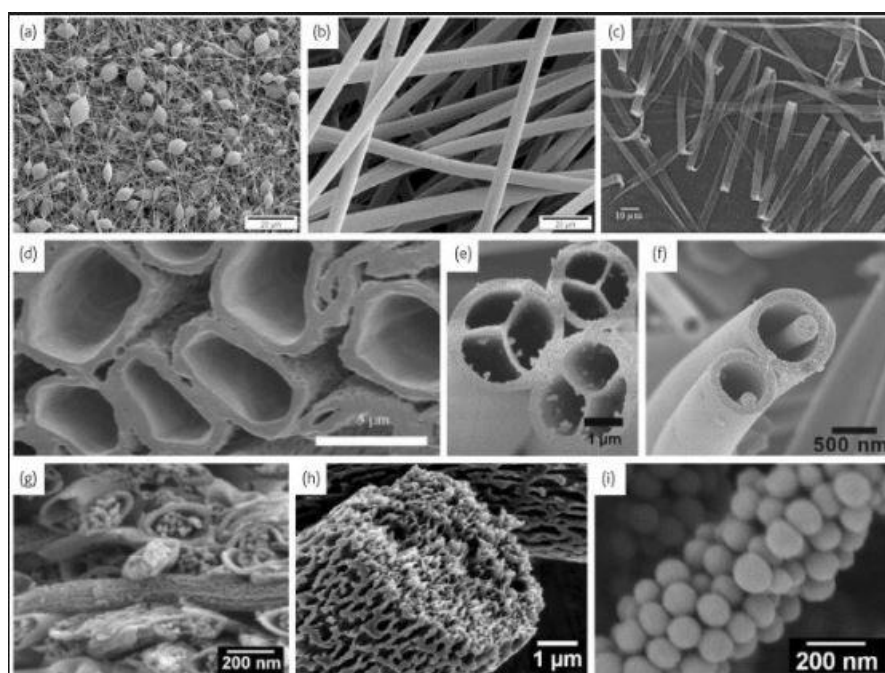
Figure 2.2: Examples of electrospun fibers with differentes morphologies and diameters.

2.3.1 Polymer solution parameters

The properties of the polymer solution have the most significant influence in the Electrospinning process and the resultant fiber morphology. The surface tension has a part to play in the formation of beads along the fiber length. The viscosity of the solution and its electrical properties will determine the extent of elongation of the solution. This will in turn have an effect on the diameter of the resultant electrospun fibers.

2.3.1.1 Molecular weight and solution viscosity

One of the factors that affect the viscosity of the solution is the molecular weight of the polymer. Generally, when a polymer of higher molecular weight is dissolved in a solvent, its viscosity will be higher than solution of the same polymer but with a lower molecular weight. A key condition allowing the electrospinning process to create fibers is related to the molecular weight and viscosity. As the jet leaves the needle tip during electrospinning, the polymer solution is stretched as it travels towards the collection plate. During the stretching of the polymer solution, it is the entanglement of the molecule chains that prevents the electrically driven jet from breaking up thus maintaining a continuous solution jet. The molecular weight of the polymer represents the length of the polymer chain, which in turn has an effect on the viscosity on the solution since the polymer length will determine the amount of entanglement of the polymer chains in the solvent. Another way to increase the viscosity of the solution is to increase the polymer concentration; infact, an increasing in the concentration will result in greater polymer chain entanglements within the solution which is necessary to maintain the continuity of the jet during electrospinning. With increased viscosity, the diameter of the fiber also increases (**Baugmarten, P. K., 1971; Demir, M. M**

et al., 2002; Deitzel, J. M et al., 2001b; Megelski, S. et al., 2002). At a low viscosity, it is common to find beads along the fibers deposited on the collection plate. When the viscosity increases, there is a gradual change in the shape of the beads from spherical to spindle-like until a smooth fiber is obtained **(Fong, H et al., 1999; Mit-uppatham, C. et al., 2004).** The interaction between the solution and the charges on the jet will determine the distribution of the fiber diameters obtained. During electrospinning process, there may be secondary jet erupting from the main electrospinning jet **(Reneker, D. H et al., 2000)** which is stable enough to yield fibers of smaller diameter at certain viscosity. This may explain the differential fiber diameter distribution observed in some cases **(Kim, M. S. et al., 2005); Demir, M. M. et al., 2002).** However, when the viscosity is high enough, it may discourage secondary jets from breaking off from the main jet which may contribute to the increased fiber diameter **(Zhao, S. L. et al., 2004).** Another effect due to a higher concentration is confirmed by a smaller deposition area. Higher concentration means that the viscosity of the solution is so strong to prevent a jet from the tip of the needle at a greater distance. As a result, the path of jet is reduced and it covers a smaller area **(Mit-uppatham, C. et al., 2004).** This reduced jet path also means that there is less stretching of the solution resulting in a larger fiber diameter.

2.3.1.2 Surface tension

The initiation of electrospinning requires the charged solution to overcome its surface tension. However, as the jet travels towards the collection plate, the surface tension may cause the formation of beads along jet. Surface tension has the effect of decreasing the surface area per unit mass of a fluid. In this case, when there is a high concentration of free solvent molecules, there is a greater tendency for the solvent molecules to congregate and adopt a spherical shape due to surface tension. A higher viscosity will means that there is a

greater interaction between the solvent and polymer molecules, thus when the solution is stretched under the influence of the charges, the solvent molecules will tend to spread over the entangled polymer molecules thus reducing the tendency for the solvent molecules to come together under the influence of the surface tension. Solvent such as ethanol (EtOH) has a low surface tension thus it can be added to encourage the formation of smooth fibers **(Fong, H. et al., 1999).** Another way to reduce the surface tension is to add a surfactant to the solution. The addition of a surfactant was found to yield more uniform fibers. Even when insoluble surfactant is dispensed in a solution as fine powders, the fiber morphology is also improved **(Zeng, J. et al., 2003).**

2.3.1.3 Solution Conductivity

Electrospinning involves stretching of the solution caused by repulsion of the charges at its surface. Thus if the conductivity of the solution is increased, more charges can be carried by the electrospinning jet. The conductivity of the solution can be increased by the addition of ions. For instance, drugs and proteins, too, form ions when dissolved in water. As previously mentioned, beads formation will occur if the solution is not fully stretched. Therefore, when a small amount of salt or polyelectrolyte is added to the solution, the increased charges carried by the solution will increase the stretching of the solution. As a result, smoother fibers are formed. The increased in the stretching of the solution also will tend to yield fibers of smaller diameter **(Zhong, X. H. et al., 2002).** However, there is a limit to the reduction in the fiber diameter. As the solution is being stretched, there will be a greater viscoelastic force acting against the columbic forces of the charges **(Choi, J. S. et al., 2004a).** Since the presence of ions increases the conductivity of the solution, the critical voltage for electrospinning to occur is also reduced **(Son, W. K. et al., 2004c).** Another effect of the increased charges is that it results

in a greater bending instability. As a result, the deposition area of the fibers is increased **(Choi, J. S. et al., 2004a)**. This will also favor the formation of finer fiber since the jet path is now increased. The size of the ions may have an influence in the fiber morphology. Electrospun fibers from a solution with dissolved NaCl was found to have the smallest diameter while fibers from a solution with dissolved KH_2PO_4 dissolved had intermediate diameter. As sodium and chloride ions have a smaller atomic radius than potassium and phosphate ions, they may have a greater mobility under an external electrostatic field. As a result, the greater elongational force on the electrospinning jet caused by the more mobile smaller ions could yield fibers with smaller diameter **(Zhong, X. H. et al., 2002).** To increase the conductivity of the solution at the same time reducing the surface tension, ionic surfactant (Lin et al., 2004) such as triethyl benzyl ammonium chloride **(Zeng, J. et al., 2003)** can be added. This was found to cause a reduction in fiber diameter. Another way to increase the conductivity of the solution is by changing the pH of the solution. Under a basic condition, electrospinning cellulose acetate (CA) solution results in a significant reduction in fiber diameter compared to those obtained in a neutral condition **(Son, W. K et al., 2004c).** Since CA will undergo deacetylation under basic condition, OH^- ions may be able to exert a greater influence in the conduction and the stretching of the solution.

2.3.1.4 Dielectric effect of solvent

The dielectric constant of a solvent has a significant influence on electrospinning. Generally, a solution with a greater dielectric property reduces the beads formation and the diameter of the resultant electrospun fiber **(Son, W. K. et al., 2004a).** Solvents such as N,N-Dimethylformamide (DMF) may be added to a solution to increase its dielectric property, to improve the bending instability of the electrospinning jet that also increases with higher

dielectric constant. This is shown by increased deposition area of the fibers. This may also facilitate the reduction of the fiber diameter due to the increased jet path **(Hsu, C. M. et al., 2004).** However, if a solvent of a higher dielectric constant is added to a solution to improve the electrospinnability of the solution, the interaction between the mixture such as the solubility of the polymer will also have an impact on the morphology of the resultant fibers. When DMF is added to polystyrene (PS) solution, beads are formed even though electrospinnability should improve due to the higher dielectric constant of DMF. This could be the result of the retraction of PS molecule due to poor interaction between PS and the solvent molecules **(Wannatong, L. et al., 2004).**

2.3.2 Process parameters

Further parameters that affect the electrospinning process are related to the environment of deposition and its various external factors acting on the electrospinning jet. These involve the voltage supplied, the feed rate, the temperature of the solution and of the collector, the type of collector, the diameter of needle and distance between the needle tip and collector. These parameters have a certain influence in the fiber morphology although they are less significant than the solution parameters.

2.3.2.1 Voltage

A crucial element in electrospinning is the application of a high voltage to the solution. The high voltage will induce the necessary charges on the solution and together with the external electric field, will initiate the electrospinning process when the electrostatic force in the solution overcomes the surface tension of the solution. Generally, both high negative or positive voltage of

more than 6 KV is able to cause the solution drop at the tip of the needle to distort into the shape of a Taylor Cone during jet initiation **(Taylor, G., 1964).** Depending on the feed rate of the solution, a higher voltage may be required so that the Taylor Cone is stable. The Coulomb repulsive force in the jet will then stretch the viscoelastic solution. If the applied voltage is higher, the greater amount of charges will cause the jet to accelerate faster and more volume of solution will be drawn from the tip of the needle. This may result in a smaller and less stable Taylor Cone **(Zhong, W. H. et al., 2002).** When the drawing of the solution to the collection plate is faster than the supply from the source, the Taylor Cone may recede into the needle **(Deitzel, J. M. et al., 2001b).** As both the voltage supplied and the resultant electric field have an influence in the stretching and the acceleration of the jet, they will have an influence on the morphology of the fibers obtained. In most cases, a higher voltage will led to greater stretching of the solution due to the greater Colombic forces on the jet as well as the stronger electric field. These have the effect of reducing the diameter of the fibers **(Lee, J. S. et al., 2004; Buchko, C. J. et al., 1999; Megelski, S. et al., 2002)** and also encourage faster solvent evaporation to yield drier fibers **(Pawlowski, K. J. et al., 2003).** Another factor that may influence the diameter of the fiber is the flight time of the electrospinning jet. A longer flight time will allow more time for the fibers to stretch and elongate before they are deposited on the collection plate. Thus, at a lower voltage, the reduced acceleration of the jet and the weaker electric field may increase the flight time of the electrospinning jet which may favor the formation of finer fibers. In this case, a voltage close to the critical voltage for electrospinning may be favorable to obtain finer fiber **(Zhao, S. L. et al., 2004).** At a higher voltage, it was found that there is a greater tendency for beads formations **(Deitzel, J. M. et al., 2001b;Demir, M. M. et al., 2002).** In literature an interesting observation **(Krishnappa, R. V. N. et al., 2003)** reported that increasing voltage will increased the beads density, which at an even higher voltage, the beads will join to form a thicker diameter fiber. The effect of high voltage is not only on the physical appearance of the fiber, it

also affects the crystallinity of the polymer fiber. The electrostatic field may cause the polymer molecules to be more ordered during electrospinnig inducing a greater crystallinity of the fiber. However, above a certain voltage, the acceleration of the fibers also increases.

2.3.2.2 Feed rate

The feed rate will determine the amount of solution available for electrospinning. For a given voltage, there is a corresponding feed rate if a stable Taylor Cone is to be maintained. When the feed rate is increased, there is a corresponding increase in the fiber diameter or beads size. This is apparent as there is a greater volume of solution that is drawn away from the needle tip **(Zhong, X. H. et al., 2002; Rutledge, G. C. et al., 2001).** However, there is a limit to the increase in the diameter of the fiber due to higher feed rate **(Rutledge, G. C. et al., 2001).** If the feed rate is at the same rate which the solution is carried away by the electrospinning jet, there must be a corresponding increasing in charges when the feed rate is augmented. Thus there is a corresponding increasing in diameter size due to increase volume. Due to the greater volume of solution drawn from the needle tip, the jet will take a longer time to dry. As a result, the solvents in the deposited fibers may not have enough time to evaporate given the same flight time. The residual solvents may cause the fibers to merge together where they get in contact forming webs. A lower feedrate is more desirable as the solvent will have more time for evaporation **(Yuan, X. et al., 2005).**

2.3.2.3 Temperature

The temperature of the solution affects the evaporation rate and reduces the viscosity of the polymer solution. For instance, when polyurethane is electrospun at a higher temperature, the fibers produced have a more uniform diameter **(Demir, M.M et al., 2002).** Increased polymer molecules mobility (kinetic energy) due to increased temperature also allows the Coulombic force to stretch further the solution.

2.3.2.4 Effect of collector

There must be an electric field between the source and the collector for electrospinng to initiate. Thus in most electrospinning setup, the collector plate is made out of conductive material such as aluminum foil which is electrically grounded so that there is a stable potential difference between the source and the collector. In the case when a non-conducting material is used as a collector, charges on the electrospinning jet will quickly accumulates on the collector which will result in fewer fibers deposited **(Kessick, R. et al., 2004;Liu, H. Q et al., 2002).** Fibers that are collected on the non-conducting material usually have a lower packing density compared to those collected on a conducting surface. This is caused by the repulsive forces of the accumulated charges on the collector as more fibers are deposited. For a conducting collector, charges on the fibers are dissipated thus allowing more fibers to be attracted to the collector. The fibers are able to pack closely together as a result **(Liu, H. Q et al., 2002).** For a non-conducting collector, the accumulation of the charges may result in the formation of 3D-fiber structures due to the repulsive forces. Thus, peculiar arrangements of the fibrous scaffoldings can be achieved. When there is a sufficient density of charges on the fiber mesh that is formed initially, repulsion on the fibers may

result in the formation of honey comb structures (**Deitzel, G. M. et al., 2001b**). The porosity of the collector seems also to have an effect on the deposited fibers. In a porous target, there is faster evaporation of residual fibers due to higher surface area while smooth surfaces mau cause an accumulation of solvents around the fibers due to slow evaporation rate (**Liu, H. Q. et al., 2002**). Whether or not the collector is static or moving also have an effect on the electrospinning process. While rotating collectors have been used to collect aligned fibers, they were found to assist in yielding drier fibers than in static collection . This effect is useful when certain solvents, such as dimethylformamide (DMF),having a high boiling point, have to be used. A rotating collector will give the solvent more time to evaporate (**Wannatong, L. et al., 2004**) and also increase the rate of evaporation of the solvents on the fibers. This will improve the morphology on the fiber where distinct fibers are required.

2.3.2.5 Diameter of pipette Orifice/Needle

The internal diameter of the needle or the pipette orifice has a certain effect on the electrospinning process. A smaller internal diameter was found to reduce the clogging as well as the amount of beads on the electrospun fibers (**Mo, X. M. et al., 2004**). The reduction in the clogging could be due to less exposure of the solution to the atmosphere during electrospinning. Decrease in the internal diameter of the orifice was also found to cause a reduction in the diameter of the electrospun fibers. When the size of the droplet at the tip of the orifice is decreased, such as in the case of a smaller internal diameter of the orifice, the surface tension of the droplet increases. For the same voltage supplied, a greater columbic force is required to cause jet initiation. As a result, the acceleration of the jet decreases and this allows more time for the solution to be stretched and elongated before it is collected. However, if the

diameter of the orifice is too small, it may not be possible to extrude a droplet of solution at the tip of the orifice **(Zhao, et al., 2004).**

2.3.2.6 Distance between tip and collector

In several cases, the flight time as well as the electric field strength will affect the electrospinning process and the resultant fibers. Varying the distance between the tip and the collector will have a direct influence in both the flight time and electric field strength. When the distance between the tip and the collector is reduced, the jet will have a shortened distance to travel before it reaches the collector plate. Moreover, the electric field strength will also increase at the same time and this will increase the acceleration if the jet to the collector. As a result, there may not have enough time for the solvents to evaporate when it hits the collector. When the distance is too low, excess solvent may cause the fibers to merge where they keep in contact forming a net of junctions resulting in inter and intra layer bonding **(Buchko, C. J. et al., 1999).** This interconnected fiber mesh may provide additional strength to the resultant scaffold. In some cases, changing the distance has not significant effect on the fiber diameter **(Megeleski, S. et al., 2002).**

2.3.3 Ambient Parameters

The effect of the electrospinning jet surrounding is one area which is still poorly investigated. Any interaction between the surrounding and the polymer solution may have an effect on the electrospun fiber morphology. High humidity for example was found to cause the formation of pores on the surface of the fibers. Since electrospinning is influenced by external electric field, any changes in the electrospinning environment will also affect the electrospinning process.

2.3.3.1 Humidity

The humidity of the electrospinning environment may have an influence in the polymer solution during electrospinning. A high humidity, it is likely that water condenses on the surface of the fibers when electrospinning is carried out under atmospheric pressure. As a result, this may have an influence on the fiber morphology especially polymer dissolved in volatile solvents (**Megelski, S. et al., 2002; Bognitzki, M. et al., 2001**). An increasing in the humidity during electrospinning will cause circular pores to form on the fiber surfaces. The sizes of the circular pores increase with increasing humidity until they coalesce to form larger, non uniform-shaped structures. In the study of thin films, scientists realized that the formation of pores on their surface was attributed to breath (**Srnivasarao, M. et al., 2001**).

Breath figures is the first name given to the process because it connected to the drops condensing on a cold glass when someone breathe on it. The term now refers to a wider group of phenomena, involving the arrangement of water droplets formed by the condensation of water vapor on a surface, either solid or liquid. The condensation is caused by the difference in temperature between the atmosphere and the surface, the latter is cooler. In the case of a liquid surface, the cooling is a consequence of the evaporation of the solvent. For this reason the use of volatile solvents is common in the preparation of these structures. (**Megelski, S. et al., 2002; Casper, C. L. et al., 2004**). The humidity of the environment will also determine the rate of evaporation of the solvent in the solution. At a very low humidity, a volatile solvent may dry very rapidly. The evaporation of the solvent may be faster than the removal of the solvent from the tip of the needle. As a result, the electrospinning process may only be carried out for a few minutes before the needle tip is clogged (**Buamgarten, P. K., 1971**).

2.3.3.2 The composition of the atmosphere

The composition of the air in the electrospinning environment will have an effect on the electrospinning process. Different gases have different behavior under high electrostatic field. When a gas with higher breakdown voltage is used, the fibers obtained have twice the diameter of those electrospun in air given all other condition equal **(Baumgarten, P. K., 1971).**

2.3.3.3 Pressure

Under known atmospheric condition, it is possible to investigate the effect of pressure on the electrospinning jet. Generally, reduction in the pressure does not improve the electrospinning process. When the pressure is below atmospheric pressure, the polymer solution in the syringe will have a greater tendency to flow out of the needle and there causes unstable jet initiation. As the pressure decreases, rapid bubbling of the solution will occur at the needle tip. At very low pressure, electrospinning is not possible due to direct discharge of the electrical charges.

2.4 Creation of different nanofibers

Just by varying the parameters of electrospinning, it is possible to get some variation in the morphology of the nanofibers as shown in the following **figures 2.3-2.4-2.5-2.6-2.7:**
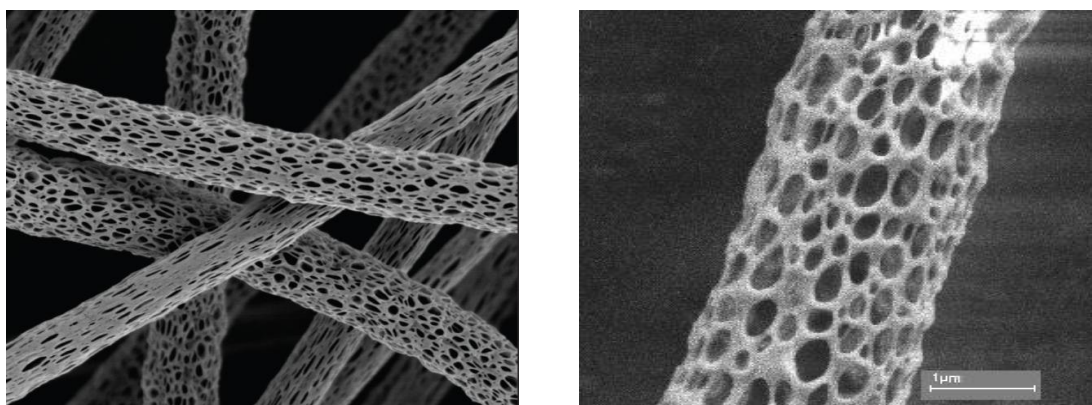
Figure 2.3: Porous nanofibers
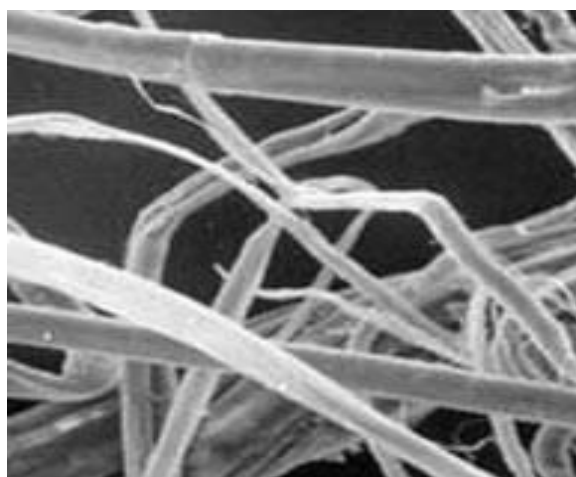
Figure 2.4: Flattened or ribbon-like fibers
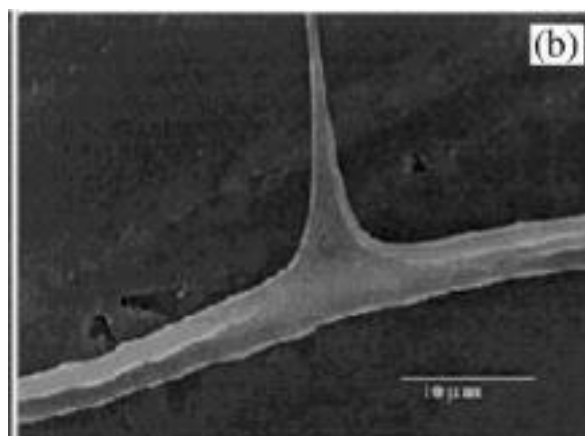
Figure 2.5: Branched fiber
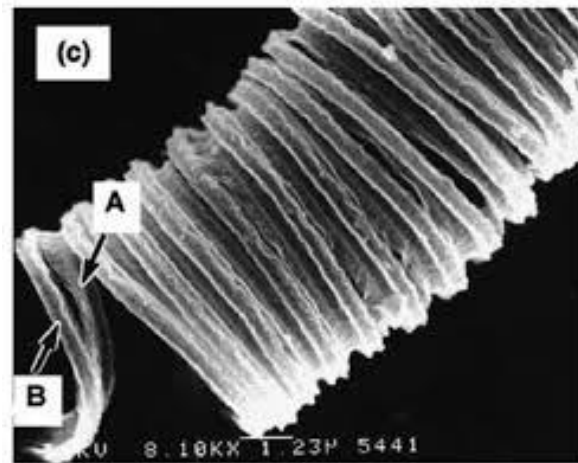
Figure 2.6: Elical fibers

Figure 2.7: Hollow nanofibers

2.5 Fictionalization of nanofiber: methods combined with electrospinning in order to produce 1D functional composite nanomaterials and thin films

The production of nanofibers by the electrospinning process is influenced both by the electrostatic forces and the viscoelastic behavior of the polymer. Up to now, more than one hundred kinds of natural and synthetic polymer have been

70

electrospun into nanofibers, comprising polystyrene (PS), polyvinylcarbazole (PVK), polyvinyl alcohol (PVA), polyurethane (PU), polycarbonate (PC), polylaactic acid (PLA), polymethacrylate (PMMA), polyethylene oxide (PEO), polyamide (PA), polyvinylpyrrolidone (PVP), polyvinylchloride (PVC), polyacrylamide (PAAM), polyvinylidene fluoride (PVDF), nylon-6,6 and 4,6 (PA6,6 and PA4,6 respectively), polyacrylonitrile (PAN) and many more. In addition, suitable sol-gel liquids can be initially electrospun and then properly calcined in order to manufacture ceramic nanofibers, such as ZnO, CuO, NiO, TiO_2, SiO_2, Co_3O_4, Al_2O_3, SnO_2, Fe_2O_3, etc **(Hui, W. et al., 2012).** A typical electrospinnable precursor solution should contain a salt precursor, a polymer and a relatively volatile solvent such as ethanol, water, isopropanol, chloroform, or dimethylformamide (DMF). Poly (vinylalcohol) (PVA) is one of the most popular polymers employed as a matrix due to its high solubility in water and its good compatibility with many salts, including zinc acetate and copper nitrate. In addition to that, PVP, PAN, PMMA, PAAM have also been widely used for testing their mechanical, thermal, electrical and, more recently, sensing features. Recently, electrospinning technique has been also used to prepare 1D composite nanomaterials. Generally, three types of 1D nanocomposites can be fabricated: polymer/polymer (organic), polymer/inorganic, inorganic/inorganic composite systems. In the following paragraph various methods combined with electrospinning in order to produce 1D functional composite nanomaterials and tune thin films will be described. By using these procedures, the resulting 1D composite nanomaterials have showed great improvements in stability, reproducibility and physicochemical properties.

2.5.1 Nanocomponents inclusions

A common strategy to insert inorganic nanocomponents into a polymer fiber is to prepare a polymer solution with a nanodispersion followed by electrospinning. Their small size and large surface area can lead to particle-particle aggregation, making physical handling of nanoparticles difficult in liquid and dry forms. Indeed the inorganic nanocomponents have an extremely high tendency of adhesion and aggregation in clusters resulting in a heterogeneous dispersion in the polymeric solution as well as in the fibers. Yang Q.B. et al. described silver nanoparticle aggregated in PAN fibers (**Figure 8**) with diameter ranging between 20 and 200 nm (**Yang, Q. B. et al., 2003**).

2.5.2 Surface modification of nanoparticles

Surface modification of nanoparticles is another conventional method to improve the dispersion stability of nanoparticles. In order to modify the nanoparticle surface, it is quite important to design the surface structure on the basis of the type of nanoparticles and the liquid media. Therefore, it is necessary to modify the particle surface by using polymeric surfactants or other modifiers in order to generate an effective repulsive force between nanoparticles. The adsorption of polymeric dispersant is one of the simplest surface modification techniques: in order to disperse hydrophilic nanoparticles into aqueous media or in organic solvents with high polarities, anionic or cationic polymer dispersants are widely used to generate steric repulsive force from the polymer chains and to increase the surface charge. As far as anionic surfactants are concerned, for instance, various types of polycarboxylic acids and their salts, such as polyacrylic acid (PAA and PAA-Na) or co-polymers can be used to disperse several kinds of oxide nanoparticles like TiO_2, Al_2O_3,

BaTiO$_3$, Fe$_2$O$_3$, etc. Additional to the molecular weight, also the structure of the polymer surfactant may affect the dispersion stability of nanoparticles. An example of such dependence is the use of polymer dispersant with both hydrophilic and hydrophobic groups. Within electrospun fibers, metal and semiconductor nanoparticles, as well as carbon nanotubes (CNTs), can be embedded to improve mechanical strength and thermal and electronic conductivity of the fibers (**Dorr, Y. et al., 2003).**

2.5.3 Chemical functionalization of the surface of the nanoparticles

The chemical functionalization of the surface of the nanoparticles is also a useful strategy to improve the stability of nanoparticles in various liquid media. As regards modifications of the nanoparticle surface of oxides, silane-coupling agent, which has 1-3 alkoxy groups and 3-1 organic functional groups, have been used since the 1960s. Metal-OH groups on the particle surface are used as reaction sites. The purpose of the silane-coupling agents was at first to improve the compatibility of hydrophilic particle surface with hydrophobic polymer surface by introducing various organic functional groups on particle surface.

The first example is grafting various polymers on particle surface by using silane-coupling agents. Typically, various reactive groups such as amines, epoxides and vinyls are firstly introduced on the particle surface by silane-coupling agents, and then polymers are grafted from or grafted to the particle surface.

2.5.4 Surface modification of TiO$_2$ nanofibers with a bi-functional chemical reagent, and decoration with nanoparticles

Bi-functional surface modification of calcined TiO$_2$ nanofibers with 3-mercaptopropionic acid (3-MPA) is used to incorporate as-synthesized (CdSe)ZnS core-shell quantum dot nanoparticles on to TiO$_2$ nanofibers **(Aykut, Y. et al., 2012; Perri, V. et al., 4th International Conference on Electrospinning 2016 Otranto; Macagnano. A. et al., International Conference on Electrospinning 2017: From Design and Processing to Advanced Nanomaterials and Applications).** The surfaces of TiO$_2$ nanofibers are relatively inert, and they do not have functional groups to enable then to bond with CdSe quantum dots. Consequently, the surfaces of the calcined TiO$_2$ nanofiber mats were modified with a bifunctional chemical reagent, 3-mercaptoprionic acid (3-MPA), which contains both carboxylic (−COOH) and thiol (−SH) functional groups. A similar approach has been used by Gao and co-workers to link CdTe to a TiO$_2$ nanotube array **(Gao, X. F. et al., 2009).** Since TiO$_2$ has a strong affinity for the carboxylate group of the linker molecules **(Gao, X. F. et al., 2009)** a bifunctional monolayer of 3-mercaptopropionic acid (3-MPA) was adsorbed on the surface of TiO$_2$ nanofibers. CdSe quantum dot nanoparticles could be bonded with the thiol groups of linker molecules **(Mann, J. R. et al., 2007).**

2.5.5 Functionalization of TiO$_2$ nanofibers through physical adsorption of nanoparticles

(CdSe)ZnS core-shell quantum dots were synthesized, according to literature, **(Benito-Alifonso, D. et al., 2014)** and then used to decorate titania nanofibers by drop-casting **(Perri, V. et al., 4th International Conference on**

Electrospinning 2016 Otranto; Macagnano, A. et al., International Conference on Electrospinning 2017: From Design and Processing to Advanced Nanomaterials and Applications).

2.5.6 Nanoparticles dispersible in aqueous or high-polar solvents

Other methods to prepare nanoparticles redispersible in low-polar solvents use a non-hydrolytic sol-gel reaction, based on the interaction between metal halides and alkoxides or ethers, with the presence of capping agents such as trioctylphosphine oxides and fatty acids **(Chen, Z. et al., 2006).** As regards the preparation of nanoparticles dispersible in aqueous or high-polar solvents, many researchers often used a polyol way. Specifically, nanoparticles, such as metal salts and metal complexes, are dissolved in polyol media (e.g. ethylene glycol, diethylene glycol, triethylene glycol) and then aged at temperature approximating the boiling temperature, thus generating oxides, sulphides, etc., which are dispersible into highly polar solvents.

2.5.7 UV-Photoreduction

Generally the photochemical reduction is an easy procedure to prepare metal colloids in water. The mechanism is inspired by the UV-irradiation of an aqueous solutions containing the metal salt, $AgNO_3$, that induces photo-oxidation of water by the excited metal cation (Ag+) and results in the formation of metal atoms (Ag°), H+, and OH· radicals; subsequently metal atoms (Ag°) will aggregate into metal clusters and colloids **(Wang W. et al., 2001).** On the basis of this idea, polymer/Ag nanocomposite films and fibres could be prepared starting from a $AgNO_3$ dispersion into a polymer matrix

followed by slow and fast photoreduction. The photoreduction mechanism, performed through a 500 W high-pressure mercury lamp (λ= 310–380nm), was gradually accentuated by the slow change in the fiber color towards light yellow (for 3 h). In order to obtain polymer composites with gold nanoparticles using UV irradiation onto a $HAuCl_4$/polymer dispersion, catalysts such as TiO_2 and organic stabilizers acting as scavengers (such as PVP, PVA and PEG) had to be used to make the reaction much faster. Depending on the nature and concentration of organic stabilizers, different shapes of Au nanoparticles, such as nanoparticles, fractal nanosheets, or nanowires can be synthesized on the surface of TiO_2 nanofibers (well-known catalyst) **(Li, D., et al., 2004).** Such a technique has been a matter of investigation of me and my research group, in order to be applied in the generation of further metal nanostructures on TiO_2 nanofibers

2.5.8 Acid gas-surface reaction

An additional strategy to incorporate semiconductors in a substrate involves three stages: the first one consists in dissolving both metal salt and polymer into a proper solvent making a homogeneous solution; the second step is the deposition (to create thin films or nanofibers) and the third one the exposure of the nanocomposite structure to acid gases at room temperature, like H_2S and HCl. Therefore, for instance, lead acetate dispersed in PVP fibers reacting with H_2S gas (reaction evidenced by change in the fiber color from white to yellow) formed PbS spherical nanoparticles in situ **(Lu, X. et al., 2005).** Comparing this method to the previous one, it actually sounds as a very simple way to disperse inorganic nanoparticles into very thin organic matrices **(Figure 2.8).**
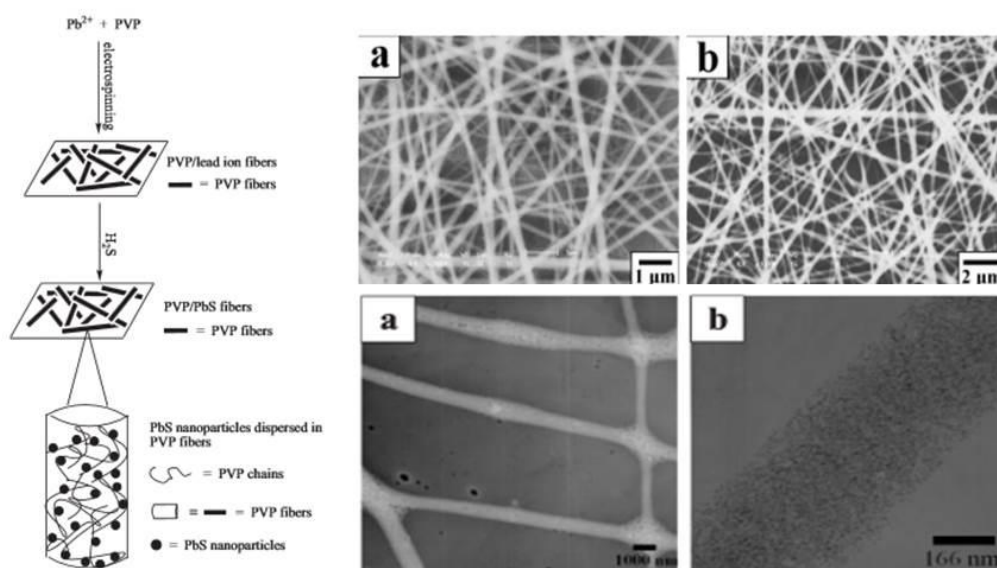
Figure 2.8: Example of Acid Gas-Surface Reaction

2.5.9 Codeposition

Combining sol–gel way with electrospinning technique, several types of composite nanofibers can be synthesized, including metal/polymer, metal oxide/polymer, sulfide/polymer and so on (**Lu, X. F. et al., 2005**; **Lu, X. F. et al. 2006; Wang, Y. Z. et al.2006; Jin, W. J. et al., 2005; Ostermann, R. et al., 2006).** When followed by calcination, metaloxide polymer nanofibers can also be converted into ceramic or metal oxide/ceramic composite nanofibers. **Ramaseshan, R., et al., 2007; Ioannis, S. C., 2005; Sawicka, K. M., et al., 2006;Viswanathamurthi, N., et al., 2004; Wang, M., et al., 2004;Bender, E., et al., 2006).** The electrospun of oil-in-aqueous-emulsions makes easy the deposition of water-soluble drugs (or hydrophilic compounds) within hydrophobic polymers (drug encapsulation), promising fibrous nanostructures for biomedical applications, especially where a controlled molecular release is desired.

77

2.6 Applications of electrospun nanofibers

The extremely fine electrospun nanofibers make them very useful in a wide range of advanced applications, and several reviews on nanofibers have been published **(Yarin, A. et al. 2001;Greiner, A. et al., 2007;Barhate, R. S. er al., 2007;Liang, D. et al., 2007).** But new applications have been explored for these fibers continuously. Here, recent progress in electrospun nanofibers has been briefly reported, covering the following main application areas:

- Filtrations;
- Affinity membranes and recovery of metal ions;
- Tissue engineering scaffolds;
- Wound healing;
- Release control ;
- Catalyst and enzyme carriers;
- Sensors;
- Energy storage;

A number of other applications are mentioned too.

2.6.1 Filtrations

Filters have been widely used in both households and industry for removing substances from air or liquid. Filters for environment protection are used to remove pollutants from air or water. In military, they are used in uniform garments and isolating bags to decontaminate aerosol dusts, bacteria and even virus, while maintaining permeability to moisture vapor for comfort. For a fiber-based filter, removal of particles is determined by different mechanisms. Large particles are blocked on the filter surface due to the sieve effect. Particles that are smaller than the surface-pores will penetrate into the filter,

which could still be collected by the fibers, via either interception or impaction, or static electrical attraction. Also, very fine particles could be captured due to the Brownian motion effect. The filtration efficiency is normally influenced by the filter physical structure (fiber fineness, matrix structure, thickness, pore size, etc), fiber surface electronic properties, and its surface chemical characteristic (e.g. surface free energy). The particle collecting capability is also related to the size range of particles being collected. Besides the filtration efficiency, other properties such as pressure drop and flux resistance are also important factors to be evaluated for a filter media. Electrospun nanofibers for filtration application have a long history. A company in US (Donaldson) has produced electrospun nanofiber-based filter products for industry, consumer and defense applications for more than 20 years and its Ultra-web® nanofiber filter has been developed for nonwoven and filtration industry for a wide range of applications. Recently another company (AMSOIL) has also developed a nanofiber-based fuel filter for automobile applications. DuPont has electrospun fabric products for HVAC, automotive and liquid filtration, bedding protection and apparel applications. Electrospun nanofiber membrane provides dramatic increases in filtration efficiency at relatively small decreases in permeability. In comparison with conventional filter fibers at the same pressure drop, nanofibers with a diameter finer than half a micron have a much higher capability to collect the fine particles, because the slip flow around the nanofibers increases the diffusion, interception and inertial impaction efficiencies (**Kosmider, K. et al., 2002**). Other works related to the filtration applications include effects of operating parameters in electrospinning on fiber morphology and pore structure for filter media (**Barhate, R. S. et al., 2006),** nanofiber membrane for separation of micro particles from liquid **(Gopal, R. et al., 2006),** and pre-filter nanofiber membrane for particulate removal **(Gopal, R. et al., 2007).**

2.6.2 Affinity membranes and recovery of metal ions

Electrospun nanofibers also have a great potential to be functionalized via incorporation of functional materials into the fibers, or via surface chemistry and coating techniques. The functionalized nanofibers may be able to collect small molecules or metal ions from a solution. For examples, electrospun cellulose nanofibers were surface functionalized with a dye Cibacron Blue F3GA (CB), and the functionalized nanofiber membrane showed strong affinity to bovine serum albumin (BSA) and bilirubin, with a capture ability of 13 mg and 4 mg per gram nanofibers, respectively (**Ma, Z. et al., 2005).** A membrane with similar BSA affinity was also prepared from electrospun polysulphone (PSU) fibers which were surface functionalized with another dye, Toluidine Blue O (**Ma, Z. et al., 2006).** Both nanofiber-based affinity membranes had a much lower pressure drop and higher flux compared with similar affinity membranes prepared with conventional microfibers. In addition, electrospun wool keratin/silk fibroin blend nanofibers have been proven to have ability to chelate absorb Cu(II) ions from water (**Ki, C. S. et al., 2007**). In some cases, the functionalized nanofiber membrane was even able to directly convert metal ions collected into elemental metal (electroless recovery). When a nanofiber membrane was surface coated with a thin layer of conducting polymer, as polypyrrole, the nanofiber membrane was able to collect gold ions from aqueous solution and simultaneously convert the gold ions into elemental gold particles (**Wang, H. et al 2007).**

2.6.3 Tissue engineering scaffolds

Tissue engineering is one of the most exciting interdisciplinary and multidisciplinary research areas today, and there has been exponential growth

in the number of research publications in this area in recent years. It involves the use of living cells, manipulated through their extracellular environment or genetically to develop biological substitutes for implantation into the body and/or to foster remodeling of tissues in some active manners. A basic principle of the tissue engineering is illustrated in **Figure 2.9** The purpose is to repair, replace, maintain, or enhance the function of a particular tissue or organ (**Nerem, R. M. et al., 1995).**
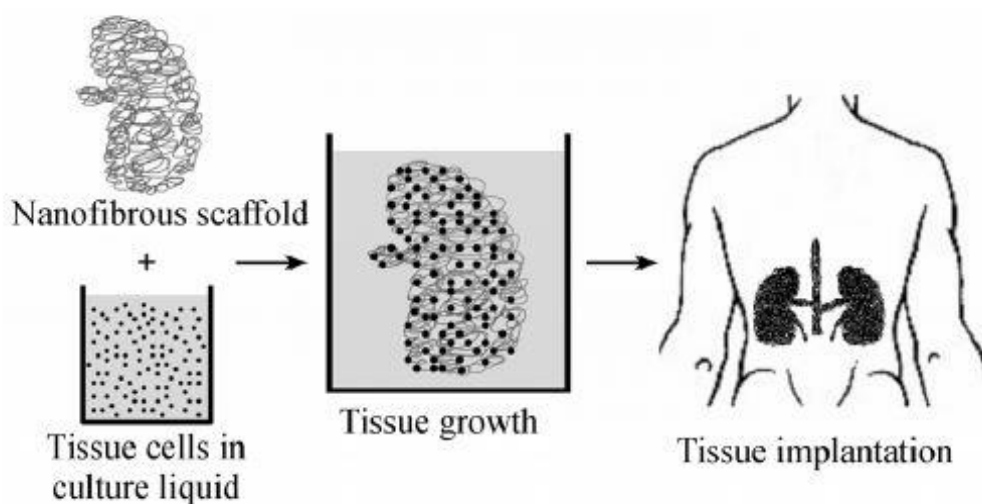
Figure 2.9: Principle of tissue engineering.

Collagen nanofibers were first used to assess the feasi-bility of culturing smooth muscle cell (**Matthews, J. A. et al., 2002).** The cell growth on collagen nanofibers was promoted and the cells were well integrated into the nanofiber network after 7 days of seeding. Smooth muscle cells also adhered and proliferated well on nanofiber membranes electrospun from other polymers, such as poly (ethylene covinly alcohol) (**Kenawy, E. R. et al., 2003),** poly(ester urethane) urea (PEUU)/collagen blend[68], poly(L-lactide-co-ε-caprolactone) (PLLA-CL)[69], poly(ε-caprolactone) (PCL)/ collagen (**Venugopal, J. et al., 2005**) and PS (**Baker, S. C. et al., 2006).** The incorporation of collagen into nanofibers was observed to improve fiber

elasticity and tensile strength, and increase the cell adhesion (**Stankus, J. J. et al., 2004; Venugopal, J. et al., 2005**). Research on engineering bone tissues using electrospun nanofibers began as early as work on the muscles (**Li, W. J. et al., 2002**). Articular cartilage, composed of primarily type-II collagen, is the connective tissue covering the ends of long bones, and serves the functions of load-bearing (shock absorber) and joint lubrication. The feasibility of using electrospun collagen (type-II) nanofibers to culture chondrocyte was studied. Culturing vascular endothelial cells (ECs) on electrospun nanofiber mats has been investigated. A comparison of cell growth on an electrospun PLLA nanofibers and a cast smooth PLLA film revealed that the function of vascular ECs on the smooth PLLA film, rather than on the electrospun nanofiber mat, was enhanced (**Xu, C. et al., 2004**). Since the electrospun nanofiber mats can give good support to the growth of vascular smooth mussel cells (**Mo, X. M. et al., 2004**), smooth film combining with electrospun nanofiber mat could.

2.6.4 Wound healing

Wound healing is a native process of regenerating dermal and epidermal tissues. When an individual is wounded, a set of complex biochemical actions take place in a closely orchestrated cascade to repair the damage. These events can be classified into inflammatory, proliferative, and remodeling phases and epithelialization. Normally, body cannot heal a deep dermal injury. In full thickness burns or deep ulcers, there is no source of cells remaining for regeneration, except from the wound edges. As a result, complete reepithelization takes a long time and is complicated with scarring of the base (**Marler, J. J. et al., 1998**). An open wound healing test for an electrospun collagen nanofiber membrane showed that the early-stage healing using collagen nanofiber mat was faster than that of using normal cotton gauze (**Rho, K. S. et al., 2006**). Besides adding antibacterial additives, antimicrobial

nanofibers can also be prepared by directly using antimicrobial polymers. For instance, polyurethanes containing different amounts of quaternary ammonium groups were electrospun into nanofiber nonwovens, and the nanofibers showed very strong antimicrobial activities against Staphylococcus aureus and Escherichia coli (**Jeong, E. H. et al., 2007**).

2.6.5 Release control

Controlled release is an efficient process of delivering drugs in medical therapy. It can balance the delivery kinetics, minimize the toxicity and side effects, and improve patient convenience **(Yih, T. C. et al., 2006).** In a controlled release system, the active substance is loaded into a carrier or device first, and then released at a predictable rate in vivo, when administered by an injected or non-injected route. As a potential drug delivery carrier, electrospun nanofibers have exhibited many advantages. The drug load-ing is very easy to implement via electrospinning process, and the high applied voltage used in the electrospinning process had little influence on the drug activity. The high specific surface area and short diffusion passage length give the nanofiber drug system higher overall release rate than the bulk material (e.g. film). The release profile can be finely controlled by modulation of nanofiber morphology, porosity and composition. Nanofibers for drug release systems mainly come from biodegradable polymers, such as PLA (**Kenawy, E. R. et al., 2002**) PCL (**Zhang, Y. Z. et al., 2006; Luong-Van, E. et al., 2006; Jiang H. et al., 2006**) poly(D-lactide)(PDLA) (**Zong, X. et al., 2002**) PLLA (**Zeng, J. et al., 2003; Qi, H. et al., 2006**), PLGA (**Luu, Y. K. et al., 2003; Kim, K. et al., 2004**), and hydrophilic polymers, such as PVA (**Taepaiboon, P. et al., 2006; Kenawy, E-R. et al., 2007**), PEG (**Kim, K. Et al., 2004; Jiang, H. et al., 2004**) and PEO (**Kim, T. G. et al., 2007**). Non-biodegradable polymers, such as PEU (**Verreck, G. et al., 2003**) were also

investigated **(Luong-Van, E. et al., 2006; Zeng, J. et al., 2003; Tungprapa, S. et al., 2007; Pornsopone, V. et al., 2007).** The release of macromolecules, such as DNA **(Luu, Y. K. et al., 2003)** and bioactive proteins **(Kim, T. G. et al., 2003; Zeng, J. et al., 2005**; **Chew, S. Y. et al., 2004),** from nanofibers was also investigated. Model drugs that have been studied include water soluble **(Kenawy, E-R. et al., 2002; Zong, X. et al., 2002; Xu, X. et al., 2005)** poor-water soluble **(Jiang, H. et al., 2004; Verreck, G. et al., 2003; Wang, M. et al., 2007)** and water- insoluble drugs **(Luong-Van, E. et al., 2006; Zeng, J. et al., 2003; Tungprapa S. et al., 2007;Pornsopone, V. et al., 2007).** The release of macromolecules, such as DNA **(Luu, Y. K. et al., 2003)** and bioactive proteins **(Kim, T. G. et al., 2007; Zeng, J. et al., 2005; Chew, S. Y. et al., 2005),** from nanofibers was also investigated.

2.6.6 Catalyst and enzyme carriers

In chemistry and biology, a carrier for catalyst is used to preserve high catalysis activity, increase the stability and life of the catalyst, and simplify the reaction process. An inert porous material with a large surface area and high permeability to reactants could be a promising candidate for efficient catalyst carriers. Using an electrospun nanofiber mat as catalyst carrier, the extremely large surface could provide a huge number of active sites, thus enhancing the catalytic capability. The well-interconnected small pores in the nanofiber mat warrant effective interactions between the reactant and catalyst, which are valuable for continuous flow chemical reactions or bio-logical processes. Also, the catalyst can be grafted onto the electrospun nanofiber surface via surface coating or surface modification. When a molecular catalyst was incorporated into nanofibers, the catalyst could leak out of the nanofibers during the catalysis reaction **(Stasiak, M. et al., 2007).** Surface coating such as catalyst-loaded nanofiber with a thin layer of polymer considerably retained the catalyst in the nanofibers and the catalyst efficiency was improved at the

same time. The catalysis performance was influenced by the type of shell polymer and coating thickness **(Ursula, E. et al., 1998).** Chemical reactions using enzyme as catalysts have high selectivity and mild reaction conditions. For easy separation from the reaction solution, enzymes are normally immobilized with a carrier. The immobilization efficiency mainly depends on the porous structure and enzyme-matrix interaction. Nanostructured materials are recently used as enzyme carriers because of their large specific surface area and the high loading capability **(Matatov-Meytal, Y. et al., 2002).** To immobilize enzyme on electrospun nanofibers, many approaches have been used **(Li, S-F. et al., 2007; Wang, Y. et al., 2004)**, including grafting enzyme on fiber surface, physical adsorption, and incorporating enzyme into nanofiber via electrospinning followed by crosslinking reaction.

2.6.7 Sensors

Sensors have been widely used to detect chemicals for environment protection, industrial process control, medical diagnosis, safety, security and defense applications. A good sensor should have a small dimension, low fabrication cost and multiple functions, besides the high sensitivity, selectivity and reliability **(Ursula, E. et al 1998)**. High sensitivity and fast response require the sensor device to have a large specific surface area and highly porous structure. The characteristics possessed by electrospun nanofibers match well with these requirements. Therefore a nanofibrous structure should be a promising physical structure to form a highly sensitive and fast response sensor. Several approaches have been used to impart nanofibers with a sensing capability, such as using a polymeric sensing material to electrospin nanofibers, incorporating sensing molecules into nanofibers, or applying sensing material on nanofiber surface via coating/grafting technique. Early work on electrospun nanofiber-based sensor used a PAA grafted with pyrene

methanol (PM) as the sensing material to detect metal ions Fe^{3+} and Hg^{2+} and a explosive 2,4-dinitrotuloene (DNT) in water **(Wang, X. et al., 2001; Wang, X. et al., 2002).** Due to the quenching effect of these chemicals to the pyrene moieties, the fluorescent intensity of nanofibers had a linear response to the concentration of quenchers, and the nanofibers showed high sensitivities. Fluorescence optical sensors were also prepared by a layer-by-layer electrostatic assembly technique to apply a conjugated polymer onto nanofiber surface for detection of methyl viologen and cytochrome c in aqueous solution **(Wang, X. et al., 2004)** and porphyrindoped silica nanofibers were used to trace TNT vapor **(Tao, S. et al. 2007).** All those nanofiber sensors showed high sensitivity and rapid response. Besides fluorescent properties, conjugated polymer embedded electrospun nanofibers were also reported to be able to sense volatile organic compounds (VOCs) based on optical absorption properties **(Huang, X-J. et al., 2007).** Electrical conductivity is an important property for a sensor device. Conducting nanofibers can be produced from semiconducting oxides, conducting polymers and non-conductive polymers. Pure oxides nanofibers are normally produced by electrospinning oxide-sol-gel and polymer solution mixture, followed by calcining treatment to remove the polymer. The detection of gas molecules using oxide nanofibers is based on the conductivity changes due to the doping effect of analyst gases to the oxide. A few oxide nanofibers have been assessed for detecting different gases, such as MoO_3 **(Gouma, P. I., 2003)** nanofibers for ammonia, WO_3 nanofibers for ammonia **(Wang, G. et al., 2006)** and NO_2 **(Sawicka, K. M. et al., 2005),** TiO_2 nanofibers for NO_2 and H_2 **(Kim, I-D. et al., 2006).** These sensors exhibited improved sensitivity, faster response and lower detection limit than that of sol-gel based films. In addition, Co-doped ZnO nanofibers were used as photoelectric oxygen sensor with fast response **(Yang, M. et al., 2007).** Conducting polymer is another interesting material for sensor applications. The electrospun polyaniline (PANi)/PS nanofibers containing glucose oxidase have been demonstrated to have a high sensitivity to glucose **(Aussawasathien, D. et al., 2005).** PANi/PVP nanofibers also exhibited

sensing ability to NO_2 (**Bishop A. et al., 2005; Bishop-Haynes, A. et al., 2007**).

2.6.8 Energy applications

2.6.8.1. Catalysis

The degradation of organic pollutants such as dyes and pesticides in aqueous solution by photocathalysis, using semiconductor metal oxides such as titanium oxide, zinc oxide, tin oxide and copper oxide (TiO_2, ZnO, SnO_2, CuO) has been the subject of great research due to their size-tunable physicochemical properties, high activities, durability and low cost. However, the fast recombination rate of photo-generated electron/hole pairs in the bulk semiconductor materials lowers their photocatalytic efficiency (**Martin, S. T. et al., 1994**). To overcome these drawbacks, composite materials have being fabricated in order to extend the light absorption spectrum as well as suppressing the recombination of photo-generated electrons by virtue of the different Fermi levels of the ingredients in the composite materials. Due to their very large aspect ratios, photo-catalyst materials with fibrous morphology are superior to particles as far as the recycling and aggregation are concerned. Titanium dioxide is widely used as a photo-catalyst due to its ability to oxidize toxic substances into nontoxic substances such as carbon dioxide and water. TiO_2 is one of the photo-catalysts widely used for fabricating composites such as TiO_2/ZnO composite nanofibers having $ZnTiO_3$ in addition to ZnO and TiO_2 crystallites (**Liu, R. L. et al., 2010**). It was observed that nearly 100% Rhodamine- B and 85% phenol was decomposed in the presence of a TiO_2/ ZnO composite catalyst. The results demonstrated that the incorporation of ZnO in the composite nanofibers improved the photocatalytic efficiency with the best result obtained for 15.76

wt% ZnO. It was inferred that slow charge recombination on the TiO_2/ZnO composite catalyst lead to higher degradation rates. Pan et al. fabricated Au/TiO_2 composite nanofibers by sputtering Au particle on TiO_2 nanofibers and then observed the morphologies of Au deposited TiO_2 nanofibers can be controlled by controlling the sputtering time (**Pan C. et al., 2009**). They found that the composite fiber achieved better photocatalytic degradation of acetaldehyde under UV irradiation in comparison to pure TiO_2.

2.6.8.2 Solar cells

Gratzel was the first person to fabricate dye-sensitized solar cells (DSCs) in 1991.Within the past decade, DSCs have gained considerable attention as a potential technique for harnessing sunlight, a largely abundant renewable-energy source. In DSCs, a sensitizer is anchored to the surface of a wide-band semiconductor oxide to absorb the sunlight. Charge separation takes place at the interface via photo-induced electron injection from NUS-Center for Nanofibers & Nanotechnology to further improve the efficiency of the solar cells.

2.6.8.3 Batteries

Among various energy storage devices available, rechargeable lithium-ion batteries with their high-energy density, long cycle lives, and flexible design, are considered as the effective solution to the ever-increasing demand for high-energy density electrochemical power sources. This demand has promoted research efforts towards the developing high-capacity alternative electrode materials with long life cycle, improved safety, reduced carbon-footprint, and low cost. In this regard, Ji et al. fabricated a variety of

composite materials through electrospinning and observed improved performance with regard to their pure counterparts **(Ji, L. W. et al., 2009)**. PVDF electrospun nanofiber membrane has been investigated as separator for lithium battery application **(Choi, S. W. et al., 2003; Gao, K. et al., 2006)**. Also, MgO nanofibers, LiCoO$_2$-MgO core-sheath nanofibers and Li$_4$Ti$_5$O12 nanofibers were investigated as electrodes in lithium ion batteries **(Fan Q. et al., 2007;Lu, H-W et al., 2007)**.

References

Aussawasathien D., Dong J. H., Dai L. Electrospun polymer nanofiber sensors. Synth Metals (2005), Vol. 154(1-3), pp. 37-40

Aykut Y., Saquing C. D., Pourdeyhimi B., Parson G. N., Khan S. A. Templating Quantum Dot to Phase-Transformed Electrospun TiO_2Nanofibers for Enhanced Photo-Excited Electron Injection. *ACS Appl Mater Interfaces* (2012), Vol. 4 (8), pp. 3837-3845

Baker S. C., Atkin N., Gunning P. A. et al. Characterisation of elec-trospun polystyrene scaffolds for three-dimensional in vitro biological studies. Biomaterials (2006), Vol. 27(16), pp. 3136-3146

Barhate R. S., Loong C. K., Ramakrishna S. Preparation and charac-terization of nanofibrous filtering media. J Membrane Sci (2006), Vol. 283(1-2), pp. 209-218

Barhate R. S., Ramakrishna S. Nanofibrous filtering media: Filtration problems and solutions from tiny materials. J Membrane Sci (2007), Vol. 296(1-2), pp. 1-8

Baugmarten P. K. Electrostatic Spinning of Acrylic Microfibers. J Collid Interf Sci (1971), Vol. 36, pp. 75-79

Bender E. T., Katta P., Lotus A., Park S. J., Chase G. G., Ramsier R. D. Identification of CO_2 sequestered in electrospun metal oxide nanofibers. Chem Phys Lett (2006), Vol. 423, pp. 302

Benito-Alifonso D., Tremel S., Hou Bo., Lockyear H., Mantell J., Fermin D. J., Verkade P., Berry M., Galan M. C. Lactose as a "Trojan horse" for quantum dot cell transport. Angewandte Chemie International Edition (2014), Vol. 53 (3), pp. 810-814

Bishop A., Gouma P. Leuco-emeraldine based polyaniline polyvinypyrrolidone electrospun composites and bio-composites: A preliminary study of sensing behavior. Rev Adv Mater Sci (2005), Vol. 10(3), pp. 209-214

Bishop-Haynes A., Gouma P. Electrospun polyaniline composites for NO_2 detection. Mater Manufact Proc, 2007, 22(6): 764-767

Bognitzki M., Hou H., Ishaque M., Frese T., Hellwing M., Schwarte C., Shaper A., Wendorff J. H., Greiner A. Polymer, metal, and hybrid nano- and mesotubes by coating degradable polymer template fibers (TUFT Process). Adv Mater (2000), Vol. 12 (9), pp. 637-640

Buchko C. J., Chen L. C., Yu S., Martin D. C. Processing and microstructural characterization of porous biocompatible protein polymer thin films. Polymer (1999), Vol. 40, pp. 7397-7407

Casper C. L., Stephens J. S., Tassi N. G., Chase D. B., Rabolt J. F. Controlling surface morphology of electrospun polystyrene fibers: Effect of humidity and molecular weight in the electrospinning process. Macromolecules (2004), Vol. 37, pp. 573-578

Chen Z., Huang, L., He J., Zhu Y., Brien S. New nonhydrolytic route to synthesize crystalline $BaTiO_3$ nanocrystals with surface capping ligands. J Mater Res (2006), Vol. 21, pp. 3187-3195

91

Chew S. Y., Wen J., Yim E. K. F. et al. Sustained release of proteins from electrospun biodegradable fibers. Biomacromolecules (2005), Vol. 6(4), pp. 2017-2024

Choi J. S., Lee S.W., Jeong L., Bae S. H., Min B. C., Youk J. H., Park W. H. Effect of organosoluble salts on the nanofibrous structure of electrospun poly(3-hydroxybutyrate-co-3-hydroxyvalerate). International Journal of Biological Macromolecules (2004a), Vol. 34 (4), pp. 249-256

Choi S. W., Jo S. M., Lee W. S. et al. An electrospun poly(vinylidene fluoride) nanofibrous membrane and its battery applications. Adv Mater (2003), Vol. 15(23), pp. 2027-203

Darrell H Reneker and Iksoo Chun. Nanometre diameter fibres of polymer, produced by electrospinning. Nanotechnology (1996), Vol. 7, pp. 216–223

Deitzel J. M., Kleinmeyer J., Harris D., Tan N. C. B. The effect of processing variables on the morphology of electrospun nanofibers and textiles. Polymer (2001b), Vol. 42, pp. 261-272

Demir M.M., Yilgor E., Erman B. Electrospinning of polyurethane fibers. Polymer (2002), Vol. 43, pp. 3303-3309

Dror Y., Salalha W., Khalfin R. L., Cohen Y., Yarin A. L., Zussman E. Carbon Nanotubes Embedded in Oriented Polymer Nanofibers by Electrospinning. Langmuir (2003), Vol. 19, pp. 7012

Fan Q., Whittingham M. S. Electrospun manganese oxide nanofibers as anodes for lithium-ion batteries. Electrochem Solid-State Lett (2007), Vol. 10(3), pp. A48-A51

92

Fong H., Reneker D.H. Elastomeric nanofibers of styrene-butadiene-styrene triblock copolymer. J Polym Sci Pt B-Polym Phys (1999), Vol. 37, pp. 3488-3493

Formhals A. US Patent 2187306, 1940.

Formhals A. US Patent 2160962, 1939

Gao K., Hu X., Dai C. et al. Crystal structures of electrospun PVDF membranes and its separator application for rechargeable lithium metal cells. Mater Sci Eng B: Solid-State Mater Adv Tech (2006), Vol. 131(1-3), pp. 100-105

Gao X. F., Li H. B., Sun W. T., Chen Q., Tang F. Q., Peng L. CdTe Quantum Dots-Sensitized TiO_2 Nanotube Array Photoelectrodes. J Phys Chem C (2009) Vol. 113, pp. 7531-7535

Gopal R., Kaur S., Feng C. Y. et al. Electrospun nanofibrous polysul-fone membranes as pre-filters: Particulate removal. J Membrane Sci (2007), Vol. 289(1-2), pp. 210-219

Gopal R., Kaur S., Ma Z. et al. Electrospun nanofibrous filtration membrane. J Membrane Sci (2006), Vol. 281(1-2); pp. 581-586

Gouma P. I. Nanostructured polymorphic oxides for advanced chemosensors. Rev Adv Mater Sci (2003), Vol. 5(2), pp. 147-154

Greiner A., Wendorff J H. Electrospinning: A fascinating method for the preparation of ultrathin fibers. Angew Chem Int Edit (2007), Vol. 46(30), pp. 5670-5703

Hsu C. M., Shivacumar S. N,N-Dimethylformamide Additions to the Solution for the Electrospinning of Poly(e-caprolactone) Nanofibers. Macromol Mater Eng (2004), Vol. 289, pp. 334-340

Huang X-J., Ge D., Xu Z-K. Preparation and characterization of stable chitosan nanofibrous membrane for lipase immobilization. Europ Polym J (2007), Vol. 43(9), pp. 3710-3718

Hui W., Wei P., Dandan L., Heping Li. Electrospinning of ceramic nanofibers: Fabrication, assembly and applications. Journal of Advanced Ceramics (2012), Vol. 1, pp. 2-23

Ioannis S. Chronakis. Novel nanocomposites and nanoceramics nased on polymer nanofibers using electrospinning process**.** J Mater Process Technol (2005), Vol. 167, pp. 283

J Nanopart Res (2006), Vol. 8, pp.769

Jeong E. H., Yang J., Youk J. H. Preparation of polyurethane cationomer nanofiber mats for use in antimicrobial nanofilter applications. Mater Lett (2007), Vol. 61(18), pp. 3991-3994

Ji L. W., Lin Z., Medford A. J., Zhang J. X. Chem-Eur J (2009), Vol. 15, pp. 1071-10722.

Jiang H., Fang D., Hsiao B. et al. Preparation and characterization of ibuprofen-loaded poly(lactide-co-glycolide)/poly(ethylene glycol)-g- chitosan electrospun membranes. J Biomater Sci Polym Edit (2004), Vol. 15(3), pp. 279-296

Jiang H., Hu Y., Zhao P. et al. Modulation of protein release from biodegradable core-shell structured fibers prepared by coaxial electrospinning. J Biomed Mater Res Part B: Appl Biomater (2006), Vol, 79B (1), pp. 50-57

Jin W. J., Lee H. K., Jeong E. H., Park W. H., Youk J. H. Macromol. Rapid Commun (2005), Vol. 26, pp.1903

Kenawy E. R., Bowlin G. L., Mansfield K. et al. Release of tetracycline hydrochloride from electrospun poly(ethylene-co-vinylacetate), poly(lactic acid), and a blend. J Contr Rel, (2002), Vol, 81(1-2), pp. 57-64

Kenawy E. R., Layman J. M., Watkins J. R. et al. Electrospinning of poly(ethylene-co-vinyl alcohol) fibers. Biomaterials (2003), Vol, 24(6), pp. 907-913

Kenawy E-R., Abdel-Hay F. I., El-Newehy M. H. et al. Controlled re-lease of ketoprofen from electrospun poly(vinyl alcohol) nanofibers. Mater Sci Eng A: Struct Mater Prop Microstruct Proc (2007), Vol. A459(1-2), pp. 390-396

Kenawy E-R., Bowlin G. L., Mansfield K.et al. Release of tetracycline hydrochloride from electrospun poly(ethylene-co-vinylacetate), poly(lactic acid), and a blend. J Contr Rel (2002), Vol. 81(1-2), pp. 57-64

Kessick R., Fenn J., Tepper G. The use of AC potentials in electrosprayng and electrospinning processes. Polymer (2004), Vol, 45, pp. 2981-2984

Khil M. S., Bhattarai S. R., Kim H. I , Kim S. Z., Lee K. H. J. Biomed. Mater. Res. B (2005), Vol. 72, pp. 117

Ki C. S., Gang E. H., Um I. C. et al. Nanofibrous membrane of wool keratose/silk fibroin blend for heavy metal ion adsorption. J Mem-brane Sci (2007), Vol, 302 (1-2), pp. 20-26

Kim I-D., Rothschild A., Lee B .H. et al. Ultrasensitive chemiresistors based on electrospun TiO_2 nanofibers. Nano Lett (2006), Vol. 6(9), pp. 2009-2013

Kim K., Luu Y. K., Chang C. et al. Incorporation and controlled release of a hydrophilic antibiotic using poly(lactide-co-glycolide)-based electrospun nanofibrous scaffolds. J Contr Rel (2004), Vol. 98(1), pp. 47-56

Kim T. G., Lee D. S., Park T. G. Controlled protein release from electrospun biodegradable fiber mesh composed of poly(e-caprolactone) and poly(ethylene oxide). Int J Pharm (2007), Vol. 338(1-2), pp. 276-283

Kosmider K., Scott J. Polymeric nanofibers exhibit an enhanced air filtration performance. Filtr Separat (2002), Vol. 39(6), pp. 20-22

Krishnappa R. V. N., Desai K., Sung C. M. Morphological study of electrospun polycarboinates as a function of the solvent and processing voltage. J Mater Sci (2003), Vol. 38, pp. 2357-2365

Lee J. S., Choi K. H., Ghim H. D., Kim S. S., Chun D. H., Kim H. Y., Lyoo W. S. Role of molecular weight of atactic poly(vinyl alcohol) (PVA) in the structure and properties of PVA nanofabric prepared by electrospinning. J Appl Polym Sci (2004), Vol. 93, pp. 1638-1646

Li D., McCann J. T., Gratt M., Xia Y. N. Chem Phys Lett (2004), 394, 387

Li S-F., Chen J-P., Wu W-T. Electrospun polyacrylonitrile nanofibrous membranes for lipase immobilization. J Mol Catal B: Enzym (2007), Vol. 47(3-4), pp. 117-124

Li W. J., Laurencin C. T., Caterson E. J. et al. Electrospun nanofibrous structure: A novel scaffold for tissue engineering. J Biomed Mater Res (2002), Vol. 60(4), pp. 613-621

Liang D., Hsiao B. S., Chu B. Functional electrospun nanofibrous scaffolds for biomedical applications. Adv Drug Deliver Rev (2007), Vol. 59(14), pp.1392-1412

Liu H. Q., Hiseh Y. L. Ultrafine Fibrous Cellulose Membranes from Electrospinning of Cellulose Acetate. J Polym Sci Pol Phys (2002), Vol, 41, pp. 953-964

Liu R. L., Ye Y. X., Xiong X. P., Liu H. Q. Mater. Chem. Phys, (2010), Vol. 121, pp. 432-439.

Lu H-W., Zeng W., Li Y-S. et al. Fabrication and electrochemical properties of three-dimensional net architectures of anatase TiO_2 and spinel $Li_4Ti_5O_{12}$ nanofibers. J Power Sources (2007), Vol. 164(2), pp. 874-879

Lu X. F., Li L. L, Zhang W. J, Wang C. Nanotechnology (2005), Vol. 16, pp. 2233

Lu X. F., Zhang J. W., Zhao Q. D., Wang F. L., Wang C. E-polymers (2006), no. 033

Lu X., Zhao Y., Wang C. Fabrication of PbS Nanoparticles in Polymer-Fiber Matrices by Electrospinning. Adv Mater (2005), Vol. 17, pp. 2485

Luong-Van E., Grondahl L., Chua K. N. et al. Controlled release of heparin from poly(e-caprolactone) electrospun fibers. Biomaterials (2006) Vol. 27(9), pp. 2042-2050

Luu Y. K., Kim K., Hsiao B. S. et al. Development of a nanostructured DNA delivery scaffold via electrospinning of PLGA and PLA-PEG block copolymers. J Contr Rel (2003), Vol. 89(2), pp. 341-353

Ma Z., Kotaki M., Inai R. et al. Potential of nanofiber matrix as tis-sue-engineering scaffolds. Tissue Eng (2005), Vol. 11(1-2), pp. 101-109

Ma Z., Kotaki M., Ramakrishna S. Surface modified nonwoven poly-sulphone (PSU) fiber mesh by electrospinning: A novel affinity membrane. J Membrane Sci (2006), Vol. 272 (1-2), pp. 179-187

Mann J. R., Watson M. D. Langmuir (2007), Vol. 23, pp. 10924-10928

Marler J. J., Upton J., Langer R. et al. Transplantation of cells in ma-trixes for tissue regeneration. Adv Drug Deliver Rev (1998), Vol. 33(1-2), pp. 165-182

Martin S. T., Herrmann H., Choi W. Y., M., Hoffmann M. R. J Chem Soc Faraday Trans (1994), Vol. 90, pp. 3315-3322.

Matatov-Meytal Y., Sheintuch M. Catalytic fibers and cloths. Appl Catal A (2002), Vo. 231(1-2), pp. 1-16

Matthews J. A., Wnek G. E., Simpson D. G. et al. Electrospinning of Col-lagen Nanofibers. Biomacromolecules (2002), Vol, 3(2), pp. 232-238

Matthews J. A., Wnek G. E., Simpson D. G., Bowlin G. L. Electrospun Collagen: A Tissue Engineering Scaffold with Unique Functional Properties in a Wide Variety of Applications. Biomacromoleculus (2002), Vol. 3, pp. 232-238

Melgeski S., Sthephens J. S., Chase D. B., Rabolt J. F. Micro- and nanostructured surface morphology on electrospun polymer fibers. Macromolecules (2002), Vol. 35, pp. 8456-8466

Mit-uppatham C., Nithitanakul M., Supaphol P. Ultrafine Electrospun Polyamide-6 Fibers: Effect of Solution Conditions on Morphology and Average Fiber Diameter. Macromol Chem Physic (2004), Vol. 205, pp. 2327-2338

Mo X. M., Xu C. Y., Kotaki M. et al. Electrospun P(LLA-CL) nanofiber: A biomimetic extracellular matrix for smooth muscle cell and endothelial cell proliferation. Biomaterials (2004), Vol, 25(10), pp. 1883-1890

Mo X. M., Xu C. Y., Kotaki M., Ramakrrishna S. Electrospun P(LLA-CL) nanofiber: a biomimetic extracellular matrix for smooth muscle cell and endothelial cell proliferation. Biomaterials (2004), Vol. 25, pp. 1883-1898

Nerem R. M., Saltzman A. Tissue engineering: From biology to bio-logical substitutes. Tissue Eng (1995), Vol. 1(1), pp. 3-13

Ostermann R., Li D., Yin Y. D., McCann J. T., Xia Y. N. Nano Lett (2006), Vol. 6, pp. 1297

Pan C., Gu Z. Z., Dong L. Acta Chim Sin (2009), Vol. 67, pp. 1981-1986.

Pawlowski K. J., Belvin H. L., Raney D. L., Su J., Harrison J. S., Siochi E. J. Electrospinning of a micro-air vehicle wing skin. Polymer (2003), Vol. 44, pp. 1309-1314

Pornsopone V., Supaphol P., Rangkupan R. et al. Electrospun methacrylate-based copolymer/indomethacin fibers and their release characteristics of indomethacin. J Polym Res (2007), Vol. 14(1), pp. 53-59

Qi H., Hu P., Xu J. et al. Encapsulation of drug reservoirs in fibers by emulsion electrospinning: morphology characterization and preliminary release assessment. Biomacromolecules (2006), Vol. 7(8), pp. 2327-2330

Raja T., Omprakash S. Preparation and Characterization of Polymer Nano Fibres Produced from Electrospinning. Journal of Optoelectronics Engineering (2014), Vol. 2 (2), pp. 24-28

Ramaseshan R., Sundarrajan S., Jose R., Ramakrishna S. Nanostructured ceramics by electrospinning. J Appl Phys (2007), Vol. 102, pp.111101

Reneker D. H., Yarin A. L., Fong H., Koombhongse S. Bending instability of electrically charged liquid jets of polymer solutions in electrospinning. J Appl Phys (2000), Vol. 87, pp. 4531-4547

Rho K. S., Jeong L., Lee G. et al. Electrospinning of collagen nanofibers: Effects on the behavior of normal human keratinocytes and early- stage wound healing. Biomaterials (2006), Vol. 27(8), pp. 1452-1461

Rutledge G. C., Li Y., Fridrikh S., Warner S. B., Kalayci V. E., Patra P. Electrostatic Spinning and Properties of Ultrafine Fibers, National Textile Center (2001) Annual Report (M98-D01), National Textile Center, pp. 1-10

Sawicka K. M., P. Gouma. Electrospun composite nanofibers for functional applications. Journal of Nanoparticle Research (2006), Vol. 8, pp. 769-781

Sawicka K. M., Prasad A. K., Gouma P. I. Metal oxide nanowires for use in chemical sensing applications. Sens Lett (2005), Vol. 3(1), pp. 31-35

Smith E., Buttner U., Sanderson R. D. Continuous yarns from electrospun fibers. Polymer (2005), Vol. 46(8), pp. 2419–2423

Son W. K., Youk J. H., Lee T. S., Park W. H. Electrospinning of ultrafine cellulose acetate fibers: studies of a new solvent system and deacetylation of ultrafine cellulose acetate fibers. J Polym Sci Pt B-Polym Phys (2004c), Vol, 42, pp. 5-11

Son W. K., Youk J. H., Lee T. S., Park W. H. The effects of solution properties and polyelectrolyte on electrospinning of ultrafine poly(ethylene oxide) fibers. Polymer (2004a), Vol. 45, pp. 2959-2966

Srnivasarao M., Collings D., Philips A., Patel. Theree-Dimensionally Order Array of Air Bubbles in a Polymer Film. Science (2001), Vol. 292, pp. 79-83

Stankus J. J., Guan J., Wagner W. R. Fabrication of biodegradable elastomeric scaffolds with sub-micron morphologies. J Biomed Mater Res Part A (2004), Vol. 70A (4), pp. 603-614

Stasiak M., Studer A., Greiner A .et al. Polymer fibers as carriers for homo-geneous catalysts. Chem A Europ J (2007), Vol. 13(21), pp. 6150-6156

Subramanian A., Vu D., Larsen G. F., Lin HY. Preparation and evaluation of the electrospun chitosan/PEO fibers for potential applications in cartilage tissue engineering. J Biomater Sci Polym Ed (2005), Vol, 16(7), pp. 861.73

Taepaiboon P., Rungsardthong U., Supaphol P. Drug-loaded electrospun mats of poly (vinyl alcohol) fibres and their release characteristics of four model drugs. Nanotechnology (2006), Vol. 17(9); pp. 2317-2329

Tao S., Li G., Yin J. Fluorescent nanofibrous membranes for trace de-tection of TNT vapor. J Mater Chem (2007), Vol. 17(26), pp. 2730-2736

Taylor G. Disintegration of Water Drops in an Electric Field. Proc R Soc Lond A (1964), Vol. 280, pp. 383-397

Taylor G. I. Proc Roy Soc London (1969), Vol. A313, pp. 453

Tungprapa S., Jangchud I., Supaphol P. Release characteristics of four model drugs from drug-loaded electrospun cellulose acetate fiber mats. Polymer (2007), Vol. 48(17), pp. 5030-5041

Ursula E., Spichiger-Keller. Chemical Sensors & Biosensors for Medical and Biological Applications. Weinheim: Wily-VCH (1998), pp. 377-378

Venugopal J., Zhang Y. Z., Ramakrishna S. Fabrication of modified and functionalized polycaprolactone nanofibre scaffolds for vascular tis-sue engineering. Nanotechnology, (2005),Vol. 16(10), pp. 2138-2142

Verreck G., Chun I., Rosenblatt J. et al. Incorporation of drugs in an amorphous state into electrospun nanofibers composed of a water- insoluble, nonbiodegradable polymer. J Contr Rel (2003), Vol. 92(3), pp. 349-360

Viswanathamurthi P., Bhattarai N., Kim H. Y., Khil M. S., Lee D. R., Suh E. K. GeO_2 fibers : Preparation, morphology, and photoluminescence property. J Chem Phys (2004), Vol. 121, pp. 441

Wang G., Ji Y., Huang X. et al. Fabrication and characterization of polycrystalline WO3 nanofibers and their application for ammonia sensing. J Phys Chem B (2006), Vol. 110(47), pp. 23777-23782

Wang H., Ding J., Lee B. et al. Polypyrrole-coated electrospun nano-fibre membranes for recovery of Au(III) from aqueous solution. J Membrane Sci (2007), Vol. 303(1-2), pp. 119-125

Wang M., Singh H., Hatton A. T., Rutledge G. C. Gallic Acid-loaded Cellulose Acetate Electrospunn Nanofibers: Thermal Properties, Mechanical Properties, and Drug Release Behavior. Polymer (2004), Vol. 45, pp. 5505

Wang M., Wang L., Huang Y. Electrospun hydroxypropyl methyl cellul

Wang W., Asher S. A. ACS Publications. J Am Chem Soc (2001), Vol. 123, pp.125-128

Wang X., Drew C., Lee S-H. et al. Electrospun nanofibrous membrane for highly sensitive optical sensors. Nano Lett (2002), Vol. 2(11), pp. 1273-1275

Wang X., Kim Y-G., Drew C.et al. Electrostatic assembly of conju-gated polymer thin layers on electrospun nanofibrous membranes for biosensors. Nano Lett (2004), Vol. 4(2), pp. 331-334

Wang X., Lee S-H., Drew C. et al. Electrospun nanofibrous membranes for optical sensing. Polym Mater Sci Eng (2001), Vol. 85, pp. 617-618

Wang Y. Z., Li Y. X., Yang S. T., Zhang G. L., An D. M., Wang C., Yang Q. B., Chen X. S., Jing X. B., Wei Y. Nanotechnology (2006), Vol. 17, pp. 3304

Wang Y., Hsieh Y-L. Enzyme immobilization to ultra-fine cellulose fibers via amphiphilic polyethylene glycol spacers. J Polym Sci Part A: Polym Chem (2004), Vol. 42(17), pp. 4289-4299

Wannatong L., Sirivat A., Suphapol P. Effects of solvents on electrospun polymeric fibers: preliminary study on polystyrene. Polym Int (2004), Vol. 53, pp. 1851-1859

Xu C., Yang F., Wang S. et al. In vitro study of human vascular endothelial cell function on materials with various surface roughness. J Biomed Mater Res Part A (2004), Vol. 71A (1), pp. 154-161

Xu X., Yang L., Xu X. et al. Ultrafine medicated fibers electrospun from W/O emulsions. J Contr Rel (2005), Vol. 108(1), pp. 33-42

Yang M., Xie T. F., Peng L. et al. Fabrication and photoelectric oxygen sensing characteristics of electrospun Co doped ZnO nanofibers. Appl Phys A Mater Sci Proc (2007), Vol. 89(2), pp. 427-430

Yang Q. B., Li D. M., Hong Y. L., Li Z. Y., Wang C, Qiu S. L., Wei Y. Preparation and characterization of a PAN nanofibre containing Ag nanoparticles via electrospinning. Synth Met (2003), Vol. 137, pp. 973

Yarin A. L., Koombhongse S., Reneker D. H. Bending instability in electro-spinning of nanofibers. J Appl Phys (2001), Vol. 89(5), pp. 3018-3026

Yih T. C., Al-Fandi M. Engineered nanoparticles as precise drug de-livery systems. J Cell Biochem (2006), Vol. 97(6), pp. 118-1190

Yuan X., Zhang Y., Dong C., Sheng J. Morphology of ultrafine polysulfone fibers prepared by electrospinning. Polym Int In Press (2005)

Zeng J., Xu X., Chen X., Liang Q., Bian X., Yang L., Jing X. Biodegradable electrospun fibers for drug delivery. J Control Release (2003), Vol. 92, pp. 227-231

Zeng J., Aigner A., Czubayko F. et al. Poly(vinyl alcohol) nanofibers by electrospinning as a protein delivery system and the retardation of enzyme release by additional polymer coatings. Biomacromolecules (2005), Vol. 6(3), pp. 1484-1488

Zeng J., Xu X., Chen X. et al. Biodegradable electrospun fibers for drug delivery. J Contr Rel (2003), Vol, 92(3), pp. 227-231

Zhang Y. Z., Feng Y., Huang Z. M. et al. Fabrication of porous elec-trospun nanofibers. Nanotechnology (2006), Vol, 17(3), pp. 901-908

Zhao S. L., Wu X. H., Wang L. G., Huang Y. Electrospinning generated fibers of ethyl-cyanoethyl cellulose / tetraydrofuran solutions. J Appl Polym Sci (2004), Vol. 91, pp. 242-246

Zhong X. H., Kim K. S., Fang D. F., Ran S. F., Hsiao B. S., Chu B. Structure and process relationship of Electrospun bioabsorbable nanofiber membranes. Polymer (2002), Vol. 43, pp. 4403-4412

Zong X., Kim K., Fang D.et al. Structure and process relationship of electrospun bioabsorbable nanofiber membranes. Polymer (2002), Vol. 43(16), pp. 4403-4412

Introduction

Numerous kinds of chemical species, natural and artificial, some of which are vital to our life, while many others are harmful more or less are contained in the atmospheric air. While the vital gases like oxygen and humidity should be kept at adequate levels in atmosphere, hazardous gases should be controlled and maintained under the designated levels. The atmospheric pollution can, however, diffuse rapidly over large areas and can cause major disasters in a short period of time. It can be emitted by a stationary or mobile source. Workplaces, the house, thermal power stations are stationary sources emitting atmospheric pollution, while mobile sources include automobiles, trains, ships, chemical plants, metal refineries, and etc. Therefore, are necessary, control systems that can monitor, detect and quantify sources of pollution quickly, to prevent or minimize the damage caused by air pollution. Among the most studied and widespread monitoring systems over the past years, we find the composite nanostructured sensors. Such devices, thanks to their small size, have greater surface area exposure, therefore more binding sites for the pollutant of interest. Electrospinning technology has been proven to be an intriguing strategy to create highly performing nanostructured sensors **(Macagnano, A. et al., 2015)** able to reveal toxic gases and VOCs in the environment. Therefore various nanocomposite fibrous layers have been synthesized and investigated for their applications as active materials for gas sensors **(Ding, B. et al., 2010).** The design of nanocomposite layers for sensor applications takes in consideration several factors, such as the arrangement of both materials within the fibers, their interfacial characteristics, electrical and optical performances, thermal and mechanical stability, etc., all of which depending significantly on each materials features and deposition process parameter.

Chapter 3

Gas Sensors

3.1 Definition of Gas Sensors

Sensors can be designed as an analogous to the human senses. In both cases, signals are collected from the environment and converted into a signal by sensory receptors in humans or by receptor and transducer systems in sensor systems. In a living organism, the receptor of the sensing organ is in direct contact with the environment. Environmental stimuli are transformed into electrical signals conducted by nerve cells (neurons) in the form of potential pulses. Strong stimuli generate a high frequency, i. e. the process is basically some kind of frequency modulation. In the amplification and processing stage, the sensory nerve system is comparable to an analog circuit. Signal amplification and signal conditioning, mainly in the form of signal reduction, take place. In the brain, information is evaluated and, finally, some action is evoked. We see many similarities between living organism and machines when we compare how modern sensors and living organism acquire and process signals. The receptor responds to environmental parameters by changing some of its inherent properties. In the adjacent transducer, primary information is transformed into electrical signals. Frequently, modern sensor systems contain additional parts for signal amplification or conditioning. The processing stage, which is obviously in the brain for humans, can be performed by a computer in the case of sensor system **(Figure 3.1).** Infact, at the end of the chain, we find a microcomputer working like the central nervous system in a living organism. Therefore, It has been demonstrated that signals processing by electronic amplifiers or by digital computers is

indispensable for sensor function, like the indispensability of neurons and the brain for physiological processes in organism.
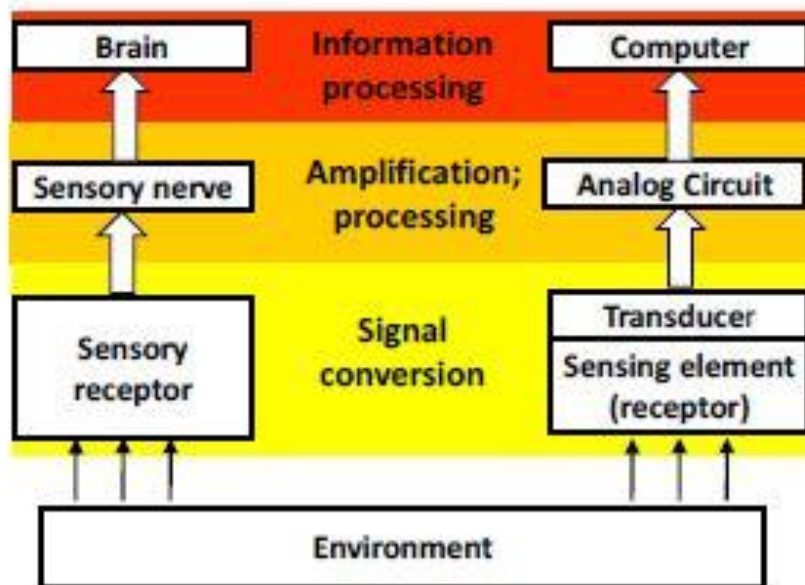
Figure 3.1: Illustrates the similarities between biological and technical systems.

According to the definition of a gas sensor, given by the International Union of Pure and Applied Chemistry (lUPAC), "a chemical sensor is a device that transforms chemical information, ranging from the concentration of a specific sample component to total composition analysis, into an analytically useful signal. The chemical information, mentioned above, may originate from a chemical reaction of the analyte or from a physical property of the system investigated" **(Hulanicki, A. et al., 1991).** Typically, chemical sensors consist of two main parts:

- a chemically interactive material (CIM) called **receptor;**
- a basic electronic device called **transducer**;

The first layer, of chemical type, is composed of a membrane whose role is to "deal with" the molecules in the environment subjected to detection by forming with them bonds (chemical) or activing further chemical reactions. Upon a suitable chemical/physical reaction with surrounding molecules, some of sensing membrane physical properties (like conductivity, temperature, mass, refractive index, function work, etc.), defined as intermediate parameters, can vary. These variations are detected by a second layer consisting of a basic electronic device whose purpose is to transduce the chemical signal into electrical. The basic device, selected according to the physical quantity of which you want to measure the variation, is then transformed by the CIM in the chemical sensor. Therefore, generally, the **receptor** transforms chemical information into a form of energy, which can be measured by the transducer **(Hulanicki, A. et al., 1991).** The **transducer** converts this energy into a useful, typically electrical, analytical signal. The receptor part of chemical sensors may be based upon various principles **(Hulanicki, A. et al., 1991):**

- physical, where no chemical reaction takes place (weak bonds). Typical examples are those based on measurement of absorbance, refractive index, conductivity, temperature or mass change.

- chemical, in which a chemical reaction occurs (strong bonds), causing analytical signal.

- biochemical, in which a biochemical process is involved. Typical examples are microbial potentiometric sensors or immunosensors. They may be considered as a subgroup of the chemical ones. Such sensors are called biosensors.

In some cases it is not possible to decide unequivocally whether a sensor operates through a chemical or on a physical principle. This is, for example, the case when the signal is due to an adsorption process. Sensors are normally designed to operate under well defined conditions for specified analytes in certain sample types. Therefore, it is not always necessary that a sensor responds specifically to a certain analyte. Under well controlled operating conditions, the analyte signal may be independent of other sample components, thus allowing the determination of the analyte without any major preliminary treatment of the sample (specific sensors). Otherwise, non-specific sensors can be used in series for a multicomponent analysis, using a proper multivariate calibration software and signal processing. Such systems for multicomponent analysis are called sensor arrays.

3.2 Chemically interacting materials: polymers, macromolecules and different types of nanocomposite films

The study of chemically interacting materials is aimed onto molecules, organics and not, capable of forming non-volatile films (able to stay on the base device) and which allow easy capturing of the compounds from the environment.

The films made with organic molecules can be polymeric, molecular or nanocomposite films; the characteristic that distinguishes one from the other is the type of bond established between the molecules. The polymers are compounds consisting of the union, by means of covalent chemical bonds, of smaller molecules, the same or not, called monomers **(Figure 3.2 (b)).** Therefore, they are chemical compounds of high molecular weight whose formation can occur by heating, for lighting or for the presence of catalysts

and can be of different type depending on the monomer used or polymerization conditions.

3.2.1 Polymers

The polymers have been used in many applications in the field of chemical sensors for the detection of organic compounds; among their main characteristics, the ability to form adhering films to the base device and the possibility of modifying the selectivity (the ability to discriminate the substance to be detected) by simply varying their chemical structure, are the most significant for sensors application. The polymers can be rubbery or glassy. Rubbery polymers allow a rapid absorption of the chemical species to be detected, so the sensor provides the related signal in short time; glassy polymers, however, while not creating troubles from a mechanical point of view, do not allow an easy penetration of the substances to be detected, then the sensor has a response time rather long.

Finally, also macromolecular films can be used for developing sensing layer: they can be composed for instance with planar molecules (e.g. phthalocyanines, porphyrins) or molecular cages (e.g. cavitands) designed to begin stable layers at the solid state only by electrostatic forces (**Figure 3.2 (a)**).
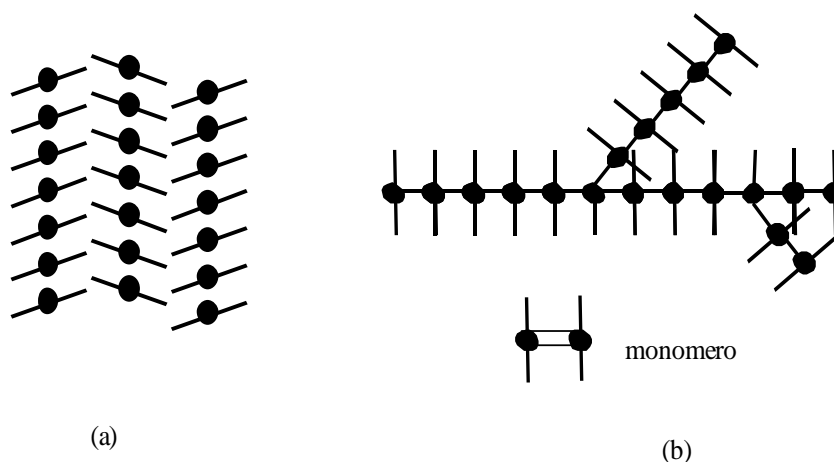
(a)   (b)

Figure 3.2: Structure of a molecular film (a) and polymer (b)

3.2.1.1 Chemical sensors based on polymers

Generally, sensors based on metal oxide semiconductors, exhibit significantly greater sensitivity to inorganic gases like ammonia and volatile organic compounds (VOCs) like formaldehyde and alcohol (C_2H_5OH). However, when the concentration of other VOCs exceeds a certain threshold, they cannot be detected by metal oxide semiconductor-based sensors. Therefore, it is important to monitor the concentration of these vapors. Furthermore to keep atmospheric emissions under control, are required sensing materials like polymers. When the polymer layers are exposed to the vapor of an analyte, the physical properties of the polymer layer such as its mass and dielectric properties will change upon gas absorption. Specifically, the various physisorption mechanisms by which VOCs interact with polymers include induced dipole/induced dipole interactions (also named London dispersion), dipole/induced dipole interactions, dipole/dipole interactions and hydrogen bonds (Lewis acidity/basicity-concept) (**Hagleitner, C. et al., 2002**).

According to the different changes in physical properties, polymers used for gas sensing can be further classified into two groups:

- **Conducting Polymers**: it is well established that the electrical conductivity of these conducting polymers is affected through exposure to diverse organic and inorganic gases. This feature has led to the investigation of these materials as gas sensing layers by a number of groups **(Shrivas, A. G. et al., 2007; Hatfid, J. V. et al., 1994; Gardner, J. W. et al., 1993).** Conducting polymers that can be used as gas sensing materials include polypyrrole (PPy), polyaniline (PANi), polythiophene (PTh) and their derivatives **(Bai, H. et al., 2007).** The conductivity of polymers can be improved through different processes of doping by redox reactions or protonation. After the doping process, which is reversible, polymers become conductors or semiconductors. The most important thing is that the doping level can be changed by chemical reactions between the polymers and target gases, making the detection of analytes based on these conducting polymers practical. Most kinds of polymer are doped through redox reactions. For those gases inactive to redox reactions at room temperature, some specific polymers can be utilized. For example, redox reactions of CO could not happen at room temperature, however, the response of PANi towards CO could be observed (**Bai, H. et al., 2007**). Conducting polymers can be directly seen as transducers to reflect changes in electrical properties.

- **Non Conducting Polymers:** Non-conducting polymers have been widely utilized as coatings on different sensor devices, where the coating and the device can be regarded as a common transducer on the whole. Polymers with different properties or physisorption mechanisms can be coated onto respective transducers. For instance, polymer layers

causing changes in resonance frequency, dielectric constant and enthalpy upon absorption/desorption of analytes can be respectively coated on mass-sensitive (e.g., Quartz Crystal Microbalance (QCM), Surface Acoustic Wave (SAW) and Surface Transverse Wave (STW)), capacitive (dielectric) and calorimetric sensor devices. Then, the sensor devices could convert changes in the monitored polymer properties into an electrical signal output (**Hagleitner, C. et al., 2002**). Additionally, non-conducting polymer membrane (e.g., polyimide) can also be used on metal oxide semiconductor gas sensors as molecular sieves, to enhance the overall selectivity by introducing the sensitivity of polymer layers (**Wong, K. K. L. et al., 1995**). Polymer-based gas sensors have advantages such as high sensitivities and short response times. Furthermore, while operation temperatures of metal oxide semiconductor-based sensors are usually more demanding, polymer-based sensors operate at room temperature. Polymer-based gas sensors also have some disadvantages such as long-time instability, irreversibility and poor selectivity. As a kind of gas sensors with lower power consumption polymer-based sensors have a promising future.

Polymer-based gas sensors have advantages such as high sensitivities and short response times. Furthermore, while operation temperatures of metal oxide semiconductor-based sensors are usually more demanding, polymer-based sensors operate at room temperature. Polymer-based gas sensors also have some disadvantages such as long-time instability, irreversibility and poor selectivity.

3.2.2 Different types of nanocomposite films

Another type of chemical interactive material is represented by nanocomposite films. Nanocomposite films consists of nanocrystalline or amorphous phase of a least two different materials. Depending on the nature of the component materials, micro/nanostructure and surface/interfacial characteristics, various unique gas sensing properties can be realized by using nanocomposite films as the active layer. Improvement in gas sensitivity, selectivity, stability, as well as reduction in the response time and operating temperature has been demonstrated by various types of nanocomposite films.

3.2.2.1 Metal-metal oxide nanocomposite films

Nanocomposite films that consist of metal nanoparticles dispersed in a matrix of metal oxides have recently attracted much interest as materials for gas sensors. Metal-metal oxide nanocomposites have physical properties that differ from those of the nanostructured single phase metal oxides. The metal nanoparticles play both passive and active roles in the sensing process. The presence of metal nanoparticles increases the active surface area and improves gas diffusion inside the film. Metal nanoparticle also reduces the electrical resistance and increases the optical absorption of metal oxide. Metal nanoparticles such as platinum (Pt), palladium (Pd), gold (Au), palladium (Pd) and silver (Ag) also show catalytic properties that can modify the analyte–metal oxide chemical interactions and enhance the sensing process. The interfacial region between metal nanoparticle and metal oxide also has very different electron band structure than inside the bulk semiconducting metal oxide, which also contribute to the unique gas sensing properties of this type of nanocomposits. The amount and distribution of the metallic nanoparticles in

a metal oxide matrix is an important parameter to be controlled in order to obtain highest gas sensing sensitivity. Different methodologies including PVD, impregnation, sol-gel, and electroless plating have been used to introduce metal nanoparticles into the metal oxide matrix. Dot- and rod-shaped Au-TiO$_2$ nanocomposite films were prepared by a sol-gel method for SPR sensing of alcohol vapours **(Manera, M. G et al., 2008).** Other metal-metal oxide nanocomposite films prepared by sol-gel processes include the SnO$_2$-Ag nanocomposite **(Gong, J. et al., 2006);** Au-TiO$_2$-NiO nanocomposites **(Della Gaspera, E. et al., 2010)** and Au-TiO$_2$ nanocomposite films for sensing vapor organic compounds by Surface Plasmon Resonance and optical absorption **(Fernandez, C. D. J. et al., 2005).** Electrophoretic deposition process can also be used to deposit metal-metal oxide nanocomposite films. For example, the mesoporous TiO$_2$ on ITO/glass was immersed in Au nanocrystal dispersion in chloroform. A potential of 25 or 50 V was applied to infuse the Au nanocrystals inside the mesoporous TiO$_2$ film to form the Au-TiO$_2$ nanocomposite films. The ligands such as dodecanethiol on the Au nanocrystals prevented aggregation. The films were highly conductive, and are suitable for sensor applications **(Patel, M. N. et al., 2007; Mehul, N. et al., 2008).**

Metal-metal oxide nanocomposite films combine the catalytic property of metal and gas reactivity of semiconducting metal oxide, thereby possess unique gas sensing properties unavailable from either the metal or metal oxide alone. Metallic nanoparticles activate or dissociate the detected gas on their surface. These activated products are easier to react with the adsorbed oxygen species on the metal oxide surface, resulting in a change of resistance. In addition, direct exchange of electrons between the semiconductor metal oxide and metallic nanoparticles causes a change in the width of the depletion layer of the semiconductor oxide, leading to a change in sensing properties. The embedded metal nanoparticles can reduce the sensing temperatures, improve the selectivity, and increase the surface area of the metal oxide.

3.2.2.2 Mixed metal oxides

Transition metal oxides have promising gas sensing performance due to their catalytic properties. Some transition metal oxides are stable, have low electric resistance and good gas sensing properties at low operating temperature, while others have high electric resistivity and require high operating temperatures. Some of the oxides are more sensitive to oxidizing gases while others are more to reducing gases. It is therefore a natural approach to combine metal oxides of different properties with an appropriate proportion so that gas sensor performance can be modified as desired. Various mixed metal oxide nanocomposite films have been prepared by the sol-gel process. For example, cobalt oxide-SiO_2 nanocomposite films were deposited on glass substrate by Musat et al. (**Musat, V. et al., 2008**) using $[Co(CH_3COO)_2].4H_2O$, tetraethoxysilane and $CH_3(CH_2)15N(CH_3)_3Br$ surfactant as starting materials. PVD process has also been used to deposit mixed metal oxide nanocomposite films. Wisitsoraat et al. (**Wisitsoraat, A. et al., 2007**) used oxygen ion-assisted electron beam evaporation to prepare various TiO_2 based mixed oxide nanocomposite films such as TiO_2-WO_3, TiO_2-MoO_3, TiO_2-NiO_x, and TiO_2-ZnO. Mixing metal oxides of complementary behaviors forms a new class of nanocomposit materials. This type of nanocomposite films show a significant improvement in gas sensing properties.

3.2.2.3 Polymer-metal or metal oxide

Gas sensors using metal oxide films always lack in selectivity and require high operating temperatures (300-500°C). High operating temperatures may leads to sensor instability and response variation. Sensing materials with low operating temperatures can inhibit structural changes, reduces the power

117

consumption and enables safer detection of combustible gases. Conducting polymers such as polypyrrole (PPy), polyaniline (PANi), polythiophene (PTh) and their derivatives typically can operate at low temperature in comparison to most of the metal oxide sensors. Conducting polymers can behave like semiconductors due to their heterocyclic compounds. As a result, reversible changes in the sensing polymer layer's conductivity can be detected upon adsorption of polar gas molecules on the surfaces at low temperature. This effect is believed to be caused by the charge transfer between gas molecules and the polymer or the polymer film's swelling. Conducting polymers are also easy to be synthesized through chemical or electrochemical processes, and their molecular chain structure can be modified conveniently by copolymerization or structural derivations. In addition, conducting polymers have good mechanical properties, which allow a facile fabrication of sensors. Conducting polymer matrices embedded with nano-scale metal or metal oxide particles (example: QDs) forms a new class of nanocomposite materials that has shown better gas sensing features. The reasons for such an improvement can be attributed either to catalytic behaviors of metal particles or to the formation of metal oxide-polymer junction. For example, the n-type SnO_2 forms a hetero pn-junction to p-type conducting polymer with a depletion region. Metal-polymer nanocomposites can easily be prepared by PVD processes such as sputter deposition and vacuum thermal evaporation, as well as wet Chemical Deposition or Electrospinning. Polymer-metal or metal oxide nanocomposite is a new class of material that combines the advantages of both organic polymer material and inorganic metal or semiconductor oxide and shows improved optical, electrical and mechanical properties for gas sensor applications. Cioffi et al. **(Cioffi, N., et al., 2004)** investigated-CFx polymer films embedded with Pd or Au nanoparticles (Pd-CFx and Au-CFx nanocomposites films) for detecting vapors of organic solvents. Mixing semiconductive metal oxide with PANi to form nanocomposites was found to be an effective way to improve the gas sensing properties of PANi. Tai et al.

(Tai, H., et al., 2007) studied a polyanilinetitanium dioxide (PANi-TiO$_2$) nanocomposite films for the NH$_3$ gas sensor.

3.2.2.4 Chemical sensors based on metal oxide semiconductors nanocomposites

Conductometric chemical sensors based on nanocrystalline metal-oxide semiconductors are the most promising among solid-state gas detectors due ti their reliability and ease of manufacture. Their sensitivity is related to change in conductivity (or resistance), resulting from chemical interaction of adsorbed target gas with active centers on the surface of the sensor. Sensor features, such as sensitivity, selectivity and response time, are mainly ruled by the reactivity of active centers of the sensor and the diffusion of gas to these sites. The main disadvantage of such sensors is the rather low selectivity to gases that have similar chemical characteristics and the relatively high operating temperature.

Semiconductor gas sensors are devices that are made up of heated metal oxides which are used for measurement of gas concentration of a target gas by measuring the electrical resistance of the device. Sensors based on metal oxide semiconductors are mainly applied to detect target gases through redox reactions between the target gases and the oxide surface **(Yamazoe, N. et al., 2002).** This process includes two steps **(Keat, G. O. et al., 2002)**: redox reactions, during which O$^-$ distributed on the surface of the materials would react with molecules of target gases, leading to an electronic variation of the oxide surface; and then this variation is transduced into an electrical resistance variation of the sensors. The resistance variation could be detected by measuring the change of capacitance, work function, mass, optical characteristics or reaction energy **(Wang, C. et al., 2010).** An intrinsic n-type

semiconductor is suitable for detecting reducing gases due to the high conductance change as a result of the injected electrons. Similarly, a p-type semiconductor is suitable for the detection of oxidizing gases. The oxides usually used for the n-type are mainly oxides: SnO_2, ZnO In_2O_3, or WO_3. They are commonly used to detect hydrogen, oxygen, alcohol and harmful gases like carbon monoxide. Gas sensors using metal oxide semiconductor were first proposed by Seiyama and Taguchi. Tin dioxide (SnO_2) is the commonly used gas sensing material. It is an n-type granular material whose electrical conductivity is dependent on the density of pre-adsorbed oxygen ions on its surface. The resistance of tin dioxide changes according to the variation of gas concentration (e.g., liquefied petroleum gas (LPG), methane (CH_4), carbon monoxide (CO) and other reducing gases **(Endres, H. E., et al., 1996; Hoefer, U. et al., 1997),** while the relationship between resistance and target gas concentration is nonlinear **(Fraiwan, L., et al., 2011).** Other metal oxide semiconductors (e.g., tungsten trioxide (WO_3)) are also widely used for gas sensing. Anodic tungsten oxide applying electrochemical etching of tungsten shows excellent responses towards hydrogen (H_2) and nitrogen oxide (NO) **(Jarmo, K., et al, 2011).** However, the response of pure WO_3 to NH_3 is rather poor, and because of the interference from NO_x, the selectivity of WO_3 sensors for NH_3 is low. Others like titanium dioxide (TiO_2) are also used as sensitive layers for their sensitivity in terms of dielectric permittivity to gas adsorption **(Hallil, H., et al., 2010).** Several influencing factors, such as the characteristics and structure of the sensing layer, affect the redox reactions and thus decide the sensitivity of metal oxides as gas sensing materials. Apart from the heating methods, there are also other methods like pre-concentration technology that could be applied to improve the sensitivity of gas sensors **(Xiao, G. et al., 2011).** While the sensitivity of SnO_2 gas sensors could be controlled mainly by temperature, there are several methods that could improve the selectivity of the sensing materials. Selectivity could be improved by doping the sensing film surface with a suitable catalyst material **(Sofian,**

M. K., et al., 2009). Studies about metal oxide nanostructures have shown that nanostructures (e.g., semiconductor nanowires) could improve gas sensors' sensitivity and response time **(Comini, E., 2005).**

3.2.2.5 Carbon nanotube based on nanocomposite films

Carbon nanotubes (CNTs) are very useful materials for gas-sensing applications because of their high surface to volume ratio. The large surface area provided by the hollow cores and outside walls in nanotubes gives them very large capacity for gas absorption. Interaction of CNTs with certain gases can change the electrical properties of semiconducting CNTs even at room temperature. However, CNTs based sensor has a number of limitations including long recovery time, and weakness to humidity. In addition, the range of gas molecules that can be detected by CNTs sensors is limited to the molecules that have large binding energies and charge transfers with the CNTs. To improve the gas sensing properties of CNTs, catalytic metal nanoparticles, semiconductive metal oxides or conductive polymers were mixed with CNTS to form nanocomposites. The composite combines the advantages of CNTs and other gas-sensing materials and provide a new class of active materials with unique gas sensing property.

3.3 Classification of chemical gas sensors

A chemical gas sensor can be described as a device that alters one or more of its physical properties (e.g. electrical conductivity, mass, etc.) after exposure to a gaseous compound or a mixture of chemical compounds. Chemical sensors can be classified in different ways. For example, according the operating principle of the receptor principles **(Hulanicki, A. et al., 1991),** chemical sensors are distinguished in: chemical sensors, biochemical sensors and physical sensors. Chemical sensors are based on chemical reactions between analyte molecules and the receptor; biochemical sensors are a subclass of chemical sensors, where the reaction is biochemical; in physical sensors, the signal is a result of a physical process, such as absorbance, temperature, mass or conductivity change and no chemical reaction takes place at the receptor. It is not always possible to discriminate between physical and chemical sensors. The chemical sensors can be also classified according to the operating principle of the transducer **(Hulanicki, A. et al., 1991).** Infact, it possible provide a large number of chemical sensors by connecting the CIM to a suitable transducer which "transforms" the variation of one of the intermediate variables into an electrical signal. Therefore, by putting the CIM in a measurement environment containing different chemicals, they are numerous physical quantities that can vary: the work function, the optical properties, conductivity, capacity, mass, and so on.

3.3.1 Optical sensors

Some chemical materials, as a result of the interaction with molecules in the gas phase, change their optical characteristics: absorption spectrum, fluorescence and spectral refractive index. An analysis of the spectrum of

122

absorption of these materials shows that the bands related to the single state (which does not interact with other molecules), to that of the solution and to that of solid are different due to the different interactions. Consequently, it is possible to measure the absorption spectrum changes of a CIM, using a broadband photodetector and an LED that emits in the blue (since a single molecule has an absorption peak in the blue). In some molecules, one can also intervene on the phenomenon of fluorescence, i.e. the absorption of high-energy photons (in the ultraviolet spectrum) and emission of photons to lower energy (in the visible spectrum). In fact, the phenomenon can be turned off (quenching) by binding to a molecule adsorbed. The refractive index variation of spectral, instead, can be used in optical fiber sensors. In these devices, the condition of entrapment of an electromagnetic wave in an optical guide depends on the ratio between the refractive indices of the core and the cladding. There is a limit angle at which the radiation is trapped in the guide. You may get a chemical sensor by coating the cladding of a substance capable of changing the refractive index as a function of the number and the type of molecules adsorbed. This variation will lead to a change in signal power that propagates in the fiber. The optical sensors are of relatively small size, they are cheap and insensitive to electronic interference. In addition, they allow monitoring the concentration of a particular gas by a complex mixture in a precise and selective. However by improving some aspects, such as reproducibility and stability over time.

3.3.2 Conductometric sensors

Chemical bonds between the CIM and the chemicals present in the measuring environment can give rise to changes in resistance of the material, ie conductivity. This phenomenon can take place, for example, thanks to a

change in the number of bearers, or the mobility of the carriers. The interaction between analyte and CIM causes, therefore, a variation of the conduction characteristics that can be measured by suitable transducers such as the quartz microbalance or interdigitated. This form of sensor operates on the principle that electrical conductivity can change in the presence or absence of some chemical species. Two configurations are commonly used. The first arrangement consists of two elements a sensitive conducting layer and contact electrodes. DC voltage is applied to the sensor and the resistance is measured. This configuration is typically used for chemiresistors in gas-sensing applications. The conducting layer can either be a porous thick film (2–300 mm), which allows the gas to diffuse through it, resulting in good sensitivity, or a thin film (5–500 nm), on which the source material is sputtered (a process where atoms are ejected from a target or source material and deposited onto a substrate) or deposited using chemical vapor deposition onto a substrate layer, mainly oxide semiconductors (Janta, 2009). In the second configuration, an electrode (often glass) with a chemically.

3.3.3 Capacitive Sensors

The capacity of a capacitor is a function of the material (permittivity of the material) and of the geometry (electrode area and distance). The changes of permittivity of the material and geometry can be obtained through deformation of the reinforcements (dielectric liquid or gaseous), variation of temperature, applications of pressure, scroll and rotations. These physical phenomena are detected by the variation of the material's ability. In sensors that utilize this effect it is important to specify the frequency range and temperature. This necessity derives from the variability in many materials of the dielectric

constant with temperature and with the frequency, which decreases with increasing of these two quantities.

3.3.4 Mass sensors

The mass sensors are made using piezoelectric transducers, such as QCM (Quartz Crystal Microbalance) and SAW (Surface Wave Acoustice), and chemically interactive materials having the absorption characteristics required by the application. When the piezoelectric devices are used as sensors, they are placed in an oscillator circuit, suitable for sensor applications, and their frequency variations are monitored, since related to the interactions between CIM (chemically interacting material) and chemical species. Although the transducers of mass are the devices easier to use, the QCM have the big drawback of a low resolution (a few nanograms). This problem can be solved by using more sophisticated devices such as SAW, whose working frequencies are, however, much higher (hundreds of MHz) and this necessitates the use of a reading instrument and of a more complex oscillator circuit.

3.3.5 Electrochemical sensors

Electrochemical devices transform the effect of the electrochemical interaction analyte – electrode into a useful signal. Such effects may be stimulated electrically or may result in a spontaneous interaction at the zero-current condition. The following subgroups may be distinguished:

a) voltammetric sensors, including amperometric devices, in which current is measured in the d.c. or a.c. mode. This subgroup may include sensors based on

chemically inert electrodes, chemically active electrodes and modified electrodes. In this group are included sensors with and without (galvanic sensors) external current source;

b) potentiometric sensors, in which the potential of the indicator electrode (ion-selective electrode, redox electrode, meta1 oxide electrode) is measured against a reference electrode;

c) chemically sensitized field effect transistor **(CHEMFET)** in which the effect of the interaction between the analyte and the active coating is transformed into a change of the source-drain current. The interactions between the analyte and the coating are, from the chemical point of view, similar to those found in potentiometric ion-selective sensors.

d) potentiometric solid electrolyte gas sensors, differing from class 2b) because they work in high temperature solid electrolytes and are usually applied for gas sensing measurements.

3.3.6 Magnetic sensors

Magnetic sensors are devices based on the change of paramagnetic properties of a gas being analyzed. These are represented by certain types of oxygen monitors.

3.3.7 Temperature sensors

Temperature sensors are devices based on the measurement of the heat effects of a specific chemical reaction or adsorption which involve the analyte. In this group the heat effects may be measured in various ways, for example in the so called catalytic sensors the heat of a combustion reaction or an enzymatic reaction is measured by use of a thermistor. The devices based on measuring optothermal effects (If) can alternatively be included in this group. Other physical properties as for example X-, β- radiation may form the basis for a chemical sensor in case they are used for determination of chemical compostion. Sensors have also been classified according to the application to detect or determine a given analyte. Examples are sensors for pH, for metal ions or for determing oxygen or other gases. Another basis for the classification of chemical sensors may be according to the mode of application, for example sensors intended for use in vivo, or sensors for process monitoring and so on. Other classification schemes can be based on the type of fabrication technology (e.g., screen-printed and vapor deposited), sensitive material (e.g, metal-oxide, polymeric and inorganic), field of application (medicine, environmental) and so on **(Hulanicki, A. et al., 1991)**.

3.4 Nanostructured commercial sensors

To date, different strategies for the detection of specific environmental pollutants have been used. Standard approaches commonly involve analytical techniques such as aerosol mass spectrometry, size-exclusion chromatography, electron microscopy, dynamic light scattering, X-ray crystallography, UV-vis-NIR absorption/fluorescence, Raman, and atomic force microscopy. These methodologies have demonstrated good performances in terms of accuracy

127

and precision but require skilled operators as well as time-consuming measurements and sample preparation/collection procedures that hinder getting information in real time. Currently, the chemical sensors mainly present on the market are based on: 1) electrochemical cells, 2) metal oxides such as SnO_2, TiO_2, WO_3, ZnO, Fe_2O_3 and In_2O_3 (first, in the form of thick films and subsequently thin films), 3) conducting polymer and polymer composites sensors, 4) surface acoustic wave sensors, 5) catalytic beads, used as monitoring systems for the detection of pollutants such as NH_3, NOx, $Hg°$, VOCs. For example, the most frequently used techniques in commercial ammonia detectors are based on inorganic semiconductors, catalytic films, conducting polymers and optical detection. The most known sensors are without doubt metal-oxide gas sensors, mostly based on SnO_2 sensors (**Zakrzewska, K., 2001**). Metal-oxide gas sensors are not selective to one particular gas and this is a major drawback. A different approach to make more selective metal-oxide gas sensors is by using metals or additives that enhance the chemisorption of specific gasses. WO_3 based sensing material is demonstrated to respond to NH_3 and NO (**Wang, X. et al., 2000; Xu, C. N. et al., 2000**). The lowest ammonia detection limit found in literature is 1 ppm, using a WO_3 ammonia sensor with Au and MoO_3 additives. The sensor is operated at an elevated temperature of more than 400°C (**Xu, C. N. et al., 2000**). Most sensors have even higher detection limits. Normal detection limits of these sensors range from 1 to 1000 ppm (**Xu, C. N. et al., 2000; Aslam, M. et al., 1999**). These sensors are commercially available and are mainly used in combustion gas detectors (**Tomchenko, A. A. et al., 2003**) or gas alarm systems, for instance for reliable ammonia leakage detection in refrigeration systems (**Jerger, A. et al., 2002**). A great number of papers reported about reactivity of catalytic metals to specific gases, for instance ammonia, hydrogen, carbon monoxide or organic vapors (**Lundstrom, I. et al., 1993; Moseley, P. T., 1997; Spetz, A. et al., 1989**). However nanotechnology is going to dramatically change the sensor market, due to its extremely attracting

potentials. Thus, for instance, NEA's sensor technology has promoted miniaturized sensing devices able to detect gases at the part-per-billion (ppb) level using a standard, packaged sensor chip that incorporates nanomaterials, algorithms, at low-power consumption and other features, operating at a high level of sensitivity and efficiency in a range of environments **[https://www.ceasiamag.com/2015/08/nano-gas-sensors-for-third-party-consumer-and-commercial-devices/].** Recently commercial sensors based on CNTs and polymer composite structures have been also proposed as miniaturized novel sensors arrays (3mmx3mm MEMS circuitry, AerNos) for gas sensing thus extending the scenario of air quality sensors **[http://www.prweb.com/releases/2017/03/prweb14143014.htm].** There are also two main optical principles for the detection of ammonia described in literature: the first one is based on a change in color when ammonia reacts with a reagent, the second one on to sense directly ammonia. Optical adsorption spectroscopy, for example, is used in the most sensitive and selective ammonia detectors for ambient ammonia. Systems with a detection limit of 1 ppb, that do a full measurement in 1 s, have been reported (**Mount, G. H. et al., 2002).** Such systems use a laser and a spectrometer. Light travels through air (**Peters, R. et al., 2000)** or an ammonia sensitive layer (**Jin, Z. et al., 2001; Lee, Y-S. et al., 2003).** The spectrum of the light reaching the detector is influenced by either the gas composition or the material characteristics as a function of the gas composition. These systems are used in all kinds of gas analyzers in different application areas. Optical absorbance analyzers that measure multiple gases are commercially available but they are very expensive. It has been tried to use inexpensive diode-lasers to overcome this problem but this also resulted in a decrease in sensitivity (**Feh´er, M. et al., 1993; Modugno, G. et al., 1999).** Secondly, the sensitivity of absorption spectroscopy is partly determined by the amount of gas between the light source and the detector. For a very accurate analysis the measurement system should be very large. Thus, miniaturization always results in an increase in the

lower detection limit. Therefore, this principle is less suited for miniaturized ammonia sensors, e.g. breath analyzers.

Company name	Abbreviation	Web address
Alfasense	AL	www.alphasense.com
Appliedsensor	AP	www.appliedsensor.com
Citytech	CT	www.citytech.com
Draeger	DR	www.draeger.com
e2V	E2	www.e2v.com
Figaro	FG	www.figarosensor.com
FIS	FS	www.fisinc.co.jp
Ionotec	IO	www.ionotec.com
Microsens	MI	www.microsens.ch
Mocon	MO	www.mocon.com
MSA	MS	www.msanet.com
Nemoto	NM	www.nemoto.eu
Nenvitech	NN	www.nenvitech.com
Synkera	SY	www.synkera.com
Unitec	UN	www.unitec-srl.com
UST	US	www.ust-india.com
UST	US	www.umweltsensortechnik.de
Wuhan Cubic	WC	www.gassensor.com.cn

Table 3.3 List of the main manufacturers of gas sensors (Aleixandre, M. et al., 2012)

Naked eye sensors also are gaining success on market for wearable or packaging systems, where plastic layers or membranes are able to change their color after chemical interaction with the ammonia traces **(Pacific Sentry LLC, [https://www.pacificsentry.com/]).** For example another pollutant globally widespread in the atmosphere is mercury. About 95 percent of atmospheric mercury is elemental. Until now, the commercial monitoring systems for mercury detection in the atmosphere are highly sensitive and capable of detecting the global mercury background mainly based on the spectroscopic features of this element. They employ, for example, atomic absorption spectroscopy (AAS), atomic fluorescence spectroscopy (AFS), atomic emission spectroscopy (AES), or mass spectrometry (MS) **(Ghaedi, M. et al., 2006; Sánchez-Rodas, D. et al., 2010).** These instruments often include a series of processes or pretreatments, such as oxidation, reduction, vapor separation and gold traps, to pre-concentrate and detect mercury from air.

Additionally, an argon carrier stream is required by the detector to avoid the quenching of the fluorescence signal by oxygen, when fluorescence is the way of detection **(Ferrua, N. et al., 2007).** Most of the commercial analytical instruments can be found onto specific websites **(such as http://www.mercury-instrumentsusa.com/; http://www.lumexinstruments.com/catalog/atomic-absorption spectrometry/ra-915m.php; http://www.tekran.com/products/ambient-air/overview/; http://www.azic.com/jerome/jerome-431/; https://www.leco.com/component/edocman/ama254-advanced-mercury-analyzer)** where parameters like resolution, sensitivity, time and way of measurement as well as specificity of applications are reported for each device.

Many sensors have been designed and investigated, too, to detect the several forms of mercury. Most of them have exploited the strong affinity between mercury and gold. Several studies have documented changes in electrical properties, work function, and resistance to thin film films after exposure to various mercury vapor concentrations. The hybrid nanomaterials studied and designed in this thesis work thanks to their properties are therefore in line with the requirements for the development of detection systems characterized by fast, low cost, poor maintenance, wide distribution, ease of use and resistance to adverse environmental conditions. Sensors and nanostructured detection systems are the most promising alternative to the traditional tools described above and can meet the required requirements.

3.5 Characteristic parameters of chemical sensors

To evaluate the performance of a chemical sensor are taken into account different parameters, each of which is able to highlight a different feature of the chemically interactive material used to make it **(Kourosh Kalantar-zadeh., 2013).**

3.5.1 Calibration curve

The chemical sensors give out an electrical or optical signal whose variation is a function of the concentration of the chemical species revealed. It is possible to draw a curve, known as the response curve, able to represent the link between the input quantity (concentration) and the output (electrical or optical signal).

The response curve **(Figure 3.4)** is obtained by a calibration process and his knowledge allows the use of the sensor as a measuring instrument: known the change in the signal, therefore the response of the sensor is infact possible to estimate the concentration of the substance.
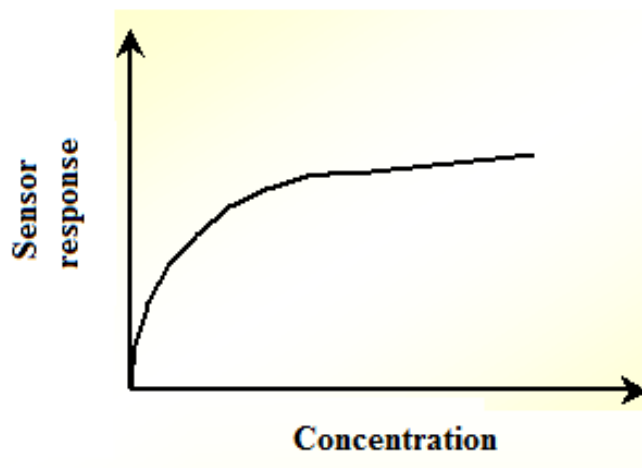
Figure 3.4 Example of a sensor response curve.

3.5.2 Reversibility

The reversibility expresses the ability of a sensor to follow, with a typical dynamic of the same sensor, the variations of the measurand. Therefore, it consist, in the ability to buy back at the end of the measurement, the electrical characteristics (or optical) initials. You can obtain reversible chemical sensors, and therefore reusable, using CIM capable of forming reversible chemical bonds with the several chemical species present in the environment of measurement. Often, however, the choice of chemically interacting materials that meet this need can lead to loss of selectivity. This problem can be solved through research and the synthesis of new chemically reactive materials.

3.5.3 Sensibility

To compare the behavior of different devices with sensitive film is often used the parameter of the sensitivity. It defines the capacity of the measuring instrument to follow the variations of the measurand. In mathematical terms, the sensitivity is obtained by calculating the first derivative of the function that defines the response curve at a given concentration (c0):

$$S(c_o) = \frac{dV}{dc}\bigg|_{c=c_0}$$

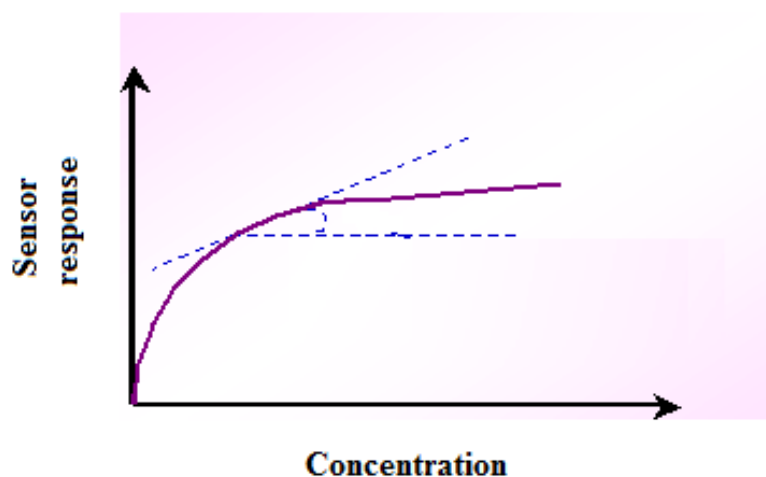where V is the response of the sensor and c the concentration of the chemical species.

Figure 3.5 Example of a sensor response curve.

As can be seen in **Figure 3.5** high sensitive sensor means that the sensor has been designed capable of detecting small variations in the concentration of the chemical species

3.5.4 Selectivity and cross-sensitivity

A selective sensor provides a higher response in the presence of a chemical species, therefore, it has the ability to discriminate between molecules in the environment **(Figure 3.6).** To achieve a selective chemical sensor, you must employ chemically interactive materials able to achieve very strong chemical bonds with the molecules of the various substances. This feature, however, implies a certain irreversibility of the device, so sometimes it is preferred to employ an array of non-selective sensors and identify the chemical species present in the environment by performing an analysis on the collected data.
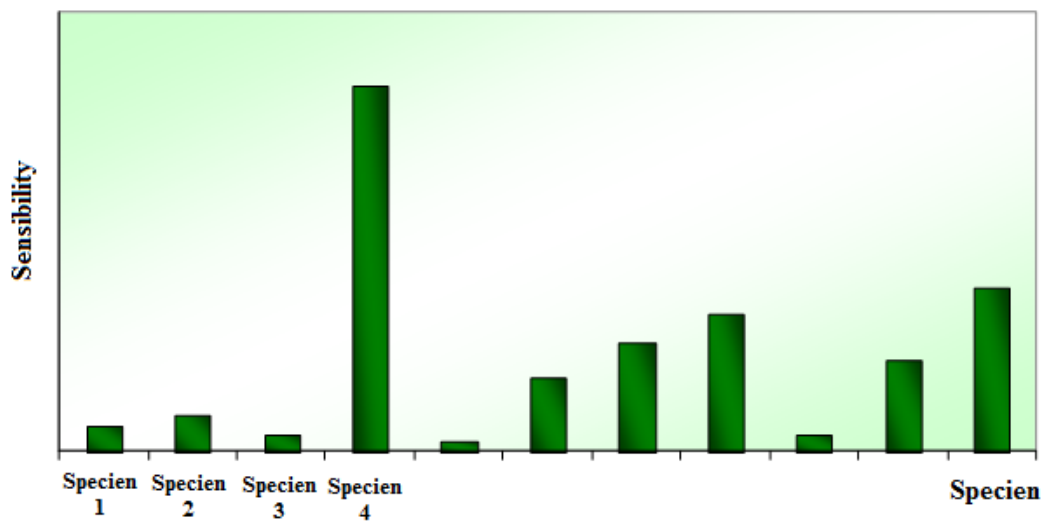
Figure 3.6: Sensitivity to the different chemical species of a selective sensor.

The presence of several chemical species is not the only factor to influence the response of a sensor: the measurement often also depends on environmental variables such as temperature, humidity, causing the phenomenon of cross-sensitivity and the consequent limitation of the use of sensors as measuring instruments.

3.5.5 Resolution and detection limit

Resolution depends on the existence of measurement errors and noise (electronic). The output signal is thus composed of a deterministic part (V) and a random (δV): $V \pm \delta V$. Where δV expresses all the measurement errors. The resolution is a parameter that indicates how the uncertainty on the output signal (δV) results in the uncertainty on the concentration (δc) of the chemical species revealed. Assuming that there are no measurement errors (and therefore that the uncertainty on the measurement is due only to electronic noise, V_{noise}), this parameter can be defined by the relation:

$$\mathrm{Re}\,solution = \lim_{\delta V \to V_{noise}} \frac{\delta V}{S(c_0)}$$

135

The resolution, calculated for V = 0 (deterministic part of the zero signal), defines the limit of detection (Limit Of Detection) **(Figure 3.7),** a parameter that indicates the theoretical detection limit of the sensor, due to electronic noise.
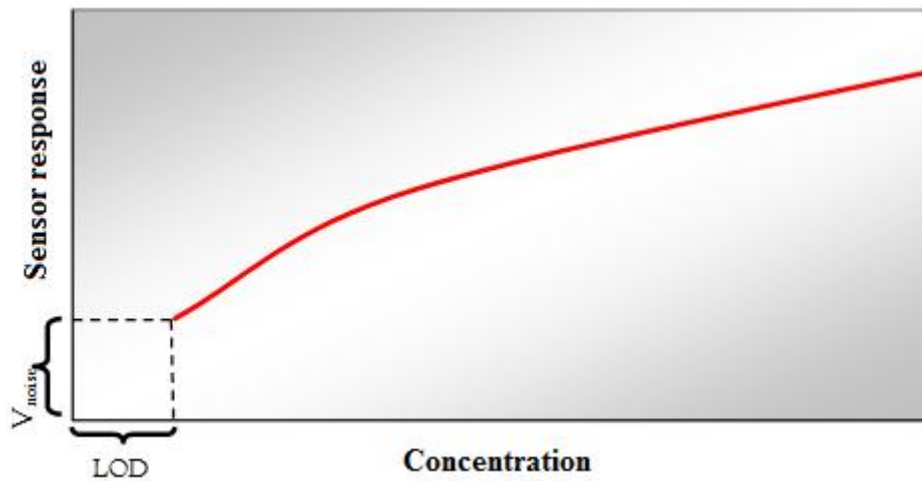

Figure 3.7: Limit of detection of a chemical sensor.

3.5.6 Accuracy and reproducibility

The accuracy is the ability of a measuring system to provide a value of the measurand equal to the true value (unknown). Reproducibility is the ability of a sensor to provide the same response curve for the same environmental conditions. Both statistical variables, as N measurements and the average value is related to the accuracy and reproducibility variance.

3.5.7 Drift

The drift is a parameter that indicates the lifetime of the sensor calibration. When several measures are performed an error can be introduced (due to aging and other factors) on the estimation of the concentration of the chemical species, which results in a shift of the calibration obtained from the response curve **(Figure 3.8).** When the estimation error becomes unacceptable the drift is eliminated by performing a new calibration or replacing the sensor itself.
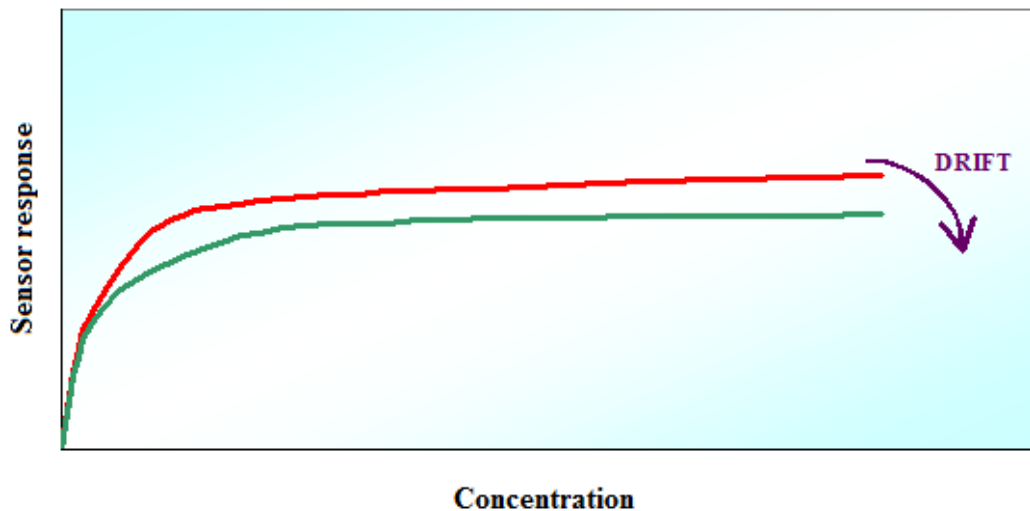

Figure 3.8: Effect on the drift of a sensor response curve.

3.5.8 Precision

Precision represents capacity of a sensing system to give the same reading when repetitively measuring the same measurand under the same conditions. The precision is a statistical parameter and can be assessed by the standard deviation (or variance) of a set of readings of the system for similar inputs.

137

3.5.9 Repeatability

When all operating and environmental conditions remain constant, repeatability is the sensing system's ability to produce the same response for successive measurements. Repeatability is closely related to precision. Both long-term and short-term repeatability estimates can be important for a sensing system.

3.5.10 Stability

Stability is the ability of a sensor to provide reproducible results for a certain period of time.

3.5.11 Error

Error is the difference between the actual value of the measurand and the value produced by the sensing system. Error can be caused by a variety of internal and external sources and is closely related to accuracy.

3.5.12 Linearity

Linearity is the relative deviation of an experimentally determined calibration graph from an ideal straight line.

3.5.13 Hysteresis

Hysteresis is the difference between output readings for the same measurand, depending on the trajectory followed by the sensor. Hysteresis may cause false and inaccurate readings. **Figure 3.9** represents the relation between output and input of a system with hysteresis. As can be seen, depending on whether path 1 or 2 is taken, two different outputs, for the same input, can be displayed by the sensing system.
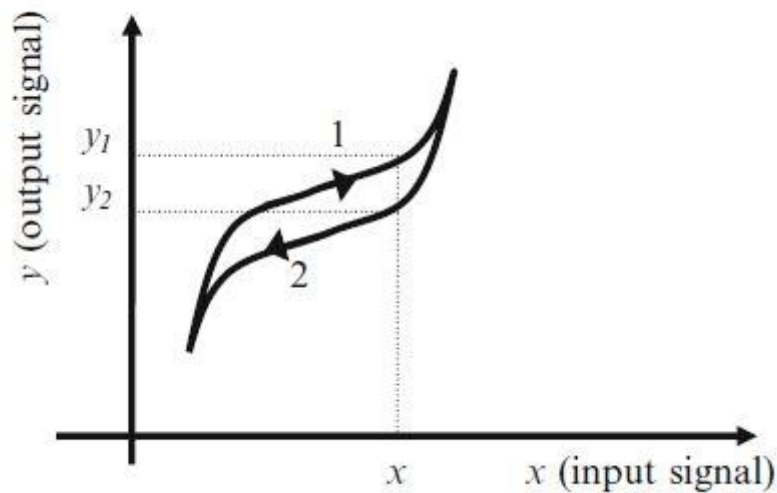

Figure 3.9: An example of a hysteresis curve

3.5.14 Detection limit

Detection limit is the lowest concentration of the analyte that can be detected by the sensor under given conditions, particularly at a given temperature.

3.5.15 Dynamic range

Dynamic range is the analyte concentration range between the detection limit and the highest limiting concentration.

3.5.16 Response time

Response time is the time required for sensor to respond to a step concentration change from zero to a certain concentration value. It can be defined as the time required for a sensor output to change from its previous state to a final settled value within a tolerance band of the correct new value.

3.5.17 Recovery time

Recovery time is the time it takes for the sensor signal to return to its initial value after a step concentration change from a certain value to zero.

3.5.18 Working temperature

Working temperature is usually the temperature that allows the sensor to get the maximum sensitivity to the selected analyte.

3.5.19 Life cycle

Life cycle is the period of time over which the sensor will continuously operate. All of these parameters are used to characterize the properties of a particular material or device. An ideal chemical sensor would possess high sensitivity, dynamic range, selectivity and stability, low detection limit good linearity small hysteresis and response time- and long life cycle. The task of creating an ideal sensor for some gases is extremely difficult because real applications usually do not require sensors with all perfect characteristics at once. For example, to monitor the concentration of a component in industrial process, a sensor does not need a detection limit at the ppb level, though the response time at range of seconds or less would be desirable. In case of environmental monitoring applications, when the concentrations of pollutants normally change slowly, the detection limit requirements can be much higher, but response time of a few minutes can be acceptable.

3.6 Characteristics of chemical gas sensors

Sensors can be used in many other fields, not only as intelligent machines and they must have the following characteristics:

- Be in direct contact with the investigated analyte;
- Respond quickly);
- Be small and cheap;
- Transform non-electric information into electric signals;
- Operate continuously or at least in repeated cycles;
- Be specific, i.e. they should respond exclusively to one analyte, or at least be selective to a group of analytes;

The above list could be extended with, e.g., the postulation of a low detection limit, or a high sensitivity. This means that low concentration values should be detected.

3.7 Mechanism of gas detection

Generally, the gas sensing mechanism takes place through three stages:

- Adsorption of the target gas molecules on the substrate or surface;
- Reaction of the active material on the surface;
- Gas desorption and any reaction products.

The most important processes in the gas sensing mechanism are the surface interactions. These may change surface properties and they have characteristic lifetimes and energies, that will control adsorption rate, desorption rate and coverage of each atmospheric compound. When a molecule (or an atom) from the gas-phase approaching a solid surface, it is more or less strongly attracted by the atoms exposed on the surface, according to the nature of the molecule and of the solid surface of the material. The surface atoms arrangement depends on the plane preferentially exposed during the formation of the surface, according to the preparation conditions of the real material (either in the single crystal form or as nanosized powder) **(Attard, G., 1998).** If they are not present structural defects, an ideal perfect homogeneous surface is obtained. However, it is rarely possible to obtain a surface such perfect unless specifically prepared for surface science studies. A real solid surface is made up of a combination of flat regions (terraces), structural defects (steps, kinks, corners, edges), point defects (vacancies of ions/atoms in the solid), compositional defects that may contribute to the "imperfections" of the solid

surface. Compositional defects may contribute to the "imperfections" of the solid surface. They include a variety of oxidation states of the atoms constituting the solid and/or a variety of heteroatoms present either as impurities, or especially introduced in order to modify the physico-chemical properties of the surface. Compositional defects may contribute to the "imperfections" of the solid surface. They include a variety of oxidation states of the atoms constituting the solid and/or a variety of heteroatoms present either as impurities, or especially introduced in order to modify the physico-chemical properties of the surface. The solids surfaces possess not only a geometrical surface, but also an internal surface where aggregation of primary particles generates pores of different size according to both the nature of the solid that origin of the surface. In all cases, porous materials exhibit high surface areas, which maximize the extension of the interface region. Generally, the surface atoms of a solid, which are unsaturated coordinated with respect to the bulk atoms, become saturated thanks to the interaction with molecules of the environment.

3.7.1 Adsorption Processes

A solid material usually exhibits a heterogeneous distribution of surface energy. Gas, vapor, or liquid molecules may become bound to the surface if they approach sufficiently close to interact. When gas or vapor is brought into contact with a surface of a solid material, it will be partly taken up by the solid until equilibrium of the concentrations in the two phases is reached. The material in the gas phase capable of being adsorbed is called adsorbate, while the solid surface, which exposes the surface sites responsible for the process is called adsorbent. The adsorbed amount depends on the pressure of the adsorbate, the temperature and the properties of the adsorbent. In **Figure 3.10**

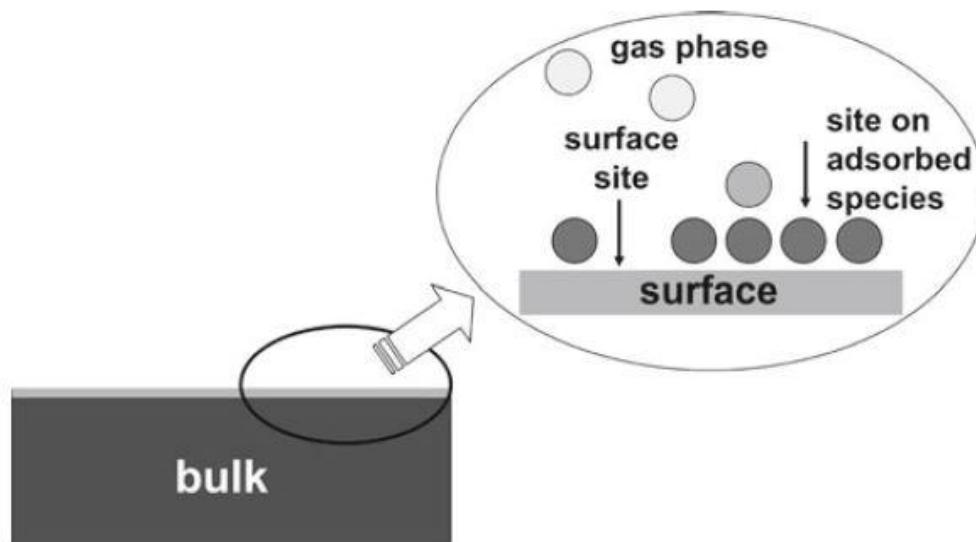the adsorption process at the surface of a solid material is schematically illustrated.

Figure 3.10: Schematic picture of adsorption process at the surface of a solid material

Adsorption is governed by physical or chemical forces. In the former case the adsorption is named physical adsorption (physisorption) whereas in the latter case chemical adsorption (chemisorption). Physisorption is a non-specific loose binding of the adsorbate to the solid via Van Der Waals type interactions. Multilayered adsorption is possible and it is easily disrupted by increasing temperatures. Chemisorption involves a more specific binding of the absorbate to the solid. It is a process that is more akin to a chemical reaction and hence, only monolayer adsorption is possible. When a solid surface is exposed in a closed space to a gas at pressure p, the weight of the solid superface typically increases and the pressure of the gas decreases: the gas is adsorbed by the solid surface. After a time, the pressure p does not change any more and correspondingly the weight ceases to increase any further: a dynamic equilibrium is reached.
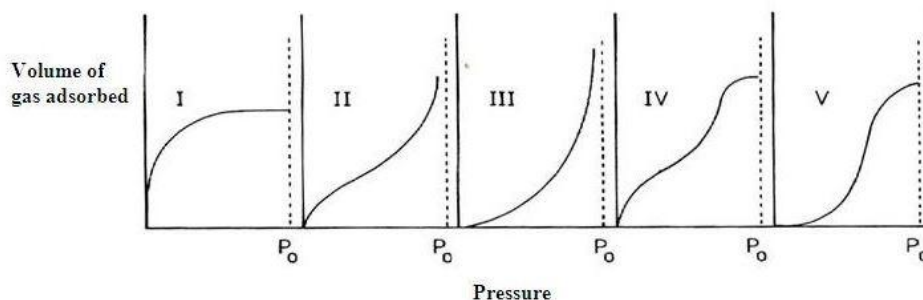
3.7.1.1 Adsorption isotherm

Figure 3.11: Types of adsorption isotherm according to Brunauer classification

Type I isotherms correspond to the Langmuir equation and are characterized by a monotonic approach to a limit value conforming to a complete monolayer surface coverage by a monolayer of adsorbed molecules. **Type II** corresponds to the case when first, a monolayer is formed, and then a multimolecular layer predominantly develops. Isotherms of **Type III** are relatively uncommon and correspond to the formation of multimolecular layer when heat of adsorption is less than or equal to adsorbate heat of condensation. **Types IV** and **V**, as a rule, are characteristic of capillary adsorbate condensation in porous solids.

When an adsorbate molecule in the gas phase comes in contact with the surface of the adsorbent, an equilibrium distribution of the adsorbate molecules takes place between the adsorbent surface and the gas phase. This equilibrium distribution depends upon various factors including partial pressure of adsorbate, temperature, nature of adsorbate, and the surface area and nature of adsorbent. Adsorption isotherm shows the amount of molecules adsorbed on the solid surface as a function of the equilibrium partial pressure at constant temperature. The process of Adsorption is usually studied through graphs know as adsorption isotherm. Adsorption isotherms are currently classified in five classes (I - V) according to the Brunauer, (**Brunauer, S., 1945**) **(Figure 3.11).**

The fractional coverage θ of the adsorbate, at a given equilibrium pressure p, is defined as the ratio of NS surface sites occupied by the adsorbate over the

total available adsorption sites *N*, i.e. the total number of substrate surface sites which are active towards the given adsorptive. The first layer of adsorbed phase is due to either chemisorption or physisorption, or both, according to the nature of the forces governing the adsorbate/adsorbent interactions. Conversely, the second layer is originated by physical forces. When the number of *NS* occupied sites matches the number of total available sites *N*, the adsorbate monolayer is complete ($\theta = 1$). In **Figure 3.12** the formationof subsequent layers of adsorbate at the surface of a solid sample is schematically illustrated.
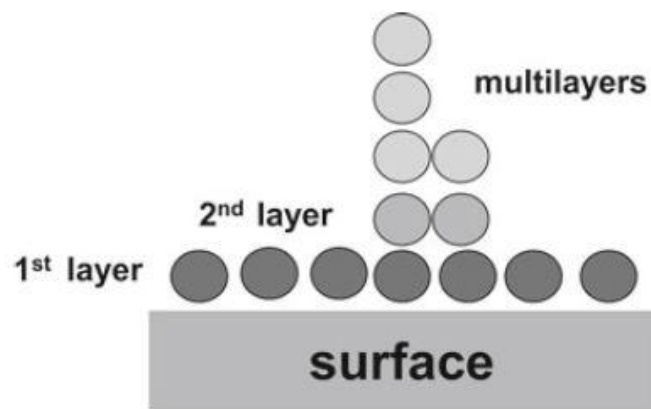

Figure 3.12: Schematic illustration of the first and second layer of adsorption;

The isotherm experimental points can be interpolated by a variety of equations according to the mechanism of the adsorption process, which in turn depends on the nature of the gas/solid interaction. Among the different equations proposed to describe quantitatively the isotherms, the only one based on a physical model is the Langmuir equation **(Thomas, J. M., et al., 1997; Van Santen, R. A., et al., 1999; Attard, G., et al., 1998; Gregg, S. J., et al., 1982; Langmuir, I. 1918).**

3.7.1.2 Langmuir isotherm

The Langmuir model assumes a dynamic equilibrium at constant T between the gas (at pressure *p*) and the adsorbed layer, and requires a number of well-defined conditions:

- the adsorption, which is limited to a monolayer, takes place at a surface consisting of a distribution of energetically equivalent, non-interacting sites;
- the ability of a molecule to bind at a site is independent of whether or not a nearby site is occupied (absence of lateral interactions);
- once adsorbed, the molecules are localized in that the activation barrier hindering migration to an adjacent site is supposed to be much larger than *kT;*
- the enthalpy of adsorption ΔaH (per site) is constant with θ.

The Langmuir adsorption isotherm is derived from a kinetic mechanism. Let us assume for sake of simplicity that the molecule M is adsorbed molecularly (i.e. without rupture/formation of chemical bonds) from the gas at a surface site S. The fractional monolayer coverage of the sites occupied by adsorbate molecules is $\theta = NS/N$. The rate of adsorption is given by the Eq. 1.1:

$$adsorption\ rate = kap\ (1 - \theta)$$

ka being the rate constant for the adsorption and *(1 − θ)* the fractional monolayer coverage of sites not occupied yet by the adsorbate molecules.
The rate of desorption, *kd* being the rate constant for desorption, is given by the Eq. 1.2:

$$desorption\ rate = kd\theta$$

When the dynamic equilibrium is reached (adsorption rate = desorption rate) the Eq. 1.3 is obtained:

$$kap\ (1 - \theta) = kd\theta \text{ (1.3)}$$

Equation 1.4 represents the Langmuir equation:

$$\theta/\ 1 - \theta = Kp \text{ (1.4)}$$

Note that the constant K is obtained by the ratio of the rate constant for adsorption over the rate constant for desorption (ka/kd).

The Langmuir equation is often written as reported by the Eq. 1.5

$$\theta = V/Vmon = Kp/(1 + Kp)$$

The term V represents the adsorbate volume and $Vmon$ the monolayer volume, i.e. the volume of adsorbate required to complete the monolayer. At very low pressure the equation reduces to a linear dependence of the coverage upon the equilibrium pressure ($\theta = hp$). Conversely, at high pressure the equation reduces to the case of coverage approaching the monolayer ($\theta \approx 1$). The monolayer coverage ($Vmon$) is hardly determined experimentally with accuracy. So, for practical purposes the Langmuir equation is suitably transformed in the so-called reciprocal linear form, as illustrated by the Eq. 1.6

$$(1/V) = 1/KVmon\ (1/p) + 1/Vmon$$

For isotherms obeying the Langmuirmodel, the reciprocal volume ($1/V$) against reciprocal pressure ($1/p$) plot is linear (Langmuir-type isotherms). Conversely, if the experimental data plot is not linear, Langmuir equation does not hold in describing the given adsorption process. The monolayer capacity is obtained from the intercept $i = 1/Vmon$ of the straight line. Once determined

Vmon, the equilibrium constant *K* is obtained by the slope $s = 1/KVmon$ of the plot. The monolayer volume and the equilibrium constant are typical of the adsorbent/ adsorbate pairs at a given temperature. In particular, the value of *K* is bound to the strength of the adsorbent-adsorbate interaction: high values of *K* indicate large strength, low values little strength. Deviations from the Langmuir model are often observed in real systems. The Langmuir model assumptions listed above are indeed very limitative and severe: the solid surface is rarely uniform: there are always "imperfections" at the surface; the mechanism of adsorption is not the same for the first molecules as for the last to adsorb. When two or more kind of sites characterized by different adsorption energies are present at the surface (as stated in point i), and when lateral interactions among adsorbed species occur (as stated in point ii), the equivalence/independence of adsorption sites assumption fails. The most energetic sites are expected to be occupied first, and the adsorption enthalpy ΔaH (per site) instead of keeping a constant, coverage-independent value, exhibits a declining trend as far as the coverage θ increases. Further, the adsorbed molecules are not necessarily inert, and on the top of the monolayer other molecules may adsorb and multi-layers build up: this is properly described by the Brunauer, Emmet and Teller (BET) model **(Van Santen, R. A., et al., 1999; Attard, G., et al., 1998; Gregg, S. J., et al., 1982).**
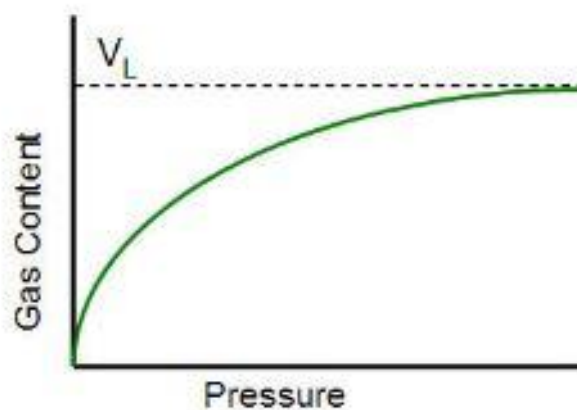

Figure 3.13: Langmuir Ishoterm

References

Aleixandre M., Gerboles M. Review of Small Commercial Sensors for Indicative Monitoring of Ambient Gas Chemical Engineering Transactions (2012), Vol. 30, pp 169-174

Aslam M., Chaudhary V. A., Mulla I. S., Sainkar S. R., Mandale A. B., Belhekar A. A., Vijayamohanan K. A highly selective ammonia gas sensor using surface-ruthenated zinc oxide. Sens Actuators A (1999), Vol 75, pp. 162-167

Attard G., Barnes C. Surfaces. Oxford Chemistry Primers N. 59 (Oxford Science Publications, Oxford (1998)

Bai H.; Shi G. Gas sensors based on conducting polymers. Sensors (2007), Vol. 7, pp. 267-307

Brunauer S. The Adsorption of Gases and Vapours (Oxford University Press, Oxford (1945)

Cioffi, N., Torsi L., Farella I., Altamura D., Valentinim A., Ditaranto N., Sabbatini L., Zambonin P. G., Bleve-Zacheo T. Deposition and analytical characterization of fluoropolymer thin films modified by palladium nanoparticles. Thin Solid Films (2004), Vol. 449(1-2), pp. 25-33

Comini E. Metal oxide nano-crystals for gas sensing. Analyt Chim Acta (2005), VGol. 568, pp. 28-40

Ding B., Wang M., Wang X., Yu J., Sun G. Electrospun nanomaterials for ultrasensitive sensors. Materials Today (2010), Vol. 13 (11), pp. 16-27

Endres H. E., Göttler W., Hartinger R., Drost S., Hellmich W., Müller G., Braunmühl C. B., Krenkow A., Perego C., Sberveglieri G. A thin-film SnO$_2$ sensor system for simultaneous detection of CO and NO$_2$ with neural signal evaluation. Sens Actuators B (1996), Vol. 36, pp. 353-357

Feh´er M., Martin P. A., Rohrbacher A., Soliva A. M., Maier J. P. Inexpensive near-infrared diode-laser-based detection system for ammonia. Appl Opt (1993), Vol. 32 (12), pp. 2028-2030

Fernandez C. D. J., Manera M. G., Spadavecchia J., Buso D., Pellegrini G., Mattei G., Martucci A., Rella R., Vasanelli L., Guglielmi M. Mazzoldi P. Gold/titania nanocomposites thin films for optical gas sensing devices. SO Source Proc SPIE (2005), Vol. SPIE-5116, pp. 703-710

Fraiwan L., Lweesy K., Bani-Salma A., Mani N. A wireless home safety gas leakage detection system. In Proceedings of the 1st Middle East Conference on Biomedical Engineering (MECBME), Sharjah, United Arab Emirates (2011), Vol. 21-24, pp. 11-14

Ferrua N., Cerutti S., Salonia J. A., Olsina R. A., Martinez L. D. On-line preconcentration and determination of mercury in biological and environmental samples by cold vapor-atomic absorption spectrometry. J Hazard Mater (2007), Vol. 141, pp. 693-699

Gardner J. W.; Bartlett P. N. Design of conducting polymer gas sensors: Modeling and experiment. Synth. Met. (1993), Vol. 55, pp. 3665-3670

Gaspera E., Guglielmi M., Agnoli S., Granozzi G., Post M. L., Bello V., Mattei G., Martucci A. Au nanoparticles in nanocrystalline TiO$_2$-NiO films

for SPR-based, selective H$_2$S gas sensing. Chemistry of Materials (2010), Vol. 22(11), pp. 3407-3417

Ghaedi M., Fathi M. R., Shokrollahi A., Shajarat F. Highly Selective and Sensitive Preconcentration of Mercury Ion and Determination by Cold Vapor Atomic Absorption Spectroscopy. Analytical Letters (2006), Vol. 39, pp. 1171-1185

Gong J., Chen Q., Lian M. R., Liu N. C., Stevenson R. G., Adami F. Micromachined nanocrystalline silver doped SnO$_2$ H$_2$S sensor. Sensors and Actuators (2006), Vol. B 114(1), pp, 32-39

Gregg S. J., Sing K.S.W. Adsorption, Surface Area and Porosity (Academic Press, London, (1982)

Hagleitner C.; Lange D.; Hierlemann A.; Brand O.; Baltes H. CMOS single-chip gas detection system comprising capacitive, calorimetric and mass-sensitive microsensors. IEEE J. Solid-St. Circ. (2002), Vol. 37, pp.1867-1878

Hallil H., Chebila F., Menini P., Pons P., Aubert H. Feasibility of wireless gas detection with an FMCW RADAR interrogation of passive RF gas sensor. In Proceedings of 2010 IEEE Sensors (2010), Vol. 1-4, pp. 759-762

Hatfid J. V.; Neaves P.; Hicks P. J.; Persaud K.; Travers P. Towards an integrated electronic nose using conducting polymer. Sens. Actuators B (1994)

Hoefer U., Böttner H., Felske A., Kühner G., Steiner K., Sulz, G. Thin-film SnO$_2$ sensor arrays controlled by variation of contact potential-A suitable tool

for chemometric gas mixture analysis in the TLV range. Sens. Actuators B (1997), Vol. 44, pp. 429-433

Hulanicki A., Glab S., Ingman F. Chemical sensors: definitions and classification**.** Pure&App/. Chern (1991), Vol. 63 (9)**,** pp. 1247-1250

Jarmo K., Jani M., Niina H., Teemu K., Géza T., Maria S., Andrey S. Jyri-Pekka M., Hell J., Krisztián K. Gas sensors based on anodic tungsten oxide. Sens Actuators B (2011), Vol. 153, pp. 293-300

Jerger A., Kohler H., Becker F., Keller H. B., Seifert R. New applications of tin oxide gas sensors. II: Intelligent sensor system for reliable monitoring of ammonia leakage. Sens Actuators B (2002), Vol. 81, pp. 301-307

Jiang Y., Xie G., Yu J., Chen X. Fabrication and gas sensitivity of polyaniline-titanium dioxide nanocomposite thin film. Sensors and Actuators (2007), Vol. B:125(2), pp. 644-650

Jin Z., Su Y., Duan Y. Development of a polyaniline-based optical ammonia sensor. Sens Actuators B (2001), Vol. 72, pp. 75-79

Keat G. O., Kefeng Z., Grimes C. A. A wireless, passive carbon nanotube-based gas sensor. IEEE Sens J (2002), Vol. 2, pp. 82-88

Kourosh Kalantar-zadeh. Sensors An Introductory Course (2013)

Langmuir I. The adsorption of gases on plane surfaces of glass, mica and platinum. J Am Chem Soc (1918), Vol. 40(9), pp. 1361-1403

Lee Y-S., Joo B-S., Choi N-J., Lim J-O, Huh J-S, Lee D-D. Visible optical sensing of ammonia based on polyaniline film. Sens Actuators B (2003), Vol. 93, pp. 148-152

Lundstrom I., Sevensson C., Spetz A., Sundgren H., Winquist F. From hydrogen sensors to olfactory images–twenty years with catalytic field-effect devices. Sens. Actuators B 13/14 (1993), pp. 16-23

Macagnano A., Zampetti E., Kny E. Electrospinning for High Performance Sensors. Springer International Pub (2015), pp. 329

Manera M. G., Spadavecchia J., Buso D., Fernández C., De J., Mattei, G., Martucci A., Mulvaney, P., Pérez-Juste J., Rella R., Vasanelli L., Mazzoldi P. Optical gas sensing of TiO_2 and TiO_2/Au nanocomposite thin films. Sensors and Actuators (2008), Vol. 132(1), pp. 107-115

Mehul N., Patel R. D., Williams R., Alan M., Hiroshi U., Keith J., Stevenson and Keith P. Johnston, Electrophoretic Deposition of Au Nanocrystals inside Perpendicular Mesochannels of TiO_2. Chem. Mater (2008), Vol. 20 (19), pp. 6029-6040

Modugno G., Corsi C. Water vapour and carbon dioxide interference in the high sensitivity detection of NH_3 with semiconductor diode lasers at 1.5 μm. Infrared Phys Technol (1999), Vol. 40, pp. 93-99

Moseley P. T. Solid state gas sensors. Meas Sci Technol (1997), Vol. 8, pp. 223-237

Mount G. H., Rumberg B., Havig J., Lamb B., Westberg H, Yonge D., Johson K., Kincaid R. Measurement of atmospheric ammonia at a dairy

using differential optical absorption spectroscopy in the mid-ultraviolet. Atmos Environ (2002), Vol. 36, pp, 1799-1810

Musat, V., Fortunato E., Botelho do Rego A. M., Monteiro R. Sol-gel cobalt oxide-silica nanocomposite thin films for gas sensing applications. Thin Solid Films (2008). Vol. 516(7), pp.1499-1502

Patel M. N., Uchida H. et al. Nanocrystal infusion in mesoporous metal oxide thin films. 2007 AIChE Annual Meeting, Salt Lake City, UT (2007)

Peeters R., Berden G., Apituley A., Meijer G. Open-path trace gas detection of ammonia base on cavity-enhanced absorption spectroscopy. Appl Phys B (2000), Vol. 71, pp. 231-236

Shrivas A. G.; Bavane R. G.; Mahajan A. M. Electronic nose: A toxic gas sensor by polyaniline thin film conducting polymer. In Proceedings of International Workshop on Physics of Semiconductor Devices (2007), pp. 621- 623

Sofian M. K., Oussama M. E., Imad A. A., Marsha C. K. Semiconducting metal oxide based sensors for selective gas pollutant detection. Sensors (2009), Vol. 9, pp. 8158-8196

Spetz A., Armgath M., Lundstrom I. Hydrogen and ammonia response of metal-silicon dioxide-silicon structures with thin platinum gates. J Appl Phys (1988), Vol. 64, pp. 1274-1283

Tomchenko A. A., Harmer G. P., Marquis B. T., Allen J. W. Semiconducting metal oxide sensor array for the selective detection of combustion gases. Sens Actuators B (2003), Vol. 93, pp. 126-134

Thomas J. M., Thomas W.J. Principles and Practice of Heterogeneous Catalysis (VCH, Weinheim (1997))

Van Santen R. A.,Van Leeuwen P. W. N. M., Moulijn J. A., Averill B. A. Catalysis an Integrated Approach. Studies in Surface Science and Catalysis (1999), Vol. 123.

Wang C., Yin L., Zhang L., Xiang D., Gao R. Metal oxide gas sensors: Sensitivity and influencing factors. Sensors (2010), Vol. 10, pp, 2088-2106

Wang X., Miura N., Yamazoe N. Study of WO_3-based sensing material for NH_3 and NO detection. Sens Actuators B (2000), Vol. 66, pp. 74-76

Wisitsoraat A., Tuantranont A., Thanachayanont C, Singjai P. Gas sensing properties of CNT-SnO_2 nanocomposite thin film prepared by e-beam evaporation. Proceedings of IEEE Sensors. The 6th IEEE Conference on SENSORS, IEEE SENSORS (2007), Article Number: 4388457, pp. 550-553

Wong K. K. L.; Tang Z.; Sin J. K. O.; Chan P. C. H.; Cheung P. W.; Hiraoka H. Study on selectivity enhancement of tin dioxide gas sensor using non conducting polymer membrane. In Proceedings of Hong Kong Electron Devices Meeting (1995), pp. 42-45

Xiao G., Zhang Z., Weber J., Ding H., McIntosh H., Desrosiers D., Nong G., Won D., Dunford J., Tunney J. et al. Trace amount formaldehyde gas detection for indoor air quality monitoring. In Proceedings of 2011 IEEE Instrumentation and Measurement Technology Conference (I2MTC), Hangzhou, China (2011), Vol. 10-12 pp.1-4

Xu C. N., Miura N., Ishida Y., Matuda K., Yamazoe N. Selective detection of NH_3 over NO in combustion exhausts by using Au and MoO_3 doubly promoted WO_3 element. Sens Actuators B (2000), Vol. 65, pp. 163-165

Yamazoe N., Shimanoe K. Theory of power laws for semiconductor gas sensors Sens Actuators B (2002), Vol. 128, pp. 566-573

Zakrzewska K. Mixed oxides as gas sensors, Thin Solid Films (2001), Vol. 391, pp. 229-238.

Chapter 4

Nanacomposite materials designed and investigated for sensing materials

4.1 Optical nanoparticles: Quantum Dots (QDs)

In the last few years a new class of hybrid fluorophores with exceptional photophysical properties has been developed: the Quantum Dots (QDs). QDs are semiconductors made by fluorescent inorganic particles with typical diameters ranging from 1 to 10 nm. Due to their quantum confinement, QDs show unique and fascinating optical properties that are advantageous in the fields of photovoltaic devices **(Kashyout, A. B., et al. 2010),** light-emitting diodes **(J. S. Steckel, J. S. et al., 2004)** biological imaging and biodiagnostics **(Pellegrino, T. et al., 2005; Michalet, X. et al., 2005).** The most studied and applied QDs are made of elements from the II and VI groups (e.g. CdSe, PbSe, CdS, and ZnO), as well as, although less commonly, from the III and V groups (e.g. InAs, InSb, and GaAs) of the periodic table of elements.

4.2 Optical properties of QDs

The quantum dots are semiconductors whose electronic characteristics are closely related to the size and shape of the individual crystal. One of the most attractive characteristics of QDs is their optical properties and the photostability over time. Generally, in a semiconductor nanoparticle, an electron (e⁻) can be excited from the valence band to the conduction band by absorption of a photon with an appropriate energy and this process generates a

158

hole (h^+) in the valence band. The formed e^--h^+ pair is called exciton **(Figure 4.1).** Recombination of this electron-hole pair results in the fluorescence process.
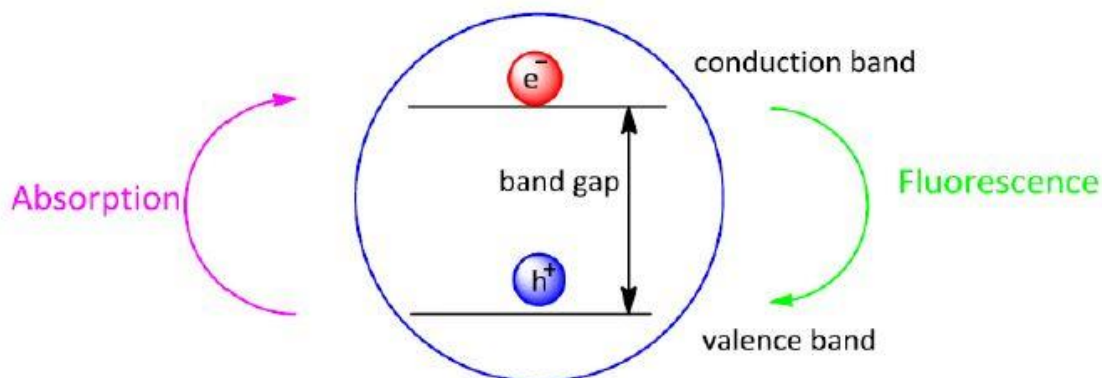

Figure 4.1: Energy difference between valence and conduction band of the QDs and processes of absorption (magenta) and fluorescent emission (green).

Therefore, the QDs fluorescence, is associated with the transition of an electron from the conducting band to the valence band. The difference between the two energy states depends on the size (the size depends on the core composition) of the QDs **(Mishra, S. et al., 2012)** the smaller is the QDs the higher is the energy that it requires to be excited and the higher is the energy emitted when the crystal returns to the resting state and the emission color of QDs moves toward blue in the UV-visible absorbance spectra; conversely, large QDs have lower band gap of energy between valence band and conduction band and the emission color of QDs moves toward red **(Figure 4.2-4.3).** They are therefore characterized by a broad absorption spectrum coupled with narrow and symmetrical photoluminescent emission spectrum **(Figure 4.4 (A) (B)).**
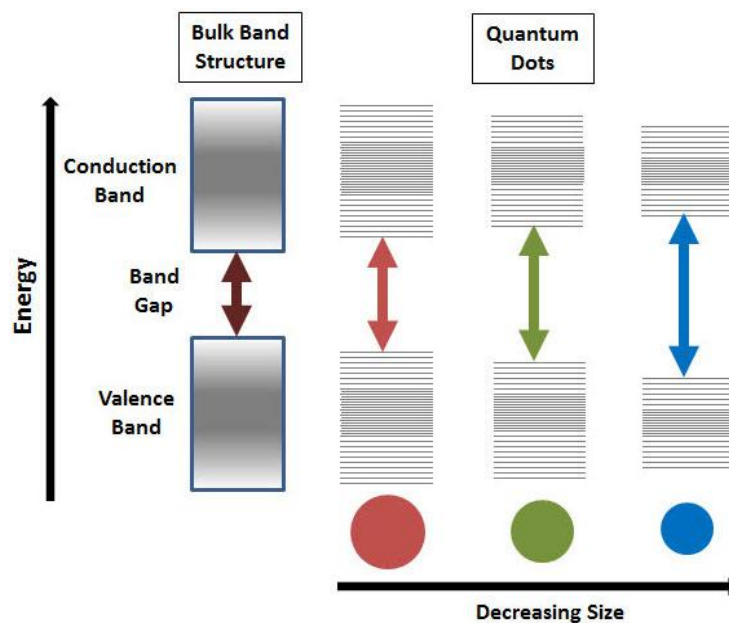
Figure 4.2: The electronic structure of quantum dots varies with the size of the dot: smalls nanoparticles have elevated band gap of energy between valence band and conduction band and the emission color of QDs moves toward blue; large nanoparticles have lower band gap of energy between valence band and conduction band and the emission color of QDs moves toward red.

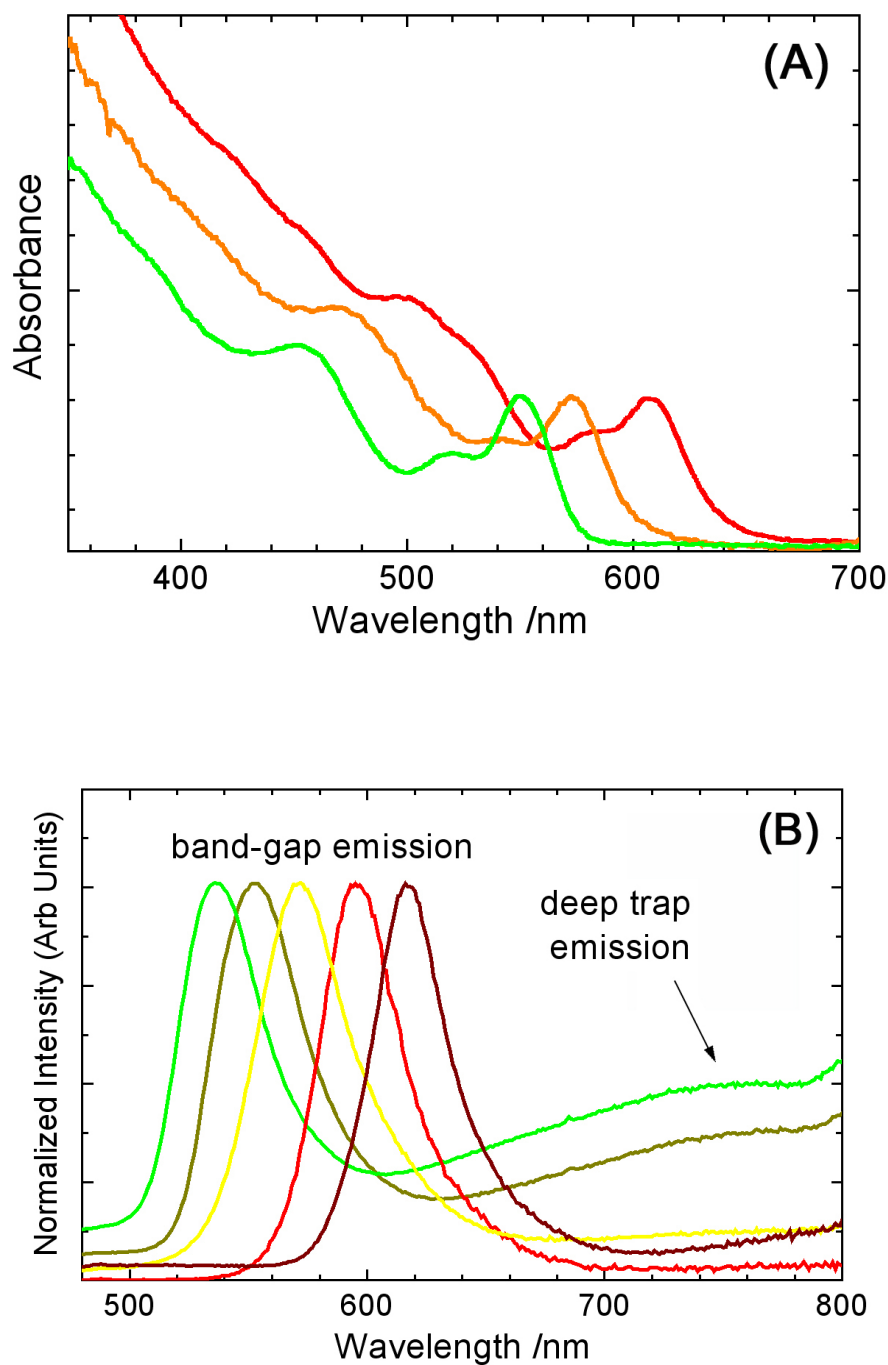**Figure 4.3: Quantum dots of different sizes under excitation from a UV-lamp at 366 nm.**

Figure 4.4: (A) Absorption and (B) emission spectra of CdSe quantum dots of different sizes.

In addition to this, QDs present high molar extinction coefficients (ε), which makes them of special interest in single molecule spectroscopy (**Maye, M. M. et al., 2010**) This molar extinction coefficient keeps a relation with the size of the nanoparticle. In addition, QDs present high fluorescence quantum yields,

which depend on the quality of the quantum dot. This means that the fluorescence quantum yield can be reduced as a result of the quenching caused by surface defects (surface trap states) **(Carrillo-Carrion, C. et al., 2009).** These trap states are imperfections in the regular geometrical arrangement of the atoms in the crystalline structure of the nanoparticle. These imperfections result from deformation of the solid, rapid cooling from high temperature, or high-energy radiation striking the solid, most of them originated in the synthesis of the QDs. Located at single points, along lines, or on whole surfaces in the solid, these defects influence their mechanical, electrical, and optical behavior **(Fu, H., et al., 1997).** Among the traps states caused during the synthesis there are those related with Cd and Se dangling bonds (i.e. absence of the Cd or Se in the crystal lattice) or small distortion of the crystal lattice. These trap states can be considerably reduced by a correct passivation of the QDs surface. Different kinds of passivation can be used in order to increase the fluorescent quantum yield, but the most common way is the use of a second semiconductor layer resulting in core-shell systems. This phenomenon will be discussed in the following paragraph.

4.3 Core-shell structures

To increase the fluorescent quantum yield of QDs, the most used strategy is the passivation of QDs surface with a shell of a second semiconductor **(Carrillo-Carrion, C. et al., 2009; Talapin, D. V. et al., 2001; Borchert, H. et al., 2003).** If on one hand, this strategy improves the fluorescence quantum yield, increasing absorbance and fluorescence intensity of CdSe core, the stability of the QDs against photo-oxidation, slows growth of nanoparticles and prevents formation possible of aggregates of nanoparticles, on the other hand, it is possible to tune the emission wavelength in a large spectral window

by selecting the suitable core and shell material. Depending on the band gap and the relative position of electronic energy levels of the semiconductors, we can design QDs core-shell with different functions. These relative positions can be observed in the **Figure 4.4** which represent the band gap of the most used materials employed in the nanocrystal field.
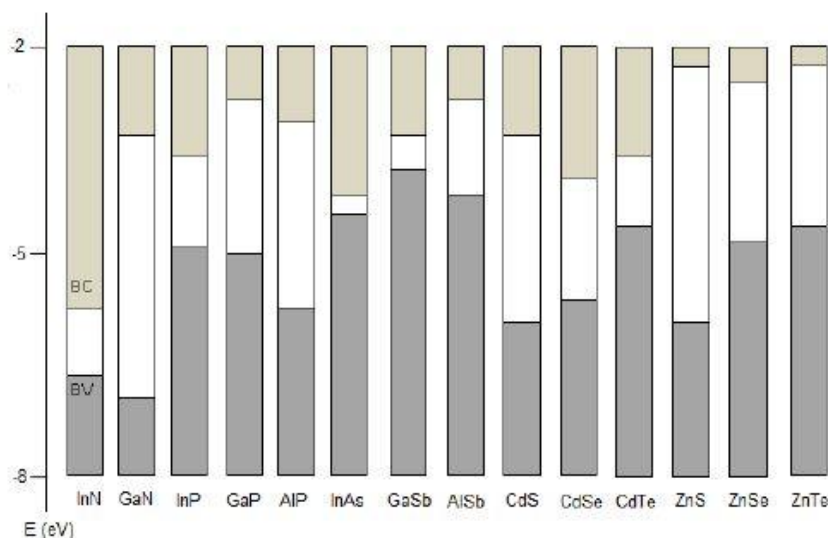

Figure 4.4: Electronic energy levels of selected 13-15 and 12-16 group semiconductors using the valence band offsets (Wei, S. H. et al., 1998).

There are two types of passivation. In the first type passivation the band gap of the shell material is greater than the band gap of the core material, with the valence band of the shell situated below the valence band of the core, and the conduction band of the shell located over the conduction band of the core. This kind of shell decreases the non-radiative pathways associated with the trapping of the electron or the hole generated after the absorption of the light by the core and the optical properties of the QDs are improved, since the shell separates physically the surface of the core from its surrounding medium, reducing the sensing of the core to the environment, such as water molecules or oxygen. Generally, nanoparticles passivated with this shell are more stable

against photodegradation. The most used is the quantum dot formed by CdSe in the core and ZnS in the shell, denominated commonly as CdSe/ZnS QDs **(Figure 4.5).** The shell growth produce a small red shift (around 5-10 nm) in the absorption and emission band spectra of the CdSe. Other kinds are: CdSe/CdS, CdTe/ZnS, or ZnSe/ZnS among others.
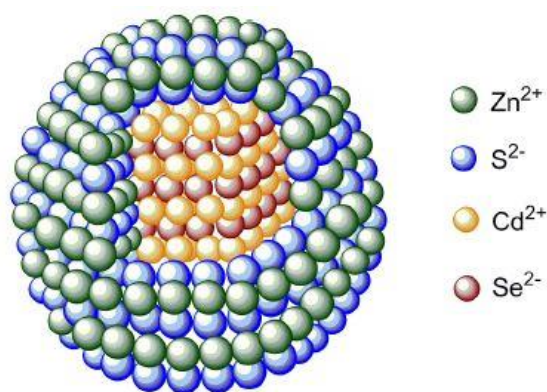

Figure 4.5: CdSe/ZnS QDs core-shell

In the second type passivation the valence band or the conduction band edge from the shell material is located among the band gap of the core. The resulting alignment of the bands, leads to a special separation of the hole and the electron in separate regions of the core-shellstructure after the QD absorption of light. This shell produces a significant red shift of the emission wavelength of the QDs. These shells are interesting because they allow the tuning of the emission color using different shell thickness, which is not possible with other kinds of materials. The principal use of these materials is in the synthesis of QDs with emission in the near infrared region. Some examples are CdTe/CdSe or CdSe/ZnTe QDs. In addition to this, with the second type passivation, the shells have large photoluminescence decays compared to the shells obtained from first type passivation, due to the lower

overlap of the electron and hole wavefunctions (**Wei, S. H. et al., 1998**) in this system, as the electron or the hole are located in the shell.

4.4 Synthesis CdSe/ZnS QDs

Quantum dots may be synthesized in different ways, grouped, depending on the reaction temperature, the precursors and ligands used, the type of the shell, QDs shape, etc. To simplify, the procedures have been classified depending on the final media in which the nanoparticle will be solubilized, i.e. organic or aqueous media.

4.4.1 Synthesis CdSe in organic media

In the laboratory the synthesis of quantum dots was carried out following the method of Benito-Alifonso, D. et al. described in literature. Benito-Alifonso, D. et al. have synthesized quantum dots soluble in organic solvents using high temperature and obtained monodisperse CdS, CdSe and CdTe nanoparticles. Their method was based on high temperature decomposition of organometallic precursors in the presence of a coordinating solvent (**Benito-Alifonso, D. et al., 2014**). LaMer and Dinegar have demonstrated that the synthesis of monodisperse colloids via homogeneous nucleation requires two separate steps: the formation of the nuclei (nucleation) and the subsequent growth stage (**LaMer, V. K. et al., 1950**). This phenomenon is illustrated in **Figure 4.6.**
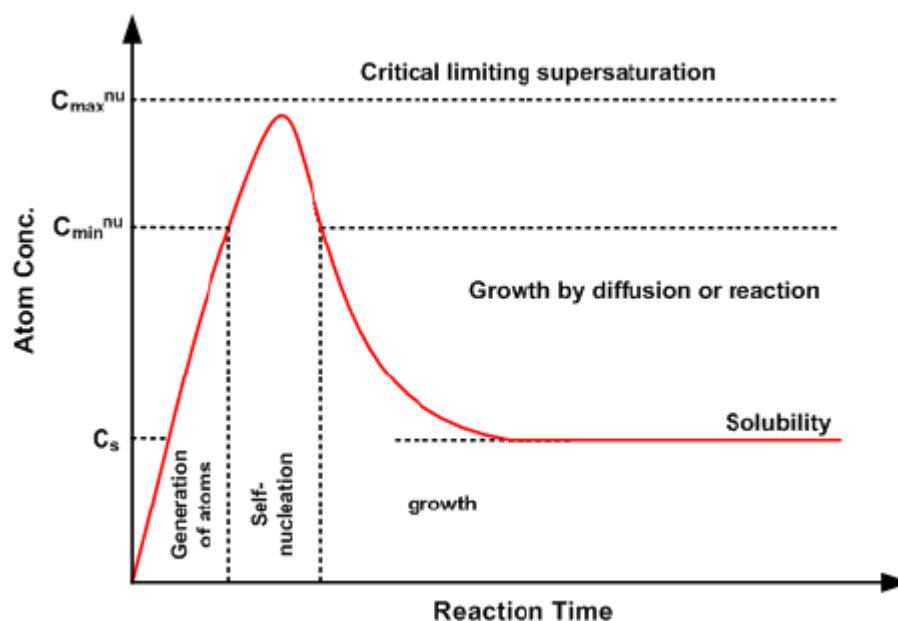
Figure 4.6: Plot of LaMer's model for the generation of atoms, nucleation, and subsequent growth of colloidal synthesis (Brandreth, D. A. et al., 1998).

As shown in **Figure 4.6**, the step of training includes three stages: the generation of the atoms, self-nucleation, and the particle growth. Initially, the concentration of monomers (minimum subunits of the crystal) increases constantly by generation in situ or by addition from the exterior. It is important to underline that no nucleation occurs even above the saturation concentration (C_s). When the reaction reaches a degree of supersaturation (C_{min}^{nu}), the nucleation and then formation of stable nuclei take place. Briefly, the consumption rate of the monomer is greater than its production, so that the monomer concentration decrease below C_{min}^{nu}. After that, the subsequent growth stages strongly govern the final morphology of the nanocrystals, determined by the chemical potentials of the different crystallographic faces, which are in turn highly dependent on the reaction environment, such as temperature and solute concentration. Experimentally, the reagent is rapidly injected into the hot solvent (~ 300) and this leads to the separation of the two phases, i.e. the nucleation and growth (**De Mello Donegá, C. et al., 2005**). In particular, you have first a decrease of the temperature around 180-200 °C

which determines the start of nucleation of the nanoparticles, subsequently the temperature increases and this results in the arrest of nucleation (to about 250 °C) and the growth of the nuclei formed **(Figure 4.7).**
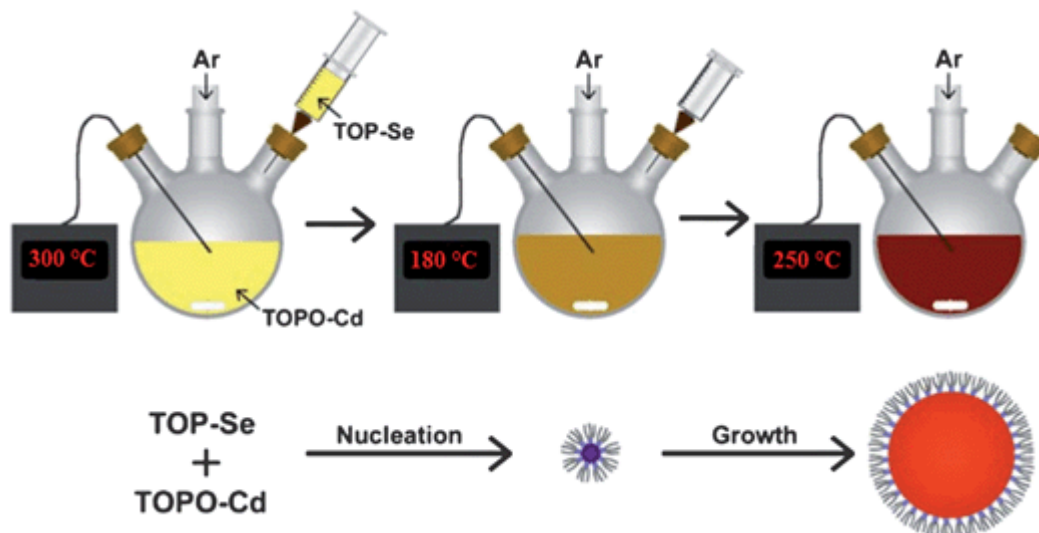

Figure 4.7: Nucleation and growth CdSe core

This methodology, called hot injection method, raises the precursor concentration in the reaction flask above the nucleation threshold. The instantaneous nucleation is immediately quenched by the fast cooling of the reaction mixture, since the solution to be injected is added at room temperature or slightly heated (~ 50 ºC) **(Figure 4.8).**

Figure 4.8: Arrest nucleation CdSe core by rapid coaling of reaction after 1.5 minutes.

167

By varying the duration of cooling is possible to obtain QDs nanoparticles of different size QDs and colors (QDs yellow-green for shorter times (0.5-1 mins) and orange-red for longer times (2.5-3 mins)).

4.4.2 Coating of the CdSe core with ZnS layer

Subsequently CdSe core were covered with a layer of ZnS. The coating of the CdSe core with ZnS layer increases the stability to the photoquenching. The mixture was allowed to cool and the particles precipitated by addition of MeOH. The solution was centrifuged, the supernatant was discarded and the CdSe/ZnS QDs were redissolved in CHCl$_3$ **(Figure 4.9).**
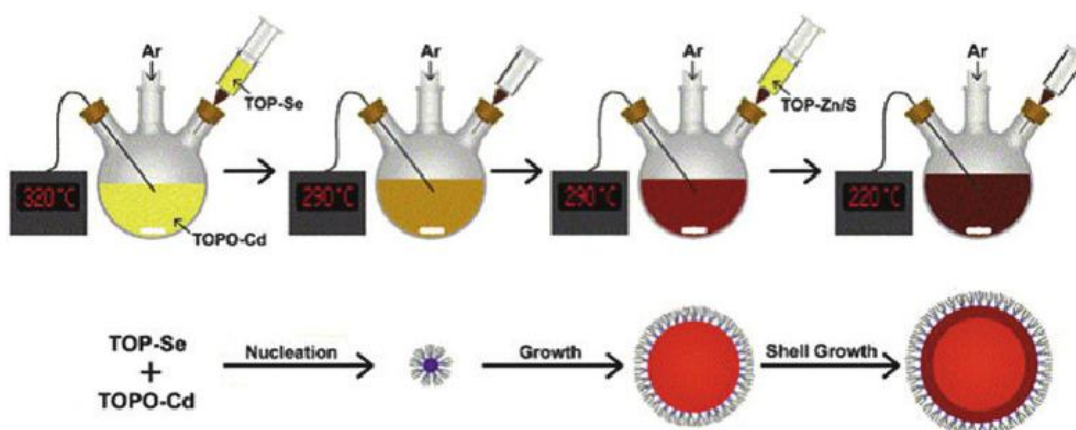
Figure 4.9: CdSe core covered with a layer of ZnS.

Figure 4.9: Precipitation, centrifugation and dissolution CdSe/ZnS QDs in CHCl$_3$

Another methodology adapted from the synthesis of metallic nanoparticles to be used is the heating-up method **(Park, J. et al., 2007).** This method consists in the gradually heating of the reaction mixture to achieve the degree of supersaturation required for the homogeneous nucleation.

4.4.3 Synthesis CdSe/ZnS in aqueous media

Chemical modifications of the surface of QDs are performed to provide good dispersibility in a given solvent, to avoid nanoparticle aggregation and precipitation, and to provide specific chemical functional groups suitable for further coupling. The common strategy to render the QDs dispersible in water includes exchanging the original hydrophobic ligands (e.g. TOPO) with ligands having one chemical group able to bind to the nanocrystal surface (e.g. thiols, amines, phosphines, carboxylic acids, and pyridines), and a polar head group (e.g. hydroxyl), directed towards water. Another approach is based on preserving the original ligands and avoiding ligand exchange by coating the QDs with amphiphilic molecules. These amphiphilic coatings will have hydrophobic groups interacting with the original ligand and hydrophilic groups providing water solubility. Alternatively, one can coat the QDs with an inorganic silica shell using the classical Stober process (base-catalyzed hydrolysis of tetraethoxysilane and subsequent condensation of the monomers onto the existing nuclei) (**Zhao, L. et al., 2012**) or by synthesis in microemulsion **(Figure 4.10).**
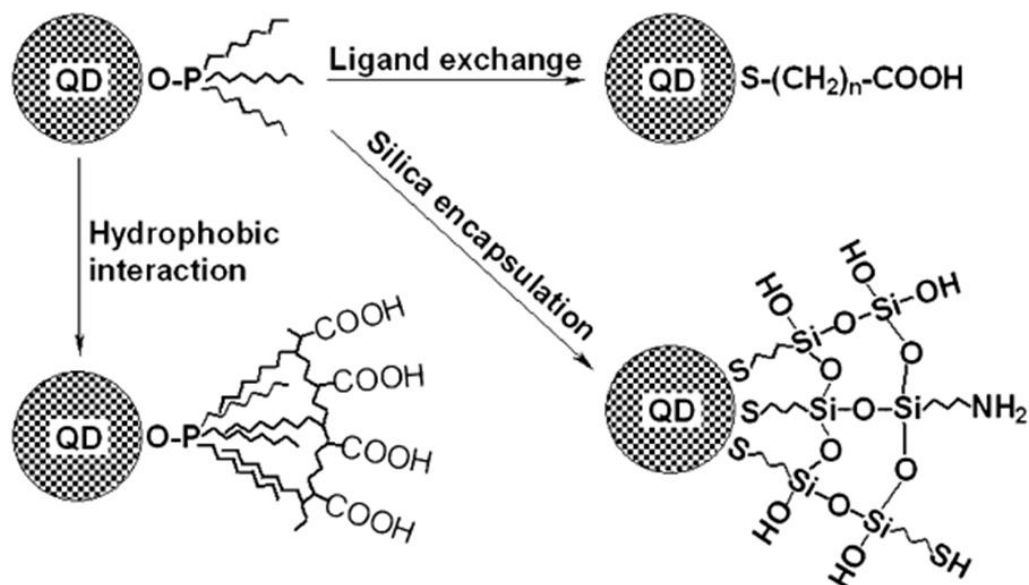
Figure 4.10: Comparison between different methods used to modify the QDs surface

4.5 The role of the ligands

The ligands on the surface of the nanocrystals are in equilibrium with free ligands in solution. For weakly bound ligands, and without excess ligand present in the solution, desorption of the molecules from the QDs surface leads to loss of functionality, deterioration of the optical properties, aggregation, and finally precipitation **(Aldana, J. et al., 2005; Aldana, J. et al., 2001).** Ligands that are able to bind with more than one chemical group were shown to provide organic shells, which were much more stable under physiological conditions and during subsequent chemical functionalization **(Giovanelli, E. et al., 2012).** These could be simple dithiol ligands, like dihydrolipoic acid, **(Uyeda, H. T. et al., 2015; Mattoussi, H. et al., 2000; Anikeeva, N. et al., 2006)** carbodithioic acid, **(Querner, C. et al., 2006; Liu, L. et al., 2010)** dithiocarbamate, **(Li, Y. et al., 2012)** polymers exhibiting functional side groups, **(Liu, L. et al., 2010; Yildiz, B. et al., 2009)** denaturated proteins like bovine serum albumin (BSA) **(Wang, Q. et al.,**

2006) or hyperbranched polymers **(Nann, T., 2005).** The optical properties of the QDs can be modified depending on the legend chased, infact the effect of the ligands mentioned above on the fluorescence intensity of the QDs is very different. For instance, Mulvaney et al. have studied the effect of the addition of different ligands (e.g oleic acid, hesanenitrile etc.) to a CdSe QDs capped with trioctylphosphine oxide (TOPO). They observed that amines produced the best fluorescence response, while the thiol and the carboxylic acid produced the largest decrease of the QDs fluorescence **(Mulvaney, P. et al., 2006).**

4.6 Doping of metal oxides with QDs

Several researchers have described the interaction between the QDs and the ligand in which the electron transfer causes the quenching of the QDs fluorescence. This phenomenon depends on the redox potential of the functional ligand and the nanoparticle, which is totally related to the QDs size. PET (Photo-induced Electron) processes have been reported for both core and core-shell QDs, but only in the case of core QDs, the nanoparticles can act in both directions, i.e. as an electron donor or as an electron acceptor. In the case of core-shell QDs, the nanoparticle can only act as electron donor, because the hole is largely confined in the core, while the electron can delocalize on the surface **(Van Embden, J. et al., 2007).** Photoinduced electron transfer from the QDs as electron donor to semiconductor metal oxide (MOs) as acceptor has been also reported by Kamat et al. **(Kamat, P. V. et al., 2010)**. This process is possible because the conduction band of the MO is located between the band gap energy of the QDs **(Figure 4.11).**
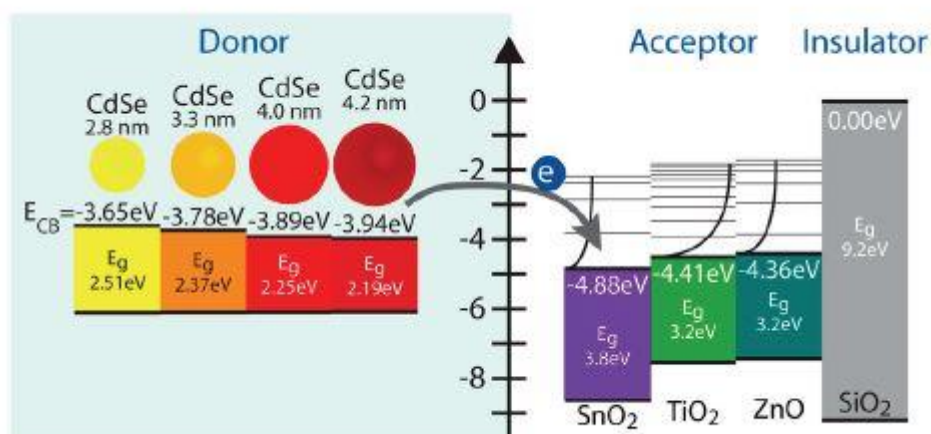
Figure 4.11: Diagram of the relative electronic energy differences between CdSe donating species and MO accepting species for all CdSe-MO combinations.

Exploiting this principle, my thesis deal with titania nanofibers decorated with QDs nanoparticles by both physical and chemical functionalization. The first one required a simple dropping of the diluted solution (1:20 v:v, $CHCl_3$) onto the fibrous layer. The second one implied an *in situ* reaction able to bind the quantum dots to TiO_2. These scaffoldings have been investigated in my PhD thesis as optically active novel nanomaterials.

4.7 Semiconductor-metal nanocomposites

Deposition of metal nanoparticles on other nanostructures made of carbon or other semiconducting materials is of great interest because the resultant metal/semiconductor composites may exhibit some intriguing properties (**Corio, P. et al., 2004; Sun, X. H. et al., 2004**). Semiconductor-metal nanocomposites have been widely employed in photocatalysis (**Kraeutler, B. et al., 1978; George Thomas, K. et al., 2003**). For example, titanium dioxide (TiO_2) is considered very close to an ideal semiconductor for photocatalysis

because of its high stability, low cost and safety toward both humans and the environment.

4.7.1 Chemical structure of TiO$_2$

TiO$_2$ belongs to the family of transition metal oxides. There are four commonly known polymorphs of TiO$_2$ found in nature: anatase (tetragonal), brookite (orthorhombic), rutile (tetragonal), and TiO$_2$ (B) (monoclinic) **(Carp, O. et al., 2004).** Rutile: rutile TiO$_2$ has a tetragonal structure and contains 6 atoms per unit cell **(Figure 4.12).** The TiO$_6$ octahedron is slightly distorted (**Chen, X. et al., 2007; Diebold, U., 2003**). The rutile phase is stable at most temperatures and pressures up to 60 kbar, where TiO$_2$ (II) becomes the thermodynamically favorable phase **(Norotsky, A. et al., 1967).** Anatase: it crystallizes in the tetragonal system; but, although the degree of symmetry is the same for rutile and anatase, there is no relation between the interfacial angles of the two minerals, except in the prism-zone of 45° and 90°. The common pyramid of anatase, parallel to the faces of which there are perfect cleavages, has an angle over the polar edge of 82°9', the corresponding angle of rutile being 56°52½'. A distortion of the TiO$_6$ octahedron is slightly larger for the anatase phase **(Linsebigler, A. L. et al., 1995; Mo, S. et al., 1995)** as depicted in **Figure 4.12.** Muscat et al. **(Muscat, J. et al., 2002)**. Found that the anatase phase is more stable than the rutile at 0 K, but the energy difference between these two phases is small (~2 to 10 kJ/mol). Brookite: brookite TiO$_2$ belongs to the orthorhombic crystal system. Its unit cell is composed of 8 formula units of TiO$_2$ and is formed by edge-sharing TiO$_6$ octahedra **(Figure 4.13).** TiO$_2$ is a large band semiconductor, with band gaps of 3.2, 3.02, and 2.96 eV for the anatase, rutile and brookite phases, respectively **(Wunderlich, W. et al., 2004).** The valence band of TiO$_2$ is composed of the 2p orbitals of

oxygen hybridized with the 3d orbitals of titanium, while the conduction band is only the 3d orbitals of titanium (**Paxton, A. T. et al., 1998**). When TiO_2 is exposed to near-UV light, electrons in the valence band are excited to the conduction band leaving behind holes (h+), as shown in Figure 3. The excited electrons (e–) in the conduction band are now in a purely 3d state and because of dissimilar parity, the transition probability of e– to the valence band decreases, leading to a reduction in the probability of e–/h+ recombination (**Banerjee, S. et al., 2006).** Anatase TiO_2 is considered to be the active photocatalytic component based on charge carrier dynamics, chemical properties and the activity of photocatalytic degradation of organic compounds.
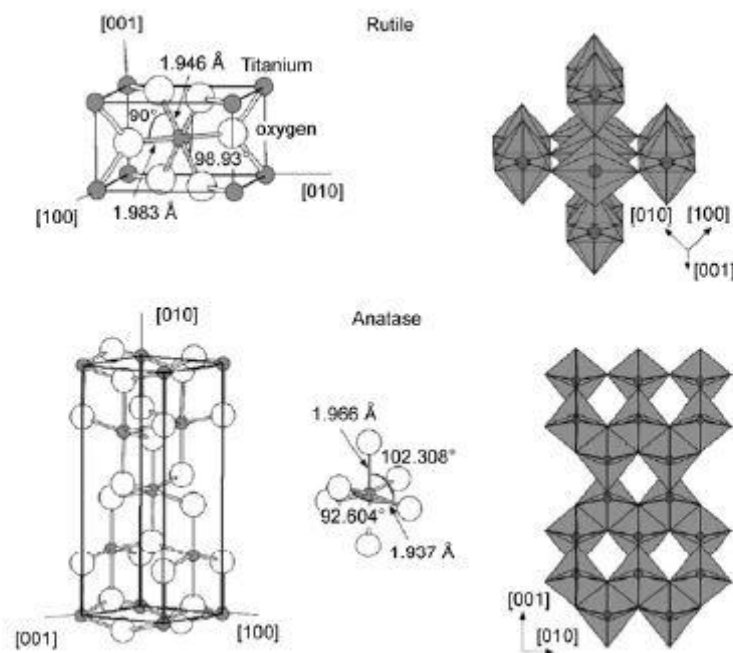

Figure 4.12: Crystal structures of the rutile and anatase phases of TiO2 (Diebold, U., 2003).
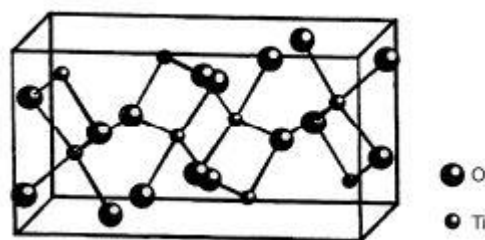
Figure 4.13: Lattice structure of brookite TiO2 (Mo, S. et al., 1995).

4.7.2 Heat treatment of TiO$_2$

Heat treatment has a vital role in the synthesis of particles, affecting morphology, crystallinity and porosity, and causing a decline in surface area, loss of surface hydroxyl groups and inducing phase transformation. At high temperatures, (400°C and above) the removal of organic materials takes place. The surface area of TiO$_2$ decreases with calcination time and heating rate because of the collapse of pores in the TiO$_2$ powder caused by the transformation of amorphous TiO$_2$ to the anatase phase. Slow heating rates provide relatively mild conditions for phase transformation (**You, X. et al., 2005**). Hu et al. (**Hu Y. et al., 2003**) have reported that TiO$_2$ normally undergoes an anatase-to-rutile phase transformation in the range from 600–700°C. The transformation was also affected by factors such as preparation conditions, precursors, impurities, oxygen vacancies and the primary particle size of the anatase phase.

4.8 Doping of metal oxides with metallic nanoparticles

Doping of TiO_2 has been an important approach in band gap engineering to change the optical response of semiconductor photocatalysts. The main objective of doping is to induce a bathochromic shift, i.e., a decrease of the band gap or introduction of intra-band gap states, which results in the absorption of more visible light. Doping may lead to photocatalytic systems that exhibit enhanced efficiency (**Carp, O. et al., 2004**). It is desirable to maintain the integrity of the crystal structure of the photocatalyst while changing its electronic structure by doping. It is easier to replace Ti^{4+} in TiO_2 with a cation than to substitute O^{2-} with another anion because of the difference in the charge states and ionic radii (**Mor, G. K. et al., 2006**). Nanomaterials show a higher tolerance to structural distortion than bulk materials due to their inherent lattice strain. As a result, the surface modification of TiO_2 nanoparticles appears to be more beneficial than the modification of bulk TiO_2 (**Burda, C. et al., 2003**). Addition of noble metals is another approach for the modifying photocatalysts. Noble metals including Pt, Ag, Au, Pd, Ni, Rh and Cu have been reported to be very effective at enhancing photocatalysis by TiO_2 (**Rupa, A. et al., 2009; Wu, N. L. et al., 2004**). Because the Fermi levels of these noble metals are lower than that of TiO_2, photoexcited electrons can be transferred from the conduction band of TiO_2 to metal particles deposited on the surface of TiO_2, while photogenerated holes in the valence band remain on TiO_2. This greatly reduces the possibility of electron-hole recombination, resulting in efficient separation and higher photocatalytic activity. Numerous studies have found that the properties of these kinds of composites depend strongly on the size of the metal particle, dispersion and composition. When the size of the metal particles is less than 2.0 nm, the composites display exceptional catalytic behavior (**Turner, M. et al., 2008**). It has been suggested that too high a concentration of metal

particles reduces photon absorption by TiO_2 and allows the metal particles to become electron-hole recombination centers, resulting in lower efficiency **(Sakthivel, S. et al., 2004).**

4.8.1 Doping of TiO_2 nanoparticles and nanofibers with gold nanoparticles

Extensive research has shown that the attachment of gold or other metal nanoparticles to TiO_2 nanoparticles could cause the Fermi level of titania to be shifted to more negative potentials and prevent the recombination of electron-hole pairs, therefore leading to significant improvement in photocatalytic activity and photoelectrochemical response **(Subramanian, V. et al., 2004; Hoffmann, M. R. et al., 1995).** The Fermi level (EF) of the semiconductor is directly related to the number of accumulated electrons as illustrated in the following expression:

$$E_F = E_{CB} + kT \ln nc/Nc$$

E_{CB} is the conduction band energy level versus NHE (Normal Hydrogen Electrode), nc is the density of accumulated electrons, and Nc is the charge carrier density of the semiconductor. If we accumulate more electrons in the TiO_2 or TiO_2-Au system, we would expect a negative shift in the Fermi level of the TiO_2. When the semiconductor and metal nanoparticles are in contact, the photogenerated electrons are distributed between TiO_2 and Au nanoparticles (Fermi level of Au=+0.45 V versus NHE). The transfer of electrons from the excited TiO_2 into Au continues until the two systems attain equilibrium. Since the electron accumulation increases the Fermi level of Au to more negative potentials, the resultant Fermi level of the composite shifts closer to the conduction band of the semiconductor. The negative shift in the

Fermi level is an indication of better charge separation and more reductive power for the composite system. **Figure 4.14** illustrates the shift in the Fermi level of the composite as a result of charge equilibration between semiconductor and metal nanoparticles.
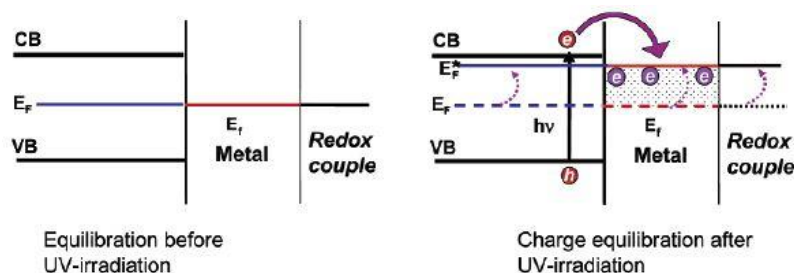

Figure 4.14: Equilibration of Semiconductor-Metal Nanocomposites with the Redox Couple before and after UV Irradiation

In the present study hybrid nanostructures Au/TiO_2 were prepared via in situ photoreduction of gold salts on the surface of TiO_2 nanofibres **(Macagnano, A. et al., 2015).** In fact, $HAuCl_4$ can be directly reduced to form well-dispersed Au colloids under UV irradiation in the presence of some organic stabilizers such as PVP, poly(ethylene glycol) (PEG), poly(vinyl alcohol) (PVA) or other surfactants **(Mayer, A. et al., 1998).** These organic stabilizers might also act as scavengers (that is, they are oxidized when $HAuCl_4$ is reduced) thereby facilitating the reduction of $HAuCl_4$. We also found that the morphology of the deposited gold nanostructures could be controlled by varying the type of capping reagent, as well as its concentration. Dan Li et al. have reported that if the concentration of organic capping regents is higher than $1.0 \cdot 10^{-3}$ M, the resultant gold nanoparticles exhibit a semispherical shape exclusively. The particle size decreased slightly as the concentration of a capping reagent increased **(Dan, Li et al., 2004).** This method is relatively simple and has been adopted to deposit various metal nanoparticles (e.g. Ag, Pt or Pd) on TiO_2 nanoparticles **(Murakata, T. et al., 2002; Cozzoli, P. D. et al., 2004).** However, morphological control of photodeposited nanoparticles has not been demonstrated previously. Recently, TiO_2 has been prepared in the

178

form of powders, crystals, thin films, nanofibers **(Macagnano, A. et al., 2015),** nanotubes and nanorods. Therefore, exploiting the photocatalytic properties of TiO_2, at low cost, gold nanoparticles were also selectively grown, under UV-light irradiation, on the electrospun titania nanofibers through the photoreduction of $HAuCl_4$ in the presence of an organic capping reagent (PVP). We have demonstrated that these nanofibers could be directly assembled into three-dimensional porous mats. We believe, infact, that these nanofibers can serve as catalysts and/or catalyst supports. Reassuming, the gold nanostructures can be, selectively deposited on electrospun anatase nanofibers by utilizing the photocatalytic feature of titania. The morphology of these gold nanostructures can be readily controlled by varying the experimental parameters.

4.9 Development of blends of polymer nanofibers

Organic polymer blends are among the most investigated materials for conductive sensors, mainly due to the easy of preparation. In the laboratory, nanofibers composed of PANi/PHB blends were prepared and deposited through electrospinning on chemoresistors in order to be investigated as potential biodegradable chemical sensors **(Macagnano, A. et al., 2016).** The electrospinning technology was used in order to design and obtain materials with high performance sensing features. PANi and PHB polymers were selected for their crucial remarkable characteristics, such as gas sensitivity and biodegradability, respectively. Six nanofibrous samples with increasing PANi/PHB mass ratio were manufactured and characterized. Thus, networks of continuous nanofibers with high porosity and covering the sensing area of the interdigitated electrodes were observed for each polymer solution. The increase in PANi concentration created a sharper distribution of the diameter

sizes (~200 nm) as well as rougher and lumpy fibers. TEM pictures reported a more homogeneous distribution of PANi within the PHB fibres, especially at higher concentrations, as confirmed by the analysis of electrical parameters. The potentials of such blended polymers were exploited, focusing the attention on the influence of humidity on the features of the resulting chemosensors. Ammonia in trace was measured in dry air and at different percentages of relative humidity, in order to evaluate the influence of PHB in the interaction of PANi with the gas in possible applications. Similarly, both acidic and basic volatile organic compounds were detected at different values of environmental humidity, until 70% RH. The peculiar structure of the nanofibrous layer as well as the physico-chemical properties of PANi/PHB, enabled ammonia and VOCs detection at high percentages of humidity, thus decreasing the response time and, specifically for VOCs, increasing the sensor responses. Moisture is generally an extremely undesirable environmental parameter for many sensors. In the case of electrospun PANi/PHB chemosensors here proposed, the natural strategy of sensing is mimicked, where an aqueous film over cilia (here represented by the nanofibers) is used to solve interacting molecules with surface thus facilitating the chemical interactions. This findings suggest the possibility for such sensors to be used in applications where monitoring strongly moist environments is required (e.g. food packaging, breath analysis, skin perspiration, soil, air in different environmental conditions, etc.), without any need to abate or reduce water vapors content.

References

Aldana J., Lavelle N., Wang Y. J., Peng X. G. Size-dependent dissociation pH of thiolate ligands from cadmium chalcogenide nanocrystals. Am Chem Soc (2005), Vol. 127, pp. 2496

Aldana J., Wang Y. J., Peng X. G. Photochemical instability of CdSe nanocrystals coated by hydrophilic thiols. Am Chem Soc (2001), Vol. 123, pp. 8844

Anikeeva N., Lebedeva T., Clapp A. R., Goldman E. R., M. L., Dustin M. L., Mattoussi H., Sykulev Y. Quantum dot/peptide-MHC biosensors reveal strong CD-8 dependent cooperation between self and viral antigens that augment the T cell response. Proc Nati Acad ScL U S A (2006), Vol. 103, pp. 16846

Australian Journal of Chemistry (2007), Vol. 60, pp. 457- 471

Banerjee S., Gopal J., Muraleedharan P. et al. Physics and chemistry of photocatalytic titanium dioxide: Visualization of bactericidal activity using atomic force microscopy. Current Sci (2006), Vol. 90, pp. 1378-1383

Borchert H., Talapin D. V., McGinley C., Adam S., Lobo A.; Castro A. R. B. D.; Moller T.; Weller H. The Journal of Chemical Physics (2003), Vol. 119, pp. 1800-1807

Brandreth D. A., Otterstedt J. E. Small particles technology New York (1998)

Bullen C., Mulvaney P. The effects of chemisorptions on the luminescence of CdSe quantum dots. Langmuir (2006), Vol. 22, pp. 3007-3013

Burda C., Lou Y., Chen X. et al. Enhanced nitrogen doping in TiO_2 nanoparticles. Nano Lett (2003), Vol. 3, pp. 1049-1051

Carp O., Huisman C. L., Reller A. Photoinduced reactivity of titanium dioxide. Prog in Solid State Chem (2004), Vol, 32, pp. 33-117

Carrillo-Carrion C., Cardenas S., Simonet B. M., Valcarcel M. Quantum dots luminescence enhancement due to illumination with UV/Vis light. Chemical Communications (2009), pp. 5214-5226

Chen X., Mao S. S. Titanium dioxide nanomaterials: Synthesis, properties, modifications, and applications. Chem Rev (2007), Vol. 107, pp. 2891-2959

Corio P., A. P. Santos A. P., Santos P. S., Temperini M. L. A., Brar V. W., Pimenta M. A., Dresselhaus M. S. Raman Spectroscopy, Fullerenes and Nanotechnology. Chem Phys Lett (2004), pp. 383- 475

Cozzoli P. D., Comparelli R., Fanizza E., Curri M. L., Agostiano A., Laub D. Photocatalytic synthesis of silver nanoparticles stabilized by TiO_2 nanorods: a semiconductor/metal nanocomposite in homogeneous nonpolar solution. J Am Chem Soc (2004), Vol. 126, pp. 3868

Dan Li., Jesse T. McCann., Matthew Gratt., Younan Xia. Photocatalytic deposition of gold nanoparticles on electrospun nanofibers of titania. Chemical Physics Letters (2004), Vol. 394, pp. 387-391

De Mello Donegá, C. Liljeroth P., Vanmaekelbergh D., Physicochemical Evaluation of the Hot-Injection Method, a Synthesis Route for εonodisperse Nanocrystals. Small (2005), Vol. 1, pp. 1152-1162

Diebold U. The surface science of titanium dioxide. Sur Sci Rep (2003), Vol. 48, pp. 53-229

Fu H., Zunger A. InP quantum dots: Electronic structure, surface effects and the red shifted emission. Physical Review B (1997), Vol. 56, pp. 1496-1508

George Thomas K., Kamat P. V. Chromophore-functionalized gold nanoparticles. Acc Chem Res (2003), Vol. 36, pp. 888

Giovanelli E., Muro E., Sitbon G., Hanafi M, Pons T, Dubertret B., Lequeux N. Highly Enhanced Affinity of Multidentate versus Bidentate Zwitterionic Ligands for Long-Term Quantum Dot Bioimaging. Langmuir (2012), Vol. 28, pp. 15177

Hoffmann M. R., Martin S. T., Choi W., Bahnemann D. W. Environmental Applications of Semiconductor Photocatalysis. Chem Rev (1995), Vol. 95, pp. 69

Hu Y., Tsai H. L., Huang C. L. Phase transformation of precipitated TiO_2 nanoparticles. Mater Sci Eng A (2003), Vol. 344, pp. 209-214

Kashyout A. B., Hesham M. A. Soliman., Fathy M., Gomaa E. A., Zidan A. A. CdSe quantum dots for solar cell devices. Hindawi Publishing Corporation International Journal of Photoenergy (2012). Vol. 2012, pp. 7

Kraeutler B., Bard A. J. J. Heterogeneous photocatalytic preparation of supported catalysts. Photodeposition of platinum on titanium dioxide powder and other substrates. Am Chem Soc (1978), Vol. 100, pp. 4317

LaMer V. K., Dinegar R. H. Theory, Production and mechanism of formation of monodispersed hydrosols. Journal of the American Chemical Society (1950), Vol. 72, pp. 4847-4854

Li Y., Shen B., Liu L., Xu H., Zhong X. H. Colloids Surf A (2012), Vol. 410**,** pp. 144

Linsebigler A. L, Lu G., Yates J. T. Photocatalysis on TiO_2 surfaces: Principles, mechanisms, and selected results. Chem Rev (1995), Vol. 95, pp.735-758

Liu L, Guo X. H., Li Y., X. H., Zhong X. H. Inorg Chem (2010), Vol. 49, pp. 3768

Macagnano A., Perri V., Zampetti E., Bearzotti A., De Cesare F. Humidity effects on a novel eco-friendly chemosensor based onelectrospun PANi/PHB nanofibres. Sensors and Actuators B (2016), Vol. 232, pp. 16-27

Macagnano A., Zampetti E., Perri V., Bearzotti A., Sprovieri F., Pirrone N., Esposito G., De Cesare F. Photocatalytically decorated Au-nanoclusters TiO$_2$ nanofibres for elemental mercury vapor detection. Procedia Engineering 120, Eurosensors (2015), pp. 422-426

Mattoussi H., Mauro J. M., Goldman E. R., Anderson G. P., Sundar V. C., Mikulec F. V., Bawendi M. G. Am Chem Soc (2000), Vol. 122, pp.12142

Maye M. M., Gang O., Cotlet M. Photoluminescence enhancement in CdSe/ZnS-DNA linked-Au nanoparticle heterodimers probed by single molecule spectroscopy. Chemical Communications (2010), Vol. 46, pp. 6111-6113

Mayer A., Antonietti M. Investigation of polymer-protected noble metal nanoparticles by transmission electron microscopy: control of particle morphology and shape. Colloid Polym Sci (1998), Vol. 276, pp. 769-779

Michalet X., Pinaud F. F., Bentolila L. A., Tsay J. M., Doose S., Li J. Quantum dots for live cells, in vivo imaging, and diagnostics. J , Sundaresan G., Wu M. A., Gambhir S. S, Weiss S. Science (2005), Vol. 307, pp. 538

Mishra S., Tripathy P., Sinna S. P. Advancements in the field of quantum dots. International journal of advancements in research & technology (2012), Vol. 1

Mo S., Ching W. Electronic and optical properties of three phases of titanium dioxide: Rutile, anatase and brookite. Phys Rev B (1995), Vol, 5, pp. 13023-13032

Mor G. K, Varghese O. K, Paulose M. et al. A review on highly ordered, vertically oriented TiO₂ nanotube arrays: Fabrication, material properties, and solar energy applications. Solar Energ Mater Solar Cell (2006), Vol. 90, pp. 2011-2075

Murakata T., Higashi Y., Yasui N., Higuchi T., Sato S. Photocatalytic Preparation of Noble Metal Nanoparticles with Use of Ultrafine TiO₂ Particles. J Chem Eng Jpn (2002), Vol. 35, pp. 1270

Muscat J., Swamy V., Harrison N. M. First-principles calculations of the phase stability of TiO₂. Phy Rev B (2002), Vol. 65, pp. 1-15

Nann T. Phase-transfer of CdSe/ZnS quantum dots using amphiphilic hyperbranched polyethylenimine. Commun (2005), pp.1735

Norotsky A., Jamieson J. C., Kleppa O. J. Enthalpy of transformation of a high pressure polymorph of titanium dioxide to the rutile modification. Science (1967), Vol. 158, pp. 338-389

Park J.; Joo, J.; Kwon, S. G.; Jang Y.; Hyeon T. Synthesis of monodisperse spherical nanocrystals. Angewandte Chemie International Edition (2007), Vol. 46, pp. 4630-4660

Paxton A. T, Thiên-Nga L. Electronic structure of reduced titanium dioxide. Phys Rev B (1998), Vol. 57, pp. 1579-1584

Pellegrino T., Kudera S., Liedl T., Javier A. M., Manna L., Parak W. On the development of colloidal nanoparticles towards multifunctional structures and their possible use for biological applications. J Small (2005), Vol. 1, pp. 48

Querner C., Benedetto A., Demadrille R., Rannou P., Reiss P. Chem. Mater (2006), Vol. 18, pp. 4817

Raichlin S., Sharon E., Freeman R., Tzfati Y., Willner I. Biosensors and Bioelectronics (2011), Vol. 26, pp. 4681-4689

Rupa A. V, Divakar D., Sivakumar T. Titania and noble metals deposited titania catalysts in the photodegradation of tartrazine. Catal Lett (2009), Vol, 132, pp. 259-267

Sakthivel S., Shankar M. V, Palanichamy M. et al. Enhancement of photocatalytic activity by metal deposition: Characterization and photonic efficiency of Pt, Au and Pd deposited on TiO_2 catalyst. Water Res (2004), Vol. 38, pp. 3001-3008

Stekel J. S., Zimmer J. P., Coe-Sullivan S., Stott N. E., Bulovic V., Bawendi M.,G. Color-Saturated Green-Emitting QD-LEDs. Angew Chem (2004), Vol. 116, pp. 2206;

Subramanian V., Wolf E. E., Kamat P. V. Catalysis with TiO_2/gold nanocomposites. Effect of metal particle size on the Fermi level equilibration. J Am Chem Soc (2004), Vol. 126 (15), pp. 4943-50

Sun X. H., Wong N. B., Li C. P., Lee S. T., Kim P. S. G, Sham T. K. Synthesis and patterning of gold nanostructures on InP and GaAs via galvanic displacement. Chem Mater (2004), Vol. 16, pp. 1143

Talapin D. V., Rogach A. L., Kornowski A., Haase M., Weller H. Highly Luminescent Monodisperse CdSe and CdSe/ZnS Nanocrystals Synthesized in a Hexadecylamine−Trioctylphosphine Oxide−Trioctylphospine Mixture. Nano Letters (2001), Vol. 1, pp. 207-211

Turner M., Golovko V. B, Vaughan O. P. H. et al. Selective oxidation with dioxygen by gold nanoparticle catalysts derived from 55-atom clusters. Nature (2008), Vol. 454, pp. 981-983

Tvrdy K., Frantsuzov P. A., Kamat P. V. The Core/Shell Structure of CdSe/ZnS Quantum Dots Characterized by X-Ray Absorption Fine Spectroscopy. Proceedings of the National Academy of Sciences (2010), Vol. 108, pp. 29-34

Uyeda H. T., Medintz I. L., Jaiswal J. K., Simon S.M., Mattoussi H. Synthesis of Compact Multidentate Ligands to Prepare Stable Hydrophilic Quantum Dot Fluorophores. Am Chem Soc (2005), Vol. 127, pp. 3870

Van Embden J., Jasieniak J., Gómez D. E., Mulvaney P., Giersig M. Rewiew of the synthetic chemistry involved in the production of core/shell semiconductor nanocrystals. Australian Journal of Chemistry (2007), Vol 60, pp. 457-471

Wang Q., Kuo Y. C., Wang Y. W., Shin G. C., Ruengruglikit and Huang Q. R. Luminescent properties of water-soluble denatured bovine serum albumin-coated CdTe quantum dots. J Phys Chem B (2006), Vol. 110, pp.16860

Wei S. H., Zunger A. Calculated natural band offsets of all II–VI and III–V semiconductors: Chemical trends and the role of cation d orbitals. Applied Physics Letters (1998), Vol. 72, pp. 2011-2013.

Wu N. L, Lee M. S. Enhanced TiO_2 photocatalysis by Cu in hydrogen production from aqueous methanol solution. Inter J Hydro Energ (2004), Vol. 29, pp. 1601-1605

Wunderlich W., Oekermann T., Miao L., et al. Electronic properties of nano-porous TiO_2-and ZnO-thin films-comparison of simulations and experiments. J Ceram Process Res (2004) Vol. 5, pp. 343-354

Yildiz B., McCaughan S. F., Cruickshank J. F., Callan and Raymo P. M. Compact Biocompatible Quantum Dots via RAFT-Mediated Synthesis of Imidazole-Based Random Copolymer Ligand. Langmuir (2009), Vol. 25, pp. 7090

You X., Chen F., Zhang J. Effects of calcination on the physical and photocatalytic properties of TiO2 powders prepared by sol-gel template method. J Sol-Gel Sci Tech (2005), Vol. 34, pp. 181-187

Zhao L., Lin Z. Q. Advanced Materials (2012), Vol. 24, pp. 4353

Introduction

A strategy to improve the sensing features of a chemical sensor is to increase the specific surface of the interacting material: the higher the specific surface area of a sensing material the higher its sensor ability to interact, such as biological sensing structures do. Many techniques have been used to augment the surface of sensing layers with fine structures, especially to form controlled nanostructures, as it happens in natural systems, taking advantage of the large specific area of nanostructured materials. Accordingly nanostructured sensors, when compared to the conventional ones, showed desired properties like faster adsorption and minimized bulk effects (i.e. long diffusion–desorption time, analyte entrapment, etc.). From recent literature, electrospinning has been confirmed to be one of the best tools, among the various nanotechnologies, for designing and developing smart sensing systems, both for the uniqueness of the resulting nanostructures and for production rate and cost. Parameters like the extremely rapid formation of the nanofibres structure, which occurs on a millisecond scale, the large coverage in continuous mode, the easy tuning of size and shape, and the nanofibres assembling in situ have raised great scientific interest **[www.electrospinning-cost.eu],** confirmed from the number of publications over the last 10 years. Since the dimension of fibers is roughly comparable to that of the interacting molecules, people may exploit the tiny size with some size effects, such as quantization, and the single molecule sensitivity to design more and more sophisticated and selective sensing systems (**Macagnano, A. et al., 2015**). The use of electrospun fibers in photonics is a promising research field aimed at developing novel microscale light sources and detectors, lasers and optical sensors. This field is growing very fast, since optically-active electrospun fibers with specific and tailored optical properties can be produced by various approaches exploiting the unique properties of organic light-emitting materials (tunability of the

189

emission, strong absorbance, high quantum yield, large Stokes shift, etc.). Thus, optically-active nanostructures are able to combine remarkable optical performances with high exposed surface. The high flexibility of the electrospinning (ES) process, in terms of number and typology of processable materials, is another feature promoting this technology as eligible candidate to a new generation of optical sensors **(Wang, X. et al., 2002).**

Chapter 5

Smart optical sensing systems for monitoring of toxic gas

5.1 CdSe/ZnS-TiO$_2$ nanofibers: a suitable combination for a low cost and effective optical sensor device to reveal NH$_3$ and H$_2$S traces in the atmosphere

Very effective electrospun fluorescent fibers have been realized by Wang et al., (2002) using transparent or optically inert polymers properly doped with inorganic quantum dots **(Wang, X. et al., 2002).** Since electron-deficient metal cations (e.g. Fe^{3+} or Hg^{2+} and nitro aromatic compounds such as DNT and TNT) are known as quenchers for fluorophores, they reported that the sensitivities of the polymer nanofibers hosting pyrene methanol (PM) were 2 to 3 order of magnitude greater of a thin film sensors (a few to tens parts per billion). Composite fibers with diameters of few hundreds of nanometers can be easily obtained starting from the well established procedures developed for the matrix polymers, whereas the photoluminescence properties can be tailored by means of organic molecules (cromophores) and/or inorganic nanoparticles which feature emission in a broad spectral range, from visible to near infrared. These nanoparticles, commonly named quantum dots (QDs), most often composed by group II-VI elements such as CdS, CdSe, CdTe, have diameters of few nanometers and, more importantly, electronic band gaps and photoluminescence wavelengths tunable upon changing their size. Indeed, in these inorganic systems, quantum confinement effects can be appreciated for particle size approaching the exciton Bohr radius, which is typically of few nanometer **(Vossmeyer, T. et al. 1994).** Larger QDs (radius of 5-6 nm, for example) emit longer wavelengths resulting in emission colors such as orange

191

or red. Smaller QDs (radius of 2-3 nm, for example) emit shorter wavelengths resulting in colors like blue and green, although the specific colors and sizes variations depend on the exact composition of the QD. The advantages of QDs over the traditional fluorescent molecules include tunable fluorescence colors, controllable excitation along with narrow emission spectra, high intensity of emission, good photostability, and long fluorescence lifetime. These features enable QDs to be used as powerful imaging and tracking tools in various biological and medical applications. Since fluorescent organic molecules have emission from the ultra-violet to the near infrared, they can be easily added and used in polymers such as poly(methyl methacrylate) (PMMA), polystyrene (PS), poly(vinyl pyrrolidone) (PVP), poly(ethylene oxide) (PEO) and polyvinyl alcohol **(Camposeo, A. et al., 2007).** For instance, QDs have been used as chemical sensors, responding selectively to physiologically important metal cations, such as $Zn^{2+,}$ Cu^{2+}, and detecting the explosive 2,4,6-trinitrotoluene (TNT) in aqueous environments **(Chen, Y. et al., 2002).** Additionally, since for optical sensing based on fluorescent systems, the control of the photoluminescence quantum yield (PLQY) is a crucial issue, electrospinning technology sounds again as a suitable strategy to preserve the optical features of QDs also at solid state, causing an increase up to a factor ranging between 3-50% when compared to drop or spin-coated films **(Morello, G. et al., 2015).** Therefore, ES provides a method for producing solid state photoluminescent structures, featuring enhanced emission efficiency mainly due to the chain alignment in the electrospun fibres formation, that produces an overall photoluminescence polarized along the fiber length. Optical sensors are generally preferred for their high sensitivity, fast response time and low power consumption. The most of reported optical sensing systems are based on the analyte induced quenching of the fluorescence of electrospun fibers, an effect that may be induced either by energy or electron transfer between the fluorescent molecules and the detected element. Parameter as fibers arrangement, morphology and sizes, porosity as

192

well as the chemistry (polymer blends, polymer functionalization) and the adhesion on the strip will be key features to be considered to create novel and highly performing sensor arrays. About the morphology of the fibers, it depends on the solution properties (system parameters), process conditions (operational parameters) and environmental conditions **(Joachim, H. et al., 2012).** The resulting aligned or non-woven nanofibers, arranged in 2D- or 3D-fibrous structures with tuneable porosity and high specific surface area, can be placed directly onto suitable strips without further expensive refinement. Since electrospinning is a technique capable of continuously creating polymeric fibers, i.e. with no interruption during the process, it sounds appropriate for the production of huge quantities of nanofibers, then also potentially appealing to the sensor market. Electrospinning apparatus, using multiple nozzles, as well as needleless electrospinning processes, is able to increase further the production rate and to control jet formation, jet acceleration and the collection of nanostructures. Another advantage of this top-down nano-manufacturing process is the relatively low cost of the equipment and its functioning compared to that of most bottom-up methods. Zhang et al. (2010) reported an enhancement of UV light emission when ZnO (QDs) were finely dispersed in ES polyvinyl pyrrolidone (PVP) nanofibers **(Zhang, Z., et al., 2010).** ES nanofibers of polystyrene and polystyrene-co-maleic anhydride nanofibers housing a dispersion of CdSe/ZnS core/sell QDs were investigated as potential conductive sensors of VOCs by Tatavarty et al. (2011), showing peculiar sensing properties. In fact, a general increase in current was reported when increasing concentrations of solvents were flowed through the sensor, in spite of the expected decrease in current due to the polymer swelling. CdSe/ZnS were also investigated in polymers **(Tan, L. Et al., 2012; Fabregat, V. et al., 2012)** and biocompatible matrices **(Eliana, F. C. et al., 2014)** also to detect selectively NO in traces by a marked quenching effect on the fluorescence intensity. Orlova et al (2013) **(Orlova A. O. et al., 2013)** embedded QDs in in terephthalate track pore membranes (TM) with pore size of 500 nm and in a

borosilicate porous glass (BG) with pore size of 17 nm reporting an increase in the luminescent average decay time of QDs. When exposed to ammonia molecule, QDs were supposed to form a complex with NH_3 via coordination onto surface Zn ion of the QD shell states. In the present study, titania nanofibrous layers were labelled with fluorescent nanoparticles (QDs) and then investigated as potential chemical sensors, at solid state, for detecting toxic gases. Titania was selected as a suitable QDs scaffolding mainly for its photo-durability, chemical and biological stability, as well as nontoxicity, low cost, and good corrosion resistance in highly humid ambient. In addition, titanium dioxide (TiO_2) is a wide energy band-gap (*anatase*, $\sim$3.2 eV) photoactive semiconductor material that can absorb UV light. Its absorption band can be extended further into the visible region by incorporating narrow band gap dye molecules and semiconductor nanocrystals (**Shi, J., et al. 2009**). Therefore first, fluorescent (CdSe)ZnS core-shell quantum dots were synthesized, according to literature, by decomposing organometallic precursors at high temperature in a suitable coordinating solvent (**Benito-Alifonso, D., et al., 2014**) and then titania nanofibers were decorated according two strategies: drop-casting and chemical functionalization *in situ* through a bi-functional linker (containing -COOH and –SH), capable of immobilizing the nanoparticles onto titania fibers. Their different arrangements over the fibers were characterized by AFM (Atomic Force Microscopy) and HR-TEM (High-Resolution Transmission Electron Microscopy), and their optical performances were investigated by spectrophotometry and spectrofluorometry as well as fluorescence microscopy. After QDs labelling of titania, both fluorescent scaffolds were investigated as a potential low cost chemical sensor, at solid state, for detecting a few toxic gases, as NH_3 and H_2S. Relative humidity effects on PL have been also investigated.

5.2 Materials, methods and characterization

5.2.1 Chemicals

Cadmium oxide (CdO), selenium (Se), trioctylphosphine oxide (TOPO, 99%), tributylphosphine (TBP, 97%), tetradecylphosphonic acid (TDPA, 97%), Zn stearate (10/12% Zn basis), hexamethyldisilathiane, chloroform anhydrous ($\geq$ 99%), methanol (ACS reagent $\geq$ 99%), toluene anhydrous (99.8%), polyvinylpyrrolidone (PVP, MW 1,300,000), ethanol (EtOHa), glacial acetic acid (Reagent Plus $\geq$ 99%), titanium(IV)isopropoxide (TiiP) were purchased from Sigma Aldrich. They were used without any further purification.

5.2.2 Synthesis of CdSe/ZnS core/shell nanoparticles

TOPO-coated CdSe quantum dots (QDs) were prepared using CdO and Se as starting materials, according to the literature **(Benito-Alifonso, D. et al., 2014; Uyeda, H. T. et al., 2005).** Specifically cadmium oxide CdO (37 mg, 0.30 mmol) was mixed to trioctylphosphine oxide (TOPO) (3.6 g, 9.3 mmol) and then dried in vacuum at 60 °C for 30 min in presence of tetradecylphosphonic acid (TDPA) (334 mg, 1.2 mmol). Under argon the mixture (brown solution) was heated to 300 °C (colourless). At this temperature, a previously prepare solution of Se (39.5 mg, 0.50 mmol) in tributylphosphine (TBP) (5 mL), was quickly added. After 1-3 mins the reaction was quenched by rapid cooling. Finally, particles were precipitated by adding MeOH (10mL), centrifuged (5 min, 6000 rpm) and then suspended in $CHCl_3$ (10 mL). Therefore CdSe QD solution (8 mL, 0.2 mmol) was added to TOPO (3.6g, 1 mmol) and subjected to solvent evaporation under vacuum at 60 °C for 1h. The resultant solution was then heated to 180 °C under argon. A previously prepared solution of

hexamethyldisilathiane (0.05 mL, 0.2 mmol) and zinc stearate (198 mg, 0.313 mmol) in toluene (under argon, at r.t., 5 mL), was added dropwise to the CdSe QD solution and mixed at 160 °C. Then the mixture was cooled and the particles precipitated by adding MeOH (10 mL). The solution was centrifuged (5 min, 6000 rpm), the supernatant was discarded and the CdSe/ZnS QDs were dissolved in $CHCl_3$ (10 mL).

5.2.3 Electrospinning of titania nanofibers

The electrospinning equipment used in the present study was specifically assembled in the IIA-Rome (Italy) and consisted of a high voltage oscillator (100 V) driving a high voltage (ranging from 1 to 50 kV), a high power AC-DC (alternative current-direct current) converter, a syringe pump (KDS 200, KD Scientific) and a rotating conductive cylinder (~ 900 rpm) with a diameter of 45 mm. The main steps for fabricating titania nanofibres comprise *i)* the deposition of the nanofibrous layer composed of a TiO_2 precursor polymer and *ii)* the thermal treatment in order to remove polyvinylpyrrolidone (PVP) and proceed to crystallize the metal oxide (anatase). ES solution (7.877×10^{-5} M) was prepared in dry atmosphere according to literature (≤5% RH) (**Zampetti, E. et al., 2013**) mixing PVP/EtOH$_a$ into a mixture of TiiP/AcAc$_g$/EtOH$_a$, in order to obtain a 1.95 (w/w) TiiP/PVP final ratio. The syringe tip, connected to a high voltage DC power source was 11 cm away from the collector and the applied voltage was 6 kV. The substrates (quartz slices and silicon wafers) selected to collect the nanofibres were fixed, through suitable holders, to the cylinder surface (T: 26°C, 32% RH) and the deposition time was set to 10 min (170 μL/h). Tiip/PVP fibres obtained were then annealed in air using a thermal ramp from room temperature up to 450 °C (1 °C min^{-1}, 6h dwell time) in order to remove PVP and proceed to crystallize the metal oxide (*anatase*). More

information on the synthesis and preparation of nanofibers are reported in Section 7.1.1 of Chapter 7.

5.2.4 Titania nanofibers labelling with CdSe/ZnS QDs

Titania nanofibers (70-90 nm diameter size) were decorated with QDs nanoparticles by both physical and chemical functionalization. The first one required a simple dropping of the diluted starting solution (1:20 v:v, $CHCl_3$) onto the fibrous layer. The second one implied an *in situ* reaction able to bind the quantum dots to TiO_2: nanofibres of titania were dipped in 3-mercaptopropionic acid (20 ml) for 24 h, then rinsed with THF and dried under air flow. Consequently, the surface of the calcined TiO_2 nanofibres was modified by a bifunctional chemical reagent, 3-mercaptoprionic acid (3-MPA), containing both carboxylic acid (-COOH) and thiol (-SH) functional groups. Due to the affinity of titania to carboxyl group, - COOH linker was linked to the surface of TiO_2 nanofibres. Treated fibers were dipped for 24 hours into the diluted QDs solution ((1:20 v:v, $CHCl_3$) in order to be bonded with the thiol groups of linker molecules by heterogeneous exchange with TOPO.

5.3 Morphological and optical characterization of samples

Optical features of QDs were investigated in solution and at the solid state by UV-Vis spectrophotometry (Spectrophotometer UV-2600, Shimadzu, UV-Vis-NIR Mini-Spectrometer Hamamtsu) and spectrofluorometry (Fluoromax, Horiba). Optical and fluorescence microscopy (Zeiss Axio Imager 2) was used

197

to check the fluorescence of fibers after functionalization with QDs. AFM micrographs were taken in tapping mode using 190Al-G tips, 190 kHz, 48N/m (Nanosurf FlexAFM). SEM micrographs were captured at 5 kV accelerating voltage (Jeol, JSM 5200, 20keV). CTEM and HRTEM micrographs were performed at 200 keV with an analytical double tilt probe ($\alpha \pm 30°$; $\beta \pm 15°$) (ZEISS LIBRA 200FE HR-TEM). TEM specimen were prepared by i) dropping QDs solutions and ii) gently scraping the QD-TiO$_2$ nanofibrous layer from the silicon support and then collecting the nanofibres through adhesion upon contact with holy carbon thin film. Nanostructures were measured by means of iTEM (TEM Imaging Platform software by Olympus). The hybrid nanofibers were photographed by a very compact and suitably designed system. It comprised a digital camera (Raspicam) to capture images, a lens system for sample focusing, a processing and data storage unit (Raspberry v.2) capable to provide a high-resolution (5 Mpx) image. The optical tool was able to hold the quartz slice coated with the fibrous layer (the upper side) and to focus a small area of fibers by an embedded lens system. Raspberry was used to interface the camera and to store the elaborated RGB image into a Portable Network Graphics (png) format. The sample was irradiated by a low power led (UV-light: 390 nm; 5 mW). The luminance (PL) of the samples, was measured through a developed software (by using Python) able to: *i)* crop the captured image to get a 400x520 pixels picture (a 8 bit color depth, 1 pixel = 34 nm, 1 pixel area= 1.156×10^{-3} μm^2); *ii)* select only the green array (related to the color of QDs photoemission) from RGB and *iii)* calculate the average value corresponding to color intensity and luminance ratio (IGreen).

5.4 Results and discussion

Optical performances of QDs nanoparticles were investigated by spectrophotometry and spectrofluorometry as well as fluorescence microscopy. UV-Vis (blu curve) and Photoluminescence analysis (red curve) of CdSe/ZnS core-shell QDs show absorption spectrum λ 536 nm-int 1.09 a.u and emission spectrum λ 560 nm-int 384 a.u, respectively. Furthermore, as showed in the *inset* the solution of QDs excited at 360 nm, it appears green **(Figure 5.1).**
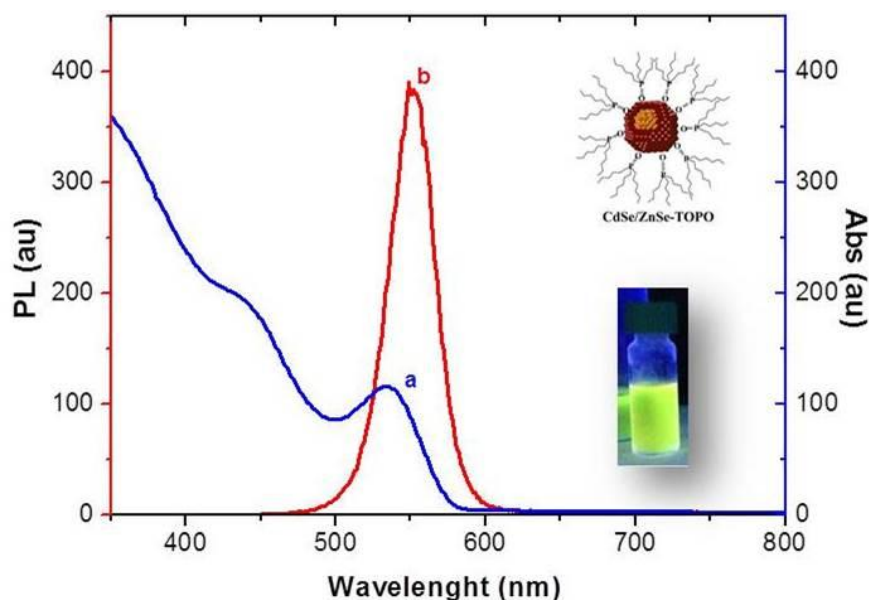

Figure 5.1: Spectra of CdSe/ZnS core-shell QDs when excited at 360 nm. The blue curve (a) is the absorption spectrum, and the red curve (b) is the emission spectrum. Both physical structure and an image of the solution when UV-light irradiated, are shown in the *inset*
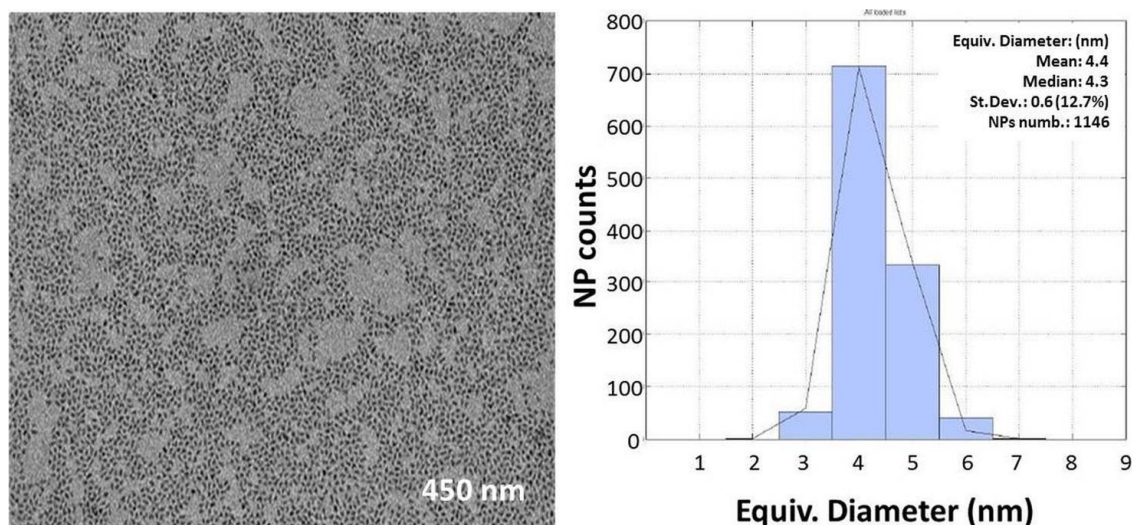
Figure 5.2: HR-TEM image of CdSe/ZnS QDs sample (*left*) and fitting of the statistical distribution of NPs diameters (*right*).

The morphological characteristics of CdSe/ZnS QDs sample were studied by mean of the techniques HR-TEM (High-Resolution Transmission Electron Microscopy). The study conducted by electron microscopy showed the presence of nanoparticles of regular shape and spherical. The mean diameter was measured by estimating 1140 nanoparticles exploiting the Pebbles program, and the statistics were calculated using the program Pebble_Juggler, both proprietors of ISTM available link http://pebbles.istm.cnr.it/. The nanoparticles contained in the sample have a mean diameter of 4.4 +/- 0.6 nm **(Figure 5.2).** The dispersion is equal to 12.7% which can be considered quite good considering the small size of the sample. Nanoparticles cannot be considered highly monodisperse (dispersion <5%).
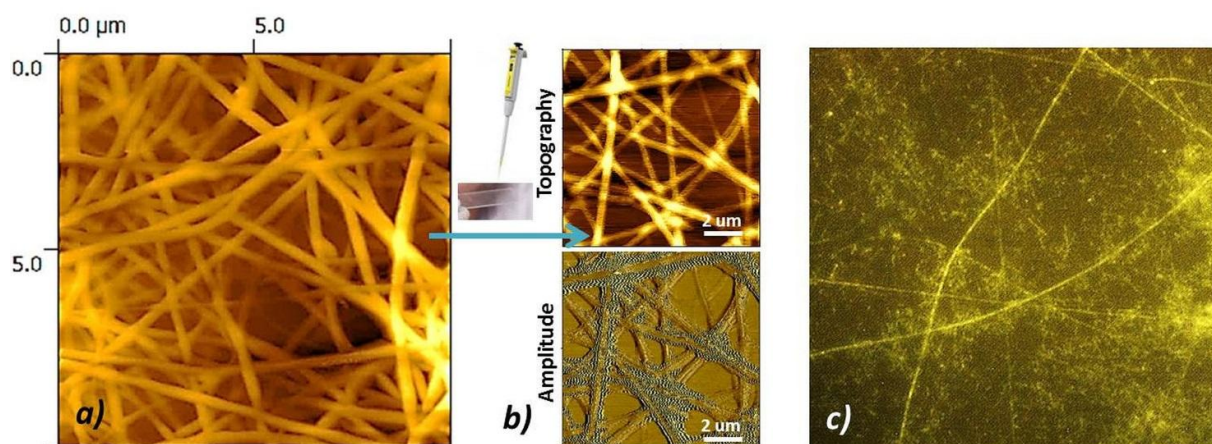
Figure 5.3: AFM micrograph of titania fibers before (a) and after QDs decoration by drop coating (b); fluorescence optical microscope picture of QDs/TiO$_2$ (c).

The first strategy adopted to decorate the titania nanofibers with QDs nanoparticles was the functionalization of the fibers by drop coating. Comparing the AFM image (a) (titania fibers without QDs nanoparticles) with the image (b) (titania fibers decorated with QDs nanoparticles by drop coating), it is evident that on the nanofibers functionalized with the nanoparticles you have the formation of agglomerates of fluorescent nanoparticles next to the fibres but also on the fibers. Furthermore AFM image (a) shows that the nanofibers of titania looked almost smooth, while after QDs decoration (image b) they appeared more rough and wrinkled respect to pristine nanofibers TiO$_2$. An additional strategy of functionalization has been adopted in the attempt to create a more ordered and reproducible fibers decoration. Firstly, the surface of nanofibers was modified with a bi-functional chemical reagent, 3-mercaptopropionic acid (3-MPA), subsequently it was decorated by CdSe/ZnS core-shell QDs **(Figure 5.4).** In particular, since TiO$_2$ has a strong affinity for the carboxylate group of the linker molecules, a bifunctional monolayer of 3-mercaptopropionic acid (3-MPA) was adsorbed on the surface of TiO$_2$ nanofibers by dipping. CdSe/ZnS quantum dot nanoparticles could be bonded with the thiol groups of linker molecules, infact they bind ZnS-shell QDs, replacing the TOPO present on its surface. As

shown from the image of fluorescence microscopy **(Figure 5.4b),** using this strategy, the nanoparticles appear evenly distributed on the fibers and without aggregation.
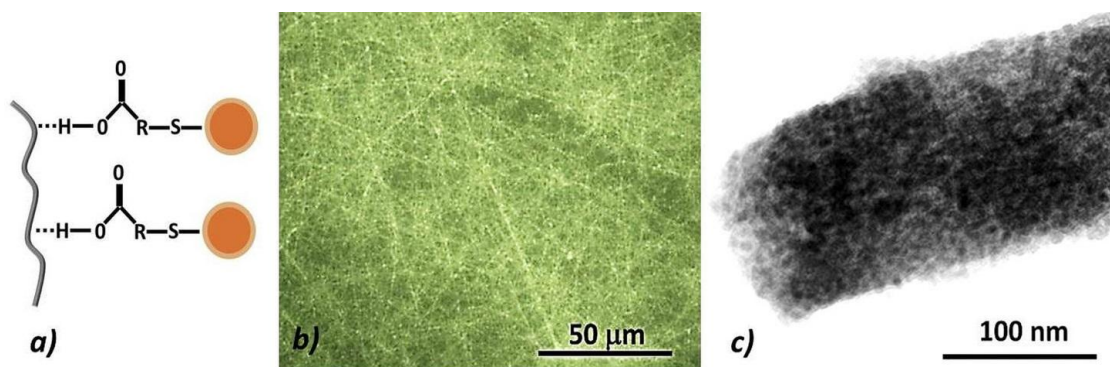

Figure 5.4: A bi-functional linker (containing -COOH and –SH), capable of immobilizing the QDs nanoparticles onto titania fibers (a, scheme); TiO₂ nanofibers after QDs functionalization by chemical functionalization *in situ* through a bi-functional linker investigated by Fluorescence Microscopy (b); TEM micrograph of a titania nanofiber finely decorated with QDs nanocrystals(c).
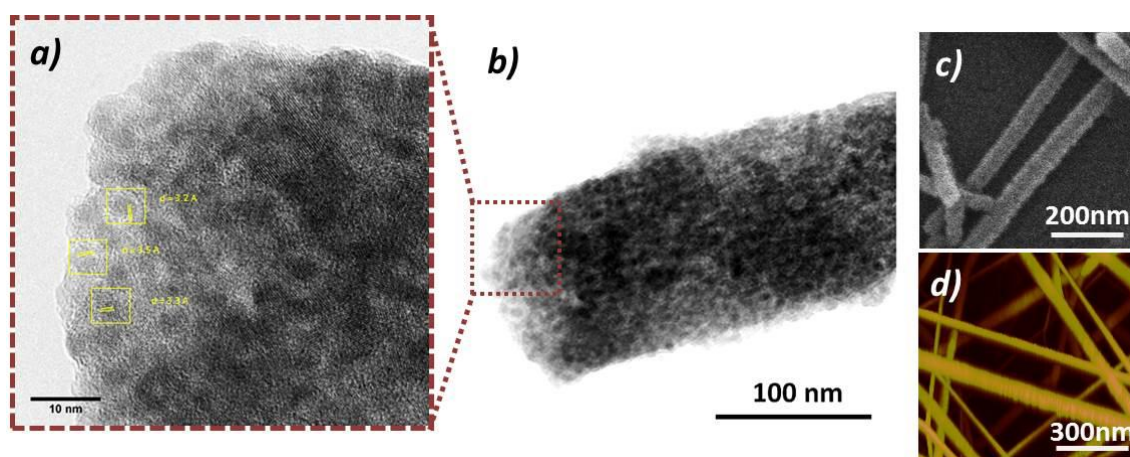
Figure 5.5:HR-TEM of a titania nanofiber finely labelled with QDs nanocrystals with different magnification: a) Measure of the distance the planes of nanocrystals CdSe/ZnS labelling a fiber: the distance 3.17 A corresponds to the plane {101} CdSe while the distance 3:32 A corresponds to the plane {100} of ZnS (a-b); SEM (c) and AFM (d) micrographs of nanofibers chemically labelled by QDs(c) depicting a slight increase in roughness.

HR-TEM analysis has allowed to identify carefully the location of the QD, confirming their monocrystalline nature **(Figure 5.5).** The measurement of some interplanar distances has confirmed the distances compatible with CdSe: 3.3 A corresponds to the interplanar distance {101} of CdSe and {110} of ZnS; 3.5 A corresponds to the {002} interplanar distance of CdSe. A further confirmation of the presence of both the compounds was obtained by analytical micro analysis (EDX). The EDX maps (**Figure 5.6 and 5.7**) show that the elements that make up the QDs are uniformly distributed on the TiO_2 fiber. Particularly in **Figure 5.7** maps you can see that Zn is less dense than Cd but it highlights the co-presence and co-location of the two elements, confirming the expected results from the synthesis.
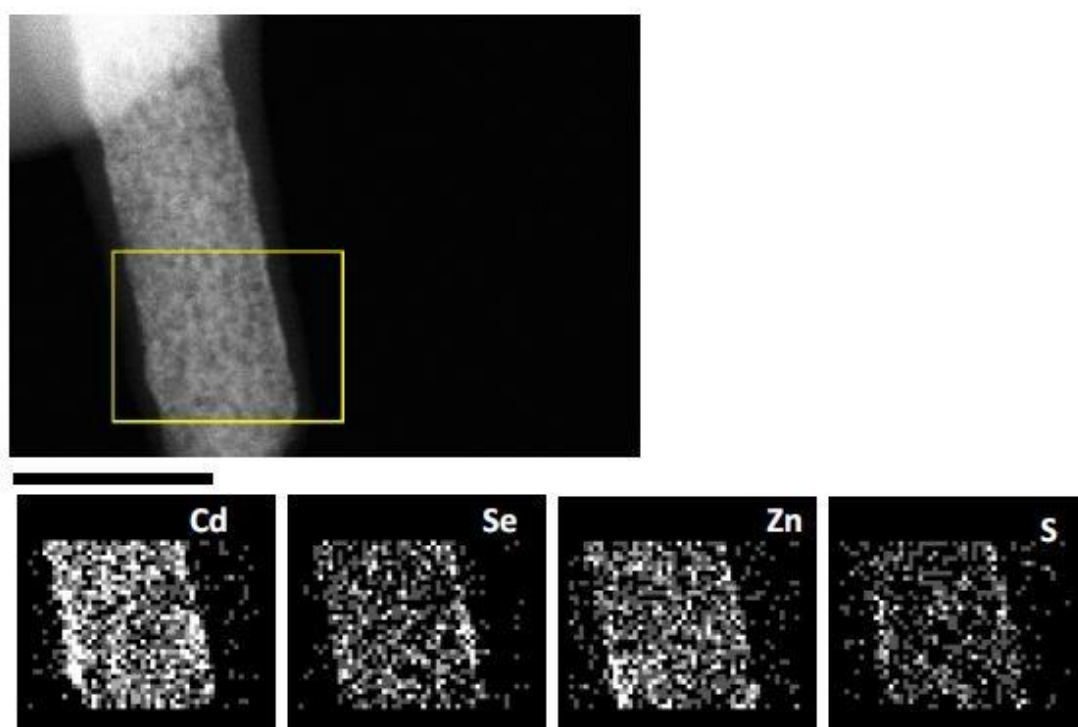
Figure 5.6: On the top is reported the STEM image of the TiO_2 nanorod decorated with QDs. The maps are the elemental maps of the following elements: Cd, Se, Zn and S respectively. The bar corresponds to 100nm
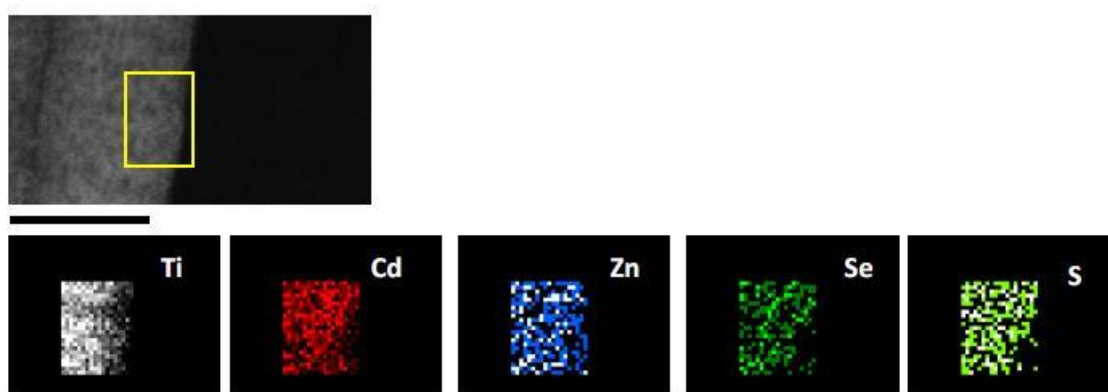
Figure 5.7: On top is reported the STEM image of the TiO₂ nanorods decorated with QDs. The yellow square highlights the area of which the EDX maps were collected. On the bottom the EDX maps of the following elements are reported: Ti white, Cd red, Zn blu, Se in green and S in light green. The bar corresponds to 100nm.

The relative quantification of the elements, except for P and Ti, reported the following results:

Element	Atomic%	sigma
S K	16.3	3.9
Zn K	15.8	3.2
Se L	21.0	3.6
Cd L	46.9	4.1

It should be emphasized that the atomic percentage of Se is half of that of the Cd while the ratio between Zn and S is stoichiometric. Also it is confirmed that the Cd is the percentage element more present.
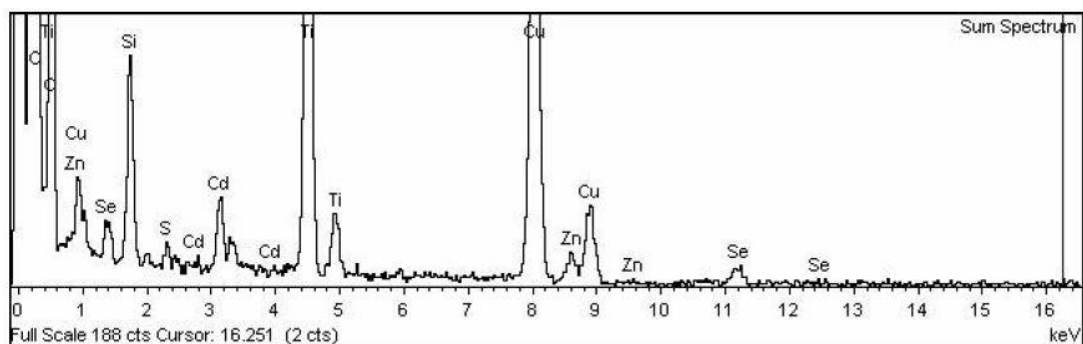
Figure 5.8: Spectrum EDX

The relative proportions of the elements of quantum dots (mother solution) is equal to:

	Atomic% value	sigma
SK	17.8	1.8
ZnK	7.5	1.9
SeL	27.5	2.0
CdL	47.2	2.1

From this analysis is observed a lower percentage of Zn that could be attributed to partial inhomogeneities of sample. This inhomogeneities could be attributed to a different degree of overlap of the CdSe core given the difficult process control. The core of CdSe maintains a ratio of Cd and Se comparable to that measured on the fibers.

After QDs labelling of titania, the hybrid nanofibers were investigated as a potential low cost chemical sensor, at solid state, for detecting a few toxic gases, as H_2S and NH_3. First of althea effect of relative humidity on luminance (PL) of sample was evaluated. Therefore, after exposition of the QDs-dropped sample in dry air, it was exposed to a low power led (UV-light: 390 nm; 5 mW) after increasing percentages of relative humidity. In **Figure 5.9** the absorbance and photoemission spectra of fibers decorated at solid state and placed on a quartz slice have been depicted. The inset photograph shows the green color emission (visualized by naked eye too) of labelled nanofibers by dropping. The system was not so sensitive to reveal also fibers chemically nanofunctionalized: a more sensitive and sophisticated device should be designed. Thus, the following measurements will concern only fibers physically decorated by drop.
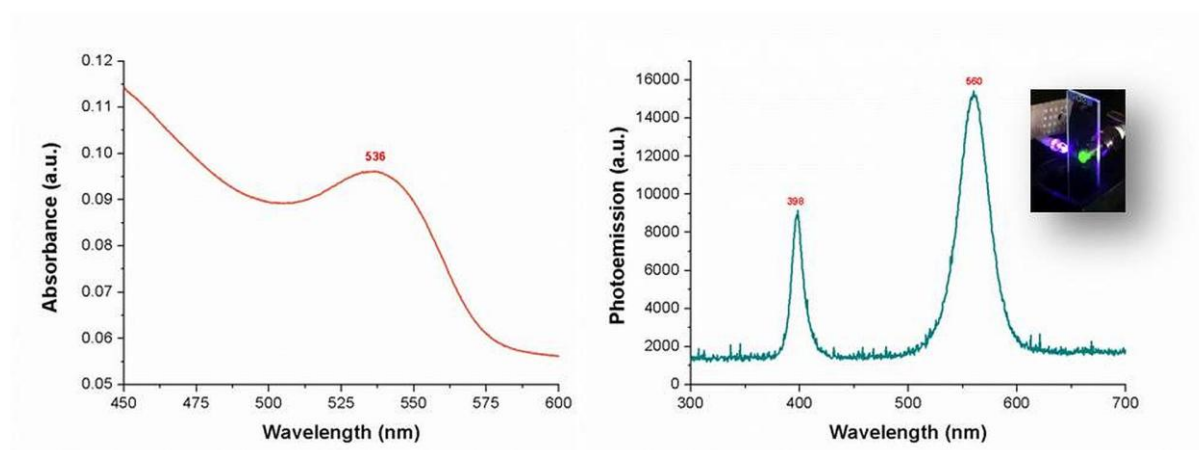
Figure 5.9: Spectra of absorbance (*left*) and Photoemission (*right*) of hybrid nanofibers TiO₂-CdSe/ZnS core-shell QDs when irradiated by a low power led (UV-light: 390 nm; 5 mW).

The hybrid nanofibers were photographed by a very compact and suitably designed system and the image was captured by a digital camera (Raspicam), contained within it, capable to provide a high-resolution (5 Mpx) image **(Figure 5.10).**The optical tool was able to hold the quartz slice coated with the fibrous layer (the upper side) and to focus a small area of fibers by an embedded lens system. Raspberry was used to interface the camera and to store the elaborated RGB image into a Portable Network Graphics (png) format. The luminance (PL) of the samples, was measured through a developed software (by using Python) as previously described.
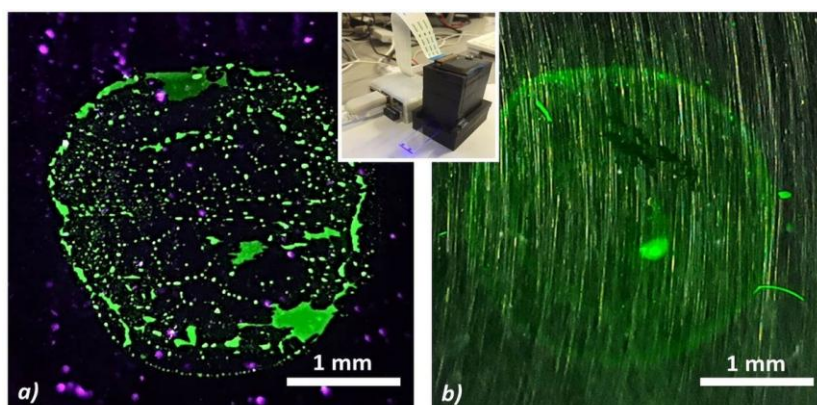
Figure 5.10: Images of QDs nanoparticles depositated directly on a quartz substrate (a) and on a quartz substrate coated of titania fibers (b).

A 2μl drop of a diluted 1:20 $CHCl_3$ solution on a clean quartz slice, shows the formation of islands with different size and shape of the nanocrystals. When the same drop was deposited on a porous layer of titania nanofibers, QDs appeared distributed along the alignment of the fibers, offering a more ordered and controllable layout. Figure 5.10, a camera picture, shows the TiO_2 fibers aligned over the quartz slice, despite the fibers observed with optical, electronic and atomic force microscopes **(Figure. 5.3).** The reason may be due to both the different substrate used to collect the fibrous mats (insulating and conducting, respectively) that can be responsible of the arrangement of fibres and to the different magnification of the images (i.e. higher when microscopy was used). In fact, when the quarts samples were investigated with microscopy, a net of fibres among the aligned ones was noticed (data not shown). The results reported in the graph **(Figure 5.11)** showed that to increasing percentage of relative humidity (20%-50%-100%) the PL of the sample increases up to about 13%. PL effect observed is confirmed by literature and shows that QDs luminance is highly dependent on the environmental humidity levels **(Pechstedt, K. et al., 2010).** In fact, under oxygen, photoluminescence features depicted the evidence of a water-molecule-stabilized state (H_2O-QD) that seemed to facilitate luminescence processes. This enhancement could be further facilitated fibers, capable of adsorbing/entrapping water molecules thus increasing the PL values according to the levels of environmental moisture percentages.
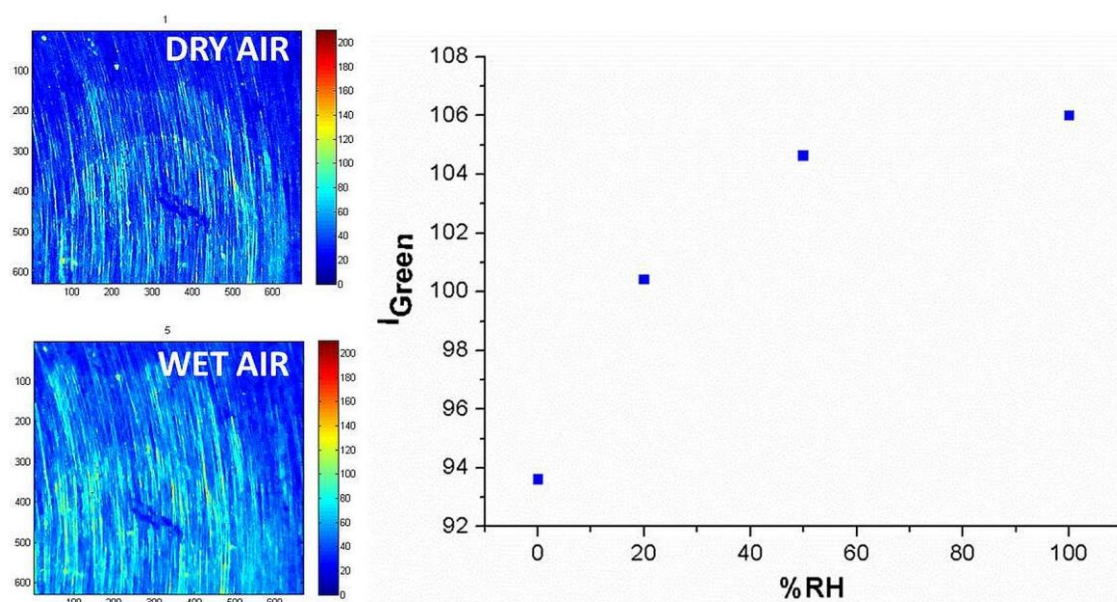
Figure 5.11: Relative humidity effects on PL of sample (image analysis, *on the left* **and Luminance variation towards %RH plot,** *on the right***).**

Subsequently, the hybrid nanofibers were investigated as a potential chemical sensor, for detecting H_2S and NH_3. It was evaluated as varies the PL of the sample after exposure to increasing concentrations of H_2S. The results reported in **Figure 5.12** show that to increasing concentration of the gas, 10 ppm-20ppm-40ppm respectively, the PL of the sample decreases (about up to 19%). This change of PL is supposed to be related to the type of interactions that occur on the shell between the hydrogen sulfide and ZnS (photoelectron traps).
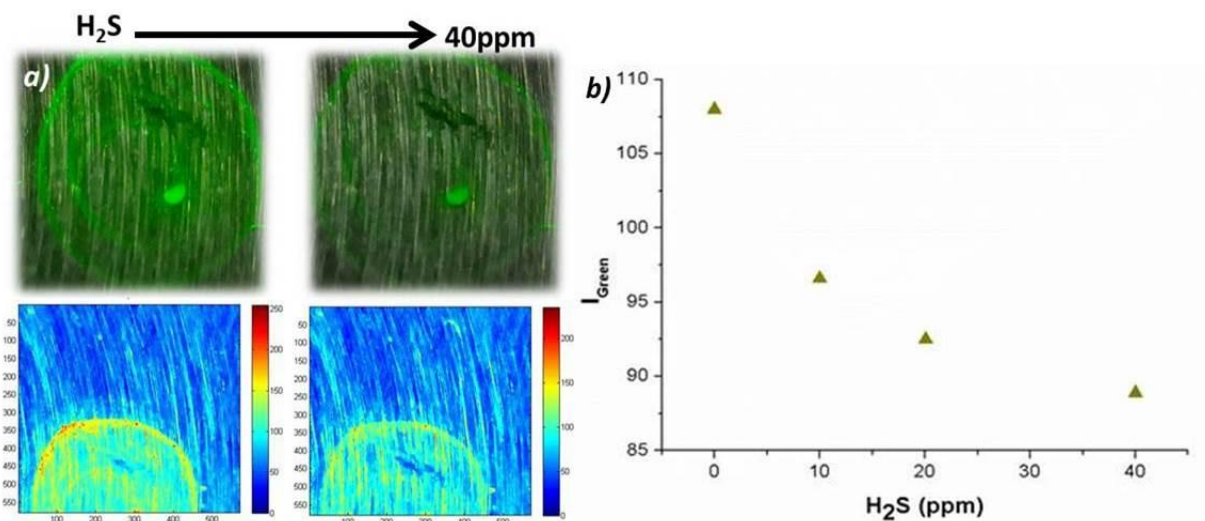
Figure 5.12: Photographs and images (green matrices) before and after H₂S exposure (a); PL sample decreasing toward increasing concentration of gas (b).

Similarly, exposing the sample to 10 ppm NH_3 for 20' the luminance of the sample decreaseed (luminance in dry air: 161 900; luminance after exposition to NH_3: 57643) **(Figure 5.13).** In addition, the graph shown in **Figure 5.14** confirms that the average of nanofiber's luminance functionalized with QDs, decreaseed upon increased exposure times (40-80-120 minutes) to H_2S and NH_3. However, the luminance of fibers exposed to NH_3 was decreased of ~30% respect to that of the fibers exposed to H_2S.
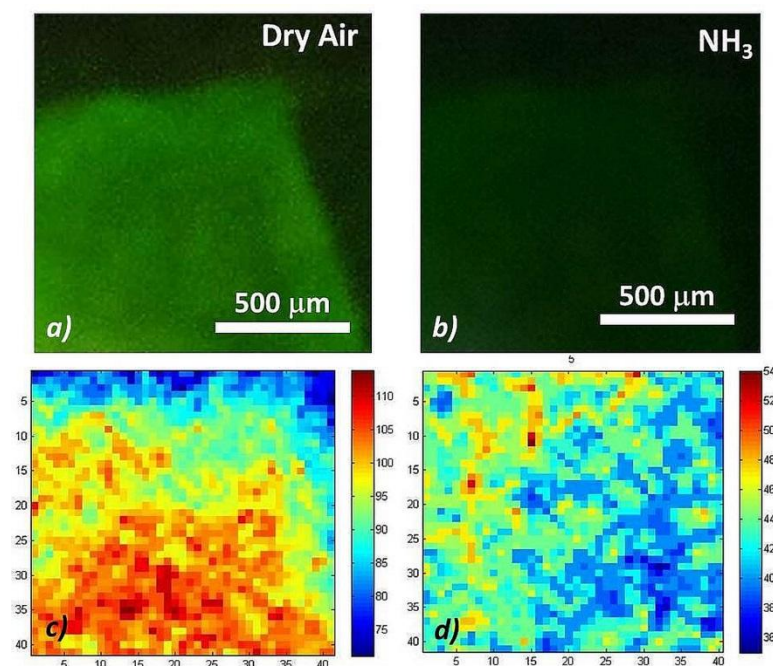
Figure 5.13:Photograph of fibers coated with QDs and UV-LED irradiated before (a) and after 10 ppm NH3 exposure for 20 min (b) ; image analysis of the GREEN matrix of pixels (among RGB matrices)before (c) and after gas exposure (d).
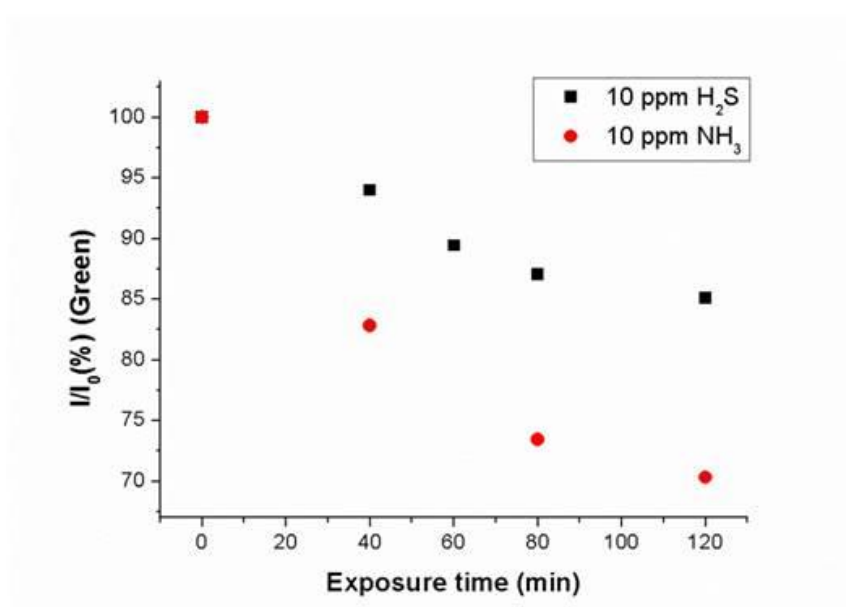

Figure 5.14: The NH$_3$ and H$_2$S exposure over time (40-80-120 minutes) of hybrid nanofibers, confirms the reduction the average of nanofiber's luminance. The luminance of fibers exposed to NH$_3$ was decreased of ~30% respect to that of the fibers exposed to H$_2$S (~19%).

210

The mechanism leading to luminescence quenching of QDs and the reduction in PL decay time is not completely clarified at present. Nonradioactive resonant energy transfer or electron transfer are considered to be the main mechanisms responsible for QD photoluminescence quenching via interaction with organic molecules (**Ji, X. et al., 2008**). In our case, however, nonradiative resonant energy transfer from QDs to ammonia molecules cannot occur due to the absence of appropriate electronic transitions in the ammonia molecule in the spectral region of interest. Electron transfer should be also improbable for a QD/ammonia pair due to the absence of a π-electron system. Also, the low energy of the Highest energy Occupied Molecular Orbital (HOMO) of -10.5 eV of ammonia makes electron transfer unlikely. QD PL quenching may originate from a long-range electronic-to-vibrational energy transfer (**Aharoni, A. et al., 2008**) from the QD to the NH-vibration of the ammonia molecule. Another possible reason for nonradiative photoexcitation energy losses is the appearance of new local sites on the QD surface at the coordination points of the ammonia molecules, which may act as photoelectron traps. This mechanism is supposed in literature (**Zenkevich, E. et al., 2009**).

References

Aharoni A., Oron D., Banin U., Rabani E., Jortner J. Long-Range Electronic-to Vibrational Energy Transfer from Nanocrystals to Their Surrounding Matrix Environment. Physical Review Letters (2008), Vol. 100, pp. 057404

Benito-Alifonso D., Tremel S., Hou B., Lockyear H., Mantell J., Fermin D. J., Verkade P., Berry M., Galan M. C. Lactose as a "trojan horse" for quantum dot cell transport. Angewandte Chemie International Edition (2014), Vol. 53, pp. 810-814

Camposeo A., Di Benedetto F., Stabile R., Pisignano D. Electrospun dye doped polymer fibers emitting in the near infrared. Appl Phys Lett (2007), Vol. 90, pp.

Chen Y., Rosenzweig Z. "Luminescent CdS Quantum Dots as Selective Ion Probes". Anal Chem (2002), Vol. 74(19), pp. 5132-5138

Eliana F. C. Simões & João M. M. Leitão & Joaquim C. G. Esteves da Silva, NO Fluorescence Quantification by Chitosan CdSe Quantum Dots Nanocomposites. J Fluoresc (2014), Vol. 24, pp. 639-648

Fabregat V., Izquierdo M. A., Burguete M. I., Galindo F., Luis S. V. Quantum dot–polymethacrylate composites for the analysis of NOx by fluorescence spectroscopy. Inorg Chim Acta (2012), Vol. 381, pp. 212-217

Gao X. F., Li H. B., Sun W. T., Peng L. M. Cd/Te Quantum Dots-Sensitized TiO$_2$ nanotube array photoelectrodes J Phys Chem C (2009), Vol. 113 (18), pp. 7531-7535

Ji X., Copenhaver D., Sichmeller C., Peng X. Ligand Bonding and Dynamics on Colloidal Nanocrystals at Room Temperature: The Case of Alkylamines on CdSe Nanocrystals. Journal of the American Chemical Society (2008), Vol. 130, pp. 5726-5735

Joachim H. Wendorff S. A., Greiner A. Electrospinning: Materials, Processing, and Applications. Wiley-VCH (2012), pp. 254, ISBN: 978-3-527-32080-6

Macagnano A., Zampetti, E., Kny E. Electrospinning for high performance sensors, in Series Nanoscience and Technology, Springer International Publishing (2015), pp. 1-329

Morello G., Polini A., Girardo S., Camposeo A., Pisignano D. Enhanced emission efficiency in electrospun polyfluorene copolymer fibers. Appl Phys Lett (2013), Vol. 102, pp. 211911

Orlova A. O., Gromova Y. A., Maslov V. G., Andreeva O. V., Baranov A. V., Fedorov A. V., Prudnikau A. V., Artemyey M. V., Berwick K. Reversible Photoluminescence quencing of CdSe/ZnS quantum dots embedded in porous glass by ammonia vapor. Nanotechnology (2013), Vol. 24 (33), pp. 335701

Pechstedt K., Whittle T., Baumberg J., Melvin T. Photoluminescence of Colloidal CdSe/ZnS Quantum Dots: The Critical Effect of Water Molecules. J Phys Chem C (2010), Vol. 28, pp. 12069-12077

Shi J., Chen J., Feng Z., Chen T., Lian Y., Wang X., Li C. Photoluminescence Characteristics of TiO_2 and Theyr Relationship to Photoassisted Reaction of Water/Methanol Mixture J Phys Chem C (2007), Vol. 111(2), pp. 693-699

Tan L., Wan A., Li H., Zhang H., Lu Q. Biocompatible quantum dots-chitosan nanocomposites for fluorescence detection of nitric oxide. Mater Chem Phys (2012), Vol.134, pp. 562-566

Uyeda H. T., Medintz I. L., Jaiswal J. K., Simon S. M., Mattoussi H. Synthesis of Compact Multidentate Ligands to Prepare Stable Hydrophilic Quantum Dot Fluorophores. J Am Chem Soc (2005), Vol. 127 (11), pp 3870-3878

Vossmeyer T, Katsikas L., Gienig M., Popovic I. G., Diesner K., Chemseddinne A., Eychmiiler A., Weller H. CdS nanoclusters: synthesis, characterization, size dependent oscillator strength, temperature shift of the excitonic transition energy, and reversible absorbance shift. J Phys Chem (1994), Vol. 98, pp. 7665-7673

Wang, X., Drew C., Lee S. H., Senecal K. J., Kumar J., Samuelson L. A. Electrospun nanofibrous membranes for highly sensitive optical sensors. Nano Lett (2002), Vol. 2, pp. 1273-1275

Zampetti E., Pantalei S., Muzyczuk A., Bearzotti A., De Cesare F., Spinella C., Macagnano A. A high sensitive NO_2 gas sensor based on PEDOT-PSS/TIO_2 nanofibres. Sensors and Actuators B (2013), Vol. 176, pp. 390-398

Zhang Z., Shao C., Gao F., Li X., Liu Y. Enhanced ultraviolet emission from highly dispersed ZnO quantum dots embedded in poly(vinyl pyrrolidone) electrospun nanofibers, Journal of Colloid and Interface Science (2010), Vol. 347 pp. 215-220

Zenkevich E., Blaudeck T., Heidernätsch M., Cichos F., Von Borczyskowski C. Effects of electron tunneling and non resonance quenching of photoluminescence in semiconducting CdSe/ZnS and CdSe nanocrystals by porphyrin molecules in joint complexes. Theoretical and Experimental Chemistry (2009), Vol. 45, pp. 23-34

Introduction

The monitoring of contaminants in environments is of utmost significance, because, as a consequence of industrialization and urbanization processes, and the employment of modern agricultural practices, gaseous and liquid pollutants are ubiquitous throughout the world and accumulate in ecosystems, thus generating great concerns and warnings for their relationships with human health diseases (**Nadadur, S. S. et al., 2015**). Smart devices integrated into the everyday surroundings capable of providing qualitative and quantitative information about pollutants, are increasingly becoming significant for each individual as well as for policy makers to protect populations from pollution exposure. From smartphone embedded sensors to those you wear or plug in wherever you are, this new wave of personal environmental sensors has the potential to really change the way data are gathered, analyzed and used. Alike, the abnormal production of electronic and smart sensing devices begins to represent a significant additional source of pollution to the environment. Although compared to the global production and consumption of plastics in the world, the electronics market (dis-plays, transistors, microelectronic interfaces, cables, cases, etc.) contributes only a small amount of waste, its contribution should not be neglected (**Irimia-Vladu, M. et al., 2012**). For example, recently in literature, a demonstration of high performance monitoring systems fabricated on a sacrificial PVA substrate has been reported by John Rogers's group, which developed a collection of multifunctional sensors for physiological measurement (i.e. temperature, strain and electrophysiological) on the surface of a thin PDMS foil on top of a sacrificial water soluble PVA sheet, which served as a temporary support for the transport and mounting of the device onto the skin, as a tattoo (**Irimia-Vladu, M., 2014; Kim, D. H. et al., 2011**). The sensing system adhering to the skin was working until the beginning of the

degradation determined by perspiration and cell regeneration. Since commonly gas and volatile organic compounds (VOCs) sensors consist of a transducer with an interacting chemical layer (the recognition element), if biodegradable circuits could be printed on sheets of silicon so thin that they dissolve in water (from a couple days to a week of submersion), or on natural biodegradable resins, the sensing layer might be degraded, too, thus preventing its persistence in the environment for generations (plastics normally biodegrade very slowly, with full degradation occurring after 500 or 1000 years) **(Kim, D. H. et al., 2011; Singh, B. et al., 2008).** Specifically among the several potential applications of biodegradable sensors, the monitoring of environmental conditions after ecological disasters, such as oil spills, would result extremely suitable and environmentally friendly if small sensors might be dispersed over a wide area without further contributing to pollution. Similarly, they might be used in sustainable agriculture by monitoring nutrients (like nitrogen, phosphorus and potassium) and water in soil to adapt fertilizers and water managements to crop demands, in order to increase agricultural productivity and maximize farm profitability, while minimizing environmental damages. In medicine, implantable sensors would have a wide variety of medical uses, such as tracking blood sugar levels in diabetes patients. Additional to the operation to implant such small devices, which is a non-invasive process, the elimination of the sensors removal process might be very attractive for both patients (who will feel safer, at least because not undergoing another operation), researchers and investors. This study focuses on creating and investigating an environmentally friendly conductive sensor for gases and VOCs based on conductive and biodegradable electrospun nanofibres. To achieve this goal, nanofibrous layers at various concentrations of polyaniline (PANi) hosted in a biodegradable polymer of poly-3-hydroxybutyrate (PHB) have been tested. To our knowledge, PANi/PHB nanofibres have never been tested in sensing application, until now. Therefore, electrical parameters of conductive sensors based on

nanofibrous layers of PHB hosting increasing concentrations of PANi have been investigated for one year. Fibres have been assembled as highly porous membranes by electrospinning technology **(Macagnano, A., 2015)** directly on the transducers. More recently, biocompatibility and toxicity of polyaniline salt and base in environment have been investigated and measured in several studies **(Humpolicek, P. et al., 2012; EYslas, E. I. et al., 2012),**

Chapter 6

Study and design of a potential biodegradable chemical sensor to measure gas and volatile organic compounds (VOCs) in moistened environments

6.1 Properties of materials selected and used: PANi, PHB and IDEs

Although biodegradability is a remarkable feature to have environmentally and health friendly sensing tools, sensors for gas monitoring should be able to preserve their sensing feature for a period of time, despite short, and have reasonable operative shelf life, relative to the specific application and the period to monitor, and should not be then water soluble. Additionally, the sensing material should not be strongly affected or corrupted by environmental parameters, such as temperature and moisture. Among these materials, the most used for gas sensing are expected to be semiconductors organics, that are inexpensive and their electrical measurements, occurring at room temperature, require simple DC. They can respond to a wide range of polar and non polar gases and vapors depending on various interaction mechanisms. For instance, the analyte can affect the charge transfer between the sensing layer and the electrode contact or change the density of charge carriers (due to oxidizing or reducing reactions), or change the carrier mobility thus affecting the resistivity of the film. In the present study, biodegradable electrospun nanofibrous scaffold based on a polymer blend containing polyaniline and poly-3-hydroxybutirrate (PANi/PHB) has been designed. Polyaniline is a biocompatible polymer and its toxicity is strictly related to its concentration

219

($\geq$400 mg $^{L-1}$). PANi is the most fascinating molecule among CPs for chemical sensing because it is environmentally stable, easily synthesized, and can react with chemical species at room temperature **(Virji, S. et al., 2004).** Its sensing features can be easily tuned for specific applications by modulating the doping process and the hosting polymers, which are mainly responsible for the conductivity and gas/VOCs surface adsorption and diffusion of the resulting material, respectively. PANi becomes an electrically conductive material when the emeraldine oxidation state is doped with an acid that protonates the iminic nitrogen on the polymer backbone. Doping and undoping processes are the key actions in the sensing mechanism of the polymer. Polyaniline is extremely sensitive to ammonia: the interaction with ammonia, causes a dedoping effect through deprotonation. The transfer of protons from PANi-NH-groups to NH_3 molecules forms ammonium ions and reverts PANi to its base, the less conductive form. On the contrary, acidic gases such as HCl, H_2S, and CO_2, in the presence of water, dope it through protonation, thus increasing PANi conductivity. All these processes are expected to be reversible **(Bai, H. et al., 2007).** Nanofibres of PANi blended with several polymer carriers have been investigated **(Laurencin, C. T. et al., 1999; Wang, X. et al., 2002)** for a multitude of applications (healthcare, filtration, biotechnology, energy generation, etc.), thus suggesting their commercial potentiality **(Ramakrishna, S. et al., 2009).** In these studies, the porous nature of these films, which enabled gas molecules to molecules to diffuse in and out of the fibres quickly shortening the doping and dedoping processes. As a consequence, the increased performances of PANi-NF films in both sensitivity and response time, relative to their conventional bulk counterpart, were due to higher effective surface area and shorter penetration depth for target molecules. Electrospun fibers of silk coated by polyaniline were investigated also as suitable sensing material for electrochemical sensors in liquid, capable to detect an electrolyte (i.e. methane-sulfonic acid) in solution **(Ismail, Y. A. et al., 2014).** Electrospinning was utilized too to synthesize a polyaniline

(PANI)/poly(-caprolactone) (PCL) blend in the form of nanofibres in order to examine its gas sensing performance to water vapor, NH_3, and NO_2 **(Low, K. et al., 2014),** where the sensitivities to analytes were modified changing the acid doping. In the present study, PHB has been selected, as biodegradable polymers, because it is water insoluble and relatively resistant to hydrolytic degradation: these features differentiate PHB from most other currently available biodegradable plastics, which are either water soluble ormoisture sensitive, i.e. mostly useless in sensing applications. Additionally, PHB is known to be permeable to oxygen, to be UV and thermal resistant, to have noteworthy tensile strength (40 Mpa), to be biocompatible and non toxic. Such features make this material as a promising candidate for biodegradable sensors. PHB is a polyhydroxyalkanoate produced by microorganisms (Ralstonia euthrophus, Bacillus megaterium, Methyl bacterium rhodesianum), apparently in response to conditions of physiological stress, such as limited nutrition **(Ackermann, J. et al., 1995).** Commonly, this polymer is used in medicine for its biocompatibility (surgery and surgical implants, blood vessels) as well as in pharmacy (microcapsules, tablets packaging), because also its biodegradation products are non-toxic. It may be functionalized on purpose or mixed with suitable chemical compounds to make it chemically attractive as a sensor. In literature, nanofibers of biodegradable poly(3-hydroxybutyrate) blends having 8–55% acid-doped polyaniline (70-100 nm in diameter) have been prepared and their biodegradability investigated **(Araujo, P. L. B. et al., 2011).** The most common electrodes used for manufacturing conductometric sensors are interdigitated electrodes (IDEs) that are implemented over insulating and flat substrates (like alumina, silicon diox-ide wafers, etc.) in various geometrical layout (one or several pair of electrodes) using photolithography and metal deposition techniques. A constant potential is applied and the output signal strength of IDEs is controlled by the design of the active area, width and spacing of the electrode fingers. The resistance value depends on both the quantity and quality of the texture covering the

electrodes, such as fiber density, shape and dimension of fibres (individual resistance value) assembled over the electrodes (aligned, nonwoven, etc.). The potentials of such blended polymers have been exploited, focusing the attention on the influence of humidity on the features of the resulting sensors, also in terms of reproducibility and stability of their responses. Indeed the presence of water vapor, functioning as interference gas, was expected to lower the gas response of the sensor in a humid atmosphere **(Matsuguchi, M. et al., 2003).** Effects of humidity on conductive nanofibres based on acid-doped polyaniline blends were previously investigated by Zampetti et al. **(Zampetti, E. et al., 2011)** and the variations in conductivity values were attributed to both the percentage of CSA-doped PANI in blends, the diverse arrangement of PANI within fibres, the kind of the electrospun polymer, the fibres size, morphologies and finally to the final texture. Briefly, in the present study, the responses of these PANi/PHB sensors to ammonia in trace were measured in dry air and at different percentages of relative humidity, in order to evaluate the role of PHB in the interactions of PANi with the gas in actual applications. Similarly, the effects of distinct moisture conditions on the responses and sensing features of PANi/PHB sensors to both acidic and basic VOCs (i.e. acetic acid and triethylamine, respectively) were investigated.

6.2 Materials, methods and characterization

6.2.1 Materials

Polyaniline emeraldine base (PANiEb, 10,000 MW), 10-camphorsulfonic acid (CSA), poly[(R)-3-hydroxybutyric acid, PHB] and 2,2,2-trifluoroethanol (TFE) were all purchased from Sigma-Aldrich and used without further purification.

6.2.2 Methods

A milky PHB solution (PHB$_{sol}$) was prepared solving 5% (w/w) polymer in TFE under magnetic stirring at 60∘C (≥72 h). A conductive solution of PANiEb, specifically doped with CSA (300:200 mg PANiEb: CSA or PANi) and dissolved in TFE (20 ml) under magnetic stirring at room temperature (≥24 h) was also prepared. The resulting deep-green solution was filtered through 1 μm pore size PTFE membrane filter (Millipore) to get a more homogeneous solution (PANi$_{sol}$). Filtering membranes were then dried and weighed, and their contribution in terms of the only PANi weight was subtracted to the initial PANi amount (the kept PANi resulted less than 2%). Six polymer blend solutions were prepared by mixing increasing volumes of PANi$_{sol}$ (hundreds microliters) into a fixed volume of PHB$_{sol}$ (1 ml, ~24 h), in order to obtain PANiEb: PHB mass ratios (w/w) of 1.4%, 2.7%, 4%, 5.45%, 8% and 11%, which were named as the first six letters of the alphabet (A-F), respectively. The transducers used to convert the physico-chemical interactions of analytes with the polymer fibres in electrical signals were interdigitated electrodes (IDEs) **(Janata J. et al., 2003)** designed and manufactured in CNR (Italy) on oxidised silicon wafer through a standard photolithographic process (lift-off procedure **(Wolf S. et al., 2000)**) followed by the evaporation of a chromium-gold layer. They comprised 40 pairs of electrodes (150 nm in electrode thickness, 20 μm in gap and electrode width and 5620 μm in length). After electrospinning coating, all electrical signals of the resulting chemoresistors were recorded through an electrometer (Keithley 6517 Electrometer). The electrospinning apparatus used in the present study consisted of a high power AC-DC (alternative current-direct current) converter, a high voltage oscillator (100 V) driving a high voltage (ranging from 1 to 50 kV), a syringe pump (Model KDS 200, KD Scientific) and a rotating conductive cylinder with a diameter of 45 mm. The fibrous layers were fabricated by applying 7-9 kV range of electrostatic DC voltage

(depending on the PANi concentration) between the tip of 1 cm long stainless steel in a syringe pump (100 μl $^{h-1}$in feed rate) and the transducer placed on the grounded collector, opposite to the syringe pump, at 15 cm distance. The depositions were carried out in a home-made clean box equipped with temperature and humidity sensors, deposition time was fixed at 20 min for all polymer materials (in order to obtain good coverage of the electrodes), the rotation speed was set to1000 rpm and depositions were carried out at about 21°C and 30% RH (relative humidity).

Synthetic dry air (5.0) was used as carrier gas (provided by Praxair-Rivoira, Italy) and was blended with ammonia from cylinders at fixed concentrations (10 ppm mol^{-1}in N_2, provided by Praxair-Rivoira, Italy) in order to test the dependency of IDE responses on gas concentrations. To test the interaction of water on the electrical properties of different polymer blends after electrospinning deposition and interaction with ammonia, humidified dilution air was prepared by running the dry atmospheric air through an H_2O bubbler containing demineralized water in order to obtain distinct percentages of water vapors. Similarly, acetic acid and trimethylamine vapors (VOCs) were diluted with dry and humidified air by using mass flow controllers. All the measurements were performed at room temperature (T = 20°C). The total gas flow passing through the measurement chamber, housing the IDEs, was set at constant 300 sccm. Each measurement was performed by flushing analytes of interest in the measurement chamber for suitable periods, according to the information to get and the specific features of analytes to test, and then cleaning sensor surfaces with air carrier gas until the complete recovery of the starting current (the baseline). IDE responses were calculated as both current (I) and normalized current (I/I_0), where I denotes the current and I0 the current under carrier gas flow before the analyte exposure.

6.2.3 Characterization

The nanofibrous materials were optically investigated through scanning electron microscopy (SEM Jeol, JSM 5200, 20 keV, X4500MAG, gold film), and transmission electron microscopy (TEM Jeol, JEM 1200 EXII). Water contact angles (WCA) measurements were provided bya USB Digital Microscope Logitech and ImageJ Free Software. The chemoresistors (IDEs) were placed in a measurement chamber (2.5 ml internal volume) made from PTFE and equipped with temperature and humidity sensors (Honeywell HIH 3602 C). Each IDE was linked to the electrometer to measure the current flowing through the IDE (DC) when a fixed potential was applied to it. Dynamic measurements were carried out at room temperature using both a 4-channel MKS 247 managing four MKS mass flow controllers, set in the range 0-200 sccm (standard cubic centime-tres per minute), with an accuracy greater than 1% at maximum flow, and an Environics S4004 system managing two mass flow controllers set in the range 10-1000 sccm and 0-50 sccm, respectively.

6.3 Results and discussion
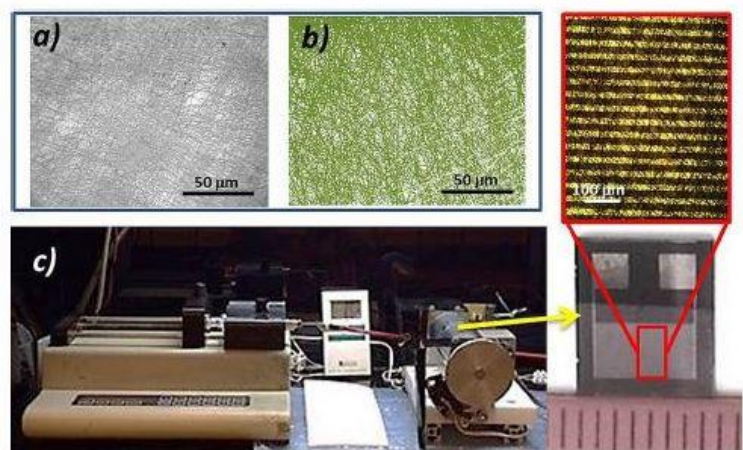
Figure 6.1: Optical micrographs of the nanofibrous layers called A (a) and F (b), respectively, coating microscope glass slides; (c) a picture of CNR-IIA home-made electrospinning equipment comprising a rotating collector where transducers were placed for deposition. The yellow arrow points to an interdigitated electrode after an electrospun deposition, where a rectangular area was magnified by optical micrograph (red framed).

The nanofibrous fabrics obtained from electrospinning deposition showed several shades of green, dependently on the amount of PANI: the most intense green corresponded to the highest PANi concentrations (E-F) **(Figure 6.1 (a) and (b)).** A dense network of continuous nanofibers covering the sensing area of the interdigitated electrodes (i.e. the area comprising the gaps and the metal fingers) was observed in all of the chemosensors created with the diverse polymer solutions employed **(Figure 6.1 (c)).** The electrospun scaffolds were characterized by high porosity deriving from both enhanced presence of openings and interconnected void volumes, and high surface-to-volume ratios (specific surface area) originating from quite small nanofibers diameters. These key features make such nanostructured fabrics potentially appealing in chemical sensing.
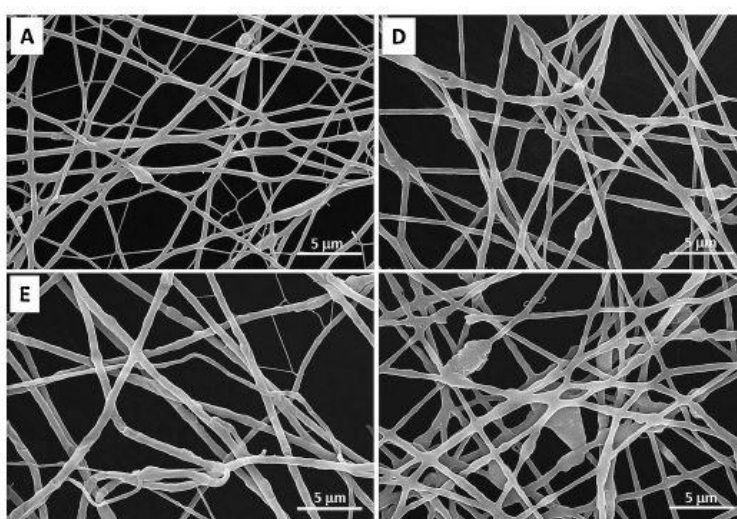
Figure 6.2: SEM micrographs show PANi/PHB nanofibres coating silicon wafers at increasing PANi mass ratios (A: 1.4%, D: 5.45%, E: 8%, F: 11%).

SEM micrographs of silicon wafers coated with the electrospun nanofibrous layers of PANi/PHB blends at several mass ratios high light the high degree of pores and interconnected void volumes, as well as the wide range of fibers diameters **(Figure 6.2).** Additionally, very slight differences in textures quality and size of fibers can be observed among nanofibers obtained with B, C and D blends, i.e. in samples where small volumes of polyaniline were added to PHB. Therefore in **Figure 6.2** only the micrograph of D will be presented. Specifically, fibers resulting from PANi/PHB blend with the smallest amount of PANi appeared branched, with a wide range of size distribution of the fibers **(A, in Figure 6.2)**, from a few nanometers to hundreds nanometers and 150 nm as mean value. By contrast, D-F fabrics looked uneven in shape, lumpy and with more roughness, but fibres were more homogeneous in size and slightly increased in diameter mean (~200 nm). The morphology of the resulting fibers was presumably depending on the different parameters of the starting solutions, such as blend conductivity, superficial tension and viscosity deriving from the increasing amounts of the non-electrospinnable PANi solution (the conducting polymer) **(Li, Z. et al., 2013)**. In the electrospinning process, it is known that by tuning several parameters such as the viscosity of polymer mixture, the nozzle-ground distance and the potential applied, fiberquality can be modified. In the present study, the diminished concentration of the insulating polymer, which generally increases its electrospinnability, decreased the viscosity of polymer mixtures. This result caused a substantial increase in the electrical performances (higher conductivity) and reproducibility probably due to the better adhesion onto the metal electrodes observed in the more conductive solutions, despite the not perfectly regular shape of the fibers. Furthermore, taking into account that: (i) the longer the distance between needle and collector (longer time of flight), the less the reproducibility of the deposition technique, because of both the instability of the jet and the small dimensions of the transducers housed in the collector; (ii) the shorter the distance, the larger the diameter of the fibers

227

produced and the larger the number of globular structures along the fibers, then the distance between needle and collector was set at 15 cm. TEM bright field micrographs reported in **Figure 6.3** show thin web-like and branched structures becoming darker depending on the increase of PANi concentration, presumably due to the greater electron density of this polymer relative to PHB. In scientific literature it is reported that it is possible to identify, in a core-shell fibers observed under TEM, the presence of a core polymer in a sheath of other polymers through sharp boundaries inside the fibers. These sharp boundaries reflect the difference between the core and shell materials ability for electron transmission **(Liu, W. et al., 2002; Golin, A. P., 2014).** On the other hand since thicker fibers appear darker in TEM analysis, the change in brightness could also be due to the fibers thickness variation. Nevertheless PHB fibers appeared homogenous in color (data not shown) but with darker patches when PANi was added **(Figure 6.3 (A)).**
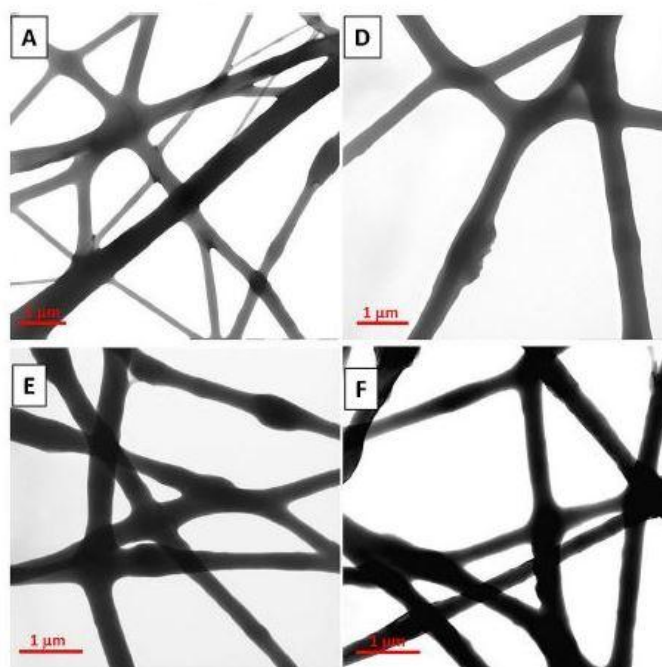
Figure 6.3: TEM micrographs show A, D, E and F samples, contrasted with uranyl acetate.

Such gradual darkening of the fibers when PANi concentration increased let suppose a relationship between the two polymers used and the brightness. Both polymers could be distinguished within the fibers for their different electron density. Indeed, the electron beam travelling through the specimen under study are scattered and disappear from the beam depending on the density of the polymer materials present in the nanofibers (related to their molecular weights), thus resulting in a different brightness and lightness. The presence of darker areas in tiny fibers of sample A similar to the electron density (darkness) of the thicker ones suggests a discontinuous distribution of PANi during electrospinning deposition. With the increasing of both fibers thickness and PANi content (D-F), fibers appeared more evenly dark colored (even the thinner fibers), suggesting a more uniform distribution of PANi throughout the fibers, more concentrated within the bulges and roughness of the surface. Further investigation should be performed to confirm the distribution of such a conductive polymer in the blended fibers.
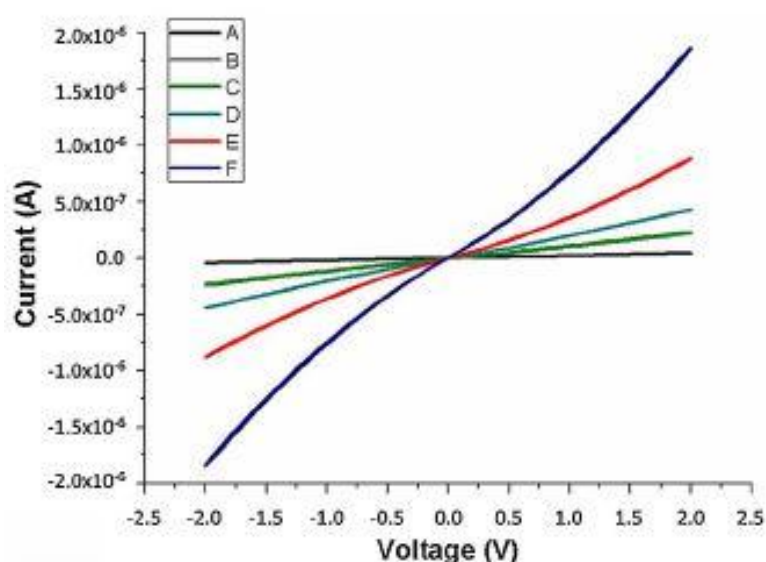
Figure 6.4: Current-Voltage curves of all the PANi/PHB sensors (A-F) between -2 V and +2 V in dry air.

229

The electrical parameters of the resulting fibrous layers were tested by measuring the current variations (Ampere) when voltage was changed (Volts). Figure 5.4 reports the current-voltage curves of the resulting chemosensors (named A-F) in dry conditions (under air flow). The linear shapes within the selected voltage range (-2 V to +2 V) showed constant resistance values for all of the polymer blends, suggesting a good adherence of the polymers to the gold electrodes additionally to Ohmic conductivity to the fibers already at the lowest concentrations of PANi **(Hao, Q. L. et al., 2003; Li, G. F. et al., 2004).** Pristine PHB fibrous layers with an applied potential set to 3 V were measured too, but current values of 10^{-12} A were recorded. However the resulting measured electrical resistance **(Figure 6.5 (a)),** related to both the individual fiber resistance (dimension and shape) and the fiber density (number of fibers per unit of surface area), showed a negative exponential-like relationships to PANi linear increasing percentage in the fibrous layers.
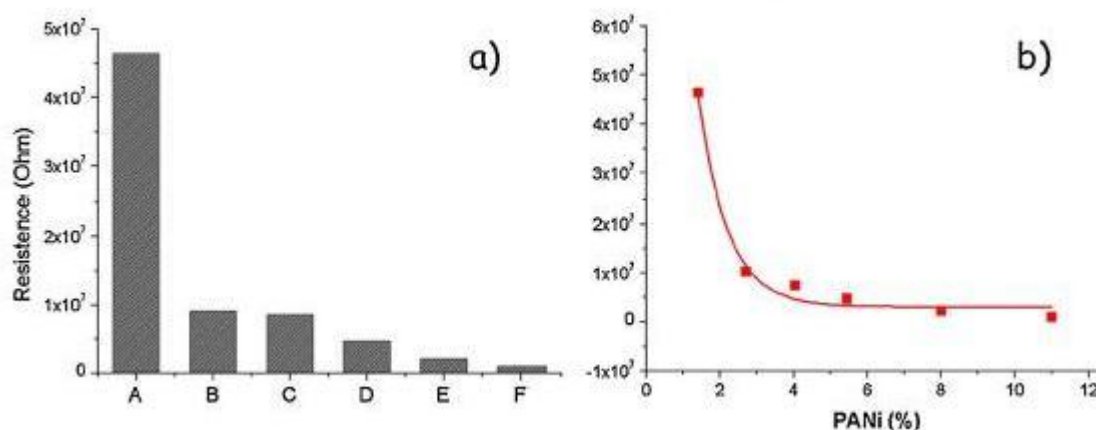
Figure 6.5: Electrical parameters of the investigated chemosensors; (a) bar plot of electrical resistance values of the nanofibrous sensors; (b) curve fitting of the electrical resistance values vs PANi/PHB mass ratio in percentage.

This result apparently suggests a deep relationship between the PANi concentration and its distribution within the fibrous layers, with a threshold value estimated about 2.5% (PANi:PHB, w:w). Below that, PANi polymer chains should be un homogeneously distributed within fibers, affecting the

conductivity of the layers that generated electrical signals extremely noisy (sample A, data not shown) at the low voltage applied (up to 3 V).

The sensor measurements, that were the electrical signals reported when interaction between the sensing layers and the analytes were happening, resulted in a change of the whole resistance (or current, i.e. I = V/R according to Ohm law) of the device according to the following Eq. (1) **(Janata, J. et al., 2003)**:

$$R = (1 / 2N - 1)p(w/h \times L)$$

where N and L are number and size of the fingers, h and w the electrode thickness and width, respectively, and p la resistivity of the overlying material. Firstly, the chemosensors were exposed to water vapors ranging between 10 and 60% RH. Each measurement was carried out for 10 min. The relative humidity percentage was measured through a commercial sensor, placed inside the measurement chamber, confirming the achievement of the equilibrium one minute after the start of measurement. It is known that the electrical response of a chemosensor (ΔR, i.e. the resistance change) is produced by the changes in the intrinsic resistivity of the polymeric chains due to electronic effects (partial electron transfer between the adsorbed molecule and the polymer chains), the resistivity changes related to variations in the electron hopping process (distance among polymer chains) and the resistivity changes due to modifications in the dielectric medium between the chains (ionic conductivity in the medium around polymer chains) **(Cavallo, P. et al., 2015).** The resulting responses to humidity of the investigated sensors showed resistance decreasing (i.e. current increasing), although with different slopes **(Figure 6.6)** depending on the concentration of PANi.
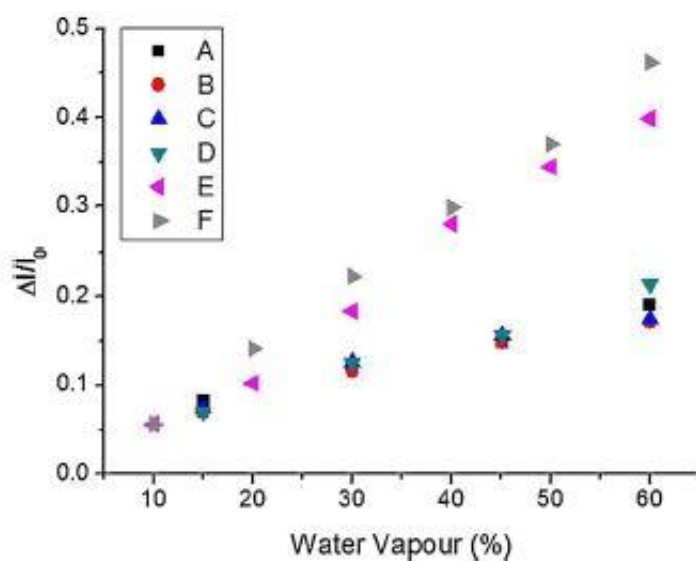
Figure 6.6: Response curves of PANi/PHB nanofibrous chemosensors to increasing percentages of relative humidity (% RH), ranging between 10%-60% (V = +2 V). For each sensor, the current values (I) were normalized to the starting current values (I$_0$) before the measuring, in order to be compared.

The interaction mechanisms at the polymeric surface of PANi/PHB fibers with water vapors can be a lot and opposite. The high dielectric constant of water for example, can interact with the N atoms of PANi, thus inducing an extension of the PANi chains into more stretching conformations and generating an increase in the crystallinity of the polymer with a decrease in its electric resistance. Additionally also H-bonds between water molecules and N atoms of PANi can induce an increase in current (ie. Electrical resistance decrease). Vice versa, water vapor can also dissolve the doping salt (CSA), thus de-doping the molecules and leading to a decrease in current. For instance, in wet atmosphere, the hosting polymer swelling could overcome the other effects, spacing out the PANi chains and causing current lowering **(Macagnano, A. et ail., 2011; Zampetti, E. et al., 2011).**The electrical responses resulted from the combination of all these parameters. Since the resulting sensitivity to water vapor, measured as the slope of the normalized sensor responses (I/I$_0$) to ppm of water vapors **(Table 1),** increased with PANi concentration, the effects of humidity on PANi/PHB fibers were supposed to be significantly depending on the PANi chains. Although PHB and PANi

232

fibers are known as hydrophobic materials in their nature, there still would have a chance of water molecules penetration because of the interstitial spaces between fibers (pores). Data obtained from WCA (water contact angle) measurements are in very close agreement with the commonly known fact which indicates the following: for hydrophobic surfaces WCA increases with surface roughness and for hydrophilic surfaces, in contrast, WCA decreases with surface roughness **(Ma, Z. et al., 2006).**

Chemosensors	Sensitivity (ppm⁻¹)	St. Error	R-Square
A (PANi 1.4%)	2.34E-3	±1.2831E-4	0.99
B (PANi 2.7%)	2.27E-3	±2.5204E-4	0.96
C (PANi 4%)	2.23E-3	±3.5832E-4	0.93
D (PANi 5.45%)	3.08E-3	±2.4662E-4	0.98
E (PANi 8%)	7.25E-3	±3.4645E-4	0.98
F (PANi 11%)	7.97E-3	±1.3288E-4	0.99

Table 1: Sensor sensitivity to relative humidity

In **Figure 6.7,** WCA measurements of A, D and F samples were 90°, 81°e 79°, respectively, confirmed the increase in roughness such as the wettability of the samples with higher PANi concentration.
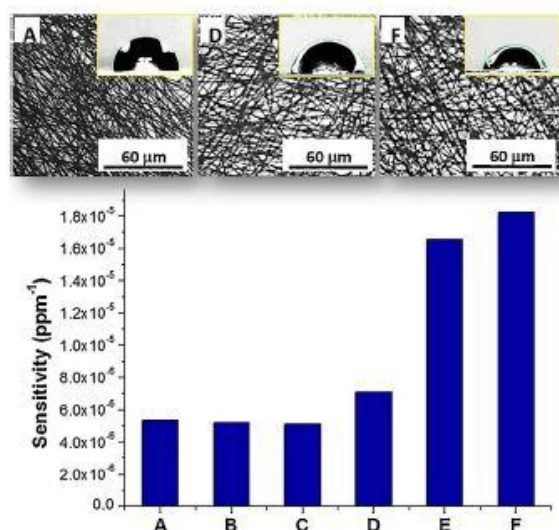
Figure 6.7: Top: WCA pictures of the A, D and F samples captured by a digital microscope and an optical microscope. Bottom: bar-plot of the sensitivity (S) of the sensors to water vapors concentrations (ppm), measured as the slope of the linear

fitting of the normalized response curve of each sensor (I_0/I_0), i.e. S = (I/I_0)/C, where C is the analyte concentration.

These results suggested a possible effect of moisture to gas/VOCs interactions. For what concerns the measurements of gas and the effects of moisture on them, the most conductive chemosensors were selected, since able to detect low concentrations of the analytes. Current-Voltage curves of E and F samples reported the huge increase in current **(Figure 6.8)**, overall in F increased more than twice (F = 2.55 x; E = 1.26 x), when measurements were carried outin a moist environment (70% RH), presumably due to the water molecules that, adhering on the surfaces, were able to create a thin layer on the fibres and among pores. The comparison of I-V curves in dry air and 50% RH, respectively, did not enhance peculiar changes of the curves shape. Furthermore, several I-V cycles were performed, but since they were perfectly overlapped, no hysteresis phenomenon, due to ions contribution to the current, was reported. This effect is extremely undesirable for many sensors because water vapor molecules are in competition with the analytes for the same interaction sites, perturbing the chemical interaction. Thus, for sensing application, in order to control or reduce the humidity effects, filters, cartridges or permeation tubes have to be used. Despite the electron donor character of both the molecules, opposite electrical effects were reported when water and ammonia reacted with PANi layers (i.e. ammonia decreased the polymer conductivity and water increased it) **(Lubentsov, B. Z. et al., 1991).** CSA-PANi exhibits p-type semiconductor characteristics, so exposure to electron-donating species gives rise to a decrease in the charge-carrier concentrations and thus an increase in the measured resistance. When PANi/PHB fibrous sensors were used for measuring ammonia (1 ppm) in different conditions of environmental humidity, the response time dramatically changed: it was relatively long in anhydrous condition, with a few minutes of inertia before a significant change of current; on the contrary it was extremely

fast when measurements were carried out to higher relative humidity percentages (ranging between 10% and 70%). This effect was enhanced overall in F, that in 200 s (70% RH) achieved the same current value that F dry (i.e. ΔI) achieved in more than 800   s **(Figure 6.8).**
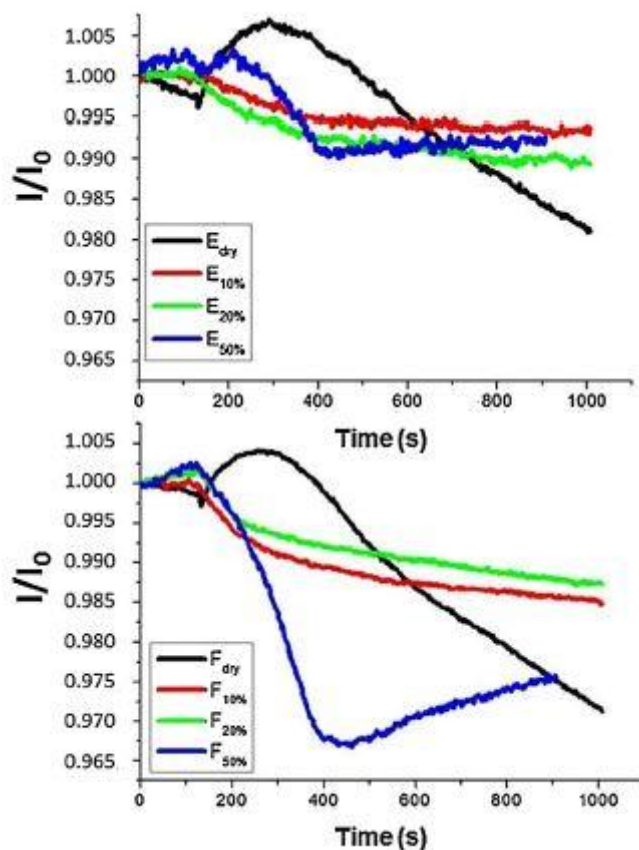

Figure 6.8: Comparison of the normalized transient responses of the sensors E (on the top) and F (on the bottom) to ammonia (1 ppm) under dry and variously humidified air (300 sccm), (V = +2 V).

It is presumed that water molecules adsorbed on the surface of the fibrous scaffold facilitated the solvation of polar molecules or soluble in water, such as it happens in nature where the fibrous sensory structures protrude in aqueous matrices (even in the mammalian olfactory system) to keep in touch faster with the molecules of the surrounding environment. Since ammonia is an electron-donor, when it interacts with PANi, deprotonation is expected to occur, transforming the emeraldine salt form into the insulating base form, and

235

then increasing the resistance value. Initially the gas is physisorbed throughout the nanofibers, then the chemisorption occurs (formation of PANi-ammonia complexes), followed by the rearrangement of the polymer structure and deprotonation, respectively **(Stamenov, P. et al., 2012).** The polymer chains rearrangement is able to generate a complete symmetrisation of the chemical bonds and a lowering of the total energy of the polymer chain (energetically favored) **(Li, W. et al., 2011).** Instead of deprotonation, this mechanism increases the conductivity of the polymer: such an effect can be noticed in dry air when ammonia starts the interaction with the fibers **(Figure 6.8).** However, the response of sensor F, the most conductive one, to NH_3 as a function of gas concentration (ppb), showed a general decrease in current within creasing concentrations of the analyte in the measurement chamber. The 90% equilibrium response was achieved after more than 20 min of gas flow in dry air. On the other hand, the response times to ammonia were shortened in moist air **(Figure 6.8).** Therefore, in a wet environment, water molecules were supposed to be sorbed on the fibers, with different amount and arrangement depending on both the humidity percentage and fibers structure and morphology. Such an organization implied higher currents than in dry air. After NH_3 introduction, the double effect of polar molecules solvation and dissolution in water should happen. The strong affinity of NH_3 molecules to PANi is able to displace the weakly adsorbed H_2O molecules **(Matsuguchi, M. et al., 2003).** The results of this competitive sorption reported a decrease in the conductivity of the film. A further increase in water vapor percentage could facilitate also the ammonia dissolution in water with the production of hydroxide ions and ammonium ions. Such an alkaline layer coating the fibers could contribute to both more quick and strong de-doping of PANi and changing the dielectric environment.
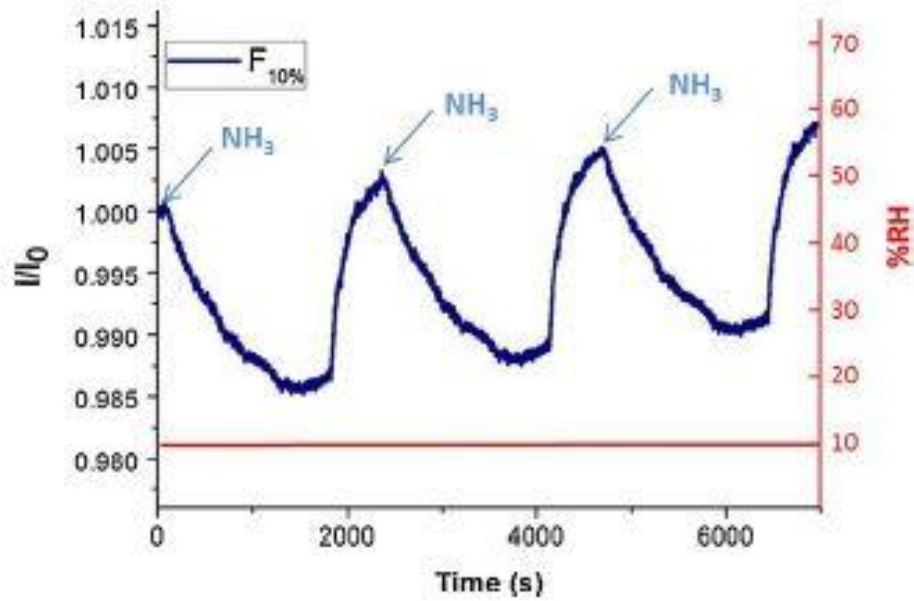
Figure 6.9: Bi-plot of three consecutive responses of F sensor, reported as normalized current (I/I$_0$) to the same concentration of NH$_3$ (834 ppb) flowed throughout the measuring chamber (300 scum) in 10% wet air (%RH) (V = +2 V).
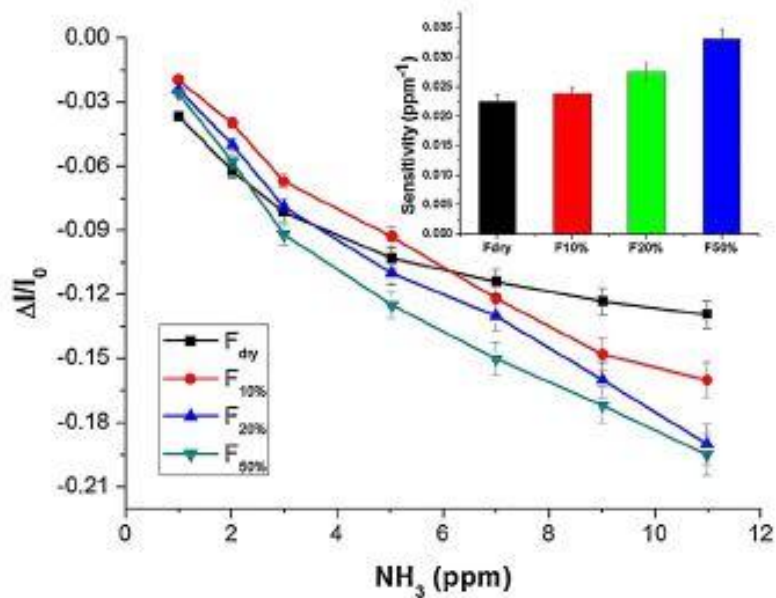

Figure 6.10: Response curves of F sensor to increasing concentrations of NH$_3$ when air ranged between dry and 50% wet (V = +2 V). The sensor sensitivity values were reported in the bar plot (inset).

237

Figure 6.9 depicts the sensor F transient responses when a defined concentration of ammonia (834 ppb) was cyclically flowed throughout the measurement chamber under 10% RH. The sensor showed both comparable responses and starting current recovery when the sensing gas was turned on, despite a slight drift of the sensor. Sensor sensitivity, calculated as the slope of each calibration curve at the lowest gas concentrations, resulted improved when humidity percentage increased too **(Figure 6.10).** Since TEA and AcAc are commonly used as chemical markers in odors smelling associated to specific phenomena, such as food spoilage (i.e. fish spoilage), monitoring their presence and concentration sounds consequently of outmost importance, for instance, in food quality applications. The response time of the chemosensors to a selected vapor pressure of triethylamine (TEA) and acetic acid (AcAc) decreased when the relative humidity increased. The sensor responses were compared and depicted in **Figure 6.11:** the very low current changes due to the VOCs interactions in dry air resulted increased when % RH also augmented. Therefore, as expected from literature, the current of F sensor decreased, specifically of 0.3%,0.9%, 34% and 68% when 0.03 $p/p°$ TEA (where p and p° denote the vapor pressure and the saturated vapor pressure, respectively) flowed throughout the measuring chamber for 187 s under increasing humidity percentages, i.e. dry, 10%, 50% and 70%, respectively. Similarly, 0.03 $p/p°$ AcAc flushing over the sensors for 450 s, increased the current of the sensor F 1.9%, 2.5%, 7.9% and 11.4% respectively. Since the sensors came to equilibrium after several tens of minutes (useless in sensors applications), only the transient response slope values were taken in consideration and calculated, there by drastically reducing measurement time in a few minutes **(Table 2).**

Analytes	$E\,[I_{norm}/s](s^{-1})$	St.Er.	R-sq	$F\,[I_{norm}/s](s^{-1})$	St.Er.	R-sq
NH$_3$ dry	$5.5962 \cdot 10^{-5}$	$\pm 2.296 \cdot 10^{-6}$	0.88	$3.4997 \cdot 10^{-5}$	$\pm 2.008 \cdot 10^{-6}$	0.84
NH$_3$ 10%RH	$-2.3406 \cdot 10^{-5}$	$\pm 6.381 \cdot 10^{-6}$	0.93	$-4.8879 \cdot 10^{-5}$	$\pm 1.103 \cdot 10^{-6}$	0.96
NH$_3$ 20%RH	$-3.2262 \cdot 10^{-5}$	$\pm 8.611 \cdot 10^{-7}$	0.95	$-4.9613 \cdot 10^{-5}$	$\pm 1.485 \cdot 10^{-6}$	0.92
NH$_3$ 50%RH	$-5.8546 \cdot 10^{-4}$	$\pm 1.353 \cdot 10^{-6}$	0.95	$-1.6044 \cdot 10^{-4}$	$\pm 1.333 \cdot 10^{-6}$	0.99
TEA dry	$-8.9840 \cdot 10^{-6}$	$\pm 3.914 \cdot 10^{-7}$	0.93	$-1.4935 \cdot 10^{-5}$	$\pm 3.914 \cdot 10^{-6}$	0.93
TEA 10%RH	$-3.5050 \cdot 10^{-5}$	$\pm 5.568 \cdot 10^{-7}$	0.95	$-4.3751 \cdot 10^{-5}$	$\pm 3.914 \cdot 10^{-6}$	0.94
TEA 60%RH	$-1.7610 \cdot 10^{-2}$	$\pm 1.037 \cdot 10^{-5}$	0.99	$-1.8101 \cdot 10^{-2}$	$\pm 3.914 \cdot 10^{-6}$	0.98
TEA 70%RH	$-1.8670 \cdot 10^{-2}$	$\pm 2.160 \cdot 10^{-3}$	0.99	$-2.2041 \cdot 10^{-2}$	$\pm 3.914 \cdot 10^{-6}$	0.99
AcAc dry(*)	$4.7944 \cdot 10^{-5}$	$\pm 9.023 \cdot 10^{-7}$	0.94	$6.1092 \cdot 10^{-5}$	$\pm 8.851 \cdot 10^{-7}$	0.96
AcAc 10%RH(*)	$4.5399 \cdot 10^{-5}$	$\pm 9.081 \cdot 10^{-7}$	0.91	$6.9097 \cdot 10^{-5}$	$\pm 1.111 \cdot 10^{-6}$	0.96
AcAc 60%RH(*)	$1.1306 \cdot 10^{-4}$	$\pm 1.671 \cdot 10^{-6}$	0.96	$2.3265 \cdot 10^{-4}$	$\pm 2.36 \cdot 10^{-6}$	0.98
AcAc 70%RH(*)	$3.8888 \cdot 10^{-4}$	$\pm 1.287 \cdot 10^{-6}$	0.99	$3.9109 \cdot 10^{-4}$	$\pm 9.62 \cdot 10^{-7}$	0.99

Table 2: The slope values of the linear fitting of the first 100 s of measurements (except for acetic acid (*): after 100 s) to several analytes under different humidity percentages.
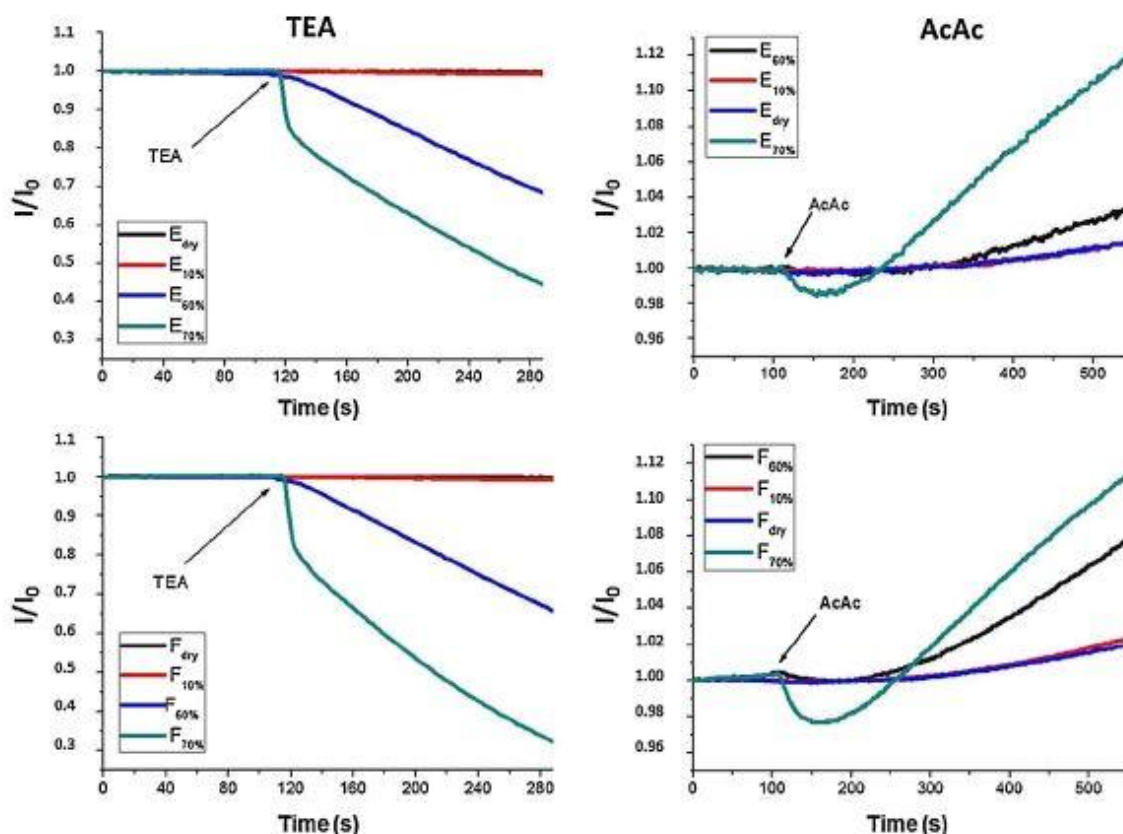

Figure 6.11: Comparison of the normalized transient responses of the sensors E (on the top) and F (on the bottom) to TEA (0.03 p/p°) and AcAc (0.03 p/p°) under dry and variously humidified air (300 sccm).

Furthermore, the protracted exposure to the several analytes irreversibly changed sensors electrical performances. Specifically, the chemical interactions of PANi with ammonia in a very humidified environment and for

a long time, were supposed to undopeand change PANi chains conformation, modifying the electrical properties of the material. Such an effect is suggested by **Figure 6.9** where sensor to 50% RH, after 300 s under flow of ammonia (1 ppm), showed a sudden reversal trend of the current, despite of the regular tendency when the measurements were carried out under lower percentages. Indeed, the contact of CSA-PANi doped with the basic vapors (i.e.TEA) leaded to a typical acid-base interaction, with consequent PANi deprotonation. Additionally, since TEA is slightly soluble in water, it could act as a weak base by accepting a proton (H^+) from water to form small and equal amounts of triethylammonium ion and (OH^-) whithin the thin layer of water molecules surrounding fibers, thus contributing to the electrical response of the sensor. This additional contribution seems to be confirmed by the noticeable response time lowering, as well as the electrical response increasing. Similar effects were reported in **Figure 6.11** when AcAc was flowed to 60% RH and more evident to 70% RH, when after a starting decreasing in current, an abrupt change of tendency reported an increasing current trend, as expected by the interaction between PANi and an acid. Indeed acetic acid vapors, wetting the surface of fibrous layer, were able to partially solve PHB, inducing a swelling of fibers (decrease in current) before interacting with PANi molecules and causing the likely current rise. For this reason, as regards the measurements related to AcAc, the linear fitting was calculated after the first 100 s of response **(Table 2),** that is when the sudden change of the current trend occurred. All sensors could be recovered after a flow of humid air to the same value percentage of the measurement when measurements were no longer than 6 min. The desorption time lowering (data not shown) suggested that the wet gas carriers carried away more quickly the analytes from fibers. All sensors were tested for more than one year, showing stability in morphology and electrical parameters, with a slight tendency to decrease in resistance probably due to irreversible moisture adsorption. After each set of measurements, they were stored in small boxes in the dark and dry environment before reuse. After

1 year, the resistance value of F, the most conductive sensor, resulted increased by ~ 6.3%. This result could be also due to a potential starting biodegradation of PHB, responsible of changing the proportion of the polymer within the fibers, but further investigation concerning the effects of the biodegradation (morphological and electrical) on the sensors are still in progress.

6.4 Conclusions

An environmentally friendly conductive sensor formed by nanofibres composed of PANi/PHB blends, deposited through electrospinning on chemoresistors, has been designed and fabricated to measure gases and volatile organic compounds (VOCs) in moistened environments. PANi and PHB polymers were selected for their crucial remarkable characteristics, such as gas sensitivity and biodegradability, respectively. The nanofibrous layers obtained through electrospinning technology carried out directly on chemoresistors resulted in highly porous membranes and the potentials of such blended scaffolds have been analyzed, focusing the attention on the influence of humidity on the features of the resulting sensors, also in terms of reproducibility and stability of their responses. The sensor responses were tested by measuring ammonia and further two chemical compounds differently interacting with PANi (i.e. triethylamine and acetic acid) in dry air and at different percentages of relative humidity, in order to assess in possible applications the influence of PHB in the interactions of PANi with the analytes tested. Due to the properties of the electrospun nanofibres used in these chemoresistors, water vapors seemed to hugely improve the chemical interactions with the selected analytes. This effect suggests a potential use of the proposed chemosensors in monitoring also strongly moist environments.

The resulting sensing features suggest the chance to integrate these electrospun chemosensors within smart devices usable anytime and anywhere and capable of providing qualitative and quantitative information about pollutants without representing a significant additional source of pollution to the environment once worn out. Noticeably, a humidity sensor will be necessary, in these cases, to relate the responses of sensors to the amount of analytes of interest. In laboratory, sensors have worked for more than one year showing stability in both morphology and electrical parameters. They were primarily designed on purpose to be biodegradable and then to fabricate an ecofriendly sensing system, but they also resulted desirable for their low cost, ease of measurement, low power consumption, dimension and good performance at room temperature.

References

Ackermann J., Müller S., Lösche A., Bley T., Babel W. Methylobacteriumrhodesianum cells tend to double the DNA content under growth limitation sand accumulate PHB. J Biotechnol (1995), Vol. 39, pp. 9-20

Araujo P. L. B, Ferreira C. R. P .C, Araujo E. S. Biodegradable conductive composites of poly(3-hydroxybutyrate) and polyaniline nanofibres: preparation, characterization and radiolytic effects. Express Polym Lett (2011), Vol. 5, pp. 12-22

Bai H., Shi G. Gas sensors based on conducting polymers. Sensors (2007), Vol. 7, pp. 267-307

Cavallo P., Acevedo D. F. M., Fuertes M. C., Soler-Illia G. J. A. A, Barbero C. A. Understanding the sensing mechanism of polyaniline resistive sensors. Effect of humidity on sensing of organic volatiles. Sens Actuators B-Chem (2015), Vol. 210, pp. 574-580

EYslas E. I., Ibarra L. E., Peralta D. O, Barbero C. A., Rivarola V. A, Bertuzzi M. L. Polyaniline nanofibres: acute toxicity and teratogenic effect on Rhinellaarenarum embryos, Chemosphere (2012), Vol. 87, pp. 1374-1380

Golin A. P. Humidity Effect on the Structure of Electrospun Core-Shell PCL-PEGFibers for Tissue Regeneration Applications (2014), Electronic Thesis and Dissertation Repository, Paper 1999, http://ir.lib.uwo.ca/etd/1999

Hao Q. L., Kulikov V., Mirsky V. A. Investigation of contact and bulk resistance of conducting polymers by simultaneous two- and four-point technique. Sens Actuators B Chem (2003), Vol. 94, pp. 352

Humpolicek P., Kasparkova V., Saha P., Stejskal J. Biocompatibility of polyaniline. Synt Met (2012), Vol. 162, pp. 722-727

Irimia-Vladu M. Green electronics: biodegradable and biocompatible materials and devices for sustainable future. Chem Soc Rev (2014), Vol. 43, pp. 588-610

Irimia-Vladu M., Głowacki E. D., Voss G., Bauer S., Sariciftci N. S. Green and biodegradable electronics. Mater Today (2012), Vol. 15, pp. 340-346

Ismail Y. A., Martìnez J. G., Otero T. F. Fibroin/polyaniline microfibrous mat. Preparation and electrochemical characterization as reactive sensor. Electrochim Acta (2014), Vol. 123, pp. 501-510

Janata J., Josowicz M. Conducting polymers in electronic chemical sensors. Nat Mater (2003), Vol 2, pp. 19-24

Janata J., Josowicz M. Conducting polymers in electronic chemical sensors. Nat Mater (2003), Vol. 2, pp. 19-24

Kim D. H., Lu N., Ma R., Kim Y. S., Kim R. H., Wang S. et al. Epidermal Electron. Science (2011), Vol. 333 (6044), pp. 838-843

Laurencin C. T., Ambrosio A. M., Borden M. D, Cooper J. A. Jr Tissue engineering: orthopedic applications. Annu Rev Biomed Eng (1999), Vol. 1, pp. 19-46

Li G. F., Martinez C., Janata J, Smith J. A., Josowicz M., Semancik S. Effect of morphology on the response on polyaniline-based conductometric gas sensors: nanofibres vs thin films. Electrochem Solid State Lett (2004), Vol. 7, pp. H44-H48

Li W., Jang D. M., An S. Y., Kim D., Hong S. K., Kim H. Polyaniline–chitosan nanocomposite: high performance hydrogen sensor from new principle. Sens Actuators B-Chem (2011), Vol. 160, pp. 1020-1025

Li Z., Wang C. Effects of Working Parameters on Electrospinning, in One-Dimensional Nanostructures, Springer (2013), pp.15-28

Liu W., Graham M., Evans E. A., Reneker D. H, Darrell H. Poly(meta-phenylene isophthalamide) nanofibres: coating and post processing. J Mater Res (2002), Vol. 16, pp. 3206-3212

Low K., Chartuprayoon N., Echeverria C., Li C., Bosze W., Myung N. W., Nam J. Polyaniline/poly(ε-caprolactone) composite electrospun nanofibre-based gassensors: optimization of sensing properties by dopants and doping concentration. Nanotechnology (2014), Vol. 25, pp. 115501

Lubentsov B. Z., Timofeeva O. N., Khidekel M. L. Conducting polymer interaction with gaseous substances II. PANI-H_2O, PANi-NH_3. Synth Met (1991), Vol. 45, pp. 235-240

Ma Z., Kotaki M. Ramakrishna S. Surface modified nonwoven polysulphone(PSU) fibre mesh by electrospinning: a novel affinity membrane. J Membr Sci (2006), Vol. 272, pp. 179-187

Macagnano A. Electrospinning for High Performance Sensors, in Nanoscienceand Technology, Springer International Publishing, Switzerland (2015), pp. 0-329 (ISBN 978-3-319-14406-1)

Macagnano A., Zampetti E., Pantalei S., De Cesare F., Bearzotti A., Persaud K. Nanofibrous PANI-based conductive polymers for trace gas analysis. Thin Solid Films (2011), Vol. 520, pp. 978-985

Matsuguchi M., Okamoto A., Sakai Y. Effect of humidity on NH_3 gas sensitivity of polyaniline blend films. Sensor Actuators B-Chem (2003), Vol. 94, pp. 46-52

Nadadur S. S., Hollingsworth J. W. Air Pollution and Health Effects, in Molecular and Integrative Toxicology Series. Springer-Verlag (2015), pp. 0-439 (ISBN. 10.1007/978-1-4471-6669-6)

Ramakrishna S., Fujihara K., Teo W. E, Yong T., Ma Z., Ramaseshan R. Electrospun nanofibres: solving global issues. Mater Today (2006), Vol. 9, pp. 40-50

Singh B., Sharma N. Mechanistic implications of plastic degradation. Polym Degrad Stab (2008), Vol. 93, pp. 561-584

Stamenov P., Madathil R., Coey J. M. D. Dynamic response of ammonia sensors constructed from polyaniline nanofibre films with varying morphology. Sens Actuators B-Chem (2012), Vol. 161, pp. 989-999

Virji S., Huang J., Kaner R. B., Weiller B. H. Polyaniline nanofibre gas sensors: examination of response mechanisms. Nano Lett (2004), Vol. 4, pp. 491-496

Wang X., Drew C., Lee S. H., Senecal K. J., Kumar J, Samuelson L. A. Electrospun nanofibrous membranes for highly sensitive optical sensors. Nano Lett (2002), Vol. 2, pp. 1273-1275

Wolf S., Tauber R. N. Silicon Processing for VLSI, Process Technology (2000), Vol. 1 pp. 0-960

Zampetti E., Muzyczuk A., Macagnano A., Pantalei S., Scalese S., Spinella C, Berazotti A. Effects of temperature and humidity on electrospun conductive nanofibers based on polyaniline blends. J Nanopart Res (2011), Vol. 13, pp. 6193-6200

Introduction

Mercury is a well-known neurotoxic (even at very low levels) and persistent worldwide pollutant **(Qui, J., 2013).** It is emitted to the air by human activities, such as manufacturing facilities, coal power plants and artisanal small scale goal mining and from natural biogeochemical processes including those related to emissions from oceans, soil and volcanoes **(Pirrone, N. et al., 2013; Lubick, N., 2009).** Recently, mercury has also been recognized as a pollutant producing significant adverse neurological damages, upon its action as a neurotoxin, as well as harmful effects on unborn children and infants. The most common way people are exposed to any form of mercury is by eating fish containing methylmercury (ingestion). Other possible ways of exposures include contact with breaking products containing elemental mercury and employing compounds that contain mercury (dermal contact) or breathing polluted air (inhalation). The factors that determine how severe the health effects are from mercury exposure include the chemical form of Hg, the duration and the route of exposure (i.e. inhalation, ingestion, dermal contact, etc.) as well as the age of the person exposed (e.g. unborn children and infants are the most susceptible). The World Health Organization has set the current Personal Exposure Limit for Hg at 0.05 mg/cm^3 or 5.6 ppb in air. Since 2010 a European project called Global Mercury Observation System (GMOS - www.gmos.eu) **(Lubick, N., 2009; Cinnirella, S. et al., 2013)**, expected to directly support the implementation of the Minamata Convention, has been involved in creating an international network capable of providing accurate measurements of Hg on a global scale. Up to now, air monitors are highly sensitive and capable of detecting the global mercury background, but are complex, costly and high-maintenance (requiring more than 40 monitoring sites and skilled operators). In the atmosphere, mercury exists in three different species: i) gaseous elemental mercury; ii) particle-bound mercury;

iii) oxidized gaseous mercury (i.e. RGM, reactive gaseous mercury), this last predominantly in water soluble forms. About 95 percent of atmospheric mercury is elemental. The detection and measurement of mercury is usually performed by spectroscopic methods, i.e. atomic absorption spectroscopy (AAS), atomic fluorescence spectroscopy (AFS), atomic emission spectroscopy (AES), or mass spectrometry (MS) **(http://www.labcompare.com).** These instruments often include a series of processes or pretreatments, such as oxidation, reduction, vapor separation and gold traps, to pre-concentrate and detect mercury from air. Additionally, an argon carrier stream is required by the detector to avoid the quenching of the fluorescence signal by oxygen, when fluorescence is the way of detection **(Ferrua, N. et al., 2007).** The need for detection systems characterized by fast measurements, low costs, low-maintenance, wide distribution, ease of use, and resistance to adverse environmental conditions is becoming more and more urgent. Sensors and sensing systems are the most promising alternative to the traditional instruments, described herein above, and capable of satisfying the requirements. Many sensors have been designed and investigated to detect the several forms of mercury. Most of them have exploited the strong affinity between mercury and gold. Several studies have documented changes in the electrical properties, work function, and resistance of thin gold films upon exposure to various concentration of mercury vapor. Ignoring any effects of the carrier gas, the rate of adsorption from a single component vapor phase (kads) can be explained by considering the sticking probability (S), that is the rate at which atoms of the Hg^0 strike the surface (v), ($S=k_{ads}/v$). The parameter S depends on the adsorbate (Hg^0 in this case), its partial pressure (P_{Hg}), the substrate (Au), and the temperature (T). The sticking probability for mercury is close to unity on a clean gold surface in vacuum, but it decreases rapidly when more than 50% of gold surface is covered with mercury. This value is furtherly decreased when an inert gas, like argon, was introduced as gas carrier (by approximately 4 order of magnitude) **(Battistoni, C. et al., 1996).**

Laboratory tests reported that the sensor sensitivity was depending on the exposed area: a larger surface allowed a greater mercury atoms adsorption over the same time and at the same vapor pressure. Real applications could be supposed by using an array of cantilevers differently sized in order to be able to work in different ranges of mercury concentration. However they had to work under dust-free gas carrier and needed to be regenerated by heating (350 °C for 20 min). Quartz crystal microbalances (QCMs) have been the first devices used as Hg vapor sensors in 1974 **(Sabri, Y. M. et al., 2009; Scheide E. P. et al., 1974)** and their sensing performances have been improved modulating the roughness of their gold pads. More recent literature reported that electrodes having rougher surface showed higher Hg^0 absorptive capacity (700 ng cm^{-2}) than polished ones **(Mohibul Kabir, K. M. et al., 2015).** Conductometric sensors, too, have been designed and used to reveal mercury vapor through their electrical resistance changes **(Mcnerney, J. et al., 1972; Raffa, V. et al., 2006).** However the sensitivity of the latter group of sensors based on gold electrodes, seemed often limited (around $1\mu g/m^3$). The employment of gold nanostructures (particles, wires, rods) provided the chance to create more sensitive sensors, overall exploiting the optical properties of these nanostructures **(Chemnasiri, W. et al., 2012; James, J. Z. et al., 2012)**, as well as electrochemical **(Merkoci, A., 2007; Dong, Z. M. et al., 2015)**, gravimetric **(Sabri, Y. M. et al., 2011)** and conductometric ones **(Keebaugh, S. et al., 2007)**. The size and the shape of these nanostructures have been demonstrated to be key parameters in defining the properties of the resulting sensors, because of the strict relationship between the surface and the bulk of the sensing materials, that here is extremely reduced **(Crosby, J., 2013)**. The increase in the number of binding sites was confirmed to be a successful strategies. Additional parameters such as energy binding, surface adsorption kinetics and the diffusion rate of mercury into the nanogold structures have been widely investigated for designing novel sensors **(Crosby, J., 2013; McNicholas, T. P. et al., 2011)**. In the present study, electrospinning

250

technology **(Macagnano, A. et al., 2015)** was used to create chemoresistors based on nanocompositi nanofibrous layers of Au/TiO$_2$ capable of adsorbing and revealing elemental mercury vapors in the atmosphere. By exploiting the photocatalytic properties of the nanofibers of titania, gold nanoparticles were selectively grown, under UV-light irradiation, on a nanofibrous scaffold of titania, using tetrachloroauric acid (HAuCl$_4$) as gold nanoparticles (AuNPs) precursor and polyvinylpyrrolidone (PVP) as organic capping reagent **(Li D. et al., 2004).** Such a nanostructured layer, fabricated by electrospinning technology, firstly improves sensor features with respect to those of compact films, by enhancing the global number of binding sites of analyte-sensor and reducing some bulk drawbacks. Secondly, the combination of metal oxides and metal nanostructures, improves the sensitivity, allows sensor to work at room temperature, tunes selectivity towards different gas species by adjusting the surface to volume ratio of nanosized structures and affect sensor lifetime. The resulting material was expected to be suitable for novel mercury sensors fabrication, since a similar nanofibrous scaffold doped with AuNPs was described in literature as filtering system capable of adsorbing and removal mercury vapor from the environment with an efficiency of about 100% **(Yuan, Y. et al., 2012)**. In fact, in previous works **(Macagnano, A. et al., 2015a)** the authors reported the ultra-high sensitivity of the sensor, capable to detect up to dozens ppt, despite of a long time necessary to reveal the analyte at these concentrations, in air. In this work the chance to apply the sensor in polluted sites and in real time has been presented and described. Additionally, the proposed method of fictionalization should provide also a chance of tuning the distribution and the size of the metal nanoparticles on the fibres. As a consequence, the possible resulting sensors could be conductive also at room temperature, due to the charge transfer among the neighboring nanoparticles under a potential application. Micro-interdigitated electrodes (IDEs) of Pt/Ti were designed in order to create 3D-nanostructured chemoresistors potentially capable of adsorbing and revealing elemental mercury vapors in the

atmosphere. As preliminary study, diverse non-woven nanofibrous layers of titania variously decorated with AuNPs were investigated in morphological and electrical properties. Chemoresistors were tested for their capacity of detecting Hg^0 vapors at room temperature. Then, properly selected chemoresistors were used to detect low concentrations of mercury vapors in both static conditions and under a carrier gas (synthetic air) flow.

Chapter 7

Development of chemoresistors employing TIO$_2$ nanofibers photocatalytically decorated with Au-nanoparticles for to detect mercury vapors in the atmosphere

7.1 Materials, methods and characterization

7.1.1 Chemicals and IDEs

All chemicals were purchased from Sigma-Aldrich and used without further purification: polyvinylpyrrolidone (PVP, Mn 1,300,000), titanium isopropoxide (TiiP, 99.999%), gold(III) chloride hydrate (HAuCl$_4$, 99.999%), anhydrous ethanol (EtOH$_a$) and glacial acetic acid (AcAc$_g$). Ultrapure water (5·5 $^{10\text{-}8}$ S $^{cm\text{-}1}$) was produced by MilliQ-EMD Millipore. The transducer adopted in the present work to convert the physico-chemical interactions of analytes with the different polymer fibers in an electrical signal was an interdigitated electrode (IDE) **(James, J. Z. et al., 2013).** Specifically, the transducer consisted of 40 pairs of electrodes (150 nm in electrode thickness, 20 μm in gap and electrode width and 5620 μm in length) was manufactured in CNR laboratories through a standard photolithographic process (lift-off procedure), then followed by Ti sputtering and Pt efiberation, suitable to generate the electrodes of the size reported above, on a 4 in. oxidized silicon wafer. After electrospinning deposition all the electrical signals of the resulting chemoresistors were recorded by an electrometer (Keithley 6517 Electrometer).

7.1.2 Electrospinning technology: solution and deposition

Electrospinning is a widely used technique for the electrostatic production of nanofibers, during which an electric field is used to make polymer fibers with diameters ranging from 2 nm to some micrometers from polymer solutions (or melts). It is currently the most economic, versatile, and efficient technology to fabricate highly porous membranes made of nano and/or micro fibers also for sensors **(Macagnano, A. et al., 2015b).** It is based on the application of a high voltage difference between a spinneret ejecting a polymeric solution and a grounded collector. The jet of solution is accelerated and stretched by the external electric field while travelling towards the collector, leading to the creation of continuous solid fibers as the solvent efiberates. The electrospinning apparatus **(Figure 7.1)** used in the present study (designed and assembled in CNR laboratories) comprised a home-made 150 clean box equipped with temperature and humidity sensors, a syringe pump (KDS 200, KD Scientific) and a grounded rotating cylindrical collector (45 mm diameter), a high voltage oscillator (100 V) driving a high voltage (ranging from 1 to 50 kV) and a high power AC-DC (alternative 153 current-direct current) converter.
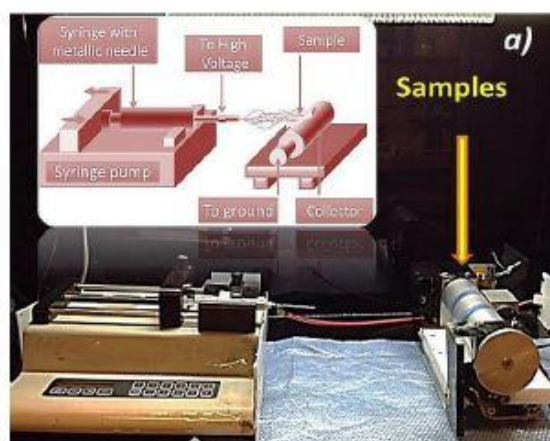
Figure 7.1: Electrospinning equipment comprising a syringe pump and a grounded rotating cylinder collector where the samples take place for their coverage (sketch and photograph).

Electrospinning solution (7.877×10^{-5} M), was prepared by dissolving PVP in EtOH$_a$ and stirring (2 hours). A 2 ml aliquot of 1:4 (w/v) solution of TiiP solved in 1:1 (v/v) mixture of AcAc$_g$ and EtOH$_a$ was freshly prepared and added to 2.5 ml PVP solution under stirring in order to obtain a 1.95 (w/w) TiiP/PVP final ratio. Both mixtures were prepared in a glove box under low humidity rate (<7% RH). The syringe filled with the TiiP/PVP solution and housed in the syringe pump was connected to a positive DC-voltage (6 kV), and set to a 15 cm far grounded rotating collector. The substrates were fixed through suitable holders onto the collector (600 rpm, 21 °C and 35% RH) and processed (feed rate 150 ml h^{-1}) for 20 min to obtain scaffolds for sensors and 1 h to get thicker fabric. After deposition, PVP/TiO$_2$ composite nanofibers were left for some hours at room temperature to undergo fully self-hydrolysis of TiiP **(Li, D. et al., 2004).** And then annealed under oxygen atmosphere (muffle furnace) using a thermal ramp from room temperature up to 550 °C (1°C min^{-1}, 4 h dwell time) in order to remove PVP and crystallize the metal oxide (anatase). Upon calcination, the diameters of fibers were extraordinarily shrunk: mean diameters of fibers were estimated through image analyses to be approximately within the range of 60-80 nm. Specifically, the resulting fibers appeared fine and rough at surface, with a fairly homogeneous fabric. The absence of beads and the good quality of the long and continuous fibers was confirmed through SEM micrographs. A highly porous and dense network of nanofibers covering the electrodes was observed, showing interconnected void volumes (porosity) and high surface-to-volume ratios (specific surface area). Zampetti et al. reported that such a fibrous layer showed a 99% of pores having an area less than 10 μm^2, with more than 80% pores being <1 mm^2 **(Zampetti, E. et al., 2013).**

7.1.3 AuNPs/TiO$_2$NFs photocatalytic decoration

Exploiting the photocatalytic properties of TiO$_2$, gold nanoparticles were selectively grown, under UV-light irradiation, on the electrospun titania nanofibers through the photoreduction of HAuCl$_4$ in the presence of an organic capping reagent (PVP). Thus the resulting fibrous scaffolds were immersed into two aqueous solutions containing HAuCl$_4$ differently diluted (called [α]=2.9 10^{-4} M and [β]=7.4 10^{-4} M) and PVP (0.1 M) as capping agent and dipped into an aqueous solution containing HAuCl$_4$ and PVP (1.5·10^{-3}M and 0.1M respectively) and exposed to UV light irradiation for specified intervals (UV lamp (365 nm) (Helios, Italquartz), to induce TiO$_2$ mediated catalytic Au oxidation onto TiO$_2$ nanofibers and formation of AuNPs/TiO$_2$ eletrospun nanofibrous scaffold. Depending on the gold nanoparticles size that were forming in photocatalysis, the dip-solution changed from light yellow to purple.

After UV irradiation, samples were rinsed extensively with water and then air-dried. Before morphological, electrical and sensing measurements, samples were heated at 450 °C per 1 h to eliminate the PVP traces.

7.1.4 Fibers characterization

Morphological characterization was provided by scanning electron microscopy (SEM), atomic force microscopy (AFM) and transmission electron microscopy (Conventional-and High Resolution-TEM (CT and HRT, respectively)). SEM micrographs were captured at 5 kV accelerating voltage (Jeol, JSM 5200, 20keV). AFM micrographs were captured in tapping mode using 190Al-G tips, 190 kHz, 48N/m (Nanosurf FlexAFM). CT and HRT micrographs were performed at 200 keV with an analytical double tilt probe (α

$\pm$ 30°; β $\pm$ 15°) (ZEISS LIBRA 200FE HR-TEM). TEM specimen were prepared by gently scraping at first the TiO_2 nanofibrous layer electrospun onto the silicon support and then collecting the nanofibres through adhesion upon contact with holy carbon thin film (**Ayache, J. et al., 2010**). SEM analyses of coatings electrospun onto IDEs were also used to assess the pattern (distribution, orientation, extent of coating and adhesion) of the electrospun fibers on the electrodes. The diameter size distribution of Au nanoparticles was evaluated through observation and statistical analysis of more than 150 nanoparticles (NPs). Images were analyzed by means of iTEM (TEM Imaging Platform software by Olympus). UV-200 Vis spectra were provided by Spectrophotometer UV-2600 (Shimadzu), analyzing quartz slices coated with nanofibers. These substrates were able to collect fibers by electrospinning (20 min), and then were subjected to calcination according to the described above procedure, and then UV irradiation in the aqueous solution. The fibrous layer stayed stuck to the substrate if the thickness was thin enough. Longer depositions caused curling of fibers during the calcination process.

7.2 Electrical measurements

The sensor was placed in a suitable PTFE-made measurement chamber (0.7 ml volume) connected to an electrometer (Keithley 6517 Electrometer) capable of measuring the current flowing through the IDE, when a fixed potential was applied to it, and to send data to a PC. Dynamic measurements were carried out at room temperature both using: (i) 4 channel MKS managing four MKS mass flow controllers (MFC), set in the range 0-200 sccm and (ii) Environics S4000 (Environics, Inc.) flow controller, containing three MFCs supplying different flow rates (up to 500, 250 and 25 sccm, 212 respectively), managed by its own software. Pure air (5.0) (Praxair–Rivoira, Italy) was used as gas

carrier. A homemade PTFE (polytetrafluoroethylene) permeation tube filled with a suitable amount of Hg^0 was included within such a delivery system to get set dilutions of Hg-saturated vapors. The tube was immersed in a thermostatically controlled bath, thus the desired Hg^0 concentration delivered to the sensor was achieved by both tuning the temperature of the permeation tube and the dilution flow. The Hg^0 concentration was checked by Tekran®2537A analyzer. Responses were calculated as $\Delta I/I_0$, where ΔI was the current variation and I_0 was the current when synthetic pure dry air was flowed. Sensor was restored after a quick thermal shot at 450°C under flow of pure air 220 (450°C).

7.3 Hg^0 vapor measurements

In order to test the responsiveness of the device to low Hg^0 vapor concentrations, a procedure was used employing an Hg^0 vapors delivery system, comprised of an Hg^0 vapor generator, namely a permeation tube, and a gas mass-flow diluting system. The working principles of such a procedure are the dependence on temperature of both dilution of a saturated source of mercury and gas permeation. The final Hg^0 concentration of interest was then obtained by both tuning the temperature of the permeation tube and the dilution flow. Briefly, the homemade PTFE (polytetrafluoroethylene) permeation tube filled with a suitable amount of Hg^0 was coupled to a mass flow controller system (4-Channel-MKS 247) to dilute the mercury-saturated gas with synthetic pure dry air (5.5 grade by Praxair-Rivoira, Italy). Specifically, the permeation tube was introduced into a quartz gas-washing bottle immersed into a thermostat controlled water bath. The permeation rate was first let equilibrating at the temperature of interest (35 °C) under a low flow rate, namely 10 sccm, passing through the mercury reservoir to ensure

the gas became saturated with mercury. The mercury-saturated gas was then diluted to the concentration of interest by flowing it into quartz mixing chamber, where it was blended at room temperature together with flowing synthetic dry air. Both gas-washing bottle and mixing chamber were continuously flowed overnight with synthetic dry air to achieve equilibrium, then fixed aliquots of Hg^0 vapor were withdrawn through a PTFE septum using a gas-tight glass syringe, and injected into a measuring chamber consisting of a 100 mL quartz bottle. The Hg^0 concentration in the gas washing bottle, in the mixing chamber and in the measuring chamber were all checked by Tekran®2537A analyzer. Alternatively, Hg^0 vapours were flowed directly into the measuring chamber at selected flow rate values after dilution by air flowed throughout the mixing chamber **(Figure 7.19, sketch).** A single sensor was housed in each measuring chamber in order to expose the sensitive area to fixed concentrations of elemental mercury vapors. Responses were calculated as $\Delta I/I_0$, where ΔI was the current variation and I_0 was the current when synthetic pure dry air was flowed. A 3 min thermal shot at 450°C under flow of pure air was carried out to restore sensors to the starting current value, after each Hg^0 vapors measurement. The outgoing air from both mixing and measuring chambers were passed through a trap of activated coal to retain the generated Hg^0 vapors.

7.4 Results and discussion

7.4.1 Morphological investigation of AuNPs/TiO$_2$ nanofibrous layer
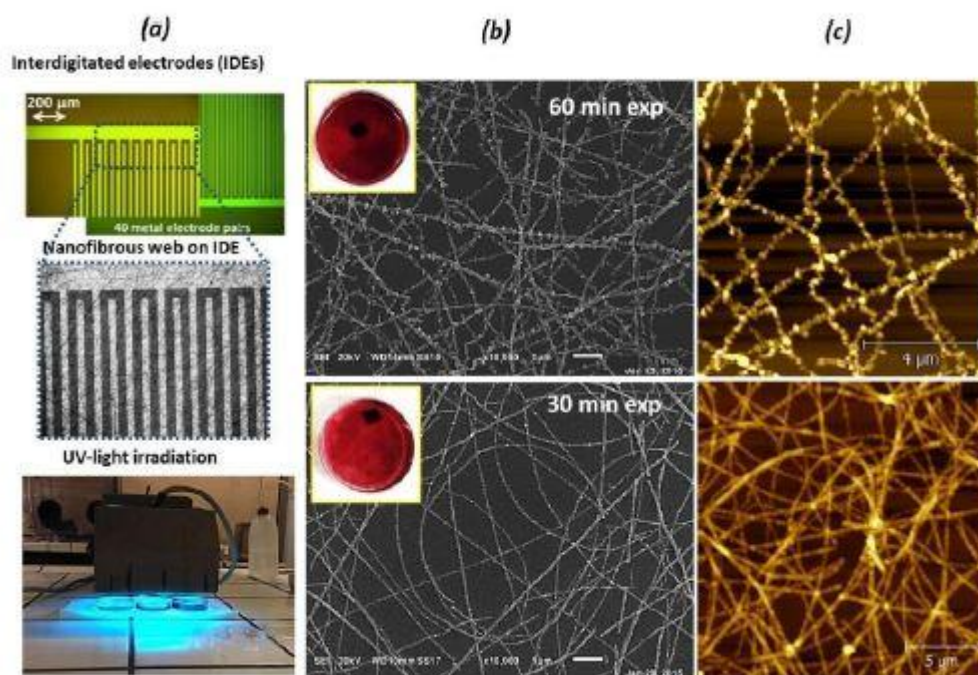
Figure 7.2: (a) Optical micrographs of the electrodes before (top) and after electrospun deposition (in the middle) and a picture of the samples (down) in solution and under UV irradiation; SEM (b) and AFM (c) micrographs of titania nanofibers after 60 min and 30 min of UV exposure, respectively. The chemical reaction can be monitored by the color change of the solution (colorless>orange>red>purple).

Specifically, titania fibers were decorated with gold nanoclusters (AuNCs) induced to grow selectively upon photocatalytic reduction of HAuCl$_4$ caused by UV light irradiation **(Figure 7.2 (a)).** Morphology, size, distribution of gold nanoclusters and the degree of AuNPs coverage of the nanofibers seemed to depend on both UV irradiation exposure **(Figures 7.2 (b)-(c)),** salt concentration and concentrations of organic capping reagent. When the samples were UV irradiated for 1 hour, fibers were completely covered with Au particles with globular shape merged together, and numerous protruding

260

buds, densely clustered and overlapping (SEM and AFM micrographs in **Figure 7.2**). On the contrary, when fibers were exposed to UV irradiation for a shorter time (30 min), they appeared more homogeneously coated with round-shaped nanoparticles. PVP as an organic polymer and its 0.1 M concentration were chosen according to the scientific literature, because enabling to get regular shaped nanoparticles (i.e. semispheres), when the photocatalytic properties of TiO_2 were used to grow AuNPs on TiO_2 nanofibers **(Wold, A., 1993).** In its study, indeed, Wold reported that the absorption of photons by TiO_2 was able to excite electrons from the valence band to the empty conduction band (>3.2 eV), thus generating electron–hole pairs (see the sketch of **Figure 7.5**). The photogenerated holes oxidised water, thus producing hydroxyl radicals capable of oxidising organic compounds (e.g. pollutants) in water, whereas the excited electrons reduced the gold ions on the surface of TiO_2 nanofibers, and induced AuNPs deposition. The photocatalytic process was pointed out by the change in color of the solution from colorless to deep purple, when a solid substrate covered with anatase nanofibers was dipped into it. A $1.47 \cdot 10^{-3}$ M $HAuCl_4$ solution was firstly prepared and then further dilution were carried out to obtain decreasing salt concentrations, until the minimum concentration providing AuNPs deposition on the fibers was identified. By combining electrospinning and sol-gel techniques, nanofibers made of PVP and amorphous TiO_2 were obtained by injecting the ethanol/acid solution, containing both PVP and TiiP, under a high voltage. The resulting fibers were collected for 20 min on oxidized silicon wafers and IDEs, properly fixed on the surface of a conducting rotating collector to form nonwoven mats. The resulting scaffolds are well known in literature for their high surface areas and relatively small pore sizes **(Zampetti, E. et al., 2013).** By changing the deposition time, both thickness and consistence of the mats changed: one hour deposition provided the formation of a thicker white and soft fabric easily peeled off **(Figure 7.3),** hygroscopic and soluble in both water and polar

solvents; a 20 min deposition generated a fibrous film adhering to substrates, too thin to be weeded.

(a)   **(b)**
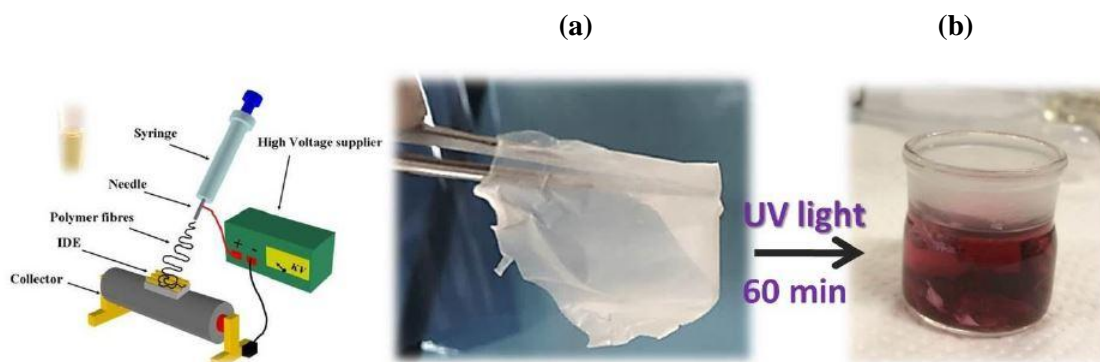
Figure 7.3: Sketch of an electrospinning set-up comprising a syringe and a grounded rotating cylinder collector where the samples take place for their coverage (a); a piece of a nanofibrous fabric of TiiP/PVP peeled from the substrate after 1 hour of electrospinning deposition (b) a red-purple aqueous solution of $HAuCl_4$/PVP after UV-light irradiation treatment holding a piece of the nanofibrous fabric of TiO_2 (anatase) obtained after TiiP/PVP annealing (c).
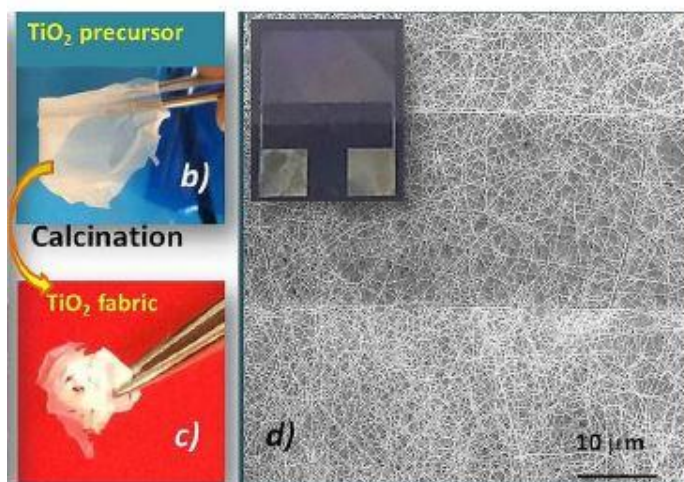
Figure 7.4: a piece of nanofibrous fabric of TiiP/PVP (b) after 1 hour of electrospinning deposition and after calcination at $550°C$ (TiO_2 nanofibrous fabric) (c); SEM picture of a dense network of nanofibres of TiO_2 covering IDEs electrodes (d). A picture of an IDE coated of nanofibers was reported as inset, too.

262

The following calcination resulted in the complete degradation of PVP with formation of crystalline TiO_2 (anatase) and a significant shrinkage of fibers dimension (60-80 nm diameter, 5-40 nm grain sixe). Calcination of 1 h fabric made it thinner (upon the diameter shrunk of the fibers), thus resulting in a clearer, glassy and highly brittle material **(Figures 7.4 (b)-(c))** but insoluble in water and all organic solvents. The 20 min deposited fibrous layer resulted finely attached to the substrate, as confirmed by electron microscopy images **(Figure 7.4 (d)).**

In the present study, among a series of differently coated fibrous layers, only the fibrous nanocomposites that were conductive at room temperature were selected and then their electrical and sensing features investigated. Initially the samples were immersed in the highest concentrated solution and irradiated with UV-light for various times **(Figures 7.2 (b)-(c)) (Macagnano, A. et al., 2015a)**: the relationship between the irradiation time and the size and distribution of the gold nanoparticles along the fibers was described. Specifically, a longer exposure generated nanofibers completely covered with Au particles with globular shape merged together and with numerous protruding budding, densely clustered and overlapping. On the contrary, when nanofibers were exposed to UV irradiation for a shorter time (30 min), they appeared more homogeneously coated with round-shaped nanoparticles **(Figure 7.5).**
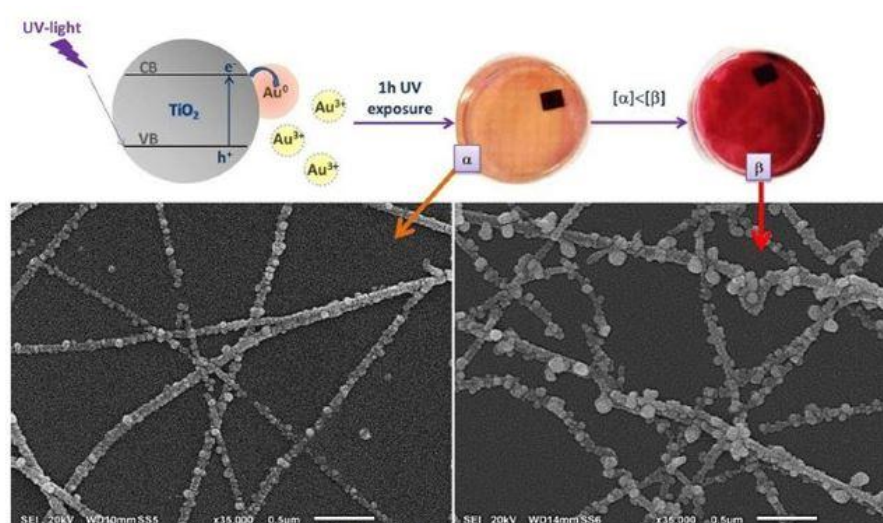
Figure 7.5: SEM micrographs of TiO$_2$ fibers after AuNPs functionalization by UV-light irradiation occurring within two HAuCl$_4$ aqueous solutions to lower (left) and higher (right) concentration, respectively. On the top both a sketch of the photocatalytic process and a picture of the two processed solutions containing the nanofibrous samples were reported.

Such AuNPs decorated nanostructured scaffolds were investigated and tested as potential sensors for mercury vapors. However, working under the described conditions, a great variability in experiments was observed, probably due to the extremely fast photocatalytic process occurring on titania fibers (starting after a few minutes by UV-irradiation). Then, 60 min was set as UV-light fiber exposure time and the samples were dipped into the diluted solutions. **Figure 6.5** (top images) shows two samples supported on silicon wafers, after irradiation for 60 min and dipping in α and β solutions, left and right, respectively. After UV exposure, both solutions turned from clear yellow into orange (α) and red purple (β) colors, respectively, depending on HAuCl$_4$ concentration. In both treatments, the surfaces of the anatase nanofibers observed in SEM micrographs (**Figure 7.5, left picture**) appeared densely decorated with globular nanoparticles, but size, arrangement and density differed, depending on the salt concentration. AuNPs particles showed a more homogeneous distribution on TiO$_2$ nanofibers upon dipping in lower HAuCl$_4$ concentrations (α). In these samples, AuNPs mostly appeared individually distributed, i.e. without forming any aggregation structure, when both analyzed by SEM (**Figure 7.5, left picture**) and TEM (**Figure 7.6 (b)).** On the contrary, TiO$_2$ nanofibers upon dipping in β solution showed aggregation structures of AuNPs with diameter until 90 nm and more (**Figure 7.5, right picture and Figure 7.6 (a)).** The controlled gold deposition was due to the photo-excited electrons on the surface of TiO$_2$ nanofibers that were able to reduce the gold ions thus inducing gold deposition (**Figure 7.7, the sketch).** The capping reagent was responsible of the shape of the particles. Furthermore, a broader size distribution of AuNPs along nanofibers was

observed, when analyzed by SEM **(Figure 7.5, right picture)** and TEM **(Figure 7.6 (a)-(d)).** The surfaces of nanofibers observed in SEM micrographs **(Figure 7.5, right)** appeared densely decorated with globular nanoparticles. In the CT image **(Figure 6.7, inset)** the gold nanoparticles appear darker and spherical or quasi-spherical. The single particles size were ranging between 2 and 20 nm and 7.8±3 nm was estimated average diameter **(Figure 7.6 (c)).** Gold nanoparticles grew directly onto the nanofibers and their adhesion appeared relatively strong (despite due to van der Waals forces), since they both resisted to water rinsing and fibers scratching for TEM analyses. Approximately spherical structures around 50 nm diameter, densely packed and forming protruding budding along fibers, were sometimes observed along the electrospun TiO_2 nanofibers **(Figure 7.8 (a)-(d)).**
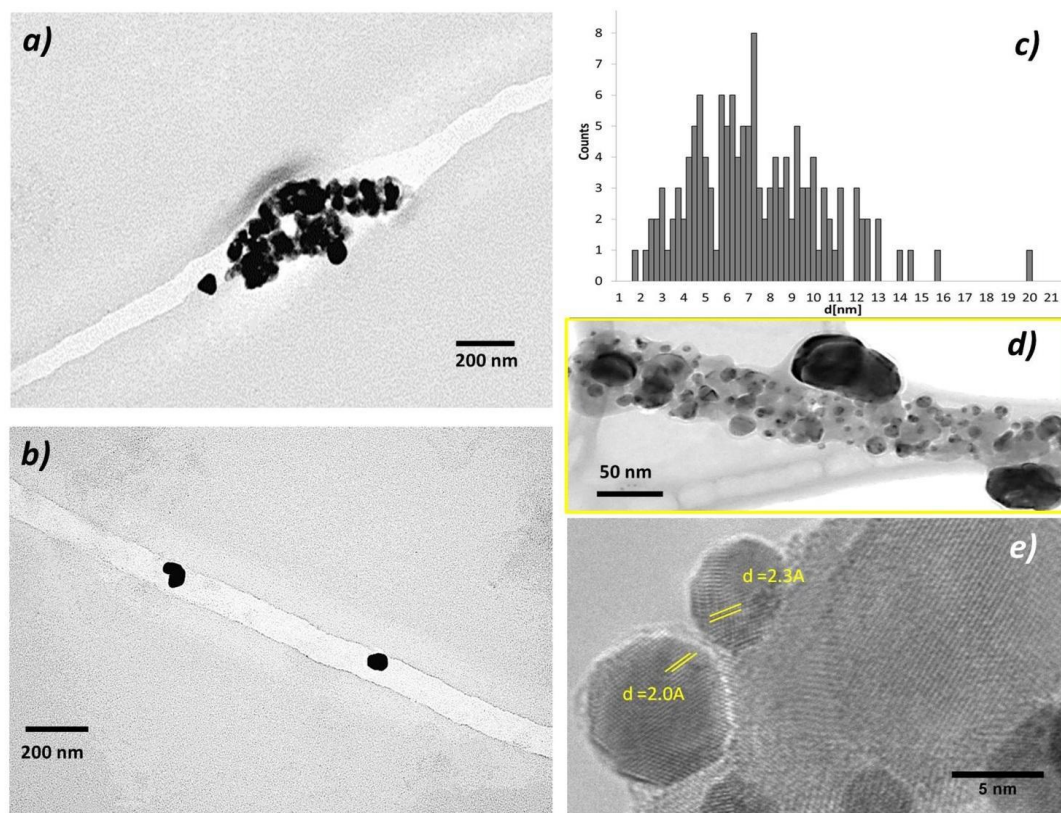
Figure 7.6: CT micrograph of a titania fiber holding a AuNPs aggregation (β sample) (a); CT micrograph of a titania fiber holding a few NPs (αsample) (b); bar-graph of the distribution of the diameter values estimated on 150 nanoparticles (c); CT image of a gold nanodecorated fiber of TiO₂ (β sample) (d); HRT micrograph of contact region between the acicular structure of titania nanofibers and the gold spheres (e).
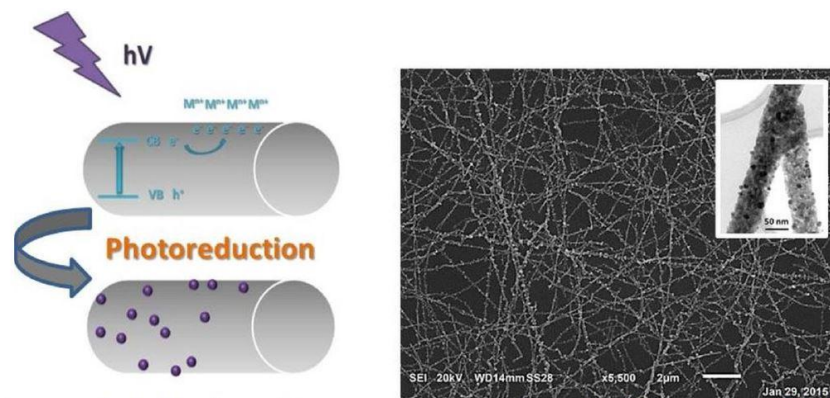
Figure 7.7: A sketch of the photocatalytic process occurring on the fibers surface (left); SEM picture of a dense nanofibrous network of AuNPs/TiO₂ coating a silicon wafer (right); a C-TEM micrograph of fibers finely decorated with gold nanoparticles (the darkest ones) fixed without using any additional linker (inset).
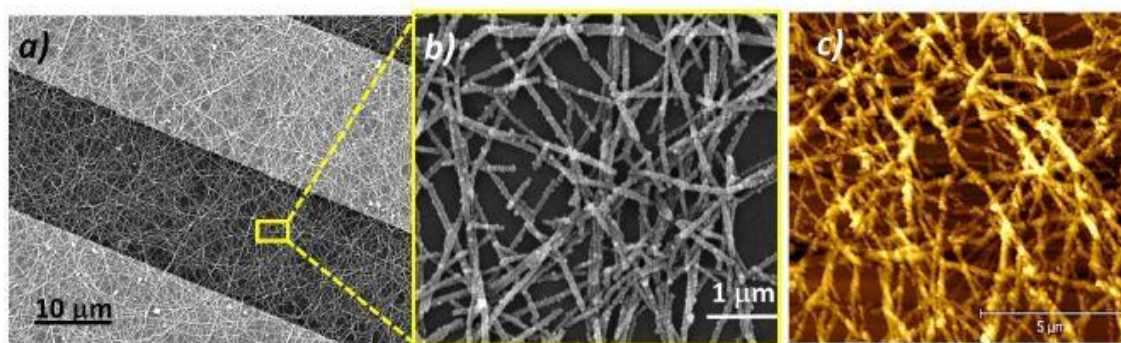
Figure 7.8: SEM micrographs of TiO₂ fibrous layer coating the electrodes of an IDE after the photocatalytic process (a) and magnification of an area (5x5µm) between the two electrodes (b); AFM micrograph of the AuNPs/TiO₂ scaffold on silicon wafer (12x12 mm) (c).

In **Figure 7.6 (e)** the HRT micrograph shows the contact region between the acicular structure of titania nanofibers and the gold spheres. The interplanar distances measured within the two darker crystals, d= 2.3 Å and d= 2.0 Å , respectively, corresponded to the gold {111} and {200} planes distances, confirming that they were gold. In both chemoresistors and silicon wafers, the TiO$_2$ nanofibrous layers were still attached to any substrate after the photocatalytic treatment in immersion. Furthermore, gold nanoparticles did not grow directly on the substrates and their immobilization onto the nanofibers appeared relatively strong (despite due to van der Waals forces), since they both resisted to water rinsing and fibres scratching for TEM analyses. After the photocatalytic treatment, the original calcined white porous scaffold **(Figure 7.4 (c))** became purple-violet, depending on the size and density of the immobilized AuNPs (data not shown). SEM micrographs reported in **Figure 7.8** confirmed the good coverage of the electrodes (a) and the persistence of the high porosity (b) even after AuNPs decoration. AFM micrograph presented in **Figure 7.8 (c)** showed a 3D-network of AuNP/TiO$_2$ nanofibers and their interconnections, which highlighted the absence of any merging effect on nanofibers, both upon UV-irradiation in solution (decoration treatment) and heating (capping agent removal treatment). Furthermore, the presence of long and continuous fibers within the fabric was confirmed.

7.4.2 UV-Vis spectra AuNPs/TiO$_2$ nanofibers before and after exposure of Hg°

After photocatalytic process, the white porous mat became purple-violet. As seen in the spectrum of the AuNP/TiO$_2$ system, a characteristic absorbance band appeared at around 543 nm **(Figure 7.9)**, which corresponded to the

surface plasmon resonance (SPR) of the AuNPs (Sun et al, 2003). A red shifting and broadening of the absorbance band was observed with the increasing in AuNP size and fiber loading, respectively. The color is strictly depending on the size of the nanoparticles, and then their agglomeration at the solid state. According to Bui et al. (2007), such a band broadening phenomenon is due to the electric dipole-dipole interactions and coupling occurring between the plasmons of neighbouring particles, whereas nanoparticle agglomeration phenomena occurred. Due to these features, UV-Vis absorption spectroscopy has been used in literature as a technique to reveal the changes in size, shape and aggregation of metal nanoparticles in liquid suspension after exposure to heavy metals, as Hg^0 (**Morris, T. et al., 2002).** Both blue-shifted wavelength and its extent were proportional to the amount of Hg^0 that entered the liquid suspension. Similarly, when the gold decorated nanofibers of titania, collected on a quartz slice, were exposed to Hg^0 vapors (2 ppm) in air for 15 min, a significant blue shifting was reported (~ 3 nm) **(Figure 7.10)** due to the atomic adsorption of GEM (gaseous elemental forms of Hg) on the surface. The nanoparticles could be regenerated by heating the sample at 550°C for 3 minutes to remove Hg^0. The recovery of the AuNPs was stated by the achieving of the original values of wavelength. The regeneration could be done for dozen times without any deterioration.
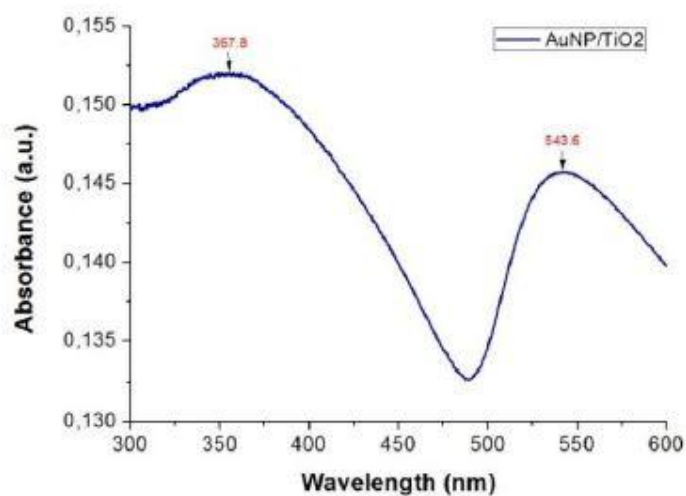
Figure 7.9: UV-Vis spectrum of a titania nanofibrous network after gold decoration (TiO$_2$: 367.8 nm; Au NPs: 543.6 nm).

.
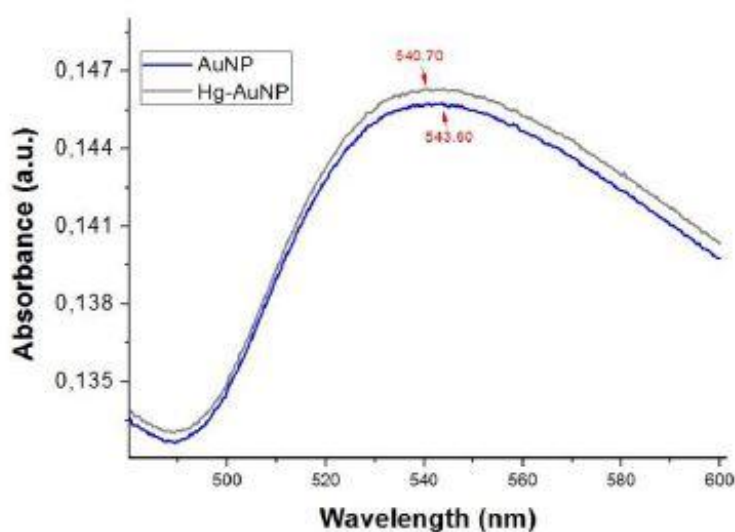
Figure 7.10: UV-Vis spectra of AuNPs/TiO$_2$ nanofibers before (blue) and after a 15 min exposure to 2 ppm of Hg^0 (gray).

Similarly, in chemoresistors, the TiO$_2$ nanofibrous layers attached to the substrates **(Figure 7.11),** changed color after photocatalytic treatment. The IDE layout **(Figure 7.11)** show a set of interdigitated electrodes which

occupies an area approximately 3x5 mm, completely coated with the sensitive fibers, and two bonding pads (2x2 mm) that will be connected to the electrometer (DC voltage). Such a planar interdigitated electrode configuration is the most commonly used for conductometric sensing applications.
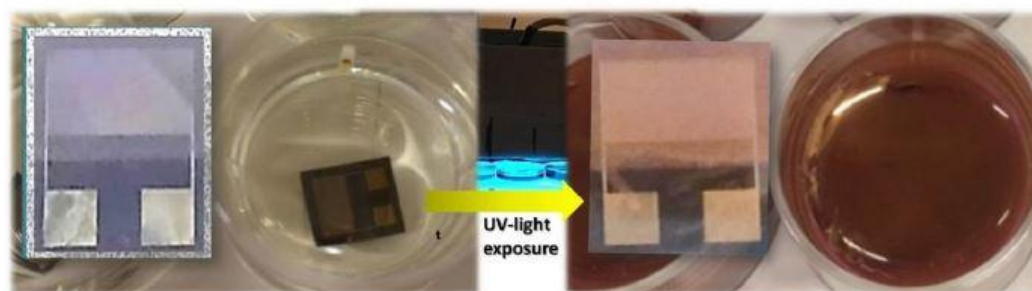
Figure 7.11: Chemosensor fabrication and final structure: IDE dipped (left) and exposed to UV-light (right) for gold decoration.

7.4.3 Electrical and sensing features

Preliminary results related to sensors coated with 1h UV-irradiated fibers (the most conductive sensors, R=580-650 Ohm) showed Ohmic behavior in air and at room temperature **(Figure 7.12)**, but with different resistance values depending on the quality of the coverage, as expected. Oxygen and relative humidity did not affect the electrical parameters of the sensors, thus comparable electrical features were reported when measurements were carried out under nitrogen or air **(Figure 7.12 (a))** and increasing percentages of relative humidity **(Figure 7.12 (b)).** The strong affinity and specificity of Au for Hg^0 explain the sensitive responsiveness of Au nanoclusters (AuNCs) on the nanofibrous scaffolds to mercury **(Lubick, N. et al., 2013),** highlighted by the current changes of the sensors upon Hg adsorption.

(a)
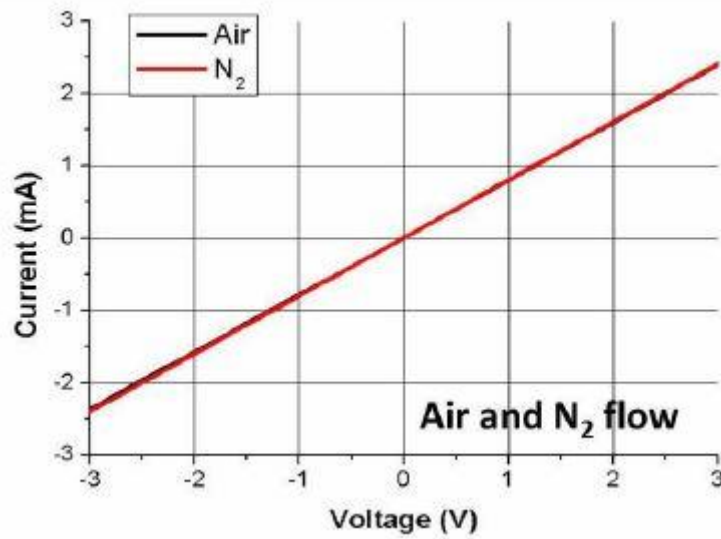
(b)
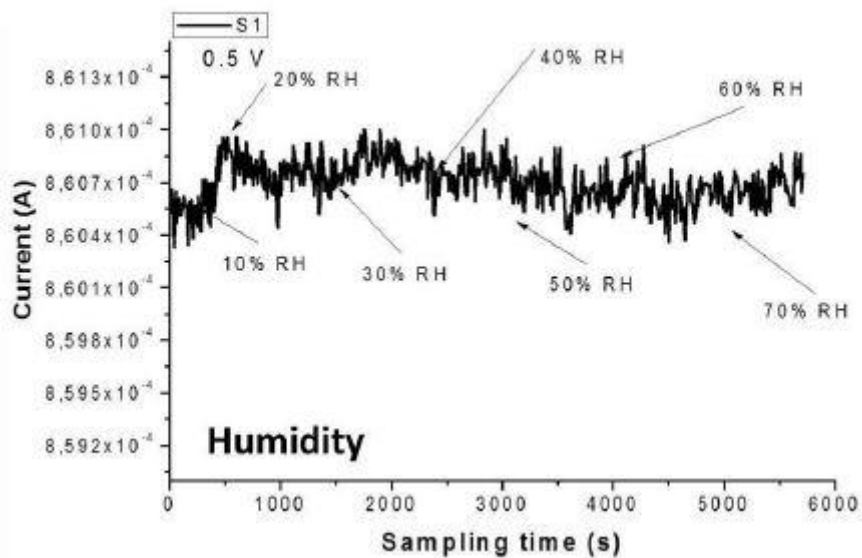
Figure 7.12 (a): Current-Voltage curve of 1h-UV-exposed sensor under air (black line) and nitrogen (red one) flow; (b) sensor transient response (current) to increasing percentage of relative humidity (10%-70% %RH) (0.5V).

271

In detail, sensors exposed to mercury vapors, pointed out a decrease in current, and the slope of the electrical signals seemed to be dependent on analyte concentration. When a sensor was exposed overnight to high concentration of Hg ($P_V = 1.6 \cdot 10^{-3}$ mbar), its resistance changed by 30% **(Figure 7.13 (a)).** In order to test the responsiveness of the device to low Hg concentration, mercury vapors were flushed, from a dynamic permeation tube, throughout the measuring chamber. The final Hg^0 concentration was obtained by tuning the oven temperature and the dilution flow. Preliminary results showed that the exposure of a sensor to 7.5ng/l of Hg resulted in decreasing current, with a rate of ~109 nA/min (+2V) and a limit of detection about 0.18 ng/l (LOD: three times the standard deviation of the blank) **(Figure 7.13 (b)).** Quick thermal shots restored sensors, due to the high porosity of the layer and the extremely reduced size of the gold nanoclusters.
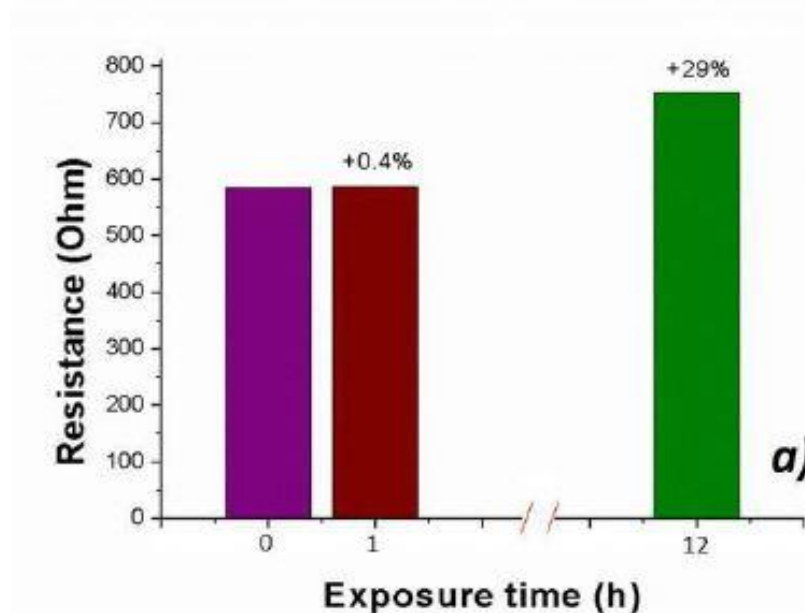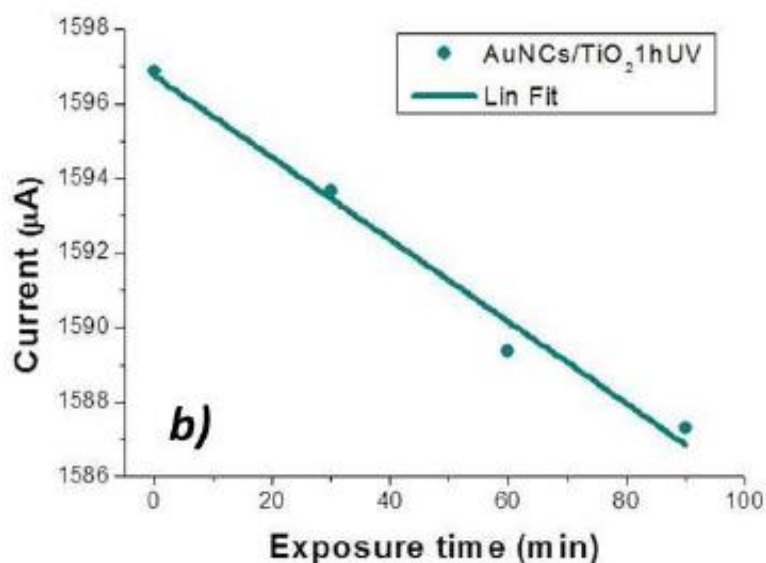
Figure 7.13 (a):Diagram of the change of resistance values of the sensor after 1 and 12 hour of exposure to mercury vapor (1.6 •10^{-3} mbar); (b) Sensor responses (current values) to 10 sccm-flow of mercury-saturated air (~7.5 ng/l) over time (30-90 min).

The resulting sensors, functioning in air and at room temperature, showed constant and low level of resistance, thus providing the potential to work at very the tested sensors to increasing concentrations of mercury vapor reported a general decrease in current. These attracting sensing features sound as encouraging premises to develop sensors for elemental mercury based on electrospun fibers of gold nanofunctionalized titania. In the second phase of the study it was carried out comparison between Current-Voltage (I-V) curves of Sα and Sβ chemoresistors, treated within [α] and [β] solutions, respectively, when synthetic dry air flowed (as shown in **Figure 7.14**). The respective shapes were unaltered when air or nitrogen were flushed over the fibers **(Macagnano, A. et al., 2015a),** suggesting that oxygen concentrations poorly affected the electrical properties of chemoresistors. The resistance of IDE coated with undecorated TiO_2 nanofibers resulted to be too high at room temperature to contribute straight to the final current. The resulting linear shape (Ohmic behaviour) within the selected voltage range (−3V to +3V)

273

indicated a constant resistance value for the Sβ **(Figure 7.14 (β)** and the absence of rectifying contact between the electrodes and developed material. The very low level of resistance ($\sim$1.2 kΩ) provided the possibility to work at low voltage, with consequent effects on the lifetime of the material and energy consumption. Moreover, the linearity of I-V curve suggested that the sensing scaffold had a good adherence to the metal electrodes. Vice versa, the Sα showed a non-linear curve (-6V to +6V) **(Figure 7.14 (α)),** probably related to the lower density of the gold-nanoparticles along the nanofibers, suggesting the formation of a Schottky barrier between nanofibrous material and metal electrodes **(Sharma, B. L., 1984).** Regarding Sα and Sβ conductivity at room temperature, it should be due to the metal nanoparticles distributed along the nanofibers and in contact to the electrodes. The electron conductivity could be described by the percolation model **(Muller, K. H. et al., 2003)** since the titania at room temperature could be supposed like an insulating organic matrix. In fact, the undoped anatase is an anisotropic, tetragonal insulator (with a bandgap of 3.2 eV).
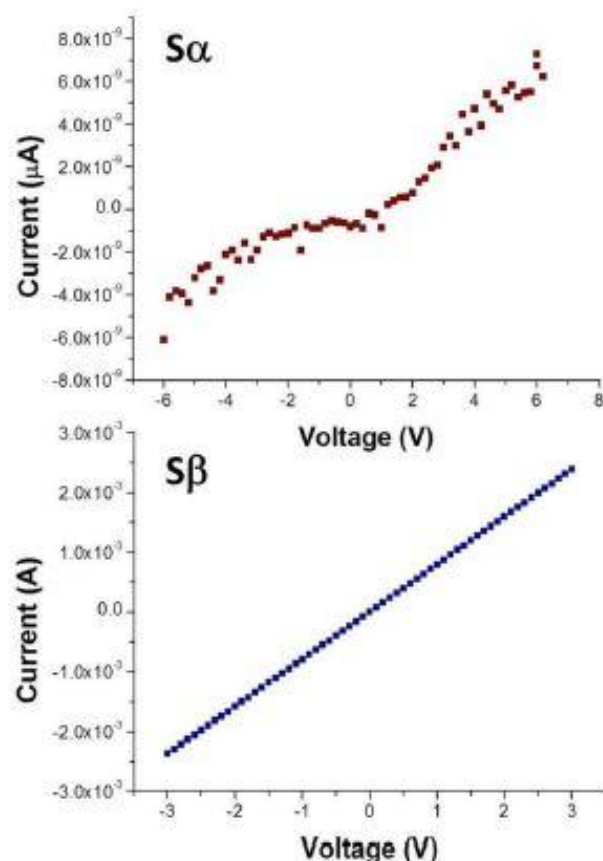
Figure 7.14: Current-Voltage curves of Sα (up) and Sβ (down) chemoresistors.

When it is metal doped, the electron conductivity is dominated by thermally activated electron tunneling from one metal island to the other. However, the conductivity of the nanocomposite is lower than that of pure metal (gold) because the electron mean free path is greatly reduced due to the inclusion of the dielectric (the titania crystals). Above the percolation threshold, continuous metallic pathways exist throughout the metal oxide matrix. In the percolation zone, adjacent metallic nanoparticles undergo extensive coalescence resulting in large irregular nanoclusters. The increase in electrical conductivity results from an increased connectivity of the metallic nanostructures, depending on the fibers size and the metal loading. The AuNPs within the Sβ, although irregular in size, were spaced from each other just a few nm (about 2 nm); whereas longer distances among NPs were estimated in Sα. Photonic and thermal energy commonly enable these devices

275

to overcome the energy gap. In the present study, only the chemoresistors showing Ohmic behavior in air and at room temperature (Sβ) were investigated for convenience in mercury vapor detection. Several sensors (Sβ) were fabricated in laboratory in order to check their reproducibility. Within a set of 20 chemoresistors fabricated in distinct periods over five months the mean resistance value was estimated to be about 1349.95 Ω, S.D.=±150.25 with a minimum of 1020 Ω and a maximum of 1600 Ω (**Figure 7.15).**
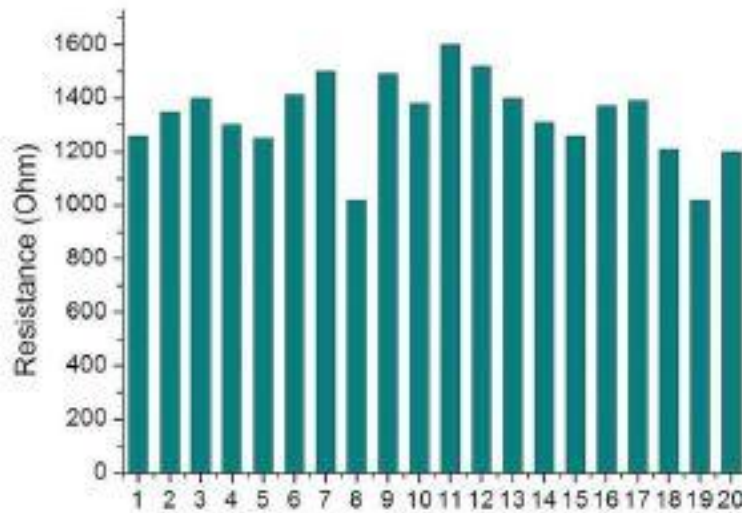
Figure 7.15: Bar-graph depicting the resistance values of 20 chemoresistors (Sβ types).

The sensor measurements, that were the electrical signals reported when interaction between the sensing layers and the analytes were occurring, resulted in a change of the whole resistance (or current, i.e. I =V/R according to Ohm's law) of the device according to the following Eq:

$$R = \frac{1}{2N-1}\rho\frac{\omega}{h \cdot L}$$

where N and L are number and size of the fingers, h and φ the electrode thickness and width, respectively, and p resistivity of the overlying material. Such a planar interdigitated electrode configuration is the most commonly used for conductometric sensing applications. A picture of an electrode is reported in **Figure 7.4 (d).** At one end of the structure there is a set of interdigitated electrodes which occupies an area approximately 3x5 mm; at the opposite end of the chip there are two bonding pads (2x2 mm) connected to the electrometer (DC voltage). Sensing measurements, i.e. current (or resistance) changes, were provided both in continuous and with pulse of potentials applied every a few minutes. The second strategy was tested in order to investigate the possibility to further decrease the power consumption, allowing the sensor to work by battery for quite a long time. Furthermore, in order to investigate the contribution of the measuring system to the sensor features, mercury was detected by injecting a defined volume of polluted air and by flushing known concentration of mercury throughout the measuring chamber. When a volume of air polluted with a known concentration of Hg^0 was injected or flowed into the measuring chamber, Sβ exposed to mercury vapors showed a decrease in current. In detail, when about 74 ppt Hg^0 were injected in the measuring chamber, the measured current value decreased with a rate of ~ $-1.93 \cdot 10^{-5}$ min^{-1} ((I/I_0)/t) until reaching a signal decrement of $-3.7 \cdot 10^{-3}$($\Delta I/I_0$) after ~200 min. In **Figure 7.16** the sensor current values after injection, normalized to the starting current in dry air free from mercury, have been reported when pulses of potential (+1V) were applied. The limit of detection, calculated as three times the standard deviation of the blank, was about 6 ppt. Despite the high sensitivity of the chemosensors to Hg^0 vapor, the response appeared to be slow, when injection procedure was used, probably due to the diffusion rate of mercury (0.14 cm^{2}s^{-1}(**Lugg, G. A., 1968**) into the measuring chamber (100 ml) and then the following adsorption onto the nanoparticles within the titania fabric.
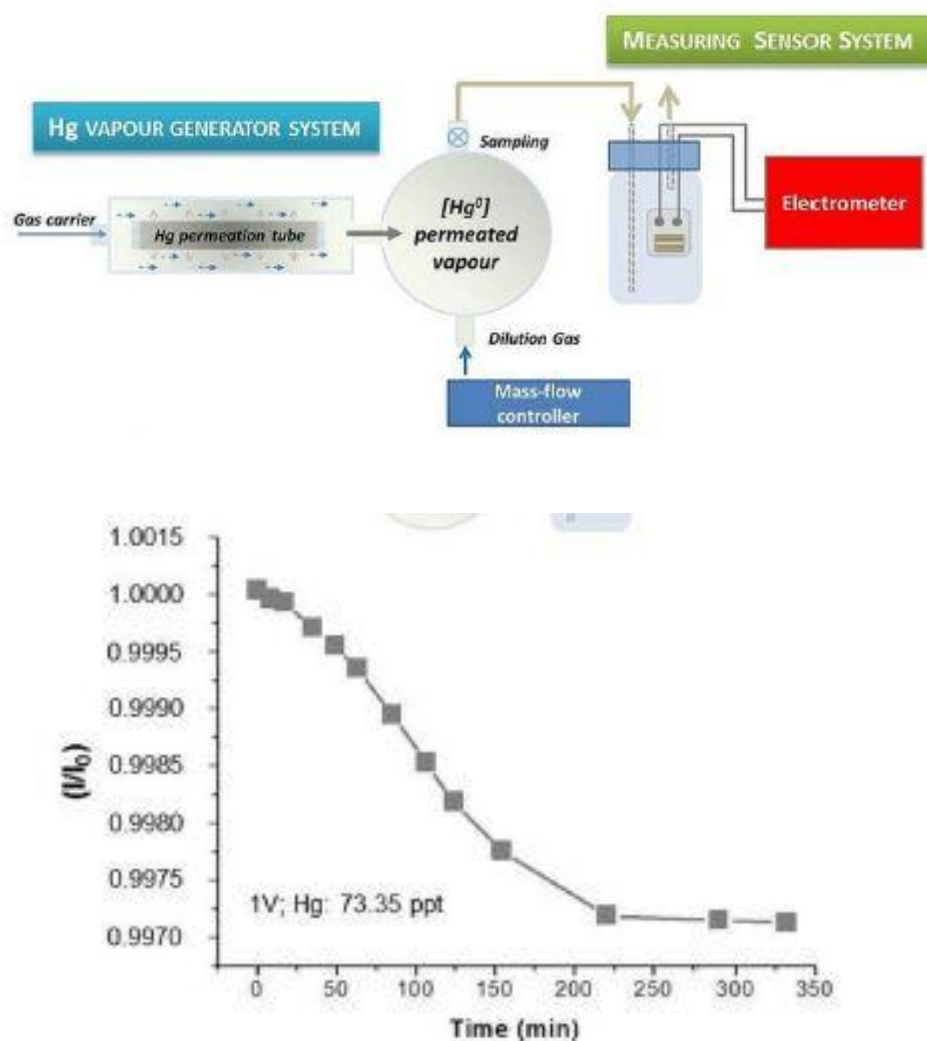
Figure 7.16: Normalized transient response of Sβ chemosensor when Hg^0 ~74ppt was injected into the measuring chamber. Pulses of potential were applied every a few minutes (V=+1V) and current values were recorded (y-axes) over time (x-axes). On the top a drawing of the measuring system set-up.

The response time taken to achieve 90% of the equilibrium point was ~180 min. Similarly the Hg^0 vapors were flowed directly throughout the measuring chamber and a remarkable improvement in response time was achieved, as expected (an increase of the mass flow rate of mercury per time unit). In **Figure 7.17** is depicted the comparison between the curve slopes of the normalized sensor responses to the same concentration of Hg^0, when injected

278

and flowed (the black and red lines, respectively). A comparison between the normalized sensor responses per concentration unit versus time reported an increase of an order of magnitude when the same concentration of the analyte was injected ($2.62 \cdot 10^{-7}$ ppt^{-1}) and flowed ($2.16 \cdot 10^{-6}$ ppt^{-1}), respectively **(Figure 7.17).**

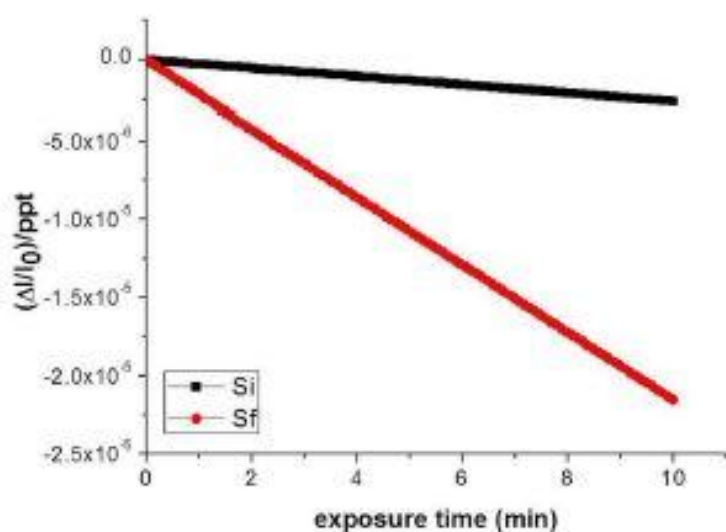**Figure 7.17: Comparison of the sensor normalized response rates per ppt over 10 min when Hg^0 was injected (Si) or flowed (Sf) into the measuring chamber.**

However, since previously the authors reported that nanostructured material could adsorb Hg^0 vapor up to change the chemosensor resistance value by 30% **(Macagnano, A. et al., 2015a)** a continuous flow of the analyte over the material was able to cause a continuous decrease in current over a long time. This effect is presumably due to the kind of interaction between mercury and gold. Indeed, the adsorption constant is orders of magnitude higher than the desorption constant, justifying the limited desorption at near room temperatures **(Crosby, J., 2013).** Mercury adsorption proceeds towards a submonolayer until the available sites are full (Langmuir isotherm model). After surface adsorption, additionally, the formation of islands of amalgam occurs hindering the release of mercury in the environment. Indeed, mercury

desorption can occur by changing the vapor partial pressure only at the initial phase of the interaction. The fabricated nanostructured chemosensors could be compared to a 3D-conductive trap for mercury vapor, which works until the saturation of all the interacting sites occurs. A complete desorption of mercury occurred heating the sensing area covered by the fibres up to 450 °C for 3 min, after each measurement. In fact, current resulted completely recovered after this treatment, as reported in **Figure 7.18 (b)**. The sensor was exposed to a flow of mercury in dry air with a concentration of 800 ppb for 5 min **(Figure 7.18 (a)),** and then dry air was used to clean the sensor surface. The current curve trend slightly changed when clean air was flowed, stabilizing at about the current values reached for Hg^0 adsorption.

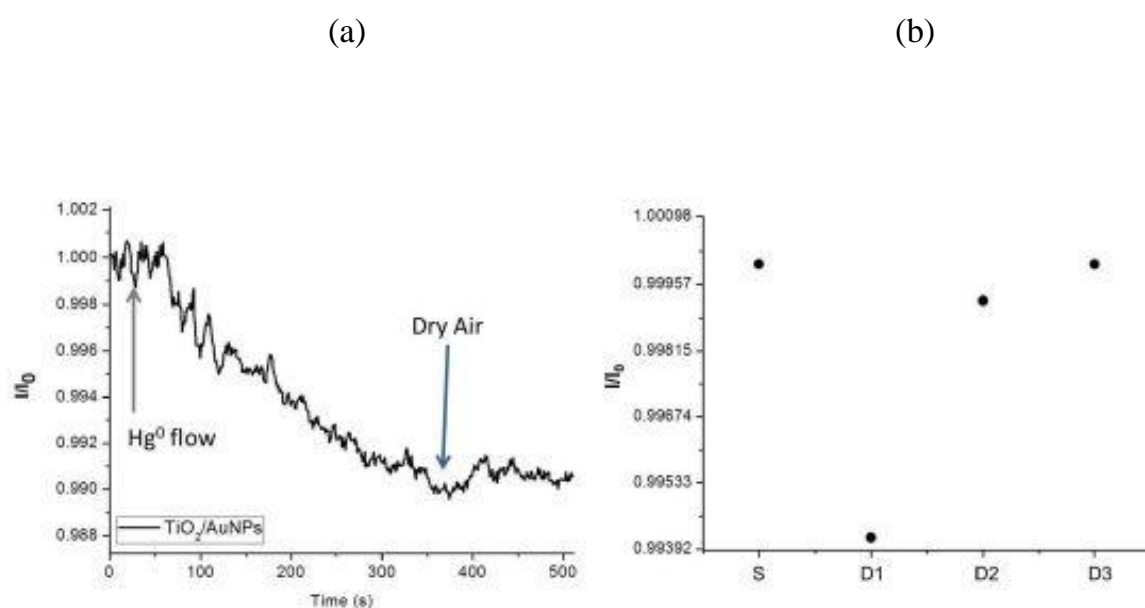(a)   (b)

Figure 7.18: Transient sensor response when Hg^0 800 ppb was flowed throughout the measuring chamber for about 5 min, followed by dry air flushing (a); normalized current values before mercury exposure (S), after mercury exposure and 450°C heating treatments for 10 s (D1), 30 s (D2) and 3 min (D3), respectively (b).

Due to the strong affinity between gold and mercury, only thermal treatments were able to remove mercury. Sensor was heated at 450°C for 10 s and 30 s,

respectively, and the current was measured under pure air showing only a partial restoring of the starting current, thus suggesting that a treatment of 3 minutes was necessary to get the same starting current value. The set temperature value (450°C) was allowed because the nanoparticles were distributed along the titania fibers and heated for a short time. This hybrid arrangement prevented their merging and shape changing, commonly happening when gold nanoparticles are tightly aggregated (**James, J. Z. et al., 2012**). To confirm the complete mercury desorption after the heating treatment, the sensor was placed in a suitable gas-washing tube of quartz (75 ml) and heated at 550°C for additional 5 min in oven under dry air flow (1L/min). The air flushing the sample was delivered to the mercury analyzer: no more Hg was detected in the sensor headspace, confirming that the analyte was completely removed by the fibrous layer. Nanostructures shortened the heating time for desorption. Indeed, usually 20 minutes, at least, are required for stripping mercury off thin gold layers (**Jasek, K. et al., 2012**) In literature, QCM sensors (**Sabri, Y. M. et al., 2009**) provided with nanostructured gold electrodes required a 30-minute at least of exposure to Hg^0 vapor, and subsequently a 90-minute of air flow for a complete recovery of the sensor frequency. They were able to work at 28°C and 89°C keeping high sensitivities (LODs of 2.4 ppbv and 17 ppbv, respectively). Instead surface acoustic wave devices (SAWs) seemed to work better at 55°C, both under humid conditions and in presence of common interfering gases (LOD ~4.5 ppbv) (**Kabir, K. et al., 2015**). Such sensors required 2 hours of exposure to the carrier gas flow to be restored. When exposed to traces of mercury, conductometric sensors based on SWNTs finely decorated with AuNPs, showed a high sensitivity (LOD: 2 ppbv), strictly related to the number and size of gold nanoparticles. However, despite their sensitivity, these sensors showed saturation at very low concentration (30 ppbv) (**McNicholas T. P. et al., 2011**) and further they required about ten hours of exposure in a clean environment to be completely recovered. In order to test the responsiveness of

the proposed sensor to Hg concentration lower than 74 ppt Hg^0, mercury vapors were flushed throughout the measuring chamber. The final Hg^0 concentration was obtained by tuning the dilution flow **(Figure 7.19, sketch).**
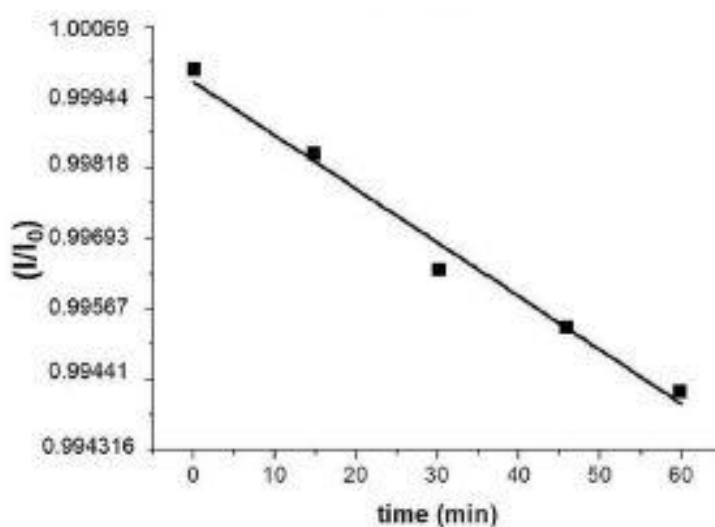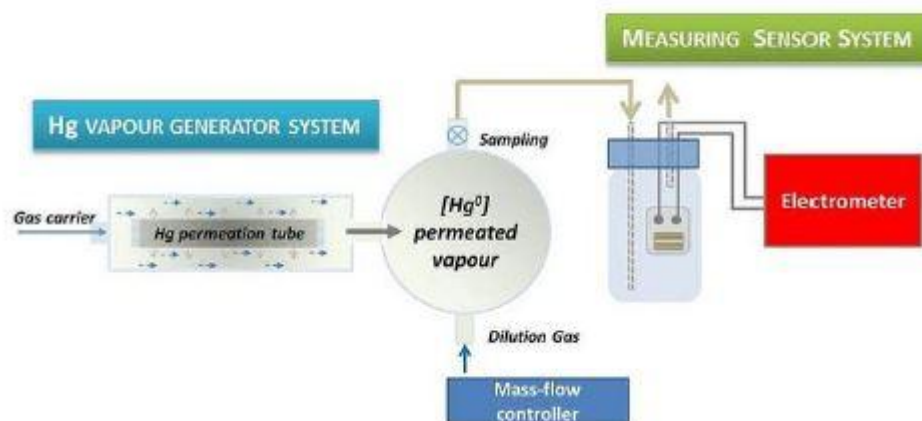

Figure 7.19: Normalized current decrease of Sβ when Hg^0 45 ppt was flowed throughout the measuring chamber for 1 hour. On the top a drawing of the measuring system set-up.

Preliminary results showed that the sensor exposure to 45 ppt of Hg^0 resulted in a decrease in current, with a rate of ~ $-9.7 \cdot 10^{-5}$ 464 min^{-1} (i.e. 5 times faster than by injection). After 60 min of measurement, the normalized current was

0.7% decreased, and the limit of detection was estimated about 1.97 ppt. When the concentration of Hg increased, the response curve slope changed too. Specifically, when the sensor was exposed to 800 ppb, the current decreased more quickly with a rate of ~ $-9 \cdot 10^{-3}$ s^{-1} **(Figure 7.18 (a)).** On the other hand, continuous mercury flowing involved a likewise continuous adsorption of the analyte to the gold free sites, thus hindering the sensor to reach the steady state unless the all binding sites saturation. A decrease in resistance value of the sensor up to 30% was reported **(Macagnano, A. et al., 2015a)** when sensor was exposed to a mercury saturated vapor pressure (P_{V0}) for 12 h. This result is supposed to be due to the high density of AuNPs within the 3D nanofibrous titania framework, that allowed a widening of the adsorption range of mercury. This result overcame the low saturation level achieved by other sensors based on gold nanoparticles assembled on nanowires **(McNicholas, T. P. et al., 2011).** Actually a long time required for measuring traces of mercury as well for sensor recovering, seems to be a common failing feature to be overcame. Strategies to create quasi real-time monitoring systems have been provided by the instruments currently available to quantify the level of elemental mercury in ambient air. Thus, technologies based on Cold Vapor Atomic Fluorescence Spectroscopy (CVAFS), are able to detect very low levels of mercury in air after that it is pumped at a known flow rate and collected on a gold trap. Desorption by heating produces mercury vapor that is flushed with argon through a cell, where the absorbance is measured using a fluorescence detector (e.g. Tekran Gas Phase Mercury Analysers). Thus, since a set time (i.e. 5 min) for mercury sampling is required, and then further a few minutes for heating and detecting are necessary, more traps are designed to work sequentially in order to reduce the total measuring time. Similarly, to reduce the detecting time, more sensors could be arranged to work in series. The mercury analyzers based on gold amalgamation and Atomic Absorption Spectrometry (AAS) detection are able to operate with ambient air as carrier gas. One or two pure gold traps are installed in series to run the dual

283

amalgamation procedure and the sampling is run at about 1 L min^{-1} with sampling times of at least 10 minutes. Under these conditions, a detection limit of about 0.1 ng $^{m-3}$ is achieved. On the other hand, some VOCs contained in ambient air may be adsorbed at the surface of the gold trap, then can cause interferences (broad bands) to UV light spectral absorption of mercury at 253.7 nm **(Ghaedi, M. et al., 2006; Ferrua, N. et al., 2007)**. Since at room temperature and in dark condition the measured current of the presented sensor is supposed to be due to AuNPs decorating titania fibers, only chemical compounds interacting with gold are expected to be mostly responsible of the current changes: halide and sulphide are the main eligible interfering compounds. Thus in a cocktail of other chemicals, this sensor has been designed as a pretty selective sensor, being able to greatly decrease the environmental disturbances allowing the investigator/manufacturer to design and then fabricate easier strategies to prevent contaminations from environment (selective filtering systems or coatings). Among common potential contaminants authors investigated previously water vapor influence (%RH) reporting no-effects on the electrical signals **(Macagnano, A. et al., 2015a).** The electrical features, such as the reproducibility of the fabrication process, of this conductive device have been previously investigated, showing, encouraging results for the development of a low cost sensor for mercury detection. However, in spite of the high sensitivity (LOD: 2ppt) of the sensor, too long response time was necessary to detect traces of Hg^{0}, when compared to the current monitoring instrumentations **(Ghaedi, M. et al., 2006; Sanchez-Rodas, D. et al., 2010; Ferrua, N. et al., 2007).** Extremely encouraging resulted if compared to other sensors currently involved in detecting mercury in air **(Drelich, J et al., 2008; Kabir, K. et al., 2015; Sabri, Y. M. et al., 2009; Mohibul Kabir, K. M. et al., 2015; Raffa, V. et al., 2006; James, J. Z. et al., 2012-2013; Chemnasiri, W. et al., 2012; Sabri, Y. M et al., 2011; Keebaugh, S. et al., 2007; Crosby, J., 2013; McNicholas, T. P. et al., 2011).** The long time in response was supposed to be in part due to the layout of the

measuring system, since the sensor was housed in a quartz bottle of 100 mL volume. In fact, an additional time was expected to be caused by the adsorption of the Hg^0 traces from the surrounding environment (measuring chamber) up to achieve a sufficient number of mercury atoms adsorbed on the surface sensor to be electrically revealed. In the present study the measuring chamber was designed in order to reduce the volume (0.7 mL) and to expose the fibers to the gas entry **(Figure 7.20).** Such a measuring layout was designed to allow the fibrous network to be exposed to the mercury atoms as delivered into the sensor chamber. The current curve trend slightly changed when clean air was flowed, stabilizing at about the current values reached for Hg0 adsorption. Due to the strong affinity between Au and Hg^0, a 3 min-thermal treatment was necessary to remove mercury from layer and get the same starting current value.
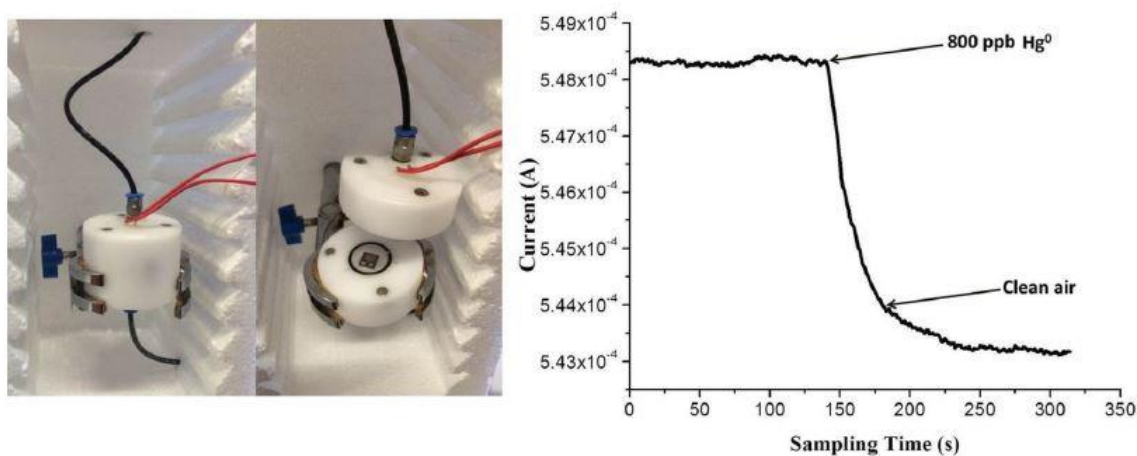

Figure 7.20: Homemade measurement chamber to house the chemosensor for laboratory experiments (left); plot depicting the transient response curve to 800 ppb Hg^0 (V=0.3 V).

Figure 7.21 depicts the normalized sensor response rate, i.e. the normalized current change per second, toward the increasing concentration of GEM (ranging between 20 and 160 ppb). The resulting logarithmic curve describes

how the Hg^0 concentration affects the response time: small variations of Hg^0 concentration up to 80 ppb are able to deeply change the response rate, on the contrary higher concentration seem to affect only slightly this sensing feature. Since a strong relationship is recorded between the concentration and the response time when the content of mercury in environment is low, is possible to correlate the slope of the transient responses within the first minutes of the sensor response to definite concentrations of Hg^0 in air.
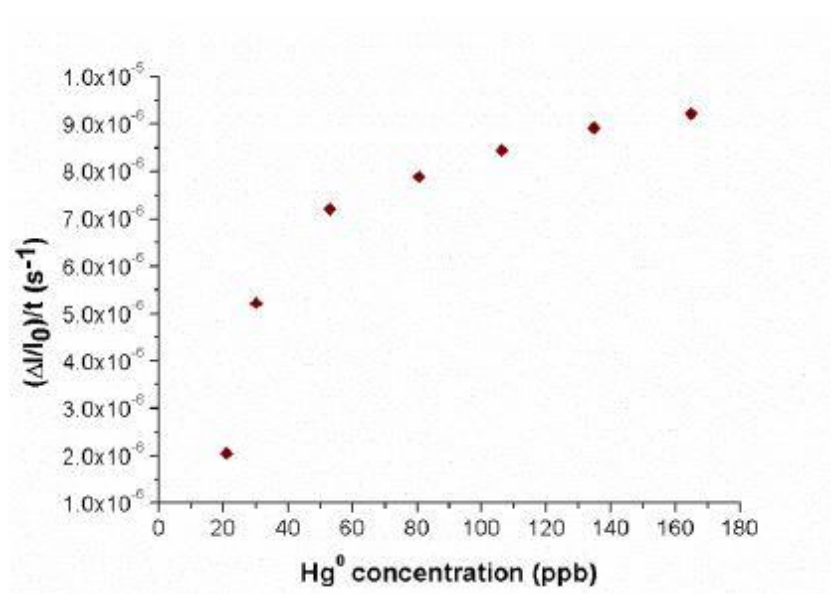
Figure 7.21: The normalized sensor response rate to the increasing concentration of vapor elemental mercury.

Figure 7.22 depicts the linear fitting of 10 min-sensor responses when increasing concentrations of mercury were flowed onto the sensor. Related data were reported in **Table 1.**

Table 1. Linear fitting parameters of 10 min-sensor responses to 21 ppb$\geq$ [Hg^0] $\leq$106ppb			
ppb	(DI/I$_0$)s^{-1}	SE($\pm$)	R^2
21	-7.12602E-10	1.75521E-11	0.86
33	-1.50647E-9	1.05521E-10	0.91
39	-1.78067E-9	1.02615E-10	0.91
40	-1.85901E-9	1.01833E-10	0,92
53	-2.44657E-9	4.24993E-11	0.91
70	-3.19082E-9	2.55882E-11	0.93
106	-4.83599E-9	2.67462E-10	0.88
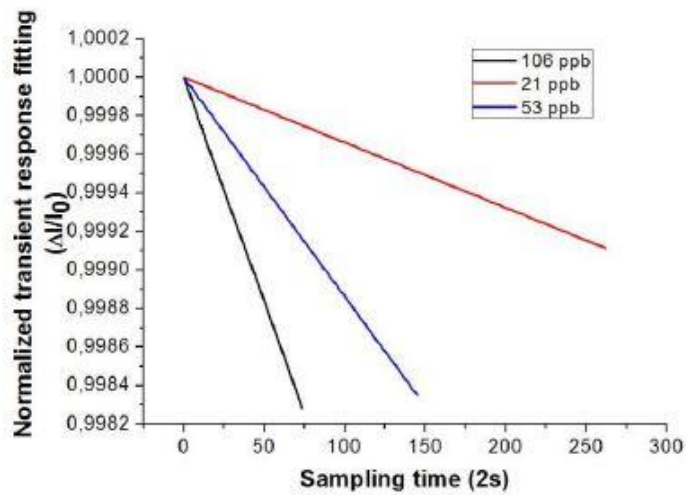
Figure 7.22: Linear fitting of the normalized sensor response within the first ten minutes

A linear relationship has been reported between the response rate and the concentration of Hg, according to the following equation (1):

(1) $y = (-4.56226E^{-11}) \cdot [Hg^0], [Hg^0] < 100$ ppb; SE:$\pm 1.504E^{-12}$; $R^2 = 0.99675$
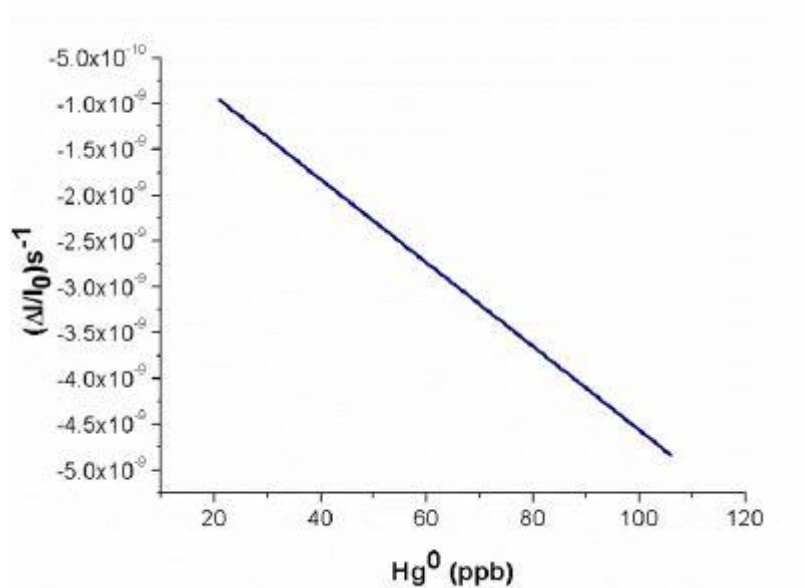
287

Figure 7.23: Linear relationships between the normalized response time and the Hg^0 concentration, within the range of 20 and 100 ppb.

Therefore when the concentration of Hg increased, the response curve slope changed too linearly, allowing a limit of detection of about 1 ppb, when the sensor is exposed to air polluted with Hg^0 per 10 min. For what concerns main interfering compounds, since at room temperature and in dark condition the measured current is supposed to be due to AuNPs decorating titania fibers, only chemical compounds interacting with gold are expected to be mostly responsible of the current changes (i.e. halides and sulphides). Thus in a blend of other chemicals, this sensor has been designed as a pretty selective sensor, being able to greatly decrease the environmental disturbances allowing the investigator/manufacturer to design and then fabricate easier strategies to prevent contaminations from environment (selective filtering systems or coatings). Among common potential contaminants authors investigated previously water vapor influence (%RH) reporting no-effects on the electrical signals **(Macagnano, A. et al., 2015).**

7.5 Conclusions

It is largely recognized that Hg contamination of the ecosystems and the consequent human exposure remains a serious hazard. Since the need for fast detection systems to be used for large area monitoring, at low cost and low maintenance, as well as ease of use are becoming ever more urgent, sensors and sensing systems looked the most promising alternative to the traditional instruments. The mainly sensing strategy has focused on the strong affinity of mercury to gold, and more recently thanks to the advances in nanotechnology, to nanostructured gold materials (such nanoparticle, nanowires and nanorods). Exploiting the photocatalytic properties of electrospun titania fibers, a conductometric sensor has been designed and fabricated to detect elemental mercury in air. Thus, gold nanoparticles have been grown on nanofibrous scaffolds of TiO_2 by photocatalysis. Electrospinning technology has been used successfully to create a 3D framework of titania covering the electrode sensing area of the properly designed chemoresistors (IDEs). Its electrical properties, depending on shape, size and number of gold nanoparticles decorating the fibers, were easily tuned, showing the sensor was able to work at room temperature and highly sensitive to Hg^0 (tens of ppt). The sensor is expected to be robust since it is composed with titania and gold, two chemical compounds considered among the most robust materials since resistant to common solvents and VOCs commonly in the air. Furthermore the sensor was able to work at room temperature being subjected to thermally treatments (450°C) only for a few minutes, necessary to desorb mercury from AuNPs. Depending on the strategy of sampling, a sensing device based on such a chemosensor, could be designed for real applications, specifically for real time monitoring of polluted sites. An encouraging reproducibility in laboratory fabrication of the chemoresistors was obtained (R_m=~1.3 kΩ). The fabricated nanostructured chemosensors worked as Hg^0 vapours highly adsorbing 3D-conductive traps,

capable of working until the saturation of all the interacting sites occurred. Depending on the strategy of sampling, the limit of detection could be improved, ~6 ppt when mercury vapor was injected and ~2 ppt when slowly flowed within the measuring chamber. However, despite the high sensitivity of the chemosensors to Hg^0 vapor, the responses appeared to be slow. Further investigations are necessary also to assess the effects of physical parameters of the environment, such as temperature fluctuations and UV-light, as well as chemical ones, such as volatile organic compounds and gas (like halides and sulphides) which are potentially interfering the adsorption process of the Hg^0 on gold. The ease of deposition (electrospinning) and preparation (UV-irradiation in aqueous solution) as well as the high Hg^0 sensitivity, suggests the chance to investigate the material features by further transduction systems.

References

Ayache J., Beaunier L., Boumendil J., Ehret G., Laub D. In Sample Preparation Handbook for Transmission Electron Microscopy. Anderson R Ed Springer: New York (2010), Chapter 4, pp. 639 153-228

Battistoni C., Bemporad E., Galdikas E., Kaciulis S., Mattogno G., Mickevicius S., Olevano V. Interaction of mercury vapour with thin films of gold. Appl Surf Sci (1996), Vol. 103, pp. 107-111

Chemnasiri W., Hernandez F. E. Gold nanorod-based mercury sensor using functionalized glass substrates. Sensors and Actuators B (2012), Vol. 173, pp. 322-328

Cinnirella S., D'Amore F., Bencardino M., Sprovieri F., Pirrone N. The GMOS cyber(e)-infrastructure: advanced services for supporting science and policy. Environmental Science and Pollution Research (2013), Vol. 21, pp. 4193-4208

Crosby J. Mercury Detection with Gold Nanoparticles. Electronic Thesis and Dissertations UC Berkeley (2013) http://eprints.cdlib.org/uc/item/3s40h5m0

Dong Z. M., Qing X. M, Zhao G. C. Highly Sensitive EQCM Sensor for Mercury Determination by Coupled Stripping Voltammetry. Int J Electrochem Sci (2015), Vol. 10, pp. 2602-2612

Drelich J., White C. L., Xu Z. Laboratory Tests on Mercury Emission Monitoring with Resonating Gold-coated Silicon Cantilevers. Environ Sci Technol (2008), Vol. 42, pp. 2072-2078

Ferrua N., Cerutti S., Salonia J. A, Olsina R. A., L., Martinez L. D. On-line preconcentration and determination of mercury in biological and environmental samples by cold vapor-atomic absorption spectrometry. J Hazard Mater (2007), Vol. 141, pp. 693-699

Ghaedi M., Fathi M. R., Shokrollahi A., Shajarat F. Highly Selective and Sensitive Preconcentration of Mercury Ion and Determination by Cold Vapor Atomic Absorption

James J. Z., Lucas D., Koshland C. P. Gold Nanoparticle Films As Sensitive and Reusable Elemental Mercury Sensors. Environ Sci Technol (2012), Vol. 46, pp. 9557-9562

James JZ., Lucas D., Koshland C.P. Elemental mercury fiber interaction with individual gold nanorods. Analyst (2013), Vol. 138, pp. 2323-2328

Jasek K., Neffe S., Pasternak M. SAW Sensor for Mercury Vapour Detection. Acta Physica Polonica A (2012), Vol. 122, pp. 825-828

Kabir K., Sabri Y., Matthews G., Jones L., Ippolito S., Bhargava S. Selective detection of elemental mercury vapor using a surface acoustic wave (SAW) sensor. Analyst (2015), Vol. 140, pp. 5508-5517

Keebaugh S., Nam W. J., Fonash S. J. Manufacturable Higly Responsive Gold Nanowire Mercury Sensors. NSTI-Nanotech (2007), Vol. 3, pp. 33-36

Li D., McCann J. T, Gratt M., Xia Y. Photocatalytic deposition of gold nanoparticles on electrospun nanofibers of titania. Chemical Physics Letters (2004), Vol. 394, pp. 387-391

Lubick N. Fundign Struggle for Mercury monitoring. Nature (2009), Vol. 459, pp. 620-621

Lugg G. A. Diffusion coefficients of some organic and other vapors in air. Anal Chem (1968), Vol. 40, pp. 1072-1077

Macagnano A., Zampetti E., Kny E. Electrospinning for High Performance Sensors. Springer International Publishing (2015), pp. 1-329

Macagnano A., Zampetti E., Perri V., Bearzotti A., Sprovieri F., Pirrone N., Esposito G., De Cesare F. Photocatalytically Decorated Au-nanoclusters TiO_2 Nanofibers for Elemental Mercury Fiber Detection. Procedia Engineering (2015a), Vol. 120, pp. 422-426

Mcnerney J., Hanson R., Buseck P. Mercury Detection by Means of Thin Gold Films. Science (1972), Vol. 178, pp. 611-612

McNicholas T. P., Zhao K., Yang C., Hernandez S. C., Mulchandani A., Myung N. V., Deshusses M. A. Sensitive Detection of Elemental Mercury Vapor by Gold-Nanoparticle-Decorated Carbon Nanotube Sensors. J Phys Chem C (2011), Vol. 115, pp. 13927-13931

Merkoci A. Electrochemical biosensing with nanoparticles FEBS. Journal (2007), Vol. 274, pp. 310-316

Mohibul Kabir K. M., Ippolito S.J., Matthews G. I., Abd Hamid S. B., Sabri Y. M., SK. Bhargava S. K. Determining the Optimum Exposure and Recovery Periods for Efficient Operation of a QCM Based Elemental Mercury Vapor. Sensor Journal of Sensors (2015), pp. 727432-9

Morris T., Kloepper K., Wilson S., Szulczewsk G. A Spectroscopic Study of Mercury Fiber Adsorption on Gold Nanoparticle Films. Journal of Colloid and Interface Science (2002), Vol. 254, pp. 49-55

Müller K. H., Wei G., Raguse B., Myers J. Three-dimensional percolation effect on electrical conductivity in films of metal nanoparticles linked by organic molecules. Phys Rev B (2003), Vol. 68, pp.155407

Pirrone N., Aas W., Cinnirella S., Ebinghaus R., Hedgecock I. M., Pacyna J., Sprovieri F., Sunderland E. M. Toward the next generation of air quality monitoring:Mercury. Atmospheric Environment (2013) doi:10.1016/j. atmosenv.2013.06.053. Plenum Press-New York (1984) DOI. 10.1007/978-1-4684-4655-5

Qui J. Tough talk over mercury treaty. Nature (2013), Vol. 493, pp. 144-145

Raffa V., Mazzolai B., Mattoli V., Mondini A., Dario P. Model validation of a mercury sensor, based on the resistivity variation of a thin gold film. Sensors And Actuators B Chemical (2006), Vol. 114, pp. 513-521

Sabri Y. M., Ippolito S. J., O'Mullane A. P., Tardio J., Bansal V., Bhargava S. K. Creating gold nanoprisms directly on quartz crystal microbalance electrodes for mercury vapor sensing. Nanotechnology (2011), Vol. 22 (30), pp. 305501.

Sabri Y. M., Ippolito S. J., Tardio J., Atanacio A. J., Sood D. K., Bhargava S. K. Mercury diffusion in gold and silver thin film electrodes on quartz crystal microbalance sensors. Sensors and Actuators B (2009), Vol. 137, pp. 246-252

Sánchez-Rodas D., Corns W. T., Chen B., Stockwell P. B. Atomic Fluorescence Spectrometry: a suitable detection technique in speciation studies for arsenic, selenium, antimony and mercury. J Anal At Spectrom (2010), Vol. 25, pp. 933-946

Scheide E. P., Taylor K. J. Piezoelectric sensor for mercury in air. Environmental Science & Technology (1974), Vol. 8, pp. 1097-1099

Sharma B. L. Metal-Semiconductor Schottky Barrier Junctions and Their Applications. Spectroscopy. Analytical Letters (2006), Vol. 39, pp. 1171-1185

Wold A. Photocatalytic properties of titanium dioxide (TiO_2). Chem Mater (1993), Vol. 5, pp. 280-283

Yuan Y., Zhao Y., Li H., Li Y., Gao X., Zheng C., Zhang J. Electrospun metal oxide-TiO_2 nanofibers for elemental mercury removal from flue gas. Journal of Hazardous Materials (2012), Vol. 227-228, pp. 427-435

Zampetti E., Pantalei S., Muzyczuk A., Bearzotti A., De Cesare F., Spinella C., Macagnano A. A high sensitive NO_2 gas sensor based on PEDOT-PSS/TiO_2 nanofibers. Sensors and Actuators B (2013), Vol. 176, pp. 390-398

Introduction

One of the more troublesome questions in recent years has been to quantify not only the strength of emission sources but also the effects of re-emission of previously deposited Hg on the overall distribution, concentration and speciation of Hg in the atmosphere **(Hedgecock, I. et al., 2003).** The deposition of atmospheric Hg depends on its chemical speciation, where the term speciation is used to distinguish between the gaseous elemental (GEM) and gaseous oxidized forms of Hg [GOM and Particle bound mercury (PBM)] and their chemical-physical characteristics **(Lyman, S. N. et al., 2010; Sprovieri, F. et al., 2016a,b).** To be precise, Total gaseous mercury (TGM) mainly comprises GEM with minor fractions of other volatile species (e.g., HgO, $HgCl_2$, $HgBr_2$, CH_3HgCl, or $(CH_3)_2Hg$). The predominant fraction of TGM (usually in excess of 99%) is often represented by GEM under normal conditions. GEM is relatively inert under atmospheric conditions, only slightly soluble and also quite volatile, whereas the oxidized Hg forms found in the atmosphere are both soluble and involatile, thus they are efficiently scavenged and consequently deposited by liquid atmospheric water, such as rain and fog droplets, but also deliquesced aerosol particles. The dispersion of GEM on global scale therefore, depends on the rate of its oxidation in the atmosphere as this determines its long atmospheric lifetime (generally >1 year), limiting local emission controls from protecting all environments. Most methods cannot yet directly or accurately determine minor Hg species infact, several limitations and difficulties have still experienced in Hg analysis **(Gustin, M. S. et al., 2013).** This limits the scientific research community's ability to long-term measure atmospheric Hg concentrations worldwide. Sampling and analysis of atmospheric Hg is made most commonly as GEM/TGM because of their greater abundance, even if both manual and automatic methods have been currently developed for different Hg forms to suit the measurement and

monitoring application. The most common sampling method employed relies on adsorption on gold amalgam and then, either directly or indirectly, through a stepwise process of thermal desorption and final detection [usually by cold-vapor atomic absorption spectroscopy (CVAAS) or cold-vapor atomic fluorescence spectroscopy (CVAFS)]. At any rate, alternative methods to measure atmospheric Hg are needed. Given the uncertainty and restrictions associated with automated and/or semi-automated Hg measurements **(Gustin, M. S. et al., 2013; Pirrone, N. et al., 2013),** and above all, responding to the technical needs of an expanding Hg global observation network, we developed a reliable, sensitive, and inexpensive nanostructured material for atmospheric Hg detection. Previously passive samplers have been developed and used to understand long-term global distribution of persistent organic pollutants (POPs) **(Harner, T. et al., 2003; Pozo, K. et al., 2004).** Other passive samplers for both TGM and GOM collection on the basis of diffusion have been constructed using a variety of synthetic materials (i.e., gold and silver surfaces, and sulfate-impregnated carbon) and housings **(Lyman, S. N. et al., 2010; Gustin, M. S. et al., 2011; Zhang, W. et al., 2012; Huang, J. et al., 2014).** However, because of the differences in design of passive samplers, ambient air Hg concentrations quantified by various samplers may not be comparable. In addition, sampling rates (SRs) using the same passive samplers may depend on environmental conditions and atmospheric chemistry at each site. It has been also highlighted that the performance of passive samplers may be influenced by meteorological factors (e.g., T °C, RH, wind speed) therefore inducing bias for the result of passive sampling **(Plaisance, H. et al., 2004; Sderstrm, H. S. et al., 2004).** On the other hand, incentive for developing simple and cost-effective samplers that are capable of monitoring over an extended period and require no technical expertise for deployment of these systems also at remote locations is now obvious. In this work we describe an alternative approach adopted in the place of conventional ones demonstrating that the combination of gold affinity for Hg with the nanoscale size of the

frameworks, gold nanostructures look the most promising nanomaterials for creating novel passive samplers with sensing features comparable to those of commercial passive sampling systems and expensive systems currently available. In particular, we investigated and demonstrated the utility of new passive sampling systems based on nanostructured materials (nanofibers and nanoparticles of titanium oxide properly functionalized with gold nanoclusters), capable of adsorbing elemental Hg as a useful alternative system for making regional and global estimates of air Hg concentrations. The novel passive samplers are a relatively simple and low cost method for measuring the most abundant Hg form in ambient air (TGM/GEM).

Chapter 8

Novel passive sampling systems of mercury based on nanostructured materials

8.1 International initiatives and programs: UNEP, GMOS, GEO, GEOSS

Several international initiatives and programs [i.e., the United Nations Environment Program (UNEP)] have also made a tremendous effort in identifying and quantifying Hg pollution across the globe, especially the ''hot-spots'', aimed at reducing risk of exposure to this neurotoxin pollutant. Policy makers are working toward a worldwide effort for supporting the constructing an accurate global Hg budget and to model the benefits or consequences of changes in Hg emissions, for example, as proscribed by the Minamata Convention. Anticipating a global policy, in 2010 the European Commission began a five-year project called the Global Mercury Observation System (GMOS, www.gmos.eu) to create a coordinated global network to gaps in emissions monitoring and in the spatial coverage of environmental observations, mostly in the tropical regions and Southern Hemisphere, thus adequate for improving models and making policy recommendations **(Sprovieri, F. et al., 2016a,b).** To date the GMOS network consists of more 43 monitoring stations worldwide distributed including high altitude and sea level monitoring sites, and located in climatically diverse regions, including polar areas **(Sprovieri, F. et al., 2016a,b).** One of the major outcomes of GMOS has been an interoperable e-infrastructure developed following the Group on Earth Observations (GEO) data sharing and interoperability principles which allows us to provide support to UNEP for the implementation of the Minamata Convention (i.e., Article 22). GMOS activities are currently

part of the GEO strategic plan (2016–2025) within the flagship on "tracking persistent pollutants". The overall goal of this flagship is to support the development of GEOSS by fostering research and technological development on new advanced sensors and passive samplers for in situ and satellite platforms, in order to lower the management costs of long-term monitoring programs and improve spatial coverage of observations. Since automated measurement methods of Hg require power, argon gas, and significant operator training, they are difficult to apply for understanding Hg air concentrations and deposition across broad regional and global scales. Therefore, the lack of passive sampling systems, low-cost, low-maintenance is a primary technical issue to be solve for the sustainability of a global network such as GMOS. Hg-concentration levels in air vary greatly across different environmental locations, remote as the Polar Regions, background or rural, and urban locations with an average range between 1.5 ngm^{-3} (GEM) and 1 pgm^{-3} (GOM and PBM), depending on the speciation. Hence, for the determination of atmospheric Hg also at such low levels, sampling and analytical methods should be sensitive enough to quantify the concentration profiles of diverse Hg species in each respective environmental setting to better understand their environmental behavior and patterns. Fortunately, many advances made in analytical methodologies have made it possible to study atmospheric Hg in different environmental locations. Since 2016 these new passive samplers of mercury based on nanostructured materials (nanofibers of titanium oxide properly functionalized with gold nanoclusters), are involved in the UNEP GEF project: "Development of a Plan for Global Monitoring of Human Exposure to and Environmental Concentrations of Mercury".

8.2 Nanostructured passive samplers advantages

Several strategies were planned by CNR-IIA to get novel passive sampling systems of mercury based on nanostructured materials and keeping in mind the main features of a passive sampler. Indeed the peculiarity of the passive samplers relies on the unassisted molecular diffusion of gaseous agents (i.e. volatile vapours of elemental mercury) through a diffusive surface onto an adsorbent scaffolding. Unlike active (pumped) sampling, passive samplers require no electricity (expensive pumps), have no moving parts, and are simple to use (no pump operation or calibration). After sampling, the adsorbed mercury should be desorbed off the adsorbent by solvent (chemical procedure) or thermal desorption (physical procedure). Passive samplers have to be commonly compact, portable, unobtrusive, and inexpensive. They are able to give information about the average pollution levels over time periods of 8 hours to weeks/months. They have not to require supervision and can be used in hazardous environments. The low cost of the materials allows the sampling at multiple locations (e.g., for highlighting pollution "hotspots"; or determining long term data trends in a specific geographical area).

8.3 Basic elements of passive air sampling

From Fick's Law, it is known that the sampling rate (Q) is a function of the diffusion coefficient of a given analyte (D) and the geometric constant of the sampler (K): $Q = D.K$. The diffusion coefficient (D) always remains constant for a given analyte; therefore, to improve sampling rate (Q), the geometric constant (K) must be improved: $K = S/l$ where S is diffusive surface and l is the distance between the diffusive and adsorbing surface. Most commercially available passive/diffusive samplers are planar or axial in shape and offer

lower sampling rates and limited sampling capacity. As a result, sensitivity can suffer during short-term analysis (due to low sampling rates), or long-term sampling (analyte back-diffusion due to low capacity). Within the project we investigated the chance to design absorbing material based on either nanofibers or nanoparticles, due to the shape, size and peculiar geometry of these structures. Electrospinning technology has been commonly used to design highly efficient filtering system, also for mercury in air as well as in water. Nowadays fibrous membranes have been used in different filtration applications (respirators for citizens, industrial gas cleaning equipment, air purifiers for cars, cleanrooms, indoor environments etc.). Depending on the application, the technology allows to create nanofibers made of a wide variety of materials, such as cellulose, glass, plastics, ceramics, metals or composites. It is known that conventional fibrous structures suffer from many structural disadvantages, like large fibre diameter, non-uniform fibre diameter and pore size, low filtration efficiency and poor high temperature resistance. On the other hand it is well documented in literature that the smaller the fibre diameter, the better the filtration performances.

8.4 Materials, methods and characterization

8.4.1 Chemicals

All chemicals were purchased from Sigma-Aldrich and used without further purification: polyvinylpyrrolidone (PVP, Mn 1,300,000), Titanium (IV) oxide (anatase, ≤ 25nm diameter, Sigma Aldrich, CAS 1317-70-0) and gold(III) chloride hydrate (HAuCl$_4$, 99.999%). Ultrapure water ($5 \cdot 5$ $^{10-8}$ S $^{cm-1}$) was produced by MilliQ-EMD Millipore. At first, the substrates adopted in the present work were Quartz disks having two different porosity (45 and 450 µm,

respectively) coated with a non-woven layer of polymer nanofibers (titanium isopropoxide (TiiP, 99.999%) through electrospinning technology and then subjected to annealing in an oven (Aprolab, 1°C/min, 550°C x 5 h). The substrates chosen and used for the manufacture of the final passive samplers were thinner quartz slices (500 μm thick).

8.4.2 Study, designing and development of different strategies for the manufacture of novel passive sampling systems of elemental mercury

In order to design proper adsorbing layer for mercury based on electrospinning, CNR-IIA developed a series of fabrics based on nanofibers of titanium oxide properly functionalised with gold nanoclusters, since similar structures exhibited, as filtering systems, the highest Hg^0 removal efficiency (100%) when compared to other nanofibrous systems. Different strategies have been developed for the production of such fabrics.

8.4.2.1 First strategy: Passive samplers based on nanofibers

Quartz disks, having two different porosity (45 and 450 μm, respectively) were provided in order to withstand the high temperature value (550°C) of the process of fibers calcination (oxidising and crystallization of TiO_2). They were easily coated with a non-woven layer of polymer nanofibers (precursor of TiO_2) through electrospinning technology and then subjected to annealing in an oven (Aprolab, 1°C/min, 550°C x 5 h). The process and the results are reported in **Figure 8.1** and show poor adherence of the fibers on quartz.
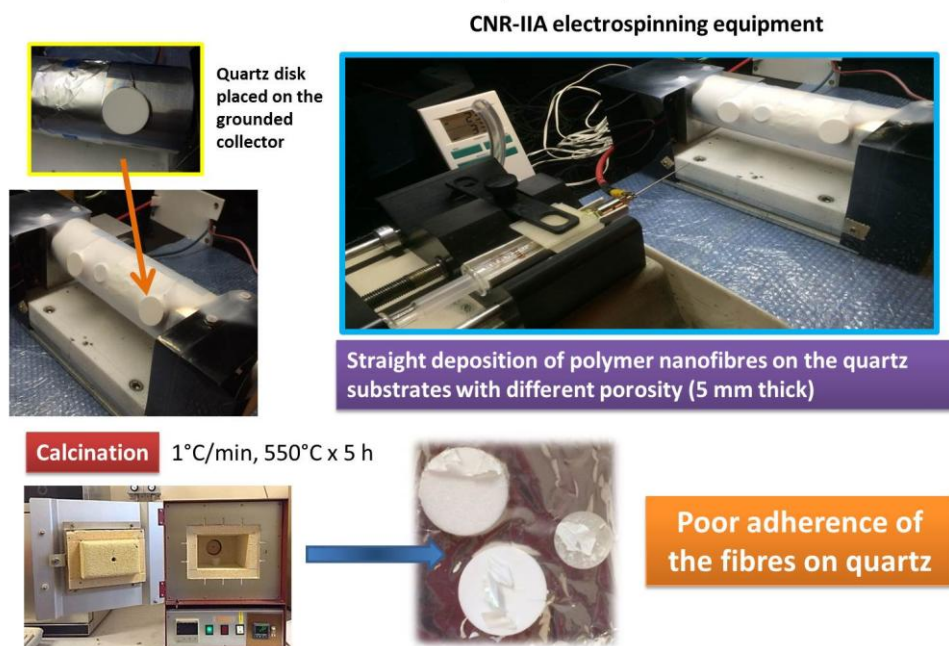
Figure 8.1: First strategy of designing and developing passive samplers for mercury in air based on electrospun nanofibers.

8.4.2.2 Second strategy: Passive samplers based on nanofibers free standing

During the thermal treatment, fibers shriveled and detached themselves from the substrates of quartz, making vain the proposed strategy. However since a polymer free standing fabric was obtained too, a second strategy was proposed. Therefore the fibrous scaffold was annealed and then successfully functionalized under UV irradiation (1 h) in a suitable aqueous solution comprising a capping agent (PVP, 0.1 M) and $HAuCl_4$ (Tetrachloroauric(III) acid, 0.5mg/ml). The process is depicted in **Figure 8.2.** Fibers were fragmented and filtered using as substrates the quartz disks with different

304

porosity. After slow heating and drying in an oven (110 °C, 1 °C min^{-1}, 24 h), fibers resulted well attached to the substrates and usable as passive sampler. However the absorbent material appeared poorly reproducible and uneven distributed on the quartz surface**.**
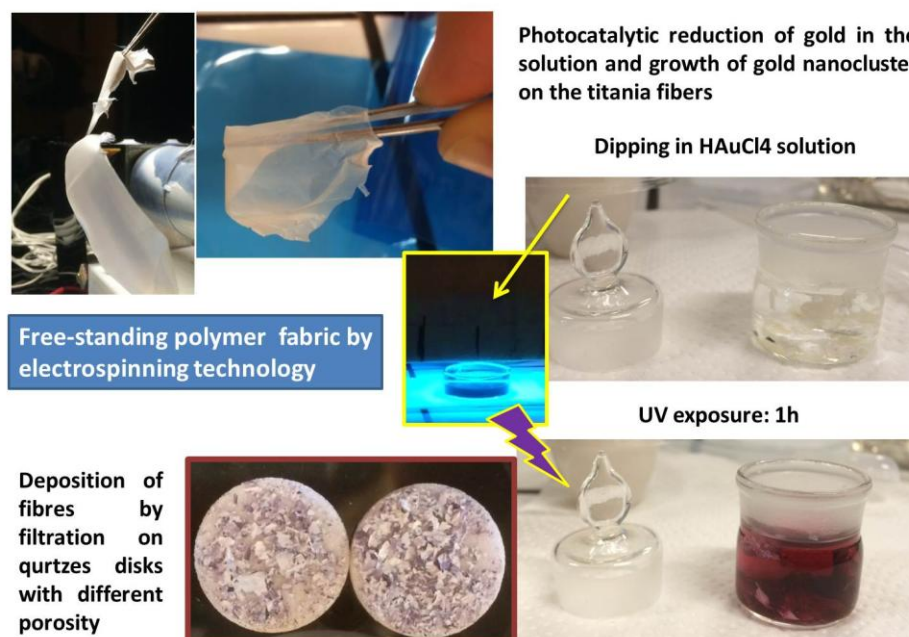
Figure 8.2: Second strategy of passive samplers preparation based on free-standing electrospun fibres of titania and following procedure of photocatalytic functionalization with gold nanoparticles.

8.4.2.3 Third strategy: Passive samplers based on nanoparticles

The third strategy proposed to design and create sorbent materials based on nanoparticles of TiO$_2$ functionalized with gold nanoparticles. The preparation of a passive sampler based on the last strategy resulted to be more simple and economical because titania nanoparticles are present on the market (Sigma

Aldrich, Titanium (IV)oxide, anatase, $\leq$25nm diameter) and are easier to handle and deposit on various substrates. In addition, the calcination process is no more required (additional energy savings). Therefore, 500 mg of Titanium (IV) oxide (anatase) (Sigma Aldrich, CAS 1317-70-0) were suspended in an aqueous solution of PVP/HAuCl$_4$ (0.1 M PVP, 0.5 mg/mL HAuCl$_4$) for the preliminary investigations. Such a suspension was UV-irradiated for 1 h, thus changing the color from yellow to blue-violet (shown in **Figure 8.3**). A series of thinner quartz slices (500 μm thick) were dipped in such a prepared suspension overnight and then removed, dried (150°C) and weighed (an average of 150 mg per sample). The layers looked homogeneous and adhering to the substrates. Each quartz disk could be easily handled and housed in the commonly used exposure glass chambers (Marbaglass, Italy) for VOCs and gases passive sampling.
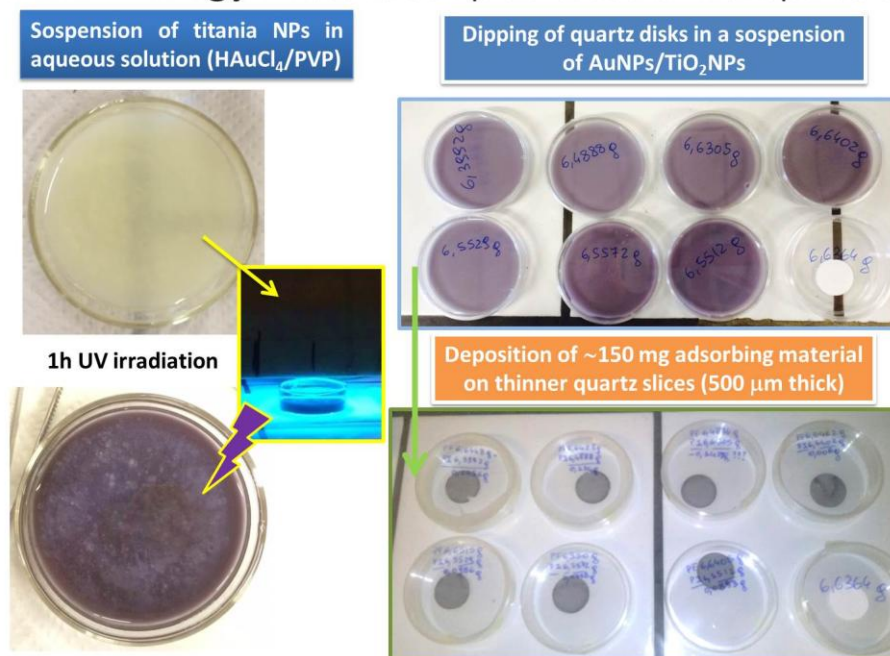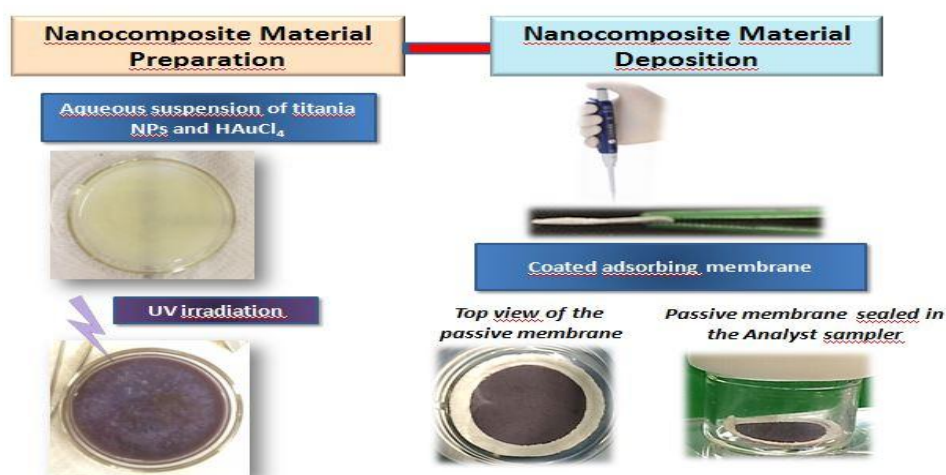

Figure 8.3: Third strategy of passive samplers preparation based on titania nanoparticles photocatalytically functionalized (UV exposure) with gold nanoparticles after dipping of a series of quartz slices in an aqueous solution containing PVP and HAuCl$_4$

306

8.4.2.4 Fourth strategy: Passive samplers based on nanoparticles and a thin quartz filtering support

The fourth and final strategy adopted, proposed to design and create passive membranes (thinner quartz slices) coated by nanoparticles of TiO_2 functionalized with gold nanoparticles. Therefore, 600 mg of Titanium (IV) oxide (anatase) (Sigma Aldrich, CAS 1317-70-0) were suspended in an aqueous solution of PVP/$HAuCl_4$ for the preliminary investigations. Such a suspension was UV-irradiated for 1 h, thus changing the color from yellow to blue-violet (shown in **Figure 8.4**) and subsequently centrifuged for three times to remove PVP. The suspension was vortexed and it was deposited (500µl) on passive membranes (thinner quartz slices, 500 µm thick), positioned on a hotplate to speed the absorption of composed nanomaterial. The thinner quartz slices coated were dried (80°C) and before being incorporated and sealed into the analyst sampler and shipped to the campaign of elemental mercury monitoring, almost all over the world, (UNEP GEF project: "Development of a Plan for Global Monitoring of Human Exposure to and Environmental Concentrations of Mercury") desorbed at 550 °C to remove any trace of mercury absorbed during preparation.

Fourth Strategy: Passive Samplers based on Nanofibers

Figure 8.4: Fourth strategy of passive samplers preparation based on titania nanoparticles photocatalytically functionalized (UV exposure) with gold nanoparticles after deposition of the composite nanomaterial on a series of quartz slices.

8.5 Morphological and Optical Characterization of samples

The layers looked homogeneous and adhering to the substrates and nanoparticles were analyzed by UV-Vis spectrophotometry (Spectrophotometer UV-2600, Shimadzu, UV-Vis-NIR Mini-Spectrometer Hamamtsu) before and after gold nanofunctionalization confirming the gold reduction and adhesion on the surfaces of the titania NPs and suggesting, according to literature results, a very small diameter (under 20 nm) of AuNPs **(Figure 8.5)**. These novel structures let us suppose a very attractive passive sampling system based on both the strong affinity between mercury and gold and a wide adsorbing surface due to the nanosize of the materials (expected high efficiency and lifetime). The absorption (and reflectivity) band at 550 nm was blue-shifted (up to 546 nm) when exposed to Hg mercury vapors.
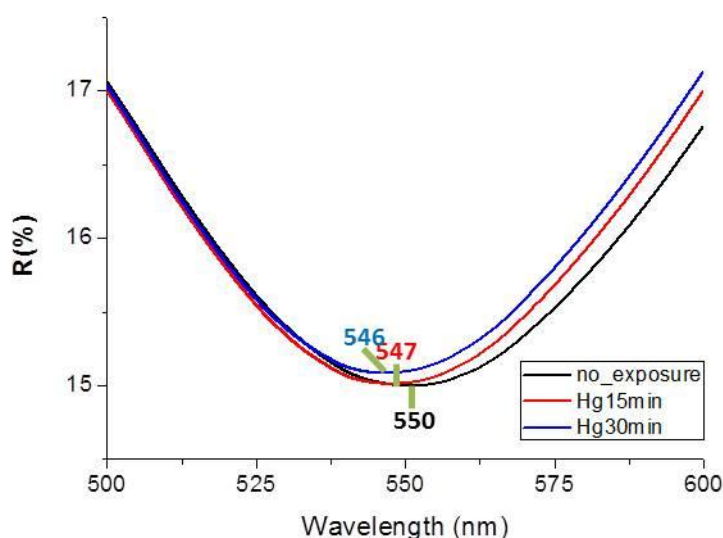

Figure 8.5: UV-VIS spectra (%R) of a thin layer of AuNPs/TiO$_2$NPs coating a silicon wafer and exposed to Hg vapors for 15 and 30 min respectively

Adsorption and desorption processes of mercury (calibration and validation) in atmosphere are actually matter of investigation. A prototype of thermal desorption system was also planned in CNR-IIA and developed (Marbaglass, Italy) in order to be connected to the most commons analytical systems of mercury. The prototype was manufactured in quartz and housed in a heater system to allow the fast desorption of the Hg adsorbed on the thin layer of the nanostructured material, flowing dry air throughout the desorption chamber. A picture of the prototype is reported in **Figure 8.6.**

Figure 8.6. CNR-IIA equipment to thermally desorb Hg from passive samplers (quartz tube (*on the left*), furnace (up to 800°C) and TEKRAN analyzer (*on the right*).

The morphological characteristics of sample (TiO$_2$ nanoparticles coated by gold nanoparticles) were studied by mean of the techniques HR-TEM (High-Resolution Transmission Electron Microscopy). The sample resulted strongly agglomerate, even after sonication the situation of TiO$_2$NP didn't change significantly. However gold nanoparticles having different size but smaller than TiO$_2$NPs resulted strictly linked to the NPs, creating a series of gold multidecorated particles, suggesting a huge recepting surface **(Figure 8.7).**
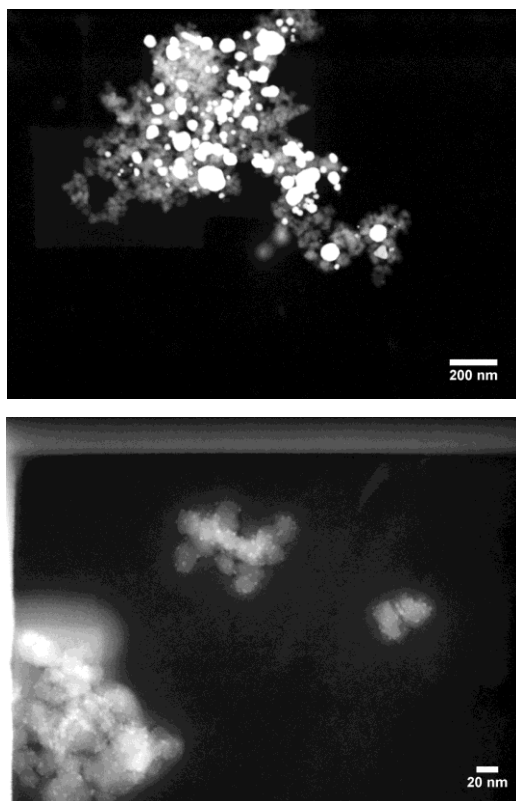
Figure 8.7: HR-TEM image of TiO2NPs-AuNPs sample (*left 200 nm*) and (*right 20 nm*).

8.6 Results and discussion

Calibration and validation of the passive samplers for mercury in atmosphere are currently under investigation. However, preliminary results obtained in the laboratory showed that such sampling systems have an efficiency of adsorption equal to ~ 98%, as showed in **Figure 8.8**
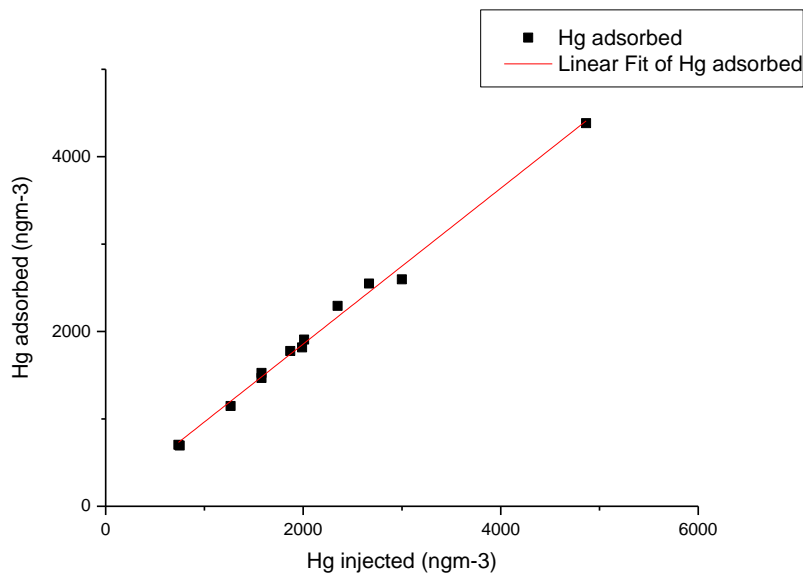
Figure 8.8: Adsorption curve of the mercury at room temperature: Linear Fitting of Hg° adsorbed that confirming an efficiency of ~98%.
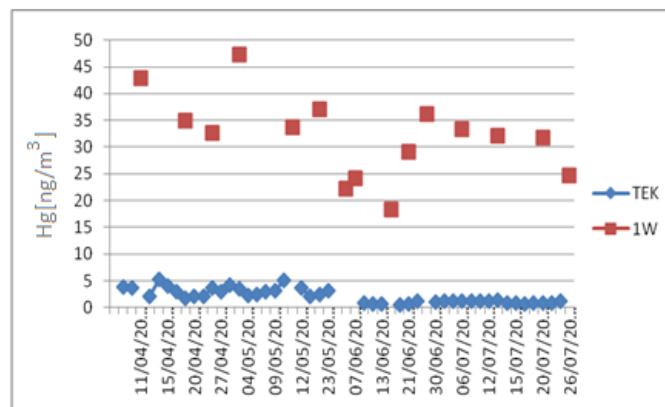
Figure 8.9: Comparison between the raw data of daily Hg concentration provided by Tekran and the raw data resulting by thermal desorption and measured by Tekran and related to the weekly exposed passive samplers to air within CNR-Area of Montelibretti.

In **Figure 8.9** it's shown the plot of a comparison between the raw data of daily Hg concentration provided by Tekran and the raw data resulting by thermal desorption and measured by Tekran and related to the weekly exposed passive samplers to air within CNR-Area of Montelibretti. These data suggest that the passive sampler follows the trand of daily variations of Hg. In particular, the Hg concentration in air is ranging between 0.5 ng/m^3 and 6

311

ng/m^3. Within these daily fluctuations, in a week you have the adsorption oscillations on the passive sampler ranging from 20 up to about 48 ng/m^3. When decreases the total concentration of external mercury, decreases the adsorbed mercury from passive samplers and vice versa. Repeating the monitoring of mercury for 1-, 2- and -3 weeks, the graph shows that the decrease of the external concentration of mercury, cause a reduction of the concentration of mercury adsorbed. The longer the exposure, the lower the correlation between the daily fluctuations and the data collected (**Figure 8.10**). However this failure seems due mainly to the sampler design, specifically to the sampler grid porosity that seems to accumulate dust and then to lose sensitivity **(Figure 8.16). Figures 8.11, 8.12 and 8.13**report the comparisons between Hg concentration mean daily measured by Tekran and Hg mass mean adsorbed on the passive samplers upon 1- 2- and 3-week exposures The preliminary results suggest best performances for passive samplers working for a week, since capable of detecting the daily fluctuations of Hg in the environment.
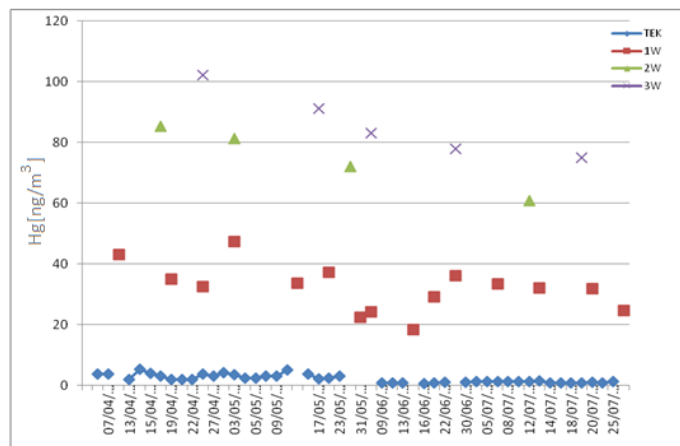

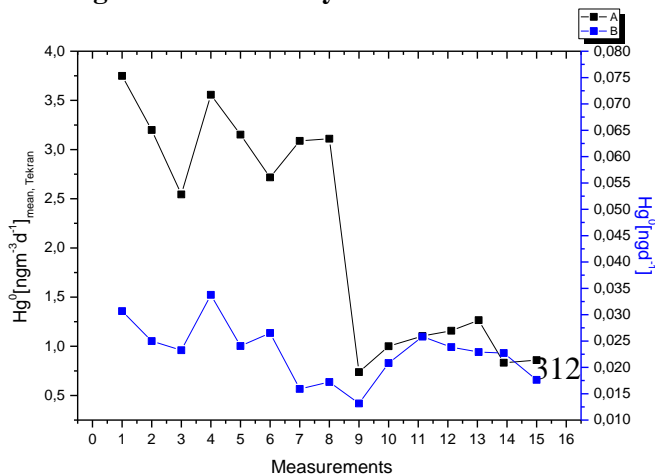**Figure 8.10: Mercury environmental monitoring for one, two and three weeks.**

Figure 8.11: Comparison Hg concentration mean daily measured by Tekran and Hg mass mean adsorbed on the passive samplers.
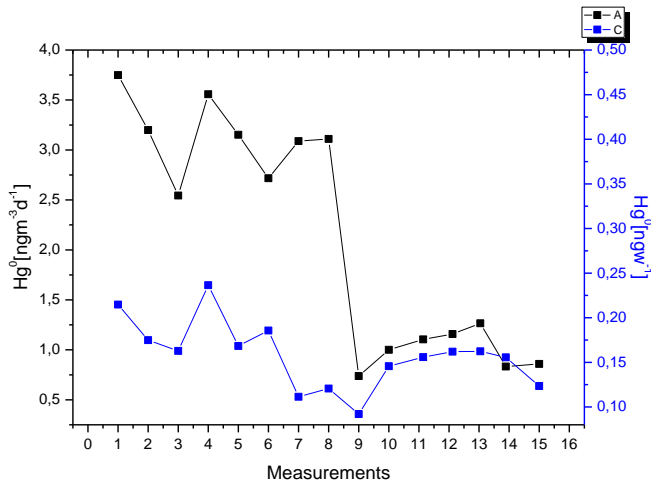
312

Figure 8.12: Comparison beteween Hg concentration mean daily measured by Tekran and Hg mass mean adsorbed on the passive samplers upon 1-week exposures.
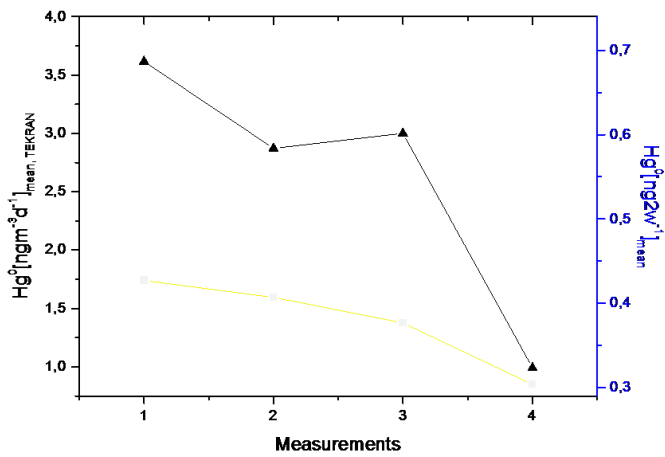

Figure 8.13: Comparison beteween Hg concentration mean daily measured by Tekran and Hg mass mean adsorbed on the passive samplers upon 2-week exposures.
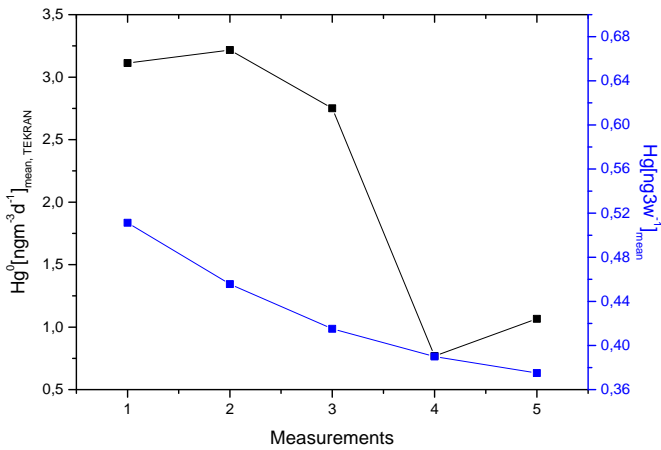

Figure 8.14: Comparison beteween Hg concentration mean daily measured by Tekran and Hg mass mean adsorbed on the passive samplers upon 3-week exposures.
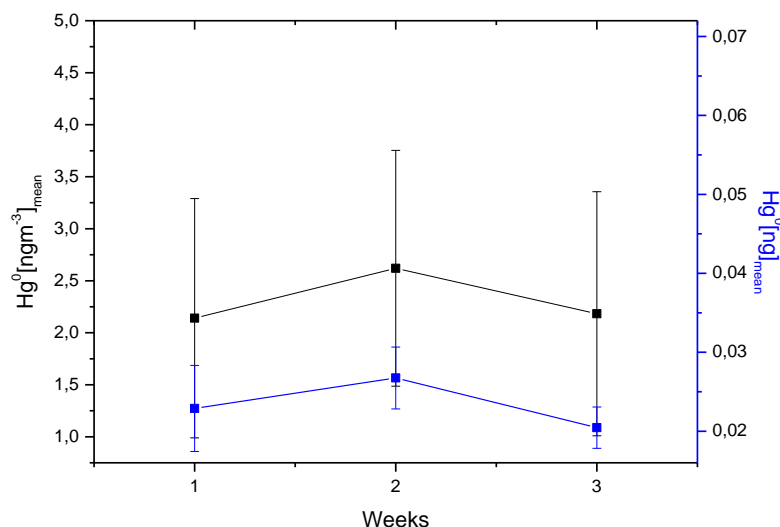
313

Figure 8.15: Comparison between Hg concentration mean daily measured by Tekran and Hg mass mean adsorbed on the passive samplers upon 1-, 2- and 3-week exposures normalized by the number of days. The bar means the standard deviation of Hg concentration, and it is related to the fluctuations of Hg in air.

However when the mass adsorbed in 1- 2- and 3-week exposed samplers and normalized for the number of exposure days are compared to the Hg concentration means daily measured, only a very slight decrease in efficiency is reported **(Figure. 8.15).** Probably a change in the sampler design will be able to reduce this drawback.

8.7 Passive sampling materials

For UNEP GEF project: "Development of a Plan for Global Monitoring of Human Exposure to and Environmental Concentrations of Mercury"), were prepared 250 passive samplers and adsorption and desorption processes of mercury (calibration and validation) in atmosphere are currently underway. Each passive sampler is composed by **(Figure 8.16):**

- Two white screw caps, open and closed, respectively;
- Two open supporting rings;

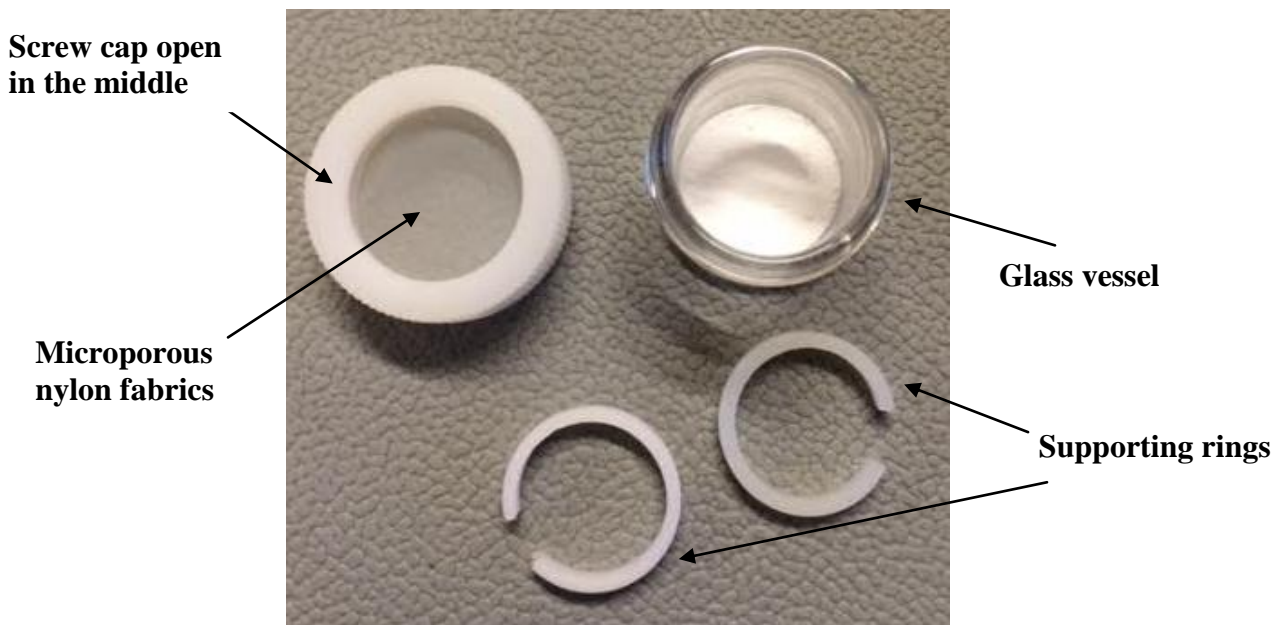- N. 1 passive membrane;
- N.1 glass vessel

Figure 8.16: Description passive sampler.

315

8.7.1 Elemental mercury sampling

In the various monitoring sites was shipped a box containing everything you need to carry out monitoring of elemental mercury. Each box comprises N. 1 shelter and N. 1 complete passive sampling set **(Figure 8.17).**

Figure 8.17: The content of a vacuum box.

Each sampling set includes up to N. 6 bags, labeled with sequential numbers, holding the samplers required for a 6-week monitoring campaign. Specifically each bag contains a well defined couples of samplers individually kept under vacuum. **(Figure 8.18)**

Figure 8.18: Bags from 1 to 6 and an under- vacuum passive

Each passive sampler is kept in a vacuum bag and each vacuum bag comprises **(Figure 8.19):**

N. 4 self-locking clear plastic bags;

N.1 sealed glass vessel (PASs);

N.1 open-cap mounting a diffusive barrier

Figure 8.19: The content of a vacuum bag

When you are ready for air sampling is necessary **(Figure 8.20):**

1) wear a pair of clean gloves picked up by a locked sachet;

2) remove the content; 4) unscrew the white cap of the glass vessel (2,3) and quickly screw the diffusive-cap (4,5);

5) immediately use one sachet to storage the unscrewed white cap, another one to keep both the remaining two sachets and the sachet with the cap, then close it (6);

6) expose the PAS for the scheduled exposure time, after having carefully placed it into the designated shelter seat, with the diffusive layer facing the air (i.e. the screw cap down) and fill in the Sampling Data Sheet **(Figure 8.21).**

All the samples as A will be subjected to a 1-week exposure, meanwhile B and C ones will be exposed to air for 2 and a 3 weeks, respectively. Finally, after 6 weeks all the exposed passive samplers will be removed and sealed. Environmental parameters (like temperature, %RH, main wind direction..)

should be daily reported on a suitable notepad and then joint to the samples at the end of monitoring, to be used for data analyses.

7) after each exposition, passive samplers will be removed and sealed with the own white cap and properly stored (dry, dark and cool place);

8) pack the sealed glass vessel in a sachet and lock it; pack it in a second sachet and lock it; pack it in a third sachet and lock it. 9) Put the diffusive-cap within the fourth bag and lock it too.

10) Depending on the planned exposure timing, replace the removed PAS with another one belonging to the same series (i.e. A with A, B with B and C with C) Contained in the following sequential bag using the same care as previously described.
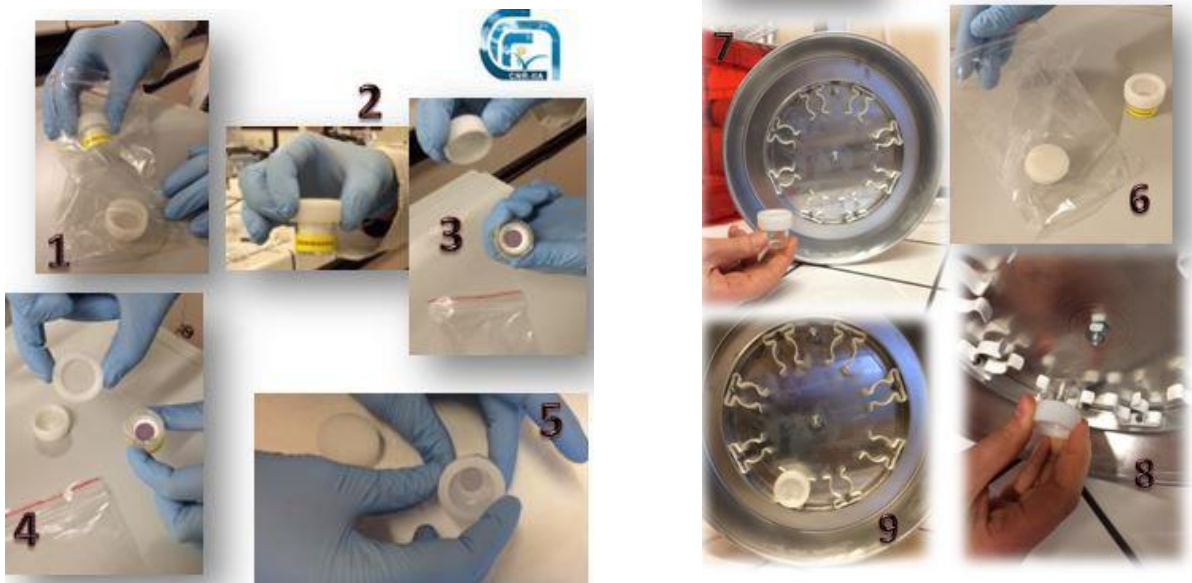

Figure 8.20: Elemental mercury sampling

Figure 8.21: The shelter placement and Passive samplers exposure

References

Gustin M. S., Huang J., Miller M. B., Peterson C., Jaffe D. A., Ambrose J., Finley B. D., Lyman S. N., Call K., Talbot R., Feddersen D., Mao H., Lindberg S. E. Do we understand what the mercury speciation instruments are actually measuring? Results of RAMIX Environ Sci Technol (2013), Vol. 47, pp. 7295-7306

Gustin M. S., Lyman S. N., Kilner P., Prestbo E. Development of a passive sampler for gaseous mercury. Atmos Environ (2011), Vol. 5, pp. 5805-5812

Harner T., Farrar N. J., Shoeib M., Jones K. C., Gobas F. Characterization of polymer-coated glass as a passive air sampler for persistent organic pollutants. Environ Sci Technol (2003), Vol. 37, pp. 2486-2493

Hedgecock I., Pirrone N., Sprovieri F., Pesenti E. Reactive Gaseous Mercury in the Marine Boundary Layer: Modeling and Experimental Evidence of its Formation in the Mediterranean. Atmospheric Environment (2003), Vol. 37/S1, pp. 41-49

Huang J., Lyman S. N., Hartman J. S., Gustin M. S. A review of passive sampling systems for ambient air mercury measurements. Environ Sci Process Impacts (2014), Vol. 16, pp. 374-392

Lyman S. N., Gustin M. S., Prestobo E. M. A passive sampler for ambient gaseous oxidized mercury concentrations. Atmos Environ (2010), Vol. 44, pp. 246-252

Pirrone N., Wenche Aas, Cinnirella S., Ebinghaus R., Hedgecock I. M., Pacyna J., Sprovieri F., Sunderland E. M. Toward the next generation of air quality monitoring: mercury. Atmos Environ (2013), Vol. 80, pp. 599-611

Plaisance H., Piechocki-Minguy A., Gracia-Fouque S., Galloo J. C. Influence of meteorological factors on the NO$_2$ measurements by passive diffusion tube. Atmos Environ (2004), Vol. 38, pp. 573-580

Pozo K., Harner T., Shoeib M., Urrutia R., Barra R., Parra O., Focardi S. Passive-sampler derived air concentrations of persistent organic pollutants on a north-south transect in Chile. Environ Sci Technol (2004), Vol. 38, pp. 6529-6537

Sderstrm H. S., Bergqvist P. A. Passive air sampling using semipermeable membrane devices at different wind-speeds in situ calibrated by performance reference compounds. Environ Sci Technol (2004), Vol. 38, pp. 4828-4834

Sprovieri F., Pirrone N., Bencardino M., D'Amore F., Angot H., Barbante C., Brunke E. G, Arcega-Cabrera F., Cairns W., Comero S., Diéguez M., Dommergue A., Ebinghaus R., Feng X. B., Fu X., Garcia P. E., Gawlik B. M., Hageström U., Hansson K., Horvat M., Kotnik J., Labuschagne C., Magand O., Martin L., Mashyanov N., Mkololo T., Munthe J., Obolkin V., Ramirez Islas M., Sena F., Somerset V., Spandow P., Vardè M., Walters C., Wängberg I., Weigelt A., Yang X., Zhang H. Five-year records of Total Mercury Deposition flux at GMOS sites in the Northern and Southern Hemispheres Atmos Chem Phys Discuss., doi:10.5194/acp-2016-517 (2016b)

Sprovieri F., Pirrone N., Bencardino M., D'Amore F., Carbone F., Cinnirella S., Mannarino V., Landis M., Ebinghaus R., Weigelt A., Brunke E. G., Labuschagne C., Martin L., Munthe J., Wängberg I.,

Artaxo P., Morais F., Barbosa H. J., Brito Cairns J., Barbante C., del Carmen Diéguez M., Garcia P. E., Dommergue A., Angot H., Magand O., Skov H., Horvat M., Kotnik J., Read K. A., Neves L. M., Gawlik B. M., Sena F., Mashyanov N., Vladimir Obolkin A., Wip D., Feng X. B., Zhang H., Fu X., Ramachandran R., Cossa D., Knoery J., Maruszczak N., Nerentorp M., Norstrom, C. Atmospheric Mercury Concentrations observed at ground-based monitoring sites globally distributed in the framework of the GMOS network. Atmos Chem Phys. (2016a), Vo. 16, pp. 1-21

Zhang W., Tong Y. D., Hu D., Ou L. B., Wang X. J. Characterization of atmospheric mercury concentrations along an urban-rural gradient using a newly developed passive sampler. Atmos Environ (2012), Vol. 47, pp. 26-32

Summary and conclusions

This research activity have concerned the development of advanced nanocomposite sensors, "smart", potentially stable and selectives, sensitive and small sizes; sensors that do not require high investment and operating costs, which allow an environmental monitoring "in situ" and the reach of all, that can be equipped with advanced interfaces for data transmission. In order to develop such systems, different hybrid nanomaterials have been designed and investigated, which thanks to their properties, resulted to be in line with the just mentioned requirements. From recent literature, electrospinning has been confirmed to be one of the best candidates among the various nanotechnologies for designing and developing smart and ultra-sensitive sensing systems, both for the uniqueness of the resulting nanostructures and for production rate and cost. More in detail, during the first phase of the study using electrospinning technology, titania nanofibers decorated with optical nanoparticles QDs have been synthesized. In particular, titania nanofibrous layers decorated with fluorescent core/shell nanoparticles (QDs) have been designed and investigated as potential optical sensors for detecting toxic gases in air (e.g. NH_3). Initially, fluorescent (CdSe)ZnS core-shell quantum dots were synthesized, according to literature, and then used to decor titania nanofibers according two strategies: the first one by drop-casting, the second one by chemical functionalization in situ. The use of electrospun fibers in photonics is a promising research field aimed at developing novel microscale light sources and detectors, lasers and optical sensors. This field is growing very quickly, since optically-active electrospun fibers with specific and tailored optical properties can be produced by various approaches exploiting the unique properties of organic light-emitting materials (tunability of the emission, strong absorbance, high quantum yield, large Stokes shift, etc.). The resulting fluorescent nanostructures combine remarkable optical performances with high exposed surface (orders of magnitude larger than flat

thin films), a property that is particularly appealing for sensing applications, indeed, the increase of exposed surface in fibers can greatly improve the sensitivity of devices. The high flexibility of the electrospinning (ES) process, in terms of number and typology of processable materials, is another feature promoting this technology as eligible candidate to a new generation of optical sensors. In the second phase of the study, an environmentally friendly conductive sensor has been designed and fabricated to measure gases and volatile organic compounds (VOCs). To achieve this goal, a biodegradable electrospun nanofibrous scaffold based on a polymer blend containing polyaniline and poly-3-hydroxybutirrate (PANi/PHB) has been employed. Several fabrics composed of distinct proportions of the two polymers have been tested. Morphology, electrical parameters and sensing features of the biodegradable nanofibrous layers have been investigated. The nanofibrous layers obtained through electrospinning technology carried out directly on chemoresistors resulted in highly porous membranes and the potentials of such blended scaffolds have been analyzed, focusing the attention on the influence of humidity on the features of the resulting sensors, also in terms of reproducibility and stability of their responses. Sensor responses to ammonia and further two volatile chemical compounds differently interacting with PANi (i.e. triethylamine and acetic acid) have been measured in dry air and at different percentages of relative humidity, in order to assess in possible applications the influence of PHB in the interactions of PANi with the analytes tested. Due to the properties of the electrospun nanofibers used in these chemoresistors, water vapours seemed to hugely improve the chemical interactions with the selected analytes. This effect suggests a potential use of the proposed chemosensors in monitoring also strongly moist environments. Subsequently it has been decided to dope the titania nanofibers also with metal nanoparticles. In particular, hybrid nanofibrous electrospun layers of TiO_2 coating Pt microelectrodes were suitably designed in order to create nanostructured 3D-frameworks, potentially capable of adsorbing and revealing elemental mercury vapors in the atmosphere. Indeed,

exploiting the outstanding photocatalytic properties of the nanofibers of titania, gold nanoclusters were selectively grown, under UV-light irradiation, on the electrospun titania nanofibers through the photocatalytic reduction of $HAuCl_4$ (tetrachloroauric acid) in the presence of an organic capping reagent. Due to the uniqueness of the resulting nanostructures (high surface to volume ratio, high fibers interconnectivity and nano-scale interstitial spaces) and for production rate and cost, the planned sensors were expected to be promising candidates for elemental mercury detection in traces. Exploiting the same principle of photocatalysis just described, titania nanoparticles have been combined with gold nanoparticles, forming novel passive sampling systems for mercury. The peculiarity of the passive samplers relies on the unassisted molecular diffusion of gaseous agents (i.e. volatile vapors of elemental mercury) through a diffusive surface onto an adsorbent scaffolding. Unlike active (pumped) sampling, passive samplers require no electricity (expensive pumps), have no moving parts, and are simple to use (no pump operation or calibration). After sampling, the adsorbed mercury should be desorbed off the adsorbent by solvent (chemical procedure) or thermal desorption (physical procedure). Passive samplers have to be commonly compact, portable, unobtrusive, and inexpensive. They are able to give information about the average pollution levels over time periods of 8 hours to weeks/months. They have not to require supervision and can be used in hazardous environments. The low cost of the materials allows for sampling at multiple locations.